POLY(L-LACTIC ACID) LANGMUIR MONOLAYERS AT THE AIR/WATER INTERFACE AND LANGMUIR-BLODGETT FILMS ON SOLID SUBSTRATES: PHASE BEHAVIOR, SURFACE MORPHOLOGY, AND CRYSTALLINITY

Suolong Ni

A dissertation submitted to the faculty of the
Virginia Polytechnic Institute and State University
in partial fulfillment of the requirement for the degree of

DOCTOR OF PHILOSOPHY
in
Chemistry

Alan R. Esker, Chair

Paul R. Carlier

T. Daniel Crawford

Hervé Marand

Judy S. Riffle

December 12, 2006

Blacksburg, Virginia

Keywords: Langmuir monolayers, Langmuir-Blodgett films, Poly(L-lactic acid), the liquid expanded to condensed (LE/LC) phase transition

POLY(L-LACTIC ACID) LANGMUIR MONOLAYERS AT THE AIR/WATER INTERFACE AND LANGMUIR-BLODGETT FILMS ON SOLID SUBSTRATES: PHASE BEHAVIOR, SURFACE MORPHOLOGY, AND CRYSTALLINITY

Suolong Ni

(Abstract)

Controlling the surface morphology and degree of crystallinity of poly(L-lactic acid) (PLLA) substrates have recently attracted considerable attention because of their applications in cell adhesion, tissue engineering, and drug delivery. Several techniques have been used to fabricate PLLA substrates, some of which may be invalid because PLLA can degrade during fabrication processes. This dissertation provides the Langmuir-Blodgett (LB) technique as a mechanism for fabricating PLLA substrates at temperatures where PLLA degradation is uncommon.

In order to fully understand surface morphologies of PLLA LB-films, studies of Langmuir monolayers at the air/water (A/W) interface using surface pressure-area (Π-A) isotherm and Brewster angle microscopy (BAM) are vital. PLLA exhibits a first-order liquid expanded to condensed (LE/LC) phase transition with molar mass dependent critical phenomena, the first such observation for a homopolymer Langmuir monolayer. Atomic force microscopy (AFM) images of PLLA LB-films prepared in the LC phase exhibit well-ordered lamellar structures. Molar mass scaling of lamellar dimensions, x-ray reflectivity, and reflection absorption infrared spectroscopy (RAIRS) measurements on PLLA LB-films are consistent with PLLA existing as single molecule 10_3-helices at the A/W interface.

Morphologies observed after collapse of the LC monolayer are dependent upon the collapse mechanism and subsequent thermal treatment. For temperatures below the LE/LC critical temperature (T_c), two mechanisms are identified for the formation of three dimensional structures: a buckling and stacking of lamellar monolayers on top of existing lamellae during constant compression rate experiments, and a modified nucleation and growth mechanism during isobaric area relaxation experiments. PLLA LB-films prepared in different Langmuir film phases at temperatures below T_c all contain lamellae with different surface roughnesses and similar helical content. Conventional thermal annealing studies on PLLA LB-films reveal that well-ordered lamellar features are destroyed after annealing the LB-films at bulk crystallization temperature through a melting-recrystallization process, which is confirmed by RAIRS and AFM.

Our results may prove useful for studying critical behavior and experimentally testing scaling predictions for two dimensions, the development and testing of theories for crystallization in confined geometries, and separating the roles that roughness and crystallinity play in cell adhesion and spreading on biocompatible polymer surfaces.

ACKOWLEDGEMENTS

I would like to thank Prof. Alan R. Esker for his guidance during my Ph. D study at Virginia Tech. As an advisor, Alan is strict, patient, and always encouraging. I appreciate his trust in letting me set the direction of my own research which kept me thinking all the time. I appreciate his trust in letting me take care of the lab, from which I have learned how to work as a team member and how to be a team leader. I appreciate his trust in letting me make my own career decisions with his valuable suggestions. Most importantly, I appreciate his high expectations for me which forced me to keep improving. I would like to thank my committee members, Profs. Paul R. Carlier, T. Daniel Crawford, Hervé Marand, and Judy S. Riffle for their many helpful conversations with respect to my courses and project. I also thank Prof. Mark Anderson for his help with my plan of study. I am also grateful to Prof. Hyuk Yu (University of Wisconsin) and Prof. A. Badia (University of Montreal) for useful discussions.

I am also grateful to all my groupmembers, Ritu Paul, Bingbing Li, Woojin Lee, Ufuk Karabiyik, Aziz Kaya, Wen Yin, Jae Hyun Sim, Qiongdan Xie, Josh Kittle, Zelin Liu, Robert Major, Vidhya Sivakumaran, Ben Vastine, Sarah Huffer, Michael Swift, and Jonathan Conyers. In particular I want to thank Woojin for his great friendship during the past four and a half years. I want to offer my sincere thanks to Bingbing and Ritu for enjoying and "suffering" together. I would like to thank Alan's first post-doc, Dr. Hyong-Jun Kim, for giving me helpful suggestions in my research. I would also like to thank two of Alan's students who have already graduated, Sheila Gradwell and Dr. Jianjun Deng for helping me settle down and training me in the lab.

I am happy that I have so many Chinese buddies here: Ting Cai, Yiqun Zhang, Ran Miao, Jun Qi, Liaosha Xu, Danny Xu, Hang Wang, Lan Yu, Xin Zhao, Xuelei Wang, Min Mao, Huimin Li, Zhenyu Huang, David Xu, Xiaodong Wang, Feihe Huang, etc. Life without them would have made my time in Blacksburg much more difficult. I also want to thank Mr. Simon Kwong for his fantastic food, which made me less homesick.

I would like to thank Mr. Steve McCartney in the Macromolecules and Interfaces Institute (MII) for training me on atomic force microscopy, Dr. Sushil Satija at National Institute of Standards and Technology for training me on x-ray reflectivity, Prof. John Morris and his student Dr. Melinda Ferguson-McPherson for help with infrared studies, Prof. Tom Ward and his student Dr. Hailing Yang, and Prof. Hervé Marand and his student Dr. Brian Okerberg for help with differential scanning calorimetry measurements.

I would like to thank my family for their support and love over the years. Special thanks to my dad, Shuchun Ni, for being extremely strong when mom was in an accident. I would have quit my study to fly back if you had not promised me everybody would be fine. I would thank my pretty wife to be, Yali Hu. Yali brings me the most happiness in my life, and I will leave what I should write in this sentence as the wedding vow. I am also grateful to Yali's parents for being considerate and supportive.

I would like to thank the department of chemistry for trusting me to teach CHEM 3615, MII for fellowship and travel awards, and the graduate school for a teaching award, and various research and travel funds. I am also grateful to the National Science Foundation (CHE-0239633) and the National Research Initiative of the USDA Cooperative State Research, Education and Extension Service, grant number 2005-35504-16088 for financial support.

Table of Contents

List of Figures

Chapter 8

List of Tables

CHAPTER 1

Overview

Controlling the surface morphology with a biodegradable and biocompatible polymer, poly(lactic acid) (PLA), has attracted considerable interest with respect to its importance in tissue engineering and drug delivery. In particular, crystallinity represents a fundamental material variable for controlling surface morphology.[1,2] For instance, poly(L-lactic acid) (PLLA) substrates with different degrees of crystallinity can be obtained by annealing spin-coated films at different temperatures. Park and Griffith-Cima suggested that cells prefer to adsorb on amorphous regions than on crystalline regions.[2] Washburn *et al.* found that the rate of cell proliferation decreases with increasing surface roughness.[1] Both results are consistent given the fact that a film's surface roughness generally increases as crystals form.[3] However, it is still not clear whether cell proliferation is controlled by crystallinity, surface roughness, or both factors. In this dissertation, we apply the Langmuir-Blodgett (LB) technique to prepare PLLA substrates which may prove useful for exploring the effects of crystallinity and/or surface roughness on cell proliferation.

Chapter 2 provides an introduction and review. In this chapter, a general introduction is made to organic thin films and techniques to fabricate thin films. The LB-technique, with advantages over other techniques for controlling thickness and orientation of surface structures, is described. In order to fully understand the surface structures on LB-films, it is crucial to understand the behavior of Langmuir films at the

air/water (A/W) interface, which is also detailed in Chapter 2. Techniques for studying Langmuir films, such as surface pressure – area per monomer (Π-*A*) isotherm studies and Brewster angle microscopy (BAM), are reviewed with examples of their application to traditional small molecule and polymers. Techniques for characterizing LB-films used in our study of PLLA, such as atomic force microscopy (AFM) and x-ray reflectivity measurements, are also summarized. In addition, the system examined in this dissertation, PLA, is reviewed with respect to its degradation and crystallization behavior as well as prior Langmuir film studies.

Chapter 3 introduces the materials and experimental methods that are used in this dissertation. Chapter 3 will be the only chapter containing a detailed description of experimental methods used in this study.

Chapter 4 describes the behavior of PLLA Langmuir monolayers at the A/W interface. Although previous researchers have studied PLLA Langmuir monolayers, a detailed interpretation has not yet been established. In this dissertation, we examine PLLA Langmuir monolayers at the A/W interface with Π-*A* isotherm studies and BAM. A first-order liquid expanded to condensed (LE/LC) phase transition is observed at low surface pressure. The observation of this LE/LC phase transition is novel as it is the first time an LE/LC phase transition has been observed for a homopolymer Langmuir monolayer. The LE/LC phase transition is both temperature and molar mass dependent. The temperature dependence of the LE/LC phase transition exhibits critical phenomena that are analogs to the critical behavior for gas/liquid transitions in three dimensions.

The molar mass dependence of the LE/LC phase transition suggests that the LE/LC phase transition is governed by free volume (area). A detailed thermodynamic analysis of the LE/LC phase transition is also provided in Chapter 4.

The LE/LC phase transition is a disorder to order transition for small molecules at the A/W interface. This feature is also confirmed by comparing the surface morphology of PLLA LB-films prepared in the LE and LC phases. Lamellar patterns are observed for LB-films prepared in the LC phase, but are absent in LB-films prepared in the LE phase. Dimensional analysis by atomic force microscopy (AFM) and x-ray reflectivity measurements suggests that the lamellar patterns are composed of 10_3-helices over the entire length of the polymer chain. These data lead to a hypothesis that PLLA single molecule helices lie flat on the water subphase like rigid rods, and can be deposited onto solid substrates by the LB-technique. The existence of 10_3-helices is also confirmed by reflection absorption infrared spectroscopy (RAIRS). This hypothesis is described in Chapter 5, and is important for understanding different surface morphologies for PLLA LB-films described in subsequent chapters.

In addition to the LE/LC phase transition described in Chapter 4, a two-dimensional (2D) to three-dimensional (3D) phase transition, known as collapse, is also present for PLLA Langmuir monolayers. Two mechanisms are proposed in Chapter 6. During compression experiments at constant rates, PLLA Langmuir monolayers appear to collapse by cracking of the lamellar monolayer followed by part of the film sliding over another part of the film much like the shifting of plates along a fault line during an

earthquake. This process is described as a "buckling and stacking" mechanism, through which 3D multilayer structures grow after collapse during constant compression rate experiments. Upon expansion, these 3D multilayer structures can respread onto the subphase. A second mechanism is proposed for isobaric area relaxation experiments. In these experiments, "slow collapse" of PLLA Langmuir monolayers is achieved by a combination of several processes: a process of molecular rearrangement into a more closely packed monolayer state, additional molecular rearrangement to form 3D nuclei, and finally the growth of 3D domains.

The hypothesis that PLLA single molecule 10_3-helices lie flat on the water subphase also suggests that the as-prepared PLLA LB-films have high helical content as all molecules are in a 10_3 helical conformation prior to transfer. RAIRS is a good technique to examine this feature. RAIRS results in Chapter 7 confirm that the as-prepared LB-films have high helical content compared to the as-received bulk and recrystallized spin-coated films. Annealing PLLA LB-films at bulk crystallization temperatures (T_x) yield infrared spectral changes that mimic a melting-recrystallization process, leading to the hypothesis that PLLA LB-films may melt at temperatures below bulk T_x values. This hypothesis is confirmed by morphological changes *via* AFM studies that well-ordered lamellar features grow into 3D structures after annealing. On the other hand, annealing PLLA LB-films above bulk melting temperature (T_m) followed with fast cooling to room temperature yields substrates with very helical content. This feature is confirmed by RAIRS and AFM studies.

Chapter 8 provides the overall conclusions for this dissertation and several suggestions for future work: (1) Determination of the binodal phase boundary for the LE/LC phase transition of PLLA Langmuir monolayers at the A/W interface; (2) Collapse of PLLA Langmuir monolayers at a temperature above the critical temperature of the LE/LC phase transition by constant compression rate experiments, hysteresis loop experiments, and isobaric area relaxation experiments; (3) Thermal properties of PLLA LB-films with differential scanning calorimetry (DSC), in-situ AFM and IR studies; (4) Cell adhesion studies with PLLA LB-films.

CHAPTER 2

Introduction and Review

2.1 General Introduction to Organic Thin Films

Organic thin films have wide spread applications in many areas. They are frequently used as components in sensors,[4] detectors, and displays,[5] as well as in organic electro-optical devices such as solar cells,[6,7] light-emitting diodes,[8] field-effect transistors,[9,10] etc. The potential applications of organic thin films become more promising because of the almost unlimited possibility to synthesize organic molecules with desired structure and functionality. In particular, organic thin films from polymers are attracting increasing interest for adhesion and biomedical applications.[11-13] For example, a thin polymer coat can act as a glue for a relatively inert surface to significantly enhance adsorption and adhesion.[11] On the other hand, polymer thin films can also be used to hinder surface adsorption.[14] For instance, a coating of hydrophilic chains can inhibit protein adsorption. Similarly, a polymer layer on industrial molding machines can prevent extensive sticking and ensure the quick release of injection molded parts such as car bumpers.[11]

Various techniques have been reported to prepare organic thin films, including spin-coating, tethering of polymer "brushes",[15] micro-imprinting lithography,[16] soft lithography,[17] direct deposition,[18] laser stereolithography,[19] laser micro-patterning,[20] nanosphere lithography,[21] in-situ polymerization on the surface,[22] thermal evaporation,[23] electrodeposition,[24] self-assembly,[25] the Langmuir-Blodgett (LB) technique,[26,27] etc.

Some of the above techniques may not be suitable to fabricate substrates with either thermal or laser degradable materials (biomaterials for instance). Furthermore, properties of organic thin films are largely affected by their morphology[4] which depends on the nanometer- or micrometer-scale order within the films. Taking these two considerations into account, the LB-technique becomes one of the best non-destructive techniques for preparing well-ordered patterns and complex architectures.[28-35] The LB-technique facilitates monolayer by monolayer control of thickness, enhances homogeneous deposition of the monolayer over large areas, and provides the possibility to fabricate multilayers with varying layer structures. More importantly, with the ability to prepare molecules with hydrophobic or hydrophilic functional groups (or blocks for co-polymers), it is possible to deposit LB-layers onto many kinds of solid substrates.

Before going further, it is necessary to address the differences in thickness for organic thin films and ultra-thin films. Organic thin films may be defined as a piece of material having a small dimension in only one direction (thickness in general). In this respect, it is a relative concept; and consequently, there is no absolute scale to describe the thickness of an organic thin film. More particularly, organic thin films are considered to have thickness values varying from a layer of atoms (or molecules) to several micrometers. In our study, we are interested in ultra-thin molecular films with thickness varying between one atomic (molecular) layer and several hundred nanometers.[29-31,33,34] Throughout this dissertation, thin films stand for ultra-thin films unless otherwise stated.

The reduction in thickness may lead to changes in physical and chemical properties. The changes in the properties are the scientific reason for this dissertation.

2.2 Langmuir Films versus Langmuir-Blodgett Films

LB-films are deposited onto solid substrates from the air/water (A/W) interface. Therefore, it is essential to understand the behavior of molecules at the A/W interface so as to thoroughly understand surface patterns and the morphology of LB-films. Unlike soluble molecules that will dissolve into the aqueous subphase after spreading, certain insoluble amphiphilic molecules can form stable spread films. The spread films of amphiphilic molecules on water are called Langmuir films, which are also known as Langmuir monolayers. Despite their conventional names as monolayers, Langmuir monolayers can be monomolecular or multimolecular. LB-films are defined as molecular films prepared by depositing films from the interface by the LB- or Langmuir-Schaeffer (LS) techniques. The LB-films can be either single layer or multilayer. This dissertation will start by trying to understand the physical properties of Langmuir monolayers followed by the characterization of LB-films.

2.3 Langmuir Monolayers at the Air/Water interface

Langmuir monolayers are primarily formed on the surface of water by amphiphiles which have two distinct parts, a hydrophobic tail and a hydrophilic head. The

hydrophilic heads favor dissolution of the amphiphiles into the subphase, while the hydrophobic tails try to keep the molecules out of the subphase. As the hydrophobicity of the tails increases, the solubility of the amphiphiles decreases. If the tails are hydrophobic enough, the molecule will be insoluble and can form an isolated essentially two-dimensional (2D) system on the surface. Many molecules which can form Langmuir monolayers on water, such as fatty acids, lipids, polymers, etc, will be summarized shortly.

Langmuir monolayers are interesting for several reasons.[36] First, a Langmuir monolayer is an excellent model system for studying ordering in 2D. The water surface severs as a very smooth substrate (root mean square roughness of 3 - 5 Å).[37] Two thermodynamic variables, temperature and surface pressure, can be directly controlled as direct analogs to temperature and pressure, respectively, in three dimensions (3D). Second, Langmuir monolayers can be used to study intramonolayer and monolayer-subphase interactions at a molecular level. By changing head and/or tail groups of the molecule or the environments (such as pH values or ionic strengths of the subphase), it is possible to widely vary the interactions. Moreover, Langmuir monolayers are excellent model systems for bio-membrane studies, because a biological membrane can be considered as two weakly coupled monolayers. Indeed, some amphiphilic molecules can assemble into stable bilayers, mimicking the behavior of biological membranes.[29] Langmuir monolayers are also used as templates for 2D chemical and biological reactions.[38] The reduced dimensionality in Langmuir

monolayers can sometimes simplify model theoretical calculations.[39,40] Furthermore, understanding thermodynamic phase transitions in Langmuir monolayers is crucial for fabricating thin molecular films onto solid substrates by the LB-technique.

2.3.1 History of Langmuir and Langmuir-Blodgett Films

People were familiar with molecular films on water in ancient times. One form of divination in Babylonia recorded on clay tablets around the 18th century B.C. was to observe the spreading of oil in a cup filled with water. This observation was used by Babylonians to predict success, marriage, birth of child, or bad luck, sickness, death, etc.[41] Ancient Greek writings also described the calming effect of oil on a rough sea. This dampening effect was attributed to Phiny the Elder, and was often utilized by sailors to insure a smooth sea surface on their travels.[42] A paper marbling technique, which originated in China over 2000 years ago, became popular in Japan 1200 years ago. In the so called "suminagashi" technique, which literally means "ink-floating" or "ink-streaming", Chinese ink, a suspension of carbon particles in a protein solution, was spread onto a water surface. A protein monolayer was formed, which was picked up by paper using a horizontal lifting technique. This was regarded as the earliest technical application of Langmuir films.[43] Centuries later, Benjamin Franklin, who was aboard one of 96 ships, noticed that ships in back seemed to have smoother sailing than ships in the front. The observation led to the first scientific recognition of the importance of surface films on water, and motivated his famous Clapman pond experiments, where a teaspoonful of oil was spread onto the water surface of the pond.[44] Franklin's

experiment inspired many investigators to consider sea surface phenomena or to conduct experiments with oil films.[42,45-47] All of these qualitative observations of oil on water were systematically investigated by Agnes Pockels in 1882 in her kitchen, using a bowl to contain water.[29,34] With the volume of the oil drop and the surface covered, the thickness of the film and the surface area of the "particles" were calculated. Different types of oil were tested, and the size of each oil element was obtained. She also used barriers which constrained oil films on water surface and compressed the films. Meanwhile she developed a rudimentary surface balance to measure surface tension (γ) of the oil-covered surface, which fell rapidly when the monolayer was compressed below a certain area. This combination allowed for quantitative measurements and her work was published in *Nature* with the recommendation of Lord Rayleigh.[48] Her surface pressure-surface area (Π-A) isotherm of stearic acid is now recognized as the first such study, and is regarded as the beginning of the monolayer odyssey.[49,50] Inspired by her work, Lord Rayleigh repeated some of her experiments, and concluded that the oil layers on the water surface were a single-molecule thick. He also obtained a value for the size of a surfactant molecule even though many scientists in that period did not believe in the existence of atoms.[51]

The next important discovery was made by William Bate Hardy in 1912. He found that unlike oils with a polar group, oils without polar functional groups did not spread on the surface of water. He stated for the first time that polar molecules might have an orientation on the water surface, and he suggested that the orientation was induced by

long range cohesive forces between the molecules.[52] His statement about orientation was correct; however his suggestion that long range cohesive forces were responsible for the orientation was later proven to be wrong. In the early 1900s, Irving Langmuir greatly extended the experimental methods for studying insoluble monolayers at the A/W interface.[53,54] He developed a surface film balance which now carries his name, Langmuir film balance, in which a film-covered surface was separated from a clean water surface with a movable float. Deflection of the float provided a direct measure of the differential surface tension ($\Delta\gamma$), or surface pressure (Π), which will be described shortly. Unlike his forerunners who were using oils, Langmuir used chemically pure substances from which he presented evidence for the monomolecular nature of the film as well as the orientation of the molecules at the A/W interface.[53] Furthermore, Langmuir showed that the forces between the molecules were short range and only existed among molecules that were in contact, which was in contrast to the proposal by Hardy.[52] His findings led to our understanding of monolayer structures at the molecular level, as well as a good understanding on why certain molecules form or do not form various kinds of films. Langmuir was also the first to show that these monomolecular films can be transferred from the A/W interface onto solid substrates.[54] Together with his assistant, Katherine Blodgett, he demonstrated that it was possible to go further and to deposit multiple monolayers successively onto the same solid substrates, building up multilayers with controlled thickness.[55,56] The deposited monolayers onto solid substrates are now known as LB-films. LB-films prepared from small molecules, such as fatty acids, have

poor thermal and mechanical stabilities and limited resistance to dissolution in organic solvent.[56-59]

2.3.2 Formation of Langmuir Monolayers

Traditional amphiphilic molecules that form Langmuir monolayers at the A/W interface contain hydrophilic ("water-loving") heads (such as an acid or alcohol group) that anchor onto the water surface and hydrophobic ("water-hating") tails (such as a long hydrocarbon chain) that point towards air. The balance between the opposing natures of the hydrophilic heads and hydrophobic tails keep the molecules at the interface.[60] Amphiphiles must have very low solubility in water to prevent dissolution and small enough vapor pressures to prevent evaporation. Classes of small molecules that commonly form Langmuir monolayers at the A/W interface include long-chain fatty acids, alcohols, esters, and phospholipids as shown in Figure 2.1.[36] These molecules consist of one or several long hydrocarbon chain(s) having at least 12 to 14 carbon atoms and a polar hydrophilic head group. Recently, molecules with multiple polar heads were synthesized which can form stable Langmuir monolayers with varying tail lengths and numbers of tails (Figure 2.2).[61]

Amphiphilic polymers can also form stable Langmuir monolayers, including polyacrylates such as poly(tert-butyl acrylate) (PtBA), polymethacrylates such as poly(tert-butyl methacrylate) (PtBMA) and poly(methyl methacrylate) (PMMA), polyesters such as poly(lactic acid) (PLA) and poly(ε-caprolactone) (PCL), polyethers such as high molar mass poly(ethylene oxide) (PEO), polyvinylesters such as

poly(vinylacetate), polyvinylhalides such as poly(vinylfluoride), silicones, comblike copolymers processing long alkyl side chains, amphiphilic block copolymers (AB, ABC, ABA, etc), etc. Langmuir monolayer studies of polymers will be summarized later in this chapter.

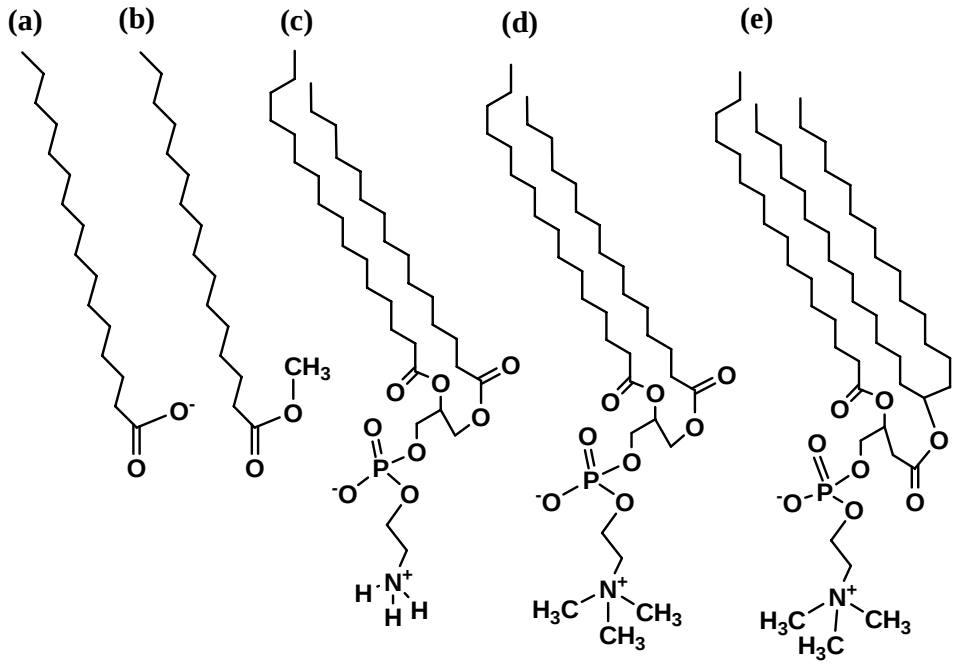

Figure 2.1: Some frequently used lipid molecules that can form Langmuir monolayers at the A/W interface: (a) ionized n-hexadecanoic (palmitic) acid, (b) n-hexadecanoic acid methyl ester, and various phospholipids: (c) dipalmitoylphosphatidylethanolamine, (d) dipalmitoylphosphatidylcholine, and (e) dipalmitoylphosphatidylcholine with an aliphatic branch.[36]

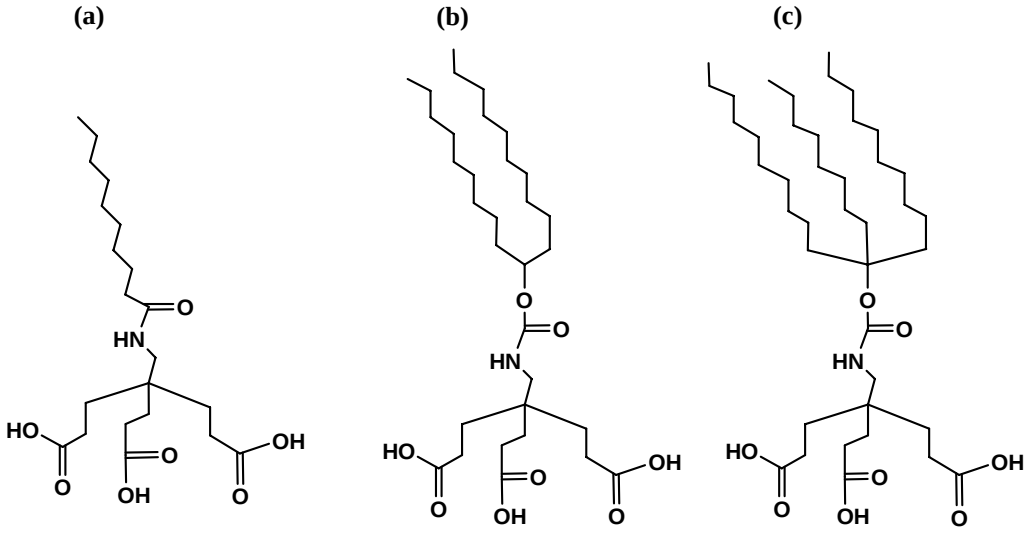

Figure 2.2: Examples of some tri-headed fatty acids with: (a) one, (b) two, and (c) three tails that can improve solubility and molecular recognition.[61]

Some insoluble amphiphiles can naturally spread onto the water surface to form Langmuir monolayers, while most molecules only form droplets on the surface. Therefore spreading solvents, which must be volatile and completely spread on water, need to be used to dissolve the amphiphiles before they are spread onto the surface. Some organic solvents have been reported to be useful as spreading solvents, such as acetone, dichloromethane, chloroform, etc.[62,63] Spreading solvents can affect the phase behavior of Langmuir monolayers, and chloroform is the most widely used because of its moderate volatility and good spreading behavior on water. When a drop of dilute spreading solution is placed on the water surface, it spreads over the surface. After the

evaporation of the spreading solvent, amphiphiles are ideally left on the surface as a monomolecular film.

2.4 Surface Pressure-Surface Area Isotherms

For over a century, surface pressure-surface area (Π-*A*) isotherms have been the major source of thermodynamic data for Langmuir monolayers. In this section, the definition of Π will be described. Experimental techniques for measuring Π, and hence Π-*A* isotherms, are also discussed.

2.4.1 Surface Tension (γ) versus Surface Pressure (Π)

The absence of stabilizing nearest neighbor interactions for surface molecules relative to bulk molecules means that the surface of a liquid always has an excess free energy. For the water surface in particular, hydrogen bonding in bulk tends to establish a loosely defined network that will unavoidably be modified near the surface. The system tends to pull molecules into the interior of the phase to minimize its surface energy, and hence to minimize the surface area. This effect leads to the definition of surface tension, γ, which manifests itself as a force per unit length.[64] At thermodynamic equilibrium, surface tension of a planar interface is given by partial derivatives of free energy functions with respect to the area of the surface:[29]

$$\gamma = \left(\frac{\partial F}{\partial A}\right)_{T,V,n} = \left(\frac{\partial G}{\partial A}\right)_{T,p,n} \qquad \text{(Eq. 2.1)}$$

where F and G are the Helmholtz and Gibbs free energies, respectively, A is the surface area, and temperature T, volume V (or pressure p), and composition n are held constant. Compared to most organic liquids, water has a very high γ value of about 73 $mN \bullet m^{-1}$ at 20 ^{o}C and 1 atm, because of its strong hydrogen bonding interactions. This feature is one of the many reasons why water is by far the most widely used subphase in Langmuir monolayer studies.

When amphiphiles are spread onto water, the interactions between water molecules and the hydrophilic heads will lower the surface energy resulting in a decrease in γ. If the monolayer molecules can be packed tightly together on the surface by compression of a barrier system, the molecules try to repel each other. The repulsive effect, as a 2D analog of pressure, is normally called surface pressure, Π. The existence of Π opposes the contracting tendency of the water subphase, thereby lowering the surface tension. For a planar surface at equilibrium, the surface pressure is generally considered to be equal to the reduction of the pure liquid surface tension by the film, *i.e.*

$$\Pi = \gamma_0 - \gamma \qquad \text{(Eq. 2.2)}$$

where γ_0 is the surface tension of pure water, and γ is the surface tension of the film covered surface.

2.4.2 Techniques to Measure Surface Pressure

In his 1917 paper, Langmuir used a strip of waxed paper as a float to measure surface pressure.[53] The float separated a clean water surface from the surface covered with the monolayer, and was connected to a conventional balance that measured the force acting

on the float. This technique later became known as Langmuir film balance. The other more commonly used method to measure surface pressure is the Wilhelmy plate technique.[65,66] In this technique, a thin plate, usually of glass, quartz, mica, platinum, or paper, is immersed into the water subphase, and is connected to a high-sensitivity electrobalance. The forces acting on the plate are: a downward gravitational force (W), a downward force because of surface tension and an upward buoyant force that arises from the weight of liquid displaced by the plate. The sum of these forces is counteracted by the observed upward force (F_{obs}) that is read by the electrobalance. The force balance on the plate yields the following equations:

$$\gamma = \frac{F_{obs,film} - W}{2(L+t)\cos\theta} \qquad \text{(Eq. 2.3)}$$

$$\Pi = \gamma_0 - \gamma = \frac{F_{obs,0} - F_{obs,film}}{2(L+t)\cos\theta} \qquad \text{(Eq. 2.4)}$$

where $F_{obs,0}$ is the observed force for pure water surface, while $F_{obs,film}$ corresponds to the observed force for the film covered surface; L is the length of the plate, t is the thickness of the plate which is usually negligible compared to L, and θ is the contact angle between the liquid subphase and the plate at the interface as shown in Figure 2.3. For plates that can be completely wet with water (filter paper for instance), the contact angle can be regarded as zero, which leads to a simplified equation:

$$\Pi = \gamma_0 - \gamma = \frac{F_{obs,0} - F_{obs,film}}{2L} \qquad \text{(Eq. 2.5)}$$

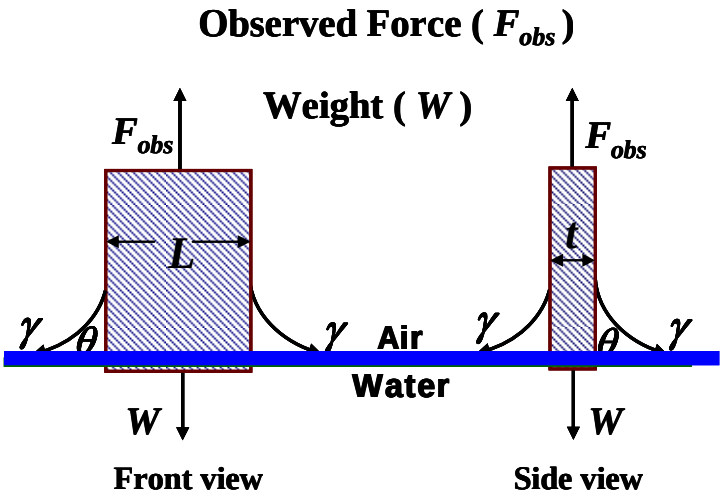

Figure 2.3: Wilhelmy plate technique to measure surface pressure, Π, at the A/W interface.

2.4.3 Langmuir Trough for Π-*A* Isotherm Measurements

Π-*A* isotherms are obtained from an apparatus traditionally referred to as a Langmuir trough (Figure 2.4). Materials used to make Langmuir troughs need to meet specific requirements: (1) they must be inert, in particular they must not release impurities; (2) they should preferably be hydrophobic for easy cleaning; (3) they should withstand organic solvents and inorganic acids; and (4) they should be easily shaped.[65] Polytetrafluoroethylene (PTFE), also known as Telfon™, is hydrophobic and resists almost all chemicals. Hence it is the material most commonly used to construct Langmuir troughs.[65,67] The most commonly used subphase is water, although mercury[68] and other materials such as glycerol[69] are also used as subphases. After monolayer formation on the water surface, movable barriers are used to alter the surface area

occupied by the molecules, thereby altering the surface concentration (Γ). Barriers are made of hydrophilic Delrin^{TM}, or hydrophobic PTFE. A Langmuir trough may contain a single barrier, or two barriers to achieve symmetric compression from both ends of a film. The barrier(s) may be moved *via* a gearing system to an electric motor, or indirectly by magnetic means.[65] Some Langmuir troughs also include a circulating system, for maintaining the subphase at a constant temperature.

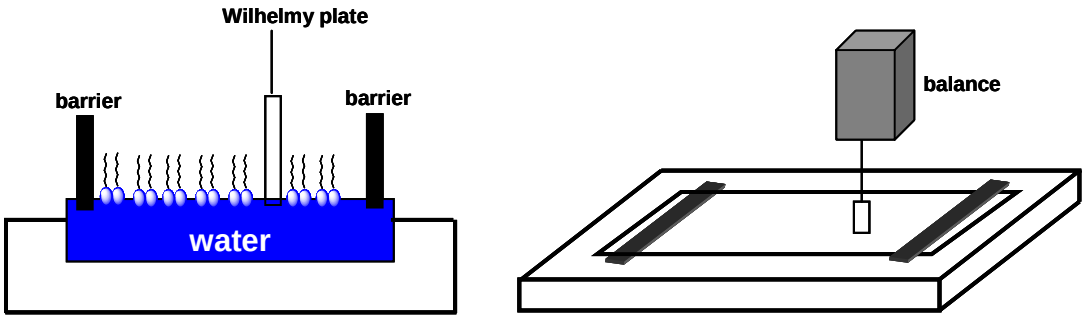

Figure 2.4: Schematic diagrams of a Langmuir trough with two barriers.

Different Langmuir troughs have different areas; hence it is not proper to compare isotherms in terms of the surface area of the trough, an extensive variable. Instead, in Π-A isotherms, A represents surface area per molecule for small molecules or per repeating unit (or monomer for short) for polymers. A is defined as the average area occupied by each insoluble amphiphilic molecule (or monomer) on water surface. It is calculated by dividing the trough area by number of spread molecules (monomers) as shown in Equations 2.6 and 2.7:

$$A = \frac{A_{trough}}{\#\ of\ molecules\ on\ the\ surface} = \frac{A_{trough}}{mol \bullet N_A} = \frac{A_{trough}}{molarity \bullet volume \bullet N_A} \qquad \text{(Eq. 2.6)}$$

and

$$A = \frac{A_{trough}}{mol \bullet N_A} = \frac{A_{trough} \bullet M_0}{mass\ concentration \bullet spreading\ mass \bullet N_A} \qquad \text{(Eq. 2.7)}$$

where M_0 is molar mass of the molecule for small molecules or repeating unit for polymers, N_A is the Avogadro's constant, and A_{trough} is the surface area of the Langmuir trough.

After the formation of a monolayer, the trough area can be changed *via* the movement of barriers. During compression, surface area available to the molecules decreases, hence A value decreases. Surface concentration (Γ), which is defined as $\Gamma = 1/A$, increases during compression. The advantage of reporting Π-A instead of Π-Γ isotherms is that A can provide direct information about the size of a molecule, monolayer structures, monolayer-bilayer transitions, etc.

2.4.4 Different Phases in Langmuir Monolayers

Π-A isotherms are analogs to p-V isotherms in 3D, as Π is just a pressure distributed over the thickness of thin films. Figure 2.5 shows a comparison between Π-A and p-V isotherms. Monolayers in 2D have several different phases such as gas, liquid, and solid, just like bulk materials in 3D. The existence of different phases and phase transitions in 2D can be elucidated from Π-A isotherms.

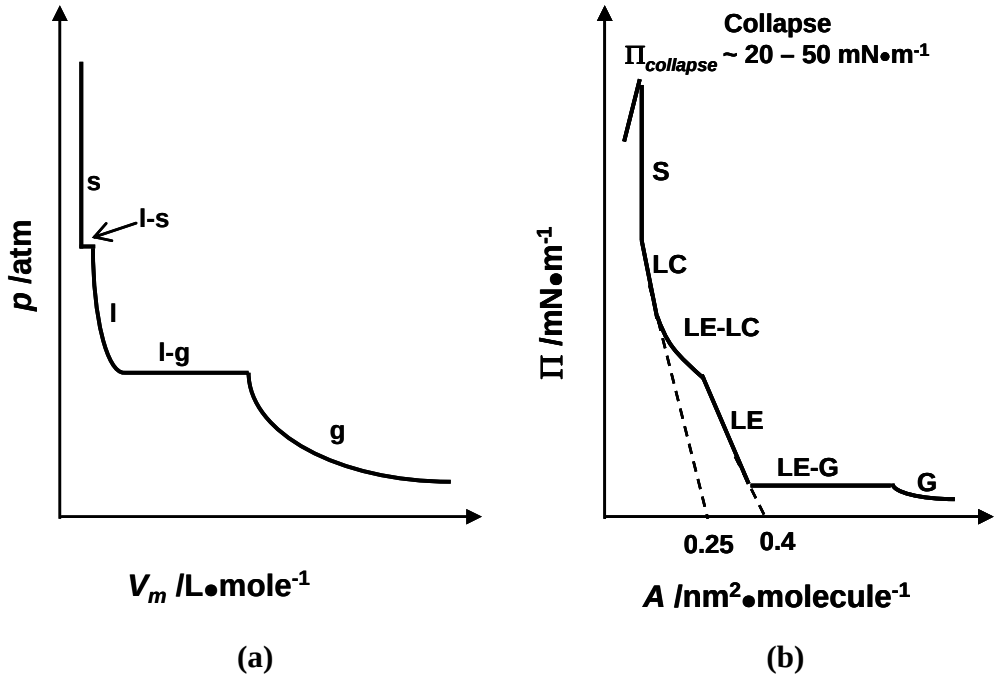

Figure 2.5: Comparison between 3D and 2D isotherms: (a) A *p*-*V* isotherm for CO_2 at 20 ^oC,[70] where g stands for gas, l for liquid, and s for solid. A first-order gas to liquid phase transition is observed. (b) A Π-*A* isotherm for n-pentadecanoic acid at 25 ^oC on a subphase with pH = 2,[71] where G is a gas phase, LE is a liquid-expanded phase, LC is a liquid-condensed phase, and S is a solid phase. Phase transitions are observed between G-LE, LE-LC, LC-S, and a 2D to 3D transition where the monolayer collapses into multilayer structures at the collapse pressure, $\Pi_{collapse}$.

At very large surface area *A* (or low surface concentration Γ), molecules are far apart from each other, therefore the interactions between adjacent molecules are very weak. This corresponds to a 2D gaseous (G) phase, which has little effect on surface tension of water and exhibits very low surface pressure values (~ 0.01 mN•m^{-1}). *A* is large

compared to the molecular dimensions in the G phase, and the hydrocarbon portions of the molecules may make significant contact with the water surface, as shown in Figure 2.6. As the surface area of the monolayer is reduced further, the hydrocarbon chains will lift from the surface and start to interact with each other, where the Langmuir monolayer enters a "liquid" state. At least two types of liquid phases exist: liquid-expanded (LE) phase and liquid-condensed (LC) phases. The difference between the LE and LC phases is the ordering. In the LE phase, the hydrocarbon chains are in a random orientation; while in the LC phase, the molecules are closely packed and are oriented with the hydrocarbon chains pointing away from the water surface (Figure 2.6). The extrapolation of the isotherm in the LC phase to the x-axis provides the limiting area value, which can be used to estimate the actual cross-sectional area of the head-groups of the amphiphiles. Upon further compression, 2D Langmuir monolayers may behave like solids (S), and can finally form 3D structures after collapse (Figure 2.5b).

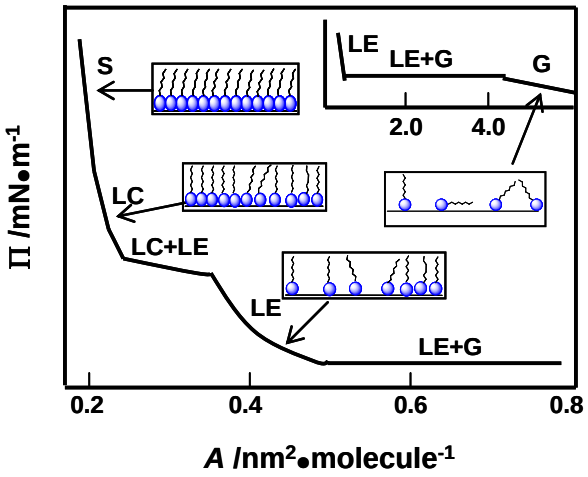

Figure 2.6: A schematic Π-*A* isotherm for typical amphiphilic molecules at the A/W interface. The area scale on the plot roughly corresponds to that found for a fatty acid at room temperature. The inset shows the transition between G and LE phases.[60]

The description of the LC phases as provided is not without its detractors. Some have argued that the LC phase is not a liquid, but is rather a 2D solid. Accordingly, both LC and solid phases are named as condensed phases. The difference between the LC and S phases is whether hydrocarbon chains are tilted or not, as shown in Figure 2.7.[36] These distinctions come not only from interpreting Π-*A* isotherms, but also require "optical" measurements. Figure 2.8 shows an experimental Langmuir monolayer phase diagram for eicosanoic acid derived mainly by locating the phase boundaries from optical measurements such as Brewster angle (BAM) and fluorescence (FM) microscopies.[72] In tilted phases, the molecular axes are tilted with respect to the surface normal, while in the untilted phases, the axes are perpendicular to the interface. Titled LC phases include L_2,

L_2', L_2'', and Ov, and untilted condensed phases include LS (superliquid), S (solid), and CS (close-packed solid) phases. In the L_2 and L_2'' phases, the alkyl chains are tilted towards the nearest neighbors (NN), and in the L_2' and Ov phases, the alkyl chains are tilted towards the next nearest neighbors (NNN, 90^o away from the L_2 tilt direction). In the untilted condensed phases, V-shaped order has been observed in the S and CS phases, while hexatic order is observed in the LS phase. In this dissertation, I will use "liquid-condensed" (LC) to describe well-aligned condensed phase because of the historical assumptions that the condensed phases are liquid like and the fact that the term "LC" is most widely used in the literature.

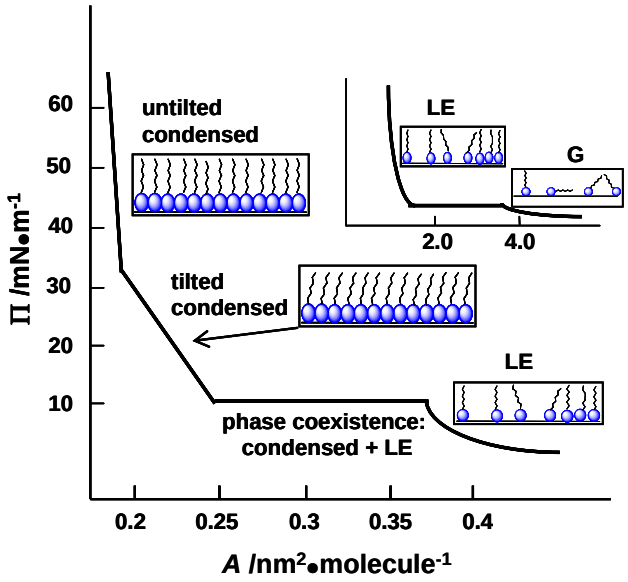

Figure 2.7: A generalized Π-*A* isotherm for a Langmuir monolayer with tilted and untilted condensed phases. First-order G/LE and LE/condensed phase transitions are observed, and the tilted to untilted condensed phase transitions are continuous.[36]

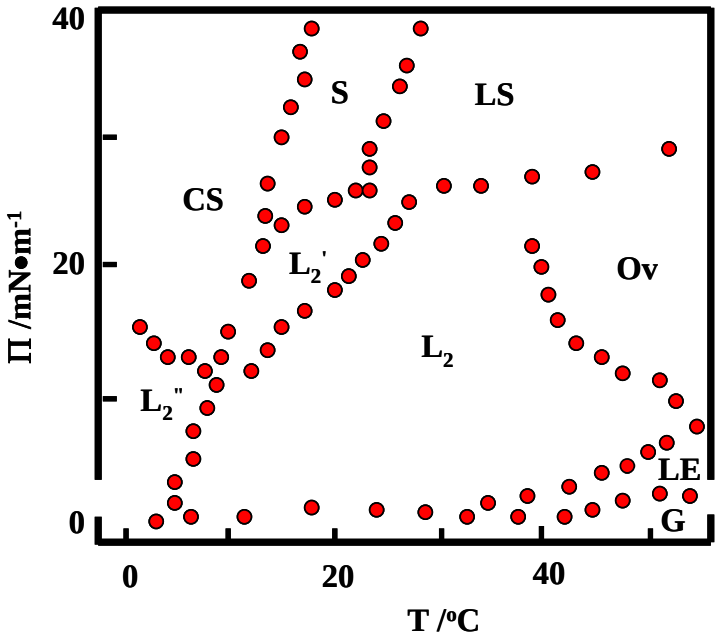

Figure 2.8: Experimental Langmuir monolayer phase diagram for eicosanoic acid (C_{22}). The phase boundaries have been determined primarily from BAM and FM results.[72]

2.4.5 Phase Transitions in Langmuir Monolayers

As seen in Figures 2.6 and 2.7, horizontal lines are observed during G/LE and LE/LC phase coexistence, while LC/S phase transitions are continuous. Horizontal lines in the isotherm reveal that the G/LE and LE/LC phase transitions are first-order, while LC/S phase transitions are second-order. The difference between first-order and second-order transitions is whether or not the first derivative of chemical potential is continuous. For first-order phase transitions, the first derivative of chemical potential is discontinuous, resulting in different volumes for two phases. Consequently, the densities of coexisting

phases during a first-order phase transition differ from each other. The density of the mixture is just an average of densities of both phases and changes during the phase transition. Hence the mixture will display a heterogeneous surface morphology. In second-order phase transitions, densities of both phases are the same, hence the surface morphology is homogeneous.

First-order G/LE phase transitions involve an interplay between translational entropy and intermolecular attraction. G/LE phase transitions occur at very low Π values, hence it requires highly precise isotherm measurements. On the other hand, LE/LC phase transitions have been observed on Π-*A* isotherms at higher Π values. Although LE/LC phase transitions are first-order, horizontal tie lines are not commonly observed on Π-*A* isotherms. Optical measurements such as fluorescent imaging,[60] electron microscopy,[73] and BAM[74,75] confirm the first-order nature of LE/LC phase transitions. Furthermore, theoretical treatments also predict that LE/LC phase transitions are first-order. Both G/LE and LE/LC phase transitions in Langmuir monolayers are temperature dependent and exhibit critical behavior, just like gas-liquid phase transitions in 3D as shown in Figure 2.9.[76]

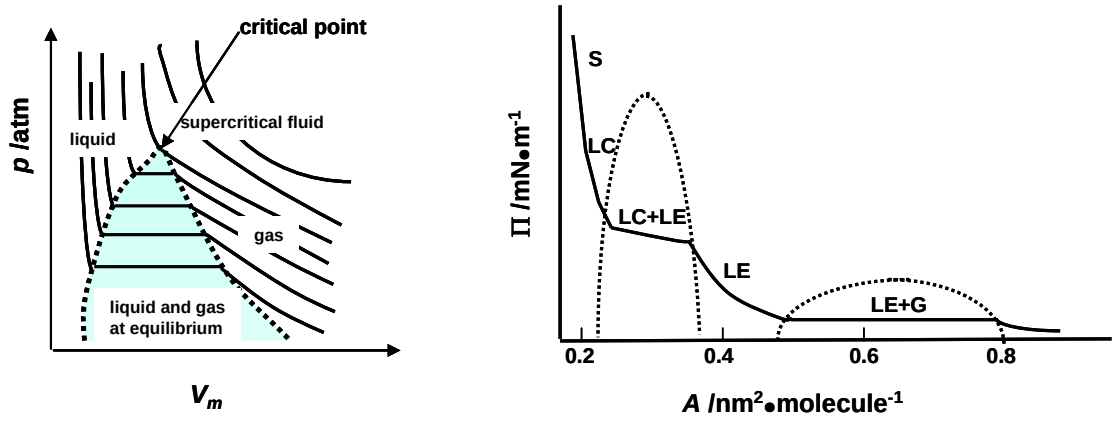

Figure 2.9: Critical behavior observed for first-order phase transitions: (a) gas/liquid phase transition for a generalized 3D *p*-*V* isotherm,[70] and (b) G/LE and LE/LC phase transitions in a generalized 2D Π-*A* isotherm. As temperature increases, the length of the tie line decreases.[76]

In spite of the fact that LE/LC phase transitions have been widely reported for small amphiphiles such as fatty acids and lipids, they have not been observed for homopolymers at the A/W interface. In our study, we observed a first-order LE/LC phase transition for poly(L-lactic acid) (PLLA), which will be discussed in Chapter 4. A review of LE/LC phase transitions will be summarized in Chapter 4 as well.

Phase transitions from 2D Langmuir monolayers to 3D structures are always called "collapse". The surface pressure corresponding to collapse is referred to as the "collapse pressure" ($\Pi_{collapse}$), which indicates the limit of the stability of a 2D condensed monolayer. The value of $\Pi_{collapse}$ depends largely on many factors, including

compression rate and history of the film. When collapse occurs, molecules are forced out of the monolayer and away from the water subphase. For most materials, this takes the form of multilayers, although some molecules like poly(ethylene oxide) (PEO) become water soluble at elevated Π. Figure 2.10 illustrates different stages of collapse of a monolayer into multilayers.[77] Different materials may have various multilayer structures, which may be random structures (Figure 2.10b), stable bilayers (Figure 2.10d), or stable trilayers (Figure 2.10f).

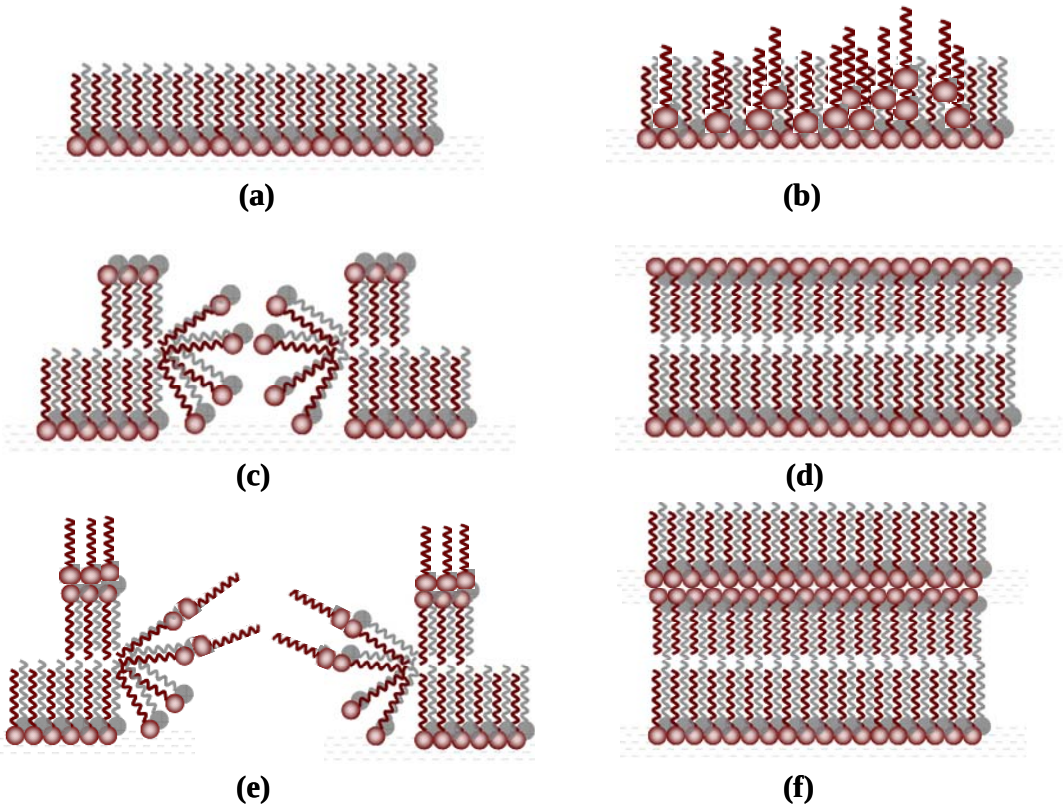

Figure 2.10: Schematic diagram of Langmuir monolayer collapse: (a) a stable 2D condensed monolayer, (b) multilayers with random structure, (c) formation of a bilayer, (d) a stable bilayer structure, (e) formation of a trilayer, and (f) a stable trilayer structure. Lipids tend to form stable trilayers after collapse, while some polymers such as poly(dimethylsiloxane) (PDMS) form stable bilayers after collapse at the A/W interface.[31,77,78]

Although Π-*A* isotherms provide information about phases and phase transitions in Langmuir monolayers, isotherm studies may lead to ambiguous results. For instance, nonzero slopes in the two phase coexistence region for LE/LC phase transitions may lead

one to errantly conclude the transition is second order (Figure 2.5b and Figure 2.9b). Hence more sophisticated techniques are required to study Langmuir monolayers along with Π-*A* isotherms, such as BAM,[79,80] fluorescence microscopy (FM),[60,81] x-ray diffraction techniques (XRD),[36,82] electron microscopy,[73] surface light scattering (SLS),[83,84] interfacial stress rheometry (ISR),[85,86] and non-linear optical techniques.[87,88] In our studies, BAM is used in situ to observe morphological changes along with the phase transitions in 2D Langmuir monolayers.

2.5 Brewster Angle Microscopy

The Brewster angle microscope (BAM) is an excellent tool for the observation of macroscopic structures in Langmuir monolayers. BAM was developed based on the properties of light reflected from a surface at Brewster's angle by Henon and Meunier,[79] and by Honig and Mobius in 1991.[80] Since its invention, BAM has been widely used in morphology studies of Langmuir monolayers, especially with respect to phase transitions.[74,75] BAM allows the visualization of long-range orientational order in floating monolayers which can also be observed by FM. However, compared to FM, BAM does not require the addition of fluorescence probes, which may behave like impurities in the monolayer, thereby altering phase transitions and phase domain growth. For instance, it is particularly difficult to determine the end of a phase transitions in the presence of the probe which enriches the fluid phase. The direct observation of domains in the absence of any probe by BAM can eliminate such problems.

2.5.1 Principle of BAM

For a planar interface, the reflectivity (R) of light mainly depends on its angle of incidence (θ) and the angle of polarization (α) of the incident light. If the polarization vector of light lies in (or parallel to) the plane of incidence, it is called *p*-polarized light. On the other hand, light which is polarized perpendicular to the plane of incidence is *s*-polarized. According to Fresnel's law, the reflectivity of *p*-polarized (R_p) and *s*-polarized (R_s) light can be written as:

$$R_p = \left(\frac{n_1 \cos\theta_t - n_2 \cos\theta_i}{n_1 \cos\theta_t + n_2 \cos\theta_i} \right)^2 = \frac{\tan^2(\theta_i - \theta_t)}{\tan^2(\theta_i + \theta_t)} \qquad \text{(Eq. 2.8)}$$

$$R_s = \left(\frac{n_1 \cos\theta_i - n_2 \cos\theta_t}{n_1 \cos\theta_i + n_2 \cos\theta_t} \right)^2 = \frac{\sin^2(\theta_t - \theta_i)}{\sin^2(\theta_i + \theta_t)} \qquad \text{(Eq. 2.9)}$$

where n_1 (incident) and n_2 are refractive indices of the two media; and θ_i and θ_t are the incident and refracted angles, respectively, as illustrated in Figure 2.11a. Subscripts *p* and *s* represent *p*- and *s*-polarization, respectively.

According to Equations 2.8 and 2.9, the reflectivity is dependent upon the incident angle (θ_i) and the refracted angle (θ_t). However, from Snell's law, we can evaluate θ_t from θ_i based on Equation 2.10:

$$n_1 \sin\theta_i = n_2 \sin\theta_t \qquad \text{(Eq. 2.10)}$$

Hence, both R_p and R_s are dependent on the incident angle and the refractive indices of both media. For a Fresnel interface where the refractive index changes steeply from n_1 to n_2 across the interface, R_s increases continuously as the incident angle increases and approaches unity at the total reflection angle, as shown in Figure 2.11b. On the other

hand, R_p shows a sharp minimum as the incident angle increases. Mathematically, R_p approaches zero when $\theta_i = \theta_t$ leading to $\tan(\theta_i - \theta_t) = 0$, or when $\theta_i + \theta_t = 90^o$ resulting in $\tan(\theta_i + \theta_t) \to \infty$. The former case is not possible when n_1 is different from n_2. The latter case is possible and leads to the definition of Brewster angle (θ_B) according to Snell's law:

$$\tan \theta_B = n_2 / n_1 \qquad \text{(Eq. 2.11)}$$

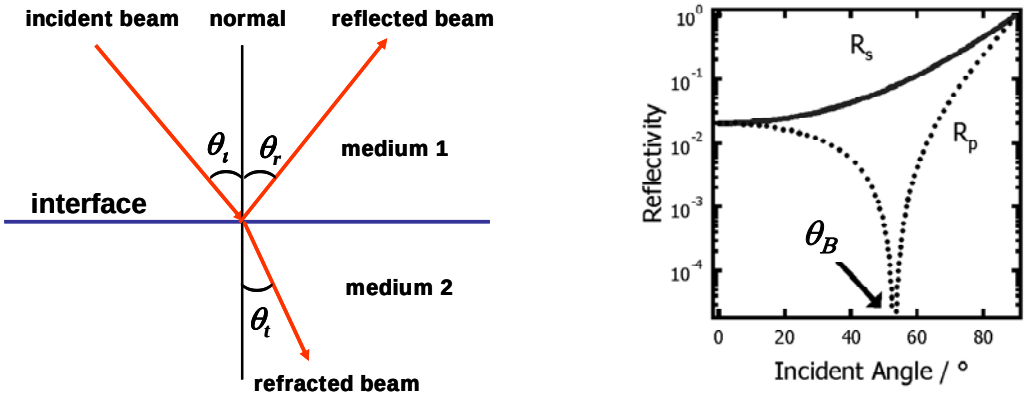

(a) **(b)**

Figure 2.11: (a) Diagram showing reflection and refraction at an interface between two media. θ_i, θ_r, and θ_t are incident, reflected, and refracted angles. (b) Calculated reflectivity of a Fresnel interface between air (n_1 = 1) and water (n_2 = 1.33) for *p*-polarized (R_p) and *s*-polarized (R_s) light according to Equations 2.8 and 2.9, respectively. At Brewster's angle ($\theta_B = 53.1^o$), R_p vanishes.

For the A/W interface, $\theta_B = 53.1^o$. Using *p*-polarized light incident at θ_B for a pure water subphase should yield no signal as R_p vanishes. Figure 2.12a shows a scheme indicating how the reflected light vanishes at θ_B for *p*-polarized light at the A/W interface. A Langmuir monolayer formed on the water subphase can be regarded as a third medium with a refractive index that is different from both air and water. Hence the incident angle is no longer θ_B for both the air/monolayer and monolayer/water interfaces. As a result, some *p*-polarized light will be reflected. For a heterogeneous structure, differences in reflectivity for different phases allow one to image the heterogeneity. Figure 2.12b shows how *p*-polarized light is reflected for a monolayer at the A/W interface at θ_B for the pure A/W interface.

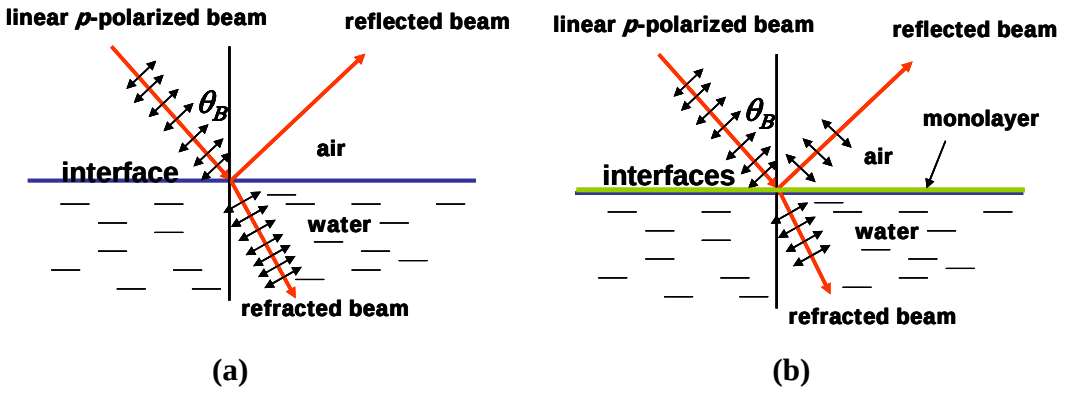

Figure 2.12: Schemes for the reflection of *p*-polarized light incident at Brewster's angle for the A/W interface: (a) without, and (b) with a Langmuir monolayer. For the pure water surface, R_p vanishes at Brewster's angle. However, for a Langmuir monolayer covered surface, some *p*-polarized light will be reflected.

The origins of the reflection of *p*-polarized light for a real interface and a monolayer-covered surface are changes in thickness and roughness of the interface, as well as the anisotropy of monolayers. For a real interface, the refractive index does not change abruptly at $z = 0$, where z is the distance from the average interfacial position. Instead it is different from n_1 and n_2, and it depends on z over the range of the interface, $n(z)$. For an interfacial layer with a small interfacial width D, which is small compared to the wavelength of the incident light, and a refractive index profile $n(z)$, Drude derived the reflectivity for the amplitude of an electromagnetic wave with *p*-polarization, $R_p(\theta_B)$:[89]

$$R_p(\theta_B) = R_s(\theta_B)\overline{\rho_B}^2 \qquad \text{(Eq. 2.12)}$$

where $R_s(\theta_B)$ is the reflectivity for *s*-polarized light of a Fresnel surface at Brewster's angle, and $\overline{\rho_B}$ is the ellipticity given as:[79,80]

$$\overline{\rho_B} = \frac{\pi}{\lambda}\frac{\sqrt{n_1^2+n_2^2}}{n_1^2-n_2^2}\int_{-\infty}^{+\infty}\frac{[n(z)^2-n_1^2][n(z)^2-n_2^2]}{n(z)^2}dz \qquad \text{(Eq. 2.13)}$$

where λ is the wavelength of the incident beam.

A dense Langmuir monolayer introduces a variation of refractive index $n(z)$ for the air/monolayer and monolayer/water interfaces. The refractive index $n(z)$ depends on phase domains of the monolayer, over a thickness of about 20 Å. Therefore, different monolayer phases may have very different reflectivity, $R_p(\theta_B)$. The phases with higher $R_p(\theta_B)$ will appear much brighter than the phases with lower $R_p(\theta_B)$, which can be observed with an imaging detector.[90]

The roughness of real interfaces will also cause reflectivity.[91] At liquid interfaces, thermal fluctuations may cause surface roughness. For monolayers on a free water surface, surface thermal fluctuations are small enough to be neglected because surface tension is large. However, roughness will still introduce a small error (~ 3 Å) to the observed thickness of the monolayer.[37]

Some concentrated phases in monolayers are optically anisotropic.[92] The anisotropy of the monolayers can greatly increase the reflected intensity which can be calculated using a 4 × 4 matrix method. For optically anisotropic monolayers which do not have an axis of vertical symmetry, the reflected light is a function of orientation of the monolayer in its plane.

2.5.2 Set-up of the BAM

Figure 2.13 shows a typical BAM instrument, which consists of a laser source, a Glan-Thompson polarizer, and a light detector such as a charge-coupled device (CCD) camera. A laser is the only possible light source for BAM because the incident beam must have high intensity and a well-defined polarization to provide uniform illumination. The Glan-Thompson polarizer is set for *p*-polarization, which can be placed either in the incident beam path or in the reflected beam path. In the former case, the radiation is polarized in the *p* direction before it contacts the surface, as in traditional BAM. In the latter case, the polarizer acts more like a filter to remove the residual *s* component before the reflected *p* radiation is detected. The second approach can yield better resolution. In a typical experiment, a flat black glass plate is normally placed underneath the water

surface to absorb the refracted beam. A set of lenses is also used to direct the reflected beam to the detector.

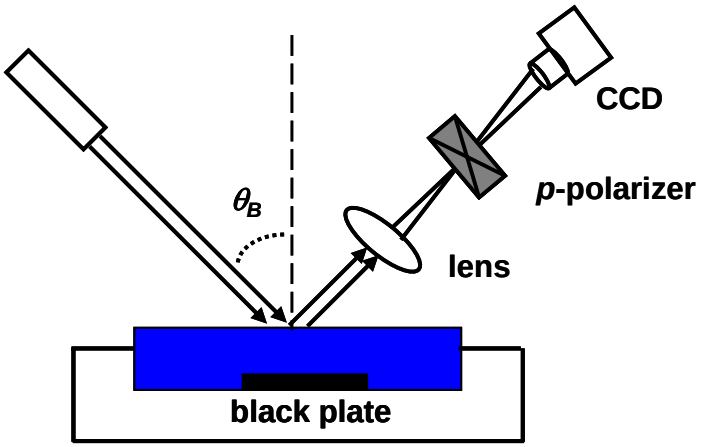

Figure 2.13: Experimental setup for a typical BAM instrument. A *p*-polarized light beam is incident on the water surface at Brewster's angle for water (θ_B = 53.1°). Light reflected by the interface is detected by a CCD camera. A *p*-polarizer can be placed in the path of either the incident or reflected (as shown in the figure) beam.

In principle, BAM is applicable to study all monolayers. There are two requirements for a morphological feature in the monolayer to be visible in BAM: (1) A domain must have sufficiently different optical properties from the ambient medium, *i.e.*, the optical contrast should be large. Different optical properties can arise from changes in density, thickness, or molecular orientation of the monolayer. (2) The morphological feature must be larger than the lateral resolution limit. The major limitation for image quality may arise from interference patterns caused by the optical components of the

system and the coherent laser light. It is much easier to observe morphological changes during a compression process through a video display than from still pictures.

BAM has been widely used to observe morphologies of Langmuir monolayers formed by fatty acids, esters, and lipids, as well as mixed monolayers at the A/W interface.[93-96] BAM has also been used to study phase transitions, crystallization, and patterning in 2D.[95,97-100] BAM can also be applied to measure the thickness of film regions, even though the optical properties of the film may be unknown.[100,101] Honig and Mobius also reported that BAM is a powerful method to characterize a single monolayer LB-film on solid substrates with high contrast.[102]

2.6 Polymer Langmuir Monolayers at the A/W Interface

Polymers can have (or be designed with) alternating hydrophilic and hydrophobic properties. After spreading at the A/W interface, amphiphilic polymers may form Langmuir monolayers adopting a configuration where the hydrophilic parts are in the water subphase and the hydrophobic parts are in the air. Langmuir monolayers of robust amphiphilic polymers exhibit less complicated Π-*A* isotherms.[103,104] Π-*A* isotherms of polymers generally show a gas phase, a liquid phase and a solid-like phase. Crisp suggested that polymer Langmuir monolayers can be classified as either "condensed" or "expanded".[104] Expanded polymer monolayers exhibit a gradual rise in the surface pressure, while condensed polymer monolayers are identified by their high viscosity or rigidity, together with much steeper slopes on Π-*A* isotherms. It is necessary to mention

that condensed or expanded polymer monolayers are different from condensed or expanded phases for fatty acids because polymer monolayers often lack the long hydrophobic tails found in lipids that lead to the existence of complicated tilted or untilted phases at the A/W interface in lipid systems. In this section, polymers that have been studied at the A/W interface will be briefly and selectively summarized.

2.6.1 Polysiloxanes

Polysiloxanes are one of the first classes of polymers to be extensively investigated as Langmuir monolayers at the A/W interface. Fox *et al.* reported in 1947 that poly(dimethylsiloxane) (PDMS) has surface active properties at the A/W interface.[105] The authors also suggested a structure-based model to explain the transitions observed in the isotherm of PDMS: (1) in the low Π region, all silicon and oxygen atoms adsorbed onto the water subphase; (2) upon compression into the monolayer region, some of the silicon and oxygen atoms were pulled out from the interface; (3) further compression caused the collapse of the monolayer with successive coiling into a helical conformation. Fox suggested that in the most concentrated regime, helices stood on the end at the interface, while Noll *et al.* proposed bilayer formation,[106] which has been observed by several groups with isotherm measurements,[107] BAM and scanning microscopy studies.[108,109] Nearly identical patterns of collapse were found in isotherms of linear and cyclic polysiloxanes, suggesting a similar collapse mechanism despite the fact the helix formation in systems of small rings is not favored.[107] On the other hand, stepwise layer growth for cyclolinear polysiloxanes has been observed through isotherm measurements

and scanning force microscopy studies.[108,109] Seven plateaus occurred at ratios of the area suggesting the growth from monolayer to bilayer, bilayer to trilayer, etc., continuing up to seven layers. BAM images of collapsing linear siloxanes showed domains of different discrete thicknesses, suggesting multilayer formation.[110]

2.6.2 Polyethers

Close in structure to the polysiloxanes are polyethers, which may be water soluble or insoluble. Watanabe *et al.* studied Langmuir monolayers of water insoluble poly(vinyl alkylals) and found that they could form stable Langmuir films at the A/W interface with an area per monomer of ~ 0.3 $nm^2 \bullet monomer^{-1}$, which does not depend on side-chain length and degree of polymerization of the starting poly(vinyl alcohol).[111,112] Interestingly, water soluble poly(ethylene oxide) (PEO) can also form stable Langmuir monolayers at the A/W interface because of the amphiphilic nature of its EO ($-CH_2CH_2O-$) repeating units.[113] Surface quasi-elastic light-scattering studies showed that both absorbed and spread films of PEO at the A/W interface have similar rheological properties.[114] However, the monolayer is only stable below some critical surface concentration. At low concentrations, PEO can form stable spreading monolayers. Neutron reflectivity studies have shown that at higher surface concentrations, PEO will loop into the subphase, and its penetration depth increases with increasing surface concentrations while the "surface" concentration of the topmost layer remains approximately constant.[115] It was found that the lowest molar mass of PEO to form stable monolayers at the A/W interface is about 18 $kg \bullet mol^{-1}$; and the collapse pressure

($\Pi_{collapse}$) of PEO monolayers increases slightly with the molar mass. However, in the molar mass range of 145 to 996 kg•mol^{-1}, $\Pi_{collapse}$ becomes molar mass independent at a value of 10.2 mN•m^{-1}.[114] Shuler suggested that a close-packed PEO monolayer should occupy an area of 0.16 nm^2•monomer^{-1} from molecular models,[113] while some experiments gave the value between 0.09 and 0.11 nm^2•monomer^{-1},[116,117] suggesting that PEO Langmuir monolayers may not be regarded as truly two-dimensional. In addition to homopolymer studies, there are also numerous surface studies of many PEO copolymers, such as PEO-PS (polystyrene), PEO-PMMA (poly(methyl methacrylate)), etc.[118-122]

PEO is a potential candidate for biomedical applications because of its non-toxicity and its ability to reduce the adsorption of soluble proteins on surfaces.[123] PEO can be covalently attached to the headgroup of lipids, to form "lipopolymers",[124] which have potential applications as novel drug delivery vehicles. Lipopolymers (and their mixtures with different phospholipids) can form stable Langmuir monolayers which can be used to study 2D physical gelation phenomena.[125-127]

2.6.3 Polyacrylates and Polymethacrylates

Polyacrylates can form stable monolayers at the A/W interface, due to the existence of hydrophobic main chain and hydrophilic ester groups on the side chains. For instance, poly(methyl methacrylate) (PMMA) and poly(tert-butyl methacrylate) (PtBMA) have been reported to form very stable condensed-type monolayers at the A/W interface.[62,128,129] On the other hand, poly(tert-butyl acrylate) (PtBA) lacks the methyl

group therefore the polymer chain is more flexible, which allows the tert-butyl groups to be oriented into the air out of the aqueous subphase, and yields a more expanded monolayer. Polyacrylates can form LB-films and have been employed as a buffer layer in nonlinear optical applications.[130] PtBMA and PtBA have also been used as a precursor for poly(methacrylic acid) (PMAA) and poly(acrylic acid) (PAA) through acid-catalyzed hydrolysis in the gas phase,[28,131] because PMAA and PAA themselves are too hydrophilic to form pure LB-multilayers. Such an approach could provide a desirable material for the study of superabsorbing polyelectrolyte networks and as scaffolds for bioadsorption, as well as a precursor for subsequent chemical modification. Other interesting LB-film studies have been conducted with poly(iso-butyl methacrylate) (PiBMA), whose iso-butyl side group has a cross-sectional area larger than that of a normal chain.[132] Meanwhile, the iso-butyl side chain is still a small group and can reorganize to accommodate a smaller area. As a consequence, the close-packed monolayers of PiBMA should be hydrophobic on both sides with the oxygen atoms being "buried" in the monolayer bulk. This model is confirmed by wetting experiments.

2.6.4 Polyesters

Polyesters that form stable monolayers at the A/W interface include poly(ε-caprolactone) (PCL), poly(lactic acid) (PLA), etc. PCL can form a "2D" close-packed monolayer with a collapse point around A = 0.20 $nm^2 \bullet monomer^{-1}$.[133] In PCL Langmuir monolayers, the ester groups tend to anchor at the interface due to their hydrophilicity, which provides a possibility to realize the optimal conditions for

hydrolysis studies. It is also possible to monitor hydrolysis processes through Π changes at the A/W interface. The water subphase may also accelerate the hydrolysis because the hydrolytic products are water soluble.[133,134] PCL Langmuir monolayers are also interesting for studying crystallization in 2D. Recently, Li *et al.* has observed the growth of PCL crystals at the A/W interface during compression, and the melting of PCL crystals during the expansion process.[135]

2.6.5 Other Preformed Polymers

The intent of this section is not to summarize all polymers that have been studied at the A/W interface as Langmuir films. There are other families of polymers that can form stable monolayers at the A/W interface, such as polyvinylesters, polyimides, polyamides, etc. Copolymers with amphiphilic segments have also been studied as Langmuir films. Developing synthetic methods allows one to design new amphiphilic polymers. For instance, it is possible to prepare the backbone to be water-soluble, to introduce hydrophilic spacer groups into the backbone, and to attach hydrophobic groups as side-chains. In particular, new amphiphilic block copolymers are an active area of research.

2.7 System of Interest – Poly(lactic acid)

In this dissertation, poly(L-lactic acid), PLLA, is studied as Langmuir monolayers at the A/W interface, and as LB-films on solid substrates. In particular, the properties of PLLA in Langmuir monolayers and LB-films are studied. By understanding these

phenomena, it may be possible to pattern PLLA substrates for biological applications such as cell adhesion and tissue engineering. In this section, the following topics of poly(lactic acid) (PLA) are summarized: general remarks, hydrolysis, crystallization behavior, and Langmuir monolayer studies.

2.7.1 General Introduction to Poly(lactic acid)

PLA can be produced from renewable carbon sources, or synthesized from lactic acid, which has L- and D- isomers.[136] PLA is one of the few polymers where the stereochemical structure can be easily modified by polymerizing a controlled mixture of isomers. Figure 2.14 provides the structure of poly(D,L-lactic acid), which is always noted as PLA or PDLLA. PLA is regarded as homopolymer instead of a copolymer. There are also two different polyenantiomers such as PLLA and poly(D-lactic acid) (PDLA), both of which generally have similar properties. The most significant difference between PLLA and PDLA relative to PLA is crystallinity which will be discussed shortly.

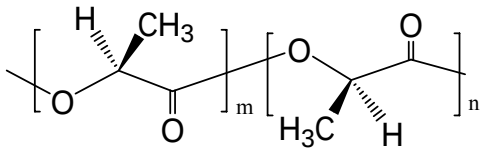

Figure 2.14: Poly(D,L-lactic acid) is composed of sequences of two isomeric forms of lactic acid.

PLA offers great promise for a wide range of commodity applications.[137] For instance, PLA has a degradation time in the environment on the order of weeks to two years, compared to 500 to 1000 years for conventional plastics such as polyethylene (PE). Therefore PLA has been used for single-use plastic packaging, agriculture mulch films, and bags. Furthermore, PLA is also biocompatible, leading to its widest applications in pharmaceutical and medical fields for controlled release of drugs and as scaffolds for tissue engineering. Techniques that are generally used to fabricate PLLA substrates include: spin-coating, electrospinning, microcontact printing, microneedle and micromolding, microtransfer, laser thinning, dipping or soaking, etc.

2.7.2 Hydrolysis of PLA

PLA is degraded by simple hydrolysis of the ester bond and does not require the presence of enzymes. Acidic or basic solutions can be used to catalyze the hydrolysis. The rate of PLA degradation is dependent on the size and shape of the particles, isomer ratio, molar mass, and degree of crystallinity.[136] Shih studied the acid-catalyzed hydrolysis of PLA in dilute solution by analyzing the *in situ* ^{1}H nuclear magnetic resonance (NMR) spectra and found that scission at the chain-ends was approximately 10-fold faster than random-scission of the internal bonds.[138] Like PCL, Langmuir monolayers are another suitable model for studying PLA degradation with the advantages of controlling and modifying the interfacial organization of the ester groups, and in particular realizing the optimal conditions for hydrolysis when all ester bonds are accessible to the underlying aqueous subphase containing OH^- and H^+. Ivanova *et al.*

have done some work on the PLA monolayer approach at the A/W interface, by measuring Π-*A* isotherms, and then watching the area decrease and surface potential change with time.[139] The fact that the area decreases with time at constant pressure is consistent with the hydrolysis process, as the hydrolysis products of PLA will be insoluble long chains and short soluble fragments. It was also found that the hydrolysis process was faster at acidic pH than at basic pH. This observation is most likely due to the formation of a net negative charge during the hydrolytic step at basic pH. Thus, the concentration of hydroxyl ions should be taken into account as well as the electrostatic potential for base catalyzed hydrolysis. Ivanova did the kinetic study for the hydrolysis process at acidic pH and modified it for basic hydrolysis by adding new terms dealing with the electric potential.[140]

Thermal degradation of PLA may also occur at temperatures above its melting point. A significant level of molecular degradation occurs when PLA is held 10 ^{o}C above its melting point for a sustained period of time in air. It has been suggested that the thermal degradation of PLA was due to chain splitting;[141] however, most people still believe that thermal degradation is conducted by hydrolysis, lactide reformation, oxidative main chain scission, and inter- or intramolecular trans-esterification reactions.[136]

PLA's hydrolysis by acid, base, or temperature is largely dependent on degree of crystallinity. It has been shown that highly crystalline PLA will take months to years, to hydrolyze fully to lactic acid, whereas an amorphous sample may degrade in weeks.

2.7.3 Crystallization Behavior of PLLA and PDLA

PLLA and PDLA both have a glass transition temperature (T_g) around 50 ^{o}C and an equilibrium crystalline melting point (T_m) of 207 ^{o}C.[142] Due to the existence of small imperfect crystallites, typical melting points for PLLA and PDLA are around 185 ^{o}C.[143] Pure PLLA (or PDLA) crystallized into left-handed (or right-handed) 10_3-helices, with a pseudo-orthorhombic unit cell containing two chains (known as the α-form).[144,145] For α-form PLLA, the unit cell dimensions are: a = 10.7 Å, b = 6.126 Å, and c = 28.939 Å, with the diameter distribution of the crystallites ranging from 390 to 440 Å.[146] PLLA in β-form was also reported with an orthorhombic unit cell containing six 3_1-helices. The dimensions of the unit cell are: a = 10.31 Å, b = 18.21 Å, and c = 9.0 Å.[142] The comparison between T_m values of α-form (185 ^{o}C) and β-form (175 ^{o}C) suggests that the α-form is more stable than the β-form.[142] On the other hand, a 1:1 mixture of pure PLLA with pure PDLA form 3_1-helices with a triclinic unit cell.[147] The mixture has a melting point of 230 ^{o}C and mechanical properties greater than pure PLLA and PDLA.[136] Furthermore, PLA (also written as PDLLA), amorphous upon preparation, can be thermally crystallized. The crystallinity of PDLLA depends on annealing temperature, annealing time, as well as molar mass, D:L molar ratio, and the presence or absence of nucleating agents.[136] Crystallization of PDLLA can be initiated at temperatures between 75 ^{o}C and T_m; and the fastest rates are found in the temperature range of 110 – 130 ^{o}C. Annealing at higher temperatures (such as 135 ^{o}C) does not necessarily produce complete crystallization. Annealing at temperatures close to T_m produces crystals with high

melting points. Shorter annealing times produce less perfect and low T_m crystals, which may be melted and reformed into more perfect and higher T_m crystals after longer annealing times. A sample of 400 kg•mol^{-1} PDLLA shows no crystallization exotherm or melting endotherm after annealing, suggesting the lack of crystalline features. Samples with molar masses less than 300 kg•mol^{-1} generally develop 30 – 50 % crystallinity.[136]

Several techniques have been used to study the crystallization of PLA. For instance, differential scanning calorimetry (DSC) can be used to determine thermal properties such as T_m, T_g, degree of crystallinity, etc.[148] Infrared (IR) and Raman spectroscopies have been applied to investigate structure, degree of crystallinity, etc. Atomic force microscopy (AFM) is used to study crystal morphology. X-ray diffraction and electron diffraction patterns are used to evaluate crystal structures. The techniques used in this dissertation will be introduced later in this chapter.

Conventional crystallization research on PLLA was conducted for bulk systems and/or thin films (on the order of several hundred nanometers to several hundred micrometers) at a temperature near the crystallization temperature for crystals formed from dilute solutions or melts.[149] Lamellar single crystals of PLLA have been observed by several research groups. For example, lamellar crystals with a lamellar thickness of around 10 nm were grown from dilute solutions in toluene and p-xylene by Kalb *et al.*,[150] lozenge-shaped crystals were grown from acetonitrile solution by Miyata *et al.*,[151] and more recently both lozenge- and hexagonal-shaped single crystals from dilute solutions in

p-xylene were reported by Iwata *et al*.[152] Such crystallization research on PLLA can be extended to monolayer studies in 2D at the A/W interface such that the crystallization environments and the film state are different from conventional crystallization research. One of the advantages of our research is that we can study crystallization at temperatures well below the temperatures where thermal degradation is common.

2.7.4 Langmuir Monolayers of PLA

In addition to serving as model systems for studying hydrolysis, PLA Langmuir monolayers can also be used to study crystallization behavior. Several semicrystalline polymers have been examined at the A/W interface and the formation of crystals has been reported. For example, isotactic poly(methyl methacrylate) (iPMMA) forms a 10_1 double helix at the A/W interface.[153,154] PCL forms dendritic crystals at the A/W interface at room temperature.[135] Studies of PLA at the A/W interface reveal that pure PLLA or PDLA and their blends spontaneously form 10_3-helices at the A/W interface.[155] Further compression into the solid-like state does not alter the helical conformation of pure PLLA and PDLA. However, in solid-like domains, PLLA/PDLA stereocomplexes change the conformation from 10_3-helices to 3_1-helices.[156]

2.8 Langmuir-Blodgett Technique

Studies of Langmuir monolayers at the A/W interface can provide a wealth of useful information about molecular size and intermolecular forces; however, the great resurgence of interest in this area has been largely due to the fact that Langmuir films can

be transferred from the water surface onto a solid substrate using the LB-technique to fabricate organic thin films. The set-up of a LB-trough is very similar to a Langmuir trough, except that a LB-trough has a dipping head to hold solid substrates and a well to facilitate LB-film deposition.

There are three different types of LB-film deposition modes: X-, Y- and Z-type.[65] For molecules that undergo Y-type deposition, it is possible to transfer monomolecular films on both the up- and downstrokes to form multilayer films. In contrast, Z-type films only transfer on the upstrokes, and X-type films only transfer on the downstrokes. Figure 2.15 depicts Y-type deposition. First, amphiphilic molecules are spread onto the surface to form a Langmuir monolayer, which is compressed into a condensed phase (Figure 2.15a). A hydrophobic solid substrate is then lowered down through the monolayer so that it dips into the subphase and picks up a layer one molecule thick with the hydrophobic tails attaching to the substrate (Figure 2.15b). The substrate is then withdrawn from the subphase to pick up another layer with the hydrophilic heads attaching to the existing layer (Figure 2.15c). Continuous upward or downward strokes will form multilayer films with head-to-head and tail-to-tail configurations. Odd layers will have headgroups pointing towards air and even layers will have the hydrophobic tails pointing towards air (Figure 2.15d). In order to maintain constant conditions during deposition, Π at which the film is prepared is kept constant by movable barriers. If a hydrophilic substrate is used, the first layer should be transferred as substrate moves up from the subphase, because the hydrophilic headgroups of the molecules are in the water.

LB-multilayers formed by Y-type deposition on hydrophilic substrates are shown in Figure 2.16b. As a comparison, Figure 2.16 also shows the expected molecular arrangement for X- and Z-type LB-films. In addition, mixed deposition modes are also possible. For instance, XY-deposition refers to complete transfer as the substrate is being lowered into the subphase, while only partial transfer as the substrate moves up from the subphase.[157] The invention of alternating LB-troughs actually facilitates the deposition of multilayers consisting of different molecules.

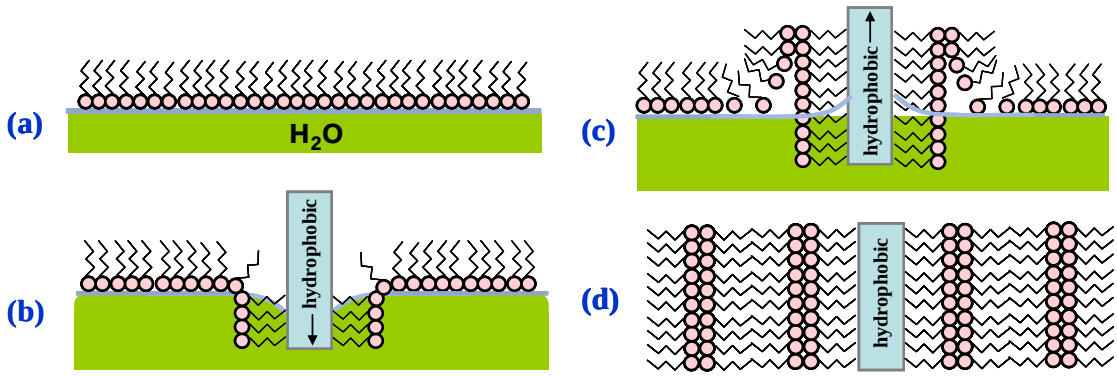

Figure 2.15: Y-type deposition of LB-multilayers onto a hydrophobic substrate: (a) formation of a stable Langmuir monolayer at the A/W interface by compression, (b) first immersion, (c) first withdrawal, and (d) LB-multilayers with head-to-head and tail-to-tail configurations.

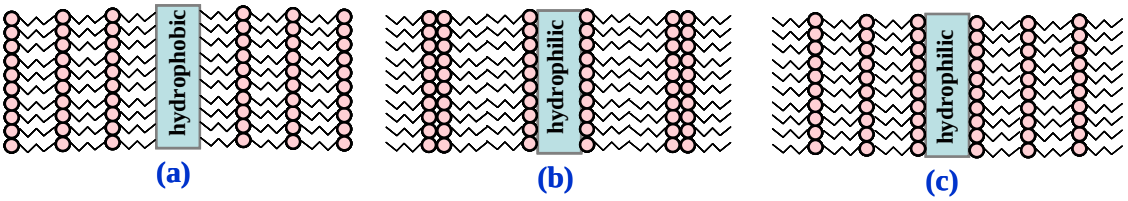

Figure 2.16: Structures of LB-multilayers: (a) X-, (b) Y-, and (c) Z-type. The structural difference between 2.15d and (b) reflects the fact that (b) depicts a hydrophilic substrate. X- and Z-type depositions do not normally guarantee that the multilayers will have the corresponding structure as rearrangement with time is possible.

It should be noted that the molecular arrangements shown in Figures 2.15d and 2.16 are what is expected for ideal LB-transfer. The final molecular orientation in a LB-film

may differ. X- and Z-type deposition typically fails to yield structures that are as ordered as those in Figure 2.16. For instance, fatty acids in X-type films can rearrange, during or after deposition, to produce a structure which is essentially identical to that of Y-type films.[158] On the other hand, LB-films of some long chain esters only show X-type structures, independent of the method used to prepare the multilayer.[59,159]

One measure of the quality of LB-deposition is through the transfer ratio (τ), which is defined as the ratio of the area of monolayer removed from water surface (A_L) to the area of substrate passed through the monolayer (A_s), as shown in Equation 2.14.[160] The area loss from the water surface (A_L) can easily be measured by maintaining a constant Π, while the area of substrate is measured prior to deposition. Honig *et al.* also suggested another parameter, ϕ, to quantify the various deposition modes, as shown in Equation 2.15:[161]

$$\tau = A_L / A_s \qquad \text{(Eq. 2.14)}$$

$$\phi = \tau_u / \tau_d \qquad \text{(Eq. 2.15)}$$

where τ_u and τ_d are the transfer ratios on the up- and downstrokes, respectively. For pure Y-type deposition, ϕ = 1; for pure X-type deposition, ϕ = 0; for pure Z-type deposition, ϕ is infinite; and for XY-deposition, ϕ is less than 1.

Under most circumstances, a transfer ratio of unity is taken as the criterion for good deposition, and the orientation of molecules on solid substrates is expected to be very similar to their orientation on water. Occasionally, there may be a large but consistent deviation from a value of unity, pointing to a situation in which the molecular orientation

may be changing during transfer. Variable transfer ratios are almost always a sign of unsatisfactory film deposition.

There is another technique for preparing multilayers from the A/W interface, which is known as the horizontal lifting method or Langmuir-Schaefer (LS) technique (Figure 2.17).[162] Unlike the LB-technique in which the substrate passes vertically through the interface, the substrate is placed horizontally onto the monolayer film during LS-deposition. When the substrate is lifted and separated from the water surface, the monolayer is transferred onto the substrate, presumably with the same molecular orientation. High-quality X-type multilayers have been reported by the LS-technique; however, rearrangement is possible during the lifting process to form multilayers with Y-type structures.[34] Films prepared by the LS-technique are called LS-films, or most of the time, LB-films, due to the fact that LS-multilayers and LB-multilayers have almost identical properties: (1) layer by layer transfer, (2) control of thickness, and (3) control of surface structures, etc. The deposition rate for the LS-technique is not reduced with increasing film viscosity, therefore the LS-technique is useful for the deposition of very rigid films and polymer films. However, the disadvantage of the LS-transfer is also obvious: the deposition is mainly conducted manually, and the control of deposition is sometimes poor.

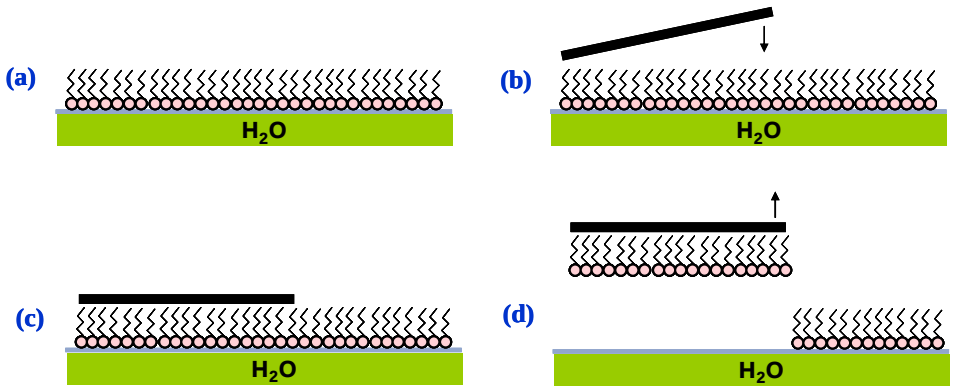

Figure 2.17: Deposition of LB-multilayers by the LS-technique: (a) formation of a stable Langmuir monolayer at the A/W interface by compression, (b) placing a solid substrate onto the subphase, (c) substrate lying flat on the surface, and (d) lifting of the substrate from the water surface.[34]

2.9 Surface Analysis Techniques

The development of analytical methods for studying organic thin films has been dramatic.[163] In this section, only those techniques used in this dissertation are introduced.

2.9.1 Atomic Force Microscopy

AFM was invented in 1986 by Binnig, Quate and Gerber, and belongs to the group of scanning probe microscopy (SPM) techniques.[164,165] AFM has been used to obtain information about 3D topography as well as to measure surface properties such as adhesion, abrasion, corrosion, etc. AFM is based on the measurement of different forces between a sharp tip and sample surface. The tip is generally made of single crystal

silicon or silicon nitride with a small radius of curvature and a high aspect ratio so as to be able to trace fine details on the surface. When the tip is raster-scanning across the surface, the interaction force is measured *via* the deflection of a cantilever on which the tip is attached. To achieve measurable deflection, the cantilever should be softer than the bonds between the sample atoms, and have a high resonance frequency to minimize noise. Many techniques can be used to detect the deflection, such as tunneling current, interferometry, capacitance, laser diodide feedback, optical lever, etc.[165,166] Among these techniques, the optical lever technique is the most widely used. For the optical lever technique, a laser beam is focused and positioned on the rear of the cantilever, and the reflected laser beam is collected by a double segment photodiode and the output signal from the detector is collected by an amplifier (Figure 2.18).[167] Usually, the tip position is fixed and the sample is scanning with a piezo transducer. A piezo transducer is normally made of piezo ceramics such as lead zirconate titanate (PZT), which can be either a piezo tripod or a single tube scanner (Figure 2.18). Some AFM instruments have sample position fixed with a moving tip which is connected to a scanner.

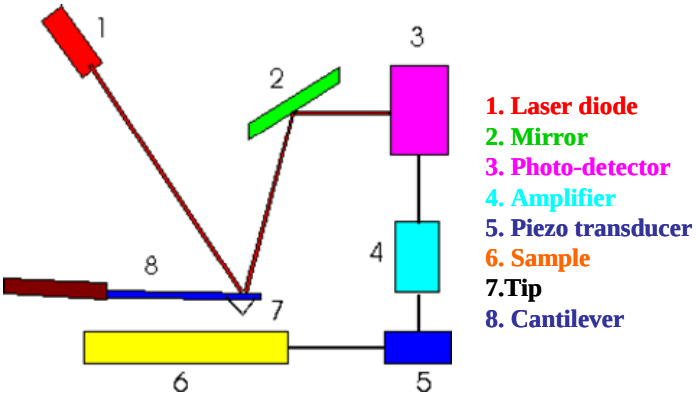

Figure 2.18: A typical AFM instrument with a moving sample connected to a piezo scanner.

There are three different modes for the tip-sample interactions: the contact mode, the non-contact mode, and the tapping mode (Figure 2.19). In the contact mode, the tip is brought to a distance at which repulsive forces dominate the tip-sample interaction. The tip and surface remain in close contact as the scanning proceeds. The contact mode may lead to sample damage because of the existence of large lateral forces on the sample as the tip is dragged over the surface. In the non-contact mode, the cantilever oscillated above the surface at a distance that is in the attractive or van der Waals force regime. To perform measurements in this attractive force region, the cantilever should oscillate with low amplitude. This mode is difficult to operate in ambient conditions, because a thin layer of water contamination that may exist on the surface can form a small capillary bridge between the tip and the sample and cause the tip to "jump-to-contact". In the tapping mode, the tip is positioned above the surface and taps the surface when the

cantilever is oscillated at its resonant frequency (usually 50,000 to 500,000 cycles/sec).[168] The tapping mode is operated in the repulsive force region. Ideally the tip is terminated with a single atom, which means that the tip is in direct contact with an extremely small area. Furthermore, the tip touches the surface only for a short period of time; hence scratching of soft samples or removal of loosely bound surface features can be minimized. The oscillation amplitude is then used as a feedback to gain topological information. More recently, there has been much interest in phase imaging, which is an extension of the tapping mode. In phase imaging, if an area of different viscoelasticity or adhesion is scanned, the time response of the cantilever oscillation changes as the tip contacts to the surface and a relative difference is detected. The phase shift can provide information about morphology at different length scales and be correlated with specific material properties that affect the tip-sample interaction. Tapping mode AFM is commonly used to study polymers because the contact mode is more likely to damage the surface and the non-contact mode usually provides low resolution images.

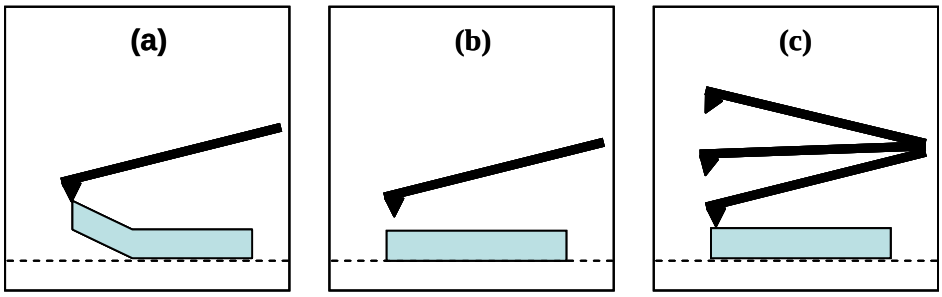

Figure 2.19: Operation modes of AFM: (a) contact, (b) non-contact, and (c) tapping mode.

The feedback in AFM can be operated in two different modes, the constant force mode, and the constant height mode. In the constant force mode, the force (and the cantilever deflection) is kept constant by re-adjusting the sample in the vertical direction according to the topographic features on the surface. The constant force mode can be applied to image large and rough surfaces without destroying the tip and/or sample surface. However, scan rates need to be low to allow the feedback system to respond to height changes. In the constant height mode, the vertical position of the sample is kept constant, while the deflection of the cantilever is measured and recorded. In this mode, scan rates can be higher to eliminate thermal drifts in high resolution imaging; however, large scan sizes should be avoided because the tip may be destroyed.

AFM has been widely used for studying the morphology of homopolymers, block copolymers, polymer blends, polymers brushes, biological systems, etc.[166] For semicrystalline homopolymers, AFM has been used to image chain-folded surfaces,[169]

and crystallographic defects of single crystals.[170] Phase separation in polymer blends and block copolymers can lead to different surface morphologies such as spheres, cylinders, and lamellae, all of which have been revealed by AFM studies. AFM is also used to study the surface morphology of LB-films. Zasadzinski *et al.* reviewed the application of AFM for studying LB-films, stating that AFM can be used to determine molecular ordering, film defects, film quality, and to refine deposition conditions.[171] It is very difficult to include all of the relevant literature that applies to AFM studies of LB-films because of the massive number of publications. Nonetheless several reviews have attempted this task.[35,172,173]

Before concluding this section, it should be noted that one limitation of AFM is that the chemical information and material specific properties of the sample can not be obtained directly from AFM images. Several AFM-related techniques have been developed to measure properties in addition to topology. For instance, friction force microscopy (FFM) or lateral force microscopy (LFM) can measure the friction between the tip and the surface; chemical force microscopy (CFM) can reveal chemical information about the sample because the chemically modified tip is sensitive to certain species; Young's modulus microscopy (YMM) allows the measurement of surface elasticity; electric force microscopy (EFM) can measure surface charges, topography, capacitance and potential; and magnetic force microscopy (MFM) measures the magnetostatic forces. In addition, AFM coupled with a heating stage allows the measurement of thermal properties and thermal transformations in thin films.[166,174]

2.9.2 X-Ray Reflectivity Measurements

X-ray reflectivity is a powerful technique for investigating the structures of organic thin films.[175] X-ray reflectivity is highly sensitive to electron density gradients irrespective of the crystalline nature of the system studied.[176] It is also one of the few techniques allowing the determination of mass density and the thickness of thin layers along the direction normal to the surface.[177]

The basic idea behind x-ray reflectivity is to compare measured reflectivity profiles to theoretical Fresnel reflectivity profiles.[178] At an interface between materials of different electron density, x-rays are both reflected and refracted. For a condensed material irradiated by x-rays, its refractive index depends on the electron density of the volume that is irradiated, and is written as:

$$n = 1 - \delta + i\beta \qquad \text{(Eq. 2.16)}$$

with the dispersion term

$$\delta = \left(\frac{\lambda^2}{2\pi}\right) r_e N_A \rho \left(\frac{Z + f'}{A}\right) = \left(\frac{\lambda^2}{2\pi}\right) r_e \rho_e \qquad \text{(Eq. 2.17)}$$

and the absorption term

$$\beta = \left(\frac{\lambda^2}{2\pi}\right) r_e N_A \rho \left(\frac{f''}{A}\right) = \left(\frac{f''}{Z + f'}\right) \delta = \frac{\lambda \mu}{4\pi} \qquad \text{(Eq. 2.18)}$$

where λ is the wavelength of x-ray, r_e = 2.828 × 10^{-15} m is the classical electron radius, N_A is the Avogadro's constant, Z is the atomic number, A is the atomic mass, ρ is the mass density, ρ_e is the electron density, f' and f'' are real (dispersion) and imaginary (absorption) part of the dispersion corrections, respectively, and μ is the linear absorption coefficient.

The magnitude of δ and β are simply related to the electron density of the material, and are generally on the order of 10^{-5} to 10^{-7}. The real part of the refractive index, $n = 1 - \delta$, is related to the phase-lag of the propagating wave, while the imaginary part, β, corresponds to the decrease of the wave amplitude.

As seen in Equation 2.16, $n < 1$. Hence according to Snell-Descartes second law, the x-rays are refracted away from the surface normal when they enter the material from air, as shown in Figure 2.20. Consequently, there exists a critical angle of incidence, θ_c, below which total reflection of x-rays occurs. When the absorption is neglected, the critical angle can be related to the dispersion term by

$$\theta_c \cong \sqrt{2\delta} \qquad \text{(Eq. 2.19)}$$

For Cu Kα x-ray radiation ($\lambda \sim 1.54$ Å), typical values of θ_c lie in the range of 0.2 – 0.6°.

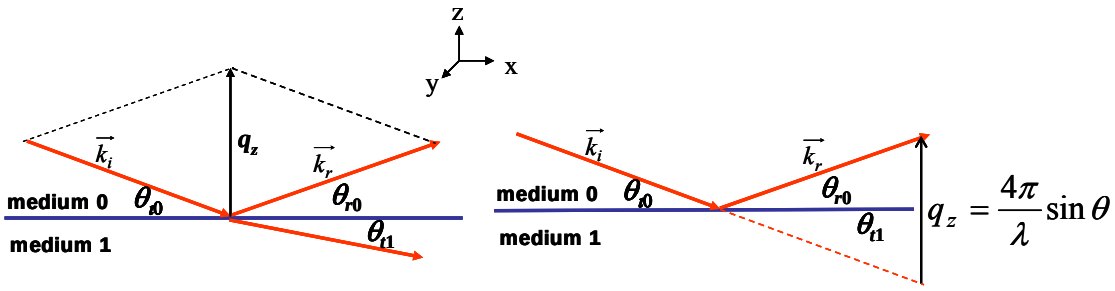

Figure 2.20: Schematic diagram of reflection and refraction at an interface. θ_{i0} is the angle between the incident beam and the surface, θ_{r0} is the angle between the reflected beam and the surface, and θ_{t1} is the angle between the refracted beam and the surface.

There are two basic types of data that are accessible from x-ray reflectivity experiments, specular and off-specular. For specular reflectivity, the reflected beam is detected at an angle which is the same as the incident angle (θ), thus the scattering angle is 2θ and the scattering vector is normal to the surface. In off-specular experiments, the incident angle is θ-ω, while the reflected x-rays are detected at an exit angle of θ+ω. As a result, the scattering vector has a component parallel to the surface.[175] In our studies, specular x-ray reflectivity was used, and the principles are summarized here.

Reflection of x-rays depends on the differences in the wave vector in the media on either side of the interface. In vacuum, the magnitude of wave vector is defined as

$$\left\|\overrightarrow{k_0}\right\| = 2\pi/\lambda \qquad \text{(Eq. 2.20)}$$

In a specular technique where the incident and the detection angles (θ) are the same (Figure 2.20), only the z component of the wave vector is of interest:

$$k_{z0} = \frac{2\pi}{\lambda}\sin\theta \qquad \text{(Eq. 2.21)}$$

For a single interface with media 0 and 1, the resultant scattering vector (Figure 2.20) is defined as

$$q_z = \frac{4\pi}{\lambda}\sin\theta \qquad \text{(Eq. 2.22)}$$

If the interface is infinitely sharp, the reflectance or reflection coefficient is given as

$$r_{01} = \frac{\sin\theta_{i0} - n_1\sin\theta_{i1}}{\sin\theta_{i0} - n_1\sin\theta_{i1}} = \frac{k_{z0} - k_{z1}}{k_{z0} + k_{z1}} \qquad \text{(Eq. 2.23)}$$

where k_{z0} and k_{z1} are z component of the wave vector for medium 0 and 1, respectively.

The Fresnel reflectivity at the interface, R_F, can be defined as

$$R_F = r_{01} r_{01}^* = \left| \frac{k_{z0} - k_{z1}}{k_{z0} + k_{z1}} \right|^2 \qquad \text{(Eq. 2.24)}$$

where the asterisk denotes the complex conjugate. Equation 2.24 can be reduced to a function of k_{z0} by treating k_{z1} as a deviation from k_{z0} due to the difference in electron density:

$$k_{z1} = \left({k_{z0}}^2 - 4\pi\rho_e \right)^{1/2} = \left({k_{z0}}^2 - {k_{c1}}^2 \right)^{1/2} \qquad \text{(Eq. 2.25)}$$

and

$$R_F = \left| \frac{1 - \left[1 - \left(k_{c1} / k_{z0} \right)^2 \right]^{1/2}}{1 + \left[1 - \left(k_{c1} / k_{z0} \right)^2 \right]^{1/2}} \right|^2 \qquad \text{(Eq. 2.26)}$$

where k_{c1} is the critical value of k_{z1} below which total reflection occurs, and R_F now can be regarded as a function of θ or q_z.

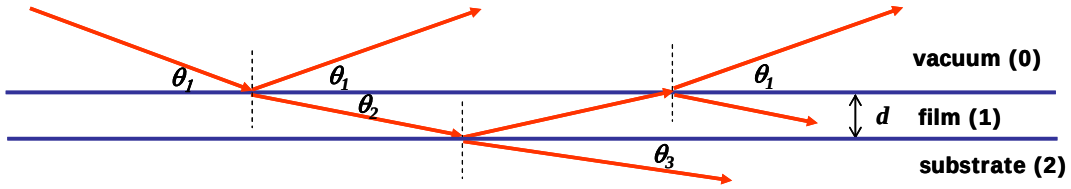

Figure 2.21: Schematic diagram of the beam path in a thin film with a thickness of d on a substrate.

For a two interface system, as shown in Figure 2.21, the reflection coefficients, r_{12} (between the substrate and the film) and r_{01} (between the film and vacuum) are of

importance. Both of these can be calculated from Equation 2.23, and the two interfaces are displaced by the thickness of the specimen, *d*, yielding

$$r = \frac{r_{01} + r_{12}\exp(2ik_{z1}d)}{1 + r_{01}r_{12}\exp(2ik_{z1}d)} \qquad \text{(Eq. 2.27)}$$

When the reflection coefficients are real, the reflectivity *R* can be written as

$$R = rr^{*} = \frac{r_{01}^2 + r_{12}^2 + 2r_{01}r_{12}\cos(2ik_{z1}d)}{1 + r_{01}^2 r_{12}^2 + 2r_{01}r_{12}\cos(2ik_{z1}d)} \qquad \text{(Eq. 2.28)}$$

Equation 2.28 shows that the reflectivity profiles will contain a series of maxima and minima as θ or q_z changes. This interference pattern was first noticed by Kiessig,[179,180] and interference fringes seen in x-ray reflectivity measurements are now referred to as "Kiessig fringes". Film thickness can be derived from the position of the interference minima or maxima:

$$d = \frac{\pi}{\Delta k_{z1}} = \frac{2\pi}{\Delta q} \qquad \text{(Eq. 2.29)}$$

Nowadays this function is not commonly used in x-ray reflectivity analysis; instead, full mathematical models combined with least-squared fitting techniques following the theory developed by Parratt are more commonly used.[181] Recently, Thompson reported a method to evaluate film thickness from refraction-corrected minima.[182]

To reduce the penetration of x-rays into a surface and thus to limit the depth from which information will be gathered, one can simply reduce the angle of the incidence, θ_{i0}. A rapid change in penetration depth near the critical angle reveals how x-ray reflectivity techniques become very surface sensitive at very low incident angles, and can

theoretically be used to study extremely thin films, including atomic monolayers.[177] X-ray reflectivity techniques are important in the study of surface modification that is either difficult or impossible to assess structurally with other methods. X-ray reflectivity has been used to study Langmuir monolayers at the A/W interface to obtain monolayer structures, phase transitions, ordering, etc.[177,178] For instance, x-ray reflectivity was used to study monolayer to bilayer transformations for stearic acid on Co ion containing subphases after collapse.[183] X-ray reflectivity was also used to study the interaction and adsorption of cytosolic phospolipase onto Langmuir monolayers of phosphocholine.[184] X-ray reflectivity can also be used to study protein folding at the A/W interface.[185] The application of x-ray reflectivity to LB-films has been widely reported for the evaluation of film thickness, surface density, surface roughness, and surface structures.[186-192] It should be noted that Bissett and Iball observed the appearance of secondary maxima between the Bragg reflections.[193] These secondary maxima, characteristic of the multilayer spacing, are due to the diffraction from a finite lattice created by the finite number of monolayers comprising the LB-multilayer. The first quantitative treatment of the reflectivity from LB-films were performed by Pomerantz and Segmuller on manganese stearate monolayer and multilayer films.[194,195]

2.9.3 Reflection Absorption Infrared Spectroscopy

Reflection absorption infrared spectroscopy (RAIRS) is also known by different acronyms, such as FT-IRAS (Fourier transform infrared reflection absorption spectroscopy), IRRAS (infrared reflection absorption spectroscopy), ERIRS (external reflection infrared spectroscopy), or grazing-angle infrared spectroscopy.[196,197] In RAIRS experiments, a beam of infrared radiation is directed towards a sample surface. The excitation of vibrational modes of molecules in thin films is governed by a "surface selection rule", and the Fourier transform technique is used to generate spectra. The surface selection rule was first described by Greenler and is summarized in Figure 2.22.[198-200] The electric field of the impinging IR beam can be resolved into *s*- and *p*-polarized components. The *s*-polarized light only has a component parallel (*S*) to the surface in the y-direction, while the *p*-polarized light has a component parallel to the substrate surface (P_p) and another component perpendicular (P_n) to the substrate surface. The electric field vector of the impinging IR beam that is normal to the surface excites dipole-active vibrational modes of surface molecules. When reflected from the surface, *p*-polarized radiation leads to a net doubling of the electric field vector amplitude, while *s*-polarized light results in a net amplitude of zero, due to a 180^o phase shift for all angles of incidence. Therefore, only vibrations with dipole components perpendicular to the substrate surface will be excited by *p*-polarized radiation and appear in the RAIRS spectra. In addition to the surface selection rule, Greenler also found that the *p*-polarized component of the electromagnetic radiation reaches a maximum at grazing

incidence.[199] For instance, with *p*-polarized radiation and incident angles near grazing incidence, an increase in sensitivity of approximately a factor of 25 can be achieved, compared to transmission experiments. This advantage is reduced to a factor of ~ 17 if the spread of incident angles is ± 5° at approximately 85°.[201]

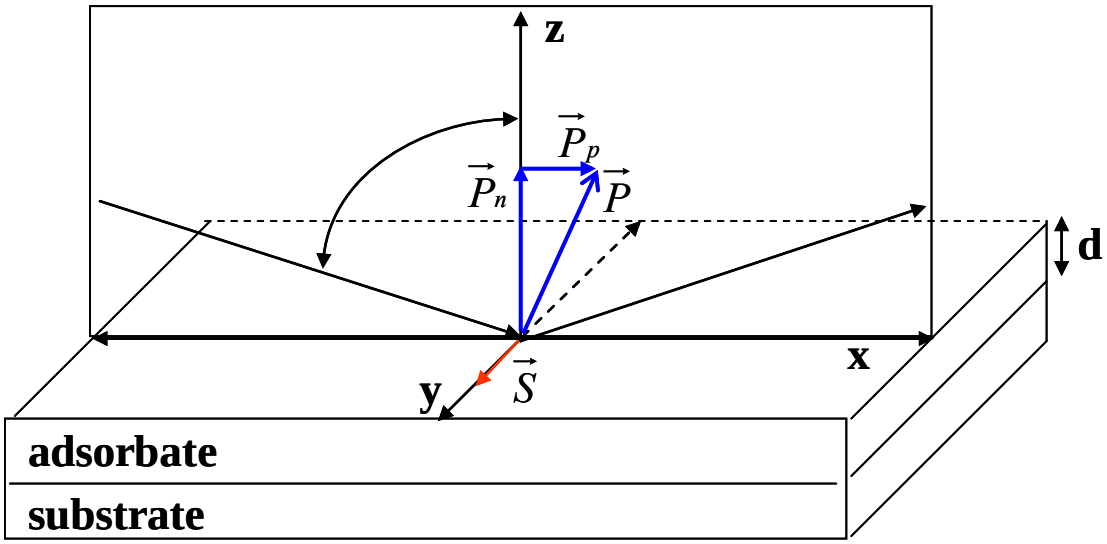

Figure 2.22: Surface selection rule for RAIRS.[198,200]

The pioneering work of applying RAIRS to monolayers was made by Allara and Swalen in 1982.[202] The structure of the alkanethiol monolayers on gold as a function of the chain length was studied by Porter *et al.* with RAIRS in 1987.[203] RAIRS has been applied to study chain orientation, structural transitions, thermally induced order-to-disorder transitions, and orientation changes in self-assembled monolayers as well as in LB-films.[34,58,204-206] RAIRS can also be used in the characterization of

membrane proteins, or the structures of other biological molecules at the A/W interface.[196] In addition, RAIRS has been reported as a suitable technique for studying crystallization behavior of organic thin films.[207]

CHAPTER 3

Materials and Experimental Methods

3.1 Materials

3.1.1 Poly(L-lactic acid) and Poly(tert-butyl acrylate)

Poly(L-lactic acid) (PLLA) and poly(tert-butyl acrylate) (PtBA) were obtained from Polymer Source, Inc., and were used without further purification. The number average molar masses (M_n) of PLLA samples were [with polydispersity indices (M_w/M_n) in parentheses]: M_n = 1.3 (1.1), 4.5 (1.32), 7.9 (1.27), 12.9 (1.24), 16.8 (1.30), 24.6 (1.33), and 40.4 (1.35) kg•mol^{-1}. The molar masses are provided by the manufacturer, and were confirmed by nuclear magnetic resonance (NMR) spectroscopy with end-group analysis (Figure 3.1). For PtBA, M_n = 23.8 kg•mol^{-1} and has a polydispersity index of 1.08. HPLC grade chloroform (Burdick & Jackson) was used to prepare ~ 0.1 mg•g^{-1} spreading solutions.

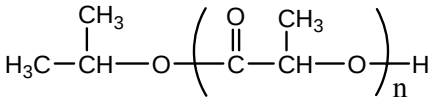

Figure 3.1: Chemical structure of PLLA samples.

3.1.2 Solid Substrates for Langmuir-Blodgett Deposition

Silicon substrates [EnCompass Materials Group, Ltd., Dopant: Phosphorous, Type N, Orientation (1,0,0)] were used as Langmuir-Blodgett (LB) film substrates. Silicon

substrates were boiled in a 5:1:1 (by volume) mixture of H_2O:NH_4OH (concentrated):H_2O_2 (30% by volume) for 1.5 hours. After rinsing off the wafers with Millipore water, the substrates were immersed in a piranha solution [a 70:30 mixture of H_2SO_4 (concentrated):H_2O_2 (30% by volume)] for 0.5 hours. The substrates were then rinsed with copious amounts of water, dried with nitrogen, and dipped into a buffered HF acid solution (CMOS Grade, J.T. Baker) for 5 minutes followed by a brief dip into a buffered NH_4F solution (CMOS Grade, J.T. Baker). The substrates were again rinsed with water and dried with nitrogen. The H_2O_2, H_2SO_4, and NH_4OH used in the cleaning process were obtained from EM Science, VWR International, and Fisher Scientific, respectively.

Glass slides with one surface covered by 1 nm of chromium and 50 nm of gold (EMF Corporation) were used to prepare LB-films for infrared spectroscopy (IR) studies. Gold substrates were placed in piranha solution for one hour, rinsed with copious amounts of Millipore water, and dried with nitrogen. The substrates were then placed into a glass chamber, and 0.5 mL 1,1,1,3,3,3-hexamethyldisilazane (99.9%, Sigma-Aldrich) was added. The glass chamber was put in an oven at 80 ^{o}C for at least three hours to hydrophobize the glass side of the substrates. The substrates were then rinsed with copious amounts of water, dried with nitrogen, and rinsed with ethanol (absolute, AAPER Alcohol). The substrates were placed in a 1 mM ethanolic solution of 1-dodecanethiol (92%, Aldrich) for approximately 18 hours to make the gold side of

the substrates hydrophobic. The substrates were then removed from the solution, rinsed with ethanol and water, and were dried with nitrogen before LB-films were deposited.

3.2 Sample Characterization

3.2.1 Differential Scanning Calorimetry

Differential scanning calorimetry (DSC) measurements were conducted using a 2920 MDSC instrument (Thermal Analysis). A PLLA sample of about 5 mg was sealed in an aluminum sample pan, and the temperature of the sample was controlled in the DSC cell. Samples were always kept under a nitrogen atmosphere. The heating rate during testing was 10 $^{o}C \bullet minute^{-1}$, and two heating cycles from 0 to 200 ^{o}C were applied, with an intermediate hold time of 1 minute at 200 ^{o}C.

3.2.2 Attenuated Total Reflectance Fourier Transform Infrared Spectroscopy

Attenuated total reflectance Fourier transform infrared spectroscopy (ATR-FTIR) was conducted using a MIDAC FTIR, with the powder sitting on a Dura SAMPLIR^{TM}. As-received PLLA powder was used.

3.3 Experimental Methods at the Air/Water Interface

3.3.1 Isotherm Studies

Isotherm studies were conducted with a standard Langmuir trough (500 or 700 cm^2, Nima Technology, Ltd., 601 BAM or 702 BAM) equipped with a Brewster angle microscope (BAM) (MiniBAM, Nanofilm Technologie GmbH, Linear resolution is ~ 20

μm). The instruments were housed in a Plexiglas™ box at 70-75% relative humidity. The entire experimental set-up (Langmuir trough, BAM, and Plexiglas box) rested on a floating optical table to minimize stray light and mechanical vibrations (Newport RS-2000 & I-2000). The Langmuir trough was made of strongly hydrophobic Teflon® and was cleaned by dichloromethane or chloroform without any chemical reaction or degradation. The Langmuir trough is filled with ultrapure 18.2 MΩ water (Millipore, Milli-Q Gradient A-10). Two movable barriers were used to sweep the water surface so as to vary the surface area symmetrically from both sides of the film. The barriers were made of either a hydrophilic acetal resin polymer (Delrin®) or hydrophobic Teflon®, and were cleaned with isopropanol or dichloromethane, respectively. The hydrophobic trough supported an approximately 1 mm brim of water above the top of the trough edge. The trough was wiped with dichloromethane and then cleaned with ultrapure water. The barriers were automatically moved toward each other thereby collecting dust and surface-active contaminations into the center of the trough. The dust and surface-active contaminations were then suctioned off by a clean pipette connected to a vacuum pump. The cleaning procedure was repeated multiple times until the surface pressure at the minimum trough area was zero for at least 30 minutes.

After spreading the chloroform solution, a minimum of 20 minutes was allowed prior to starting the isotherm measurements to ensure complete evaporation of the spreading solvent. Surface pressure, Π, was recorded by the Wilhelmy plate technique to ± 0.1 $mN \bullet m^{-1}$ during all isotherm measurements. A piece of completely wetted filter paper

was used as the Wilhelmy plate. The temperature of the subphase was maintained by circulating water through the base of the trough. The relationship between the temperature of the circulating water and the actual temperatures of the water subphase at various positions for the 702 BAM trough is shown in Figure 3.2. It was observed that the actual temperature of the subphase at different positions differed from the temperature of the circulating water; however, the values at different trough positions were quite similar for a given temperature. Deviation was observed for temperatures measured at position 3 relative to the other positions in the trough. This feature may be due to larger amounts of water inside the LB-well. During experiments, the temperature of the circulating water was recorded and used to calculate the temperature of the water subphase according to Figure 3.2. In this dissertation, the temperature of the water subphase is reported and used for analyses.

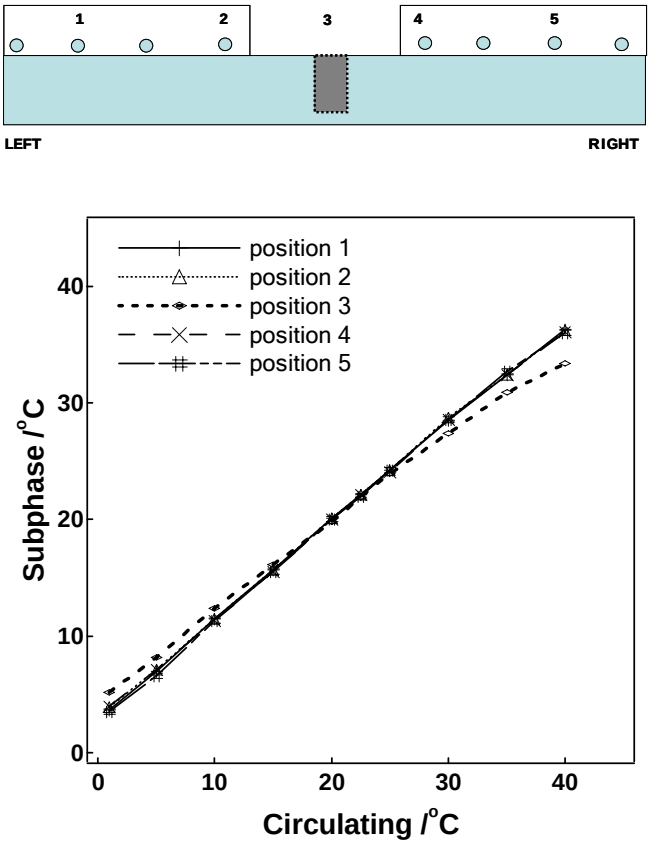

Figure 3.2: Calibration curve for the temperature of the water subphase on a 702 BAM Langmuir trough at various trough positions.

3.3.2 Constant Compression Rate Experiments

During a constant compression rate experiment, Langmuir monolayers were compressed by the barriers at a specific rate. This type of experiment was commonly used to determine the molecular area as the film went through various phase transitions. The compression rate of the barriers was 10 $cm^2 \bullet min^{-1}$, which corresponds to ~ 0.018 $nm^2 \bullet min^{-1} \bullet monomer^{-1}$ when ~ 65 mg of spreading solution (~ 0.1 $mg \bullet g^{-1}$ in $CHCl_3$) was spread onto the subphase.

3.3.3 Compression and Expansion Isotherms: Hysteresis Loops

During hysteresis loop experiments, each sample was first compressed to a target Π or area per monomer, *A*, at a fixed barrier rate (20 $cm^2 \bullet min^{-1}$), and then expanded at the same barrier rate back to the initial trough area. The hysteresis method was used to test the reversibility of different phases in the film. For this purpose, multiple hysteresis loops were also obtained: (1) second hysteresis loops obtained immediately after the completion of the first hysteresis loop versus second hysteresis loops obtained after waiting a fixed period of time between the first and second hysteresis loops; and (2) expansion of films immediately after reaching a target Π or *A* value versus expansion after waiting a fixed period of time following the compression stage.

3.3.4 Surface Pressure Relaxation Experiments

For Π relaxation experiments, the sample was compressed at a fixed rate to a target Π. Then the barriers were held at that position, and the sample was allowed to relax to a constant Π value while the Π versus time (Π-*t*) curve was recorded.

3.3.5 Isobaric Area Relaxation Experiments

To study collapse process of Langmuir monolayers through two-dimensional (2D) to three-dimensional (3D) nucleation and growth mechanisms, isobaric area relaxation experiments were carried out around the monolayer collapse point. Before an isobaric area relaxation experiment, the spread monolayer was continuously compressed to a target Π at a fixed barrier rate of 20 $cm^2 \bullet min^{-1}$, and then the area versus time (*A*-*t*) curve was recorded while maintaining a constant Π value.

3.3.6 Successive Addition Experiments

For successive addition experiments, the surface area was held constant and the surface concentration was varied by making successive additions of very dilute spreading solution (~ 0.02 $mg \bullet g^{-1}$). After each addition, Π was allowed to relax to a constant minimum value ($\Delta\Pi < 0.1$ $mN \bullet m^{-1}$ over a 15 minute period). For most surface concentrations, total relaxation time was on the order of 30-40 minutes. Addition experiments could reveal "equilibrium" properties of monolayers since compression can have dynamic effects on Π-*A* isotherms.

3.3.7 Brewster Angle Microscopy

BAM studies (MiniBAM, NanoFilm Technologie, Ltd., linear resolution of at least 20 μm) were carried out simultaneously during isotherm measurements, and the BAM images were taken by a charge-coupled device (CCD) camera under the "automatic gain control" mode to obtain an optimal average brightness rather than absolute intensity values. Although this procedure provided the greatest sensitivity for detecting morphological differences, care must be taken in comparing different images because the same feature might appear bright in one image where it had the greatest reflectivity but gray in another image as a result of the presence of more strongly reflecting objects. The original size of all BAM images taken during the measurements was 4.8×6.4 mm^2, while some BAM images presented in this dissertation with smaller sizes were cut from the original images utilizing imaging software.

3.4 Langmuir-Blodgett Deposition

Ultra-thin Langmuir-Blodgett (LB) films were obtained for PLLA at various Π values using a commercial LB-trough (KSV 2000) by Y-type deposition. The compression rate for approaching the target Π was 10 mm•min^{-1}, as was the maximum forward and reverse rate of the barriers during the dipping process to maintain a constant target Π. The dipping rates were 10 mm•min^{-1} for both the up- and downstrokes. One dipping cycle (including one up- and one downstroke) was used to prepare bilayer LB-films on silicon substrates at different Π values for atomic force microscopy (AFM) measurements. Five dipping cycles were used to prepare thicker LB-films on gold substrates at different Π values for reflection absorption infrared spectroscopy (RAIRS) studies. LB transfer ratios for PLLA LB-films varied significantly with the Π value at which the films were prepared, and will be discussed in Chapters 5 and 6. For x-ray reflectivity measurements, PLLA bilayers were deposited at Π = 7.0 mN•m^{-1} and PtBA was transferred at Π = 19.0 mN•m^{-1}. In both cases, the transfer ratios were ~ 1.0 for all the up- and downstrokes.

3.5 Surface Analysis Techniques

3.5.1 Atomic Force Microscopy

AFM images were obtained in the Tapping Mode^{TM} with a Digital Instruments Dimension 3000 Scope with a Nanoscope IIIa controller using etched single crystal silicon tips. 5×5 μm^2 or 2×2 μm^2 images were captured at a set-point ratio of ca. 0.6.

3.5.2 X-Ray Reflectivity Measurements

X-ray reflectivity was performed at the National Institute of Standards and Technology (NIST) Center for Neutron Research using Cu-K_α radiation with a wavelength of 1.542 Å on a Bruker AXS-D8 Advance Diffractometer. X-ray reflectivity profiles reported in this dissertation were corrected for the fraction of the incident beam subtended by the sample by subtracting background scans. The periodic fluctuations seen in the x-ray reflectivity profiles represent Kiessig fringes, which arise from the interference between the x-rays reflected from the Si//polymer and polymer//air interfaces. The thickness of the film was obtained by knowing the spacing between maxima or between the minima. In this dissertation, the thickness of the films was obtained by plotting the refraction-corrected minima versus minima index.[182] Roughnesses of both the film and the substrate were obtained by fitting the experimental profiles with theoretical curves in Microsoft Excel.[208,209] Data analysis will be described in Chapter 5.

3.5.3 Reflection Absorption Infrared Spectroscopy

In order to avoid interference from water vapor for IR spectra of thin films, reflection absorption infrared spectroscopy (RAIRS) was performed under vacuum using a Bruker IFS 66v/S spectrometer using *p*-polarized light at an incident angle of 86^o and a liquid-nitrogen cooled MCT (mercury-cadmium-telluride) detector. Clean gold substrates served as background references. Each spectrum was collected using a minimum resolution of 2 cm^{-1} and represents an average of 100 scans. In order to obtain

the low wavenumber (< 1000 cm^{-1}) part spectra, RAIRS was also performed using a nitrogen purge Nicolet NEXUS 670 FT-IR spectrometer with *p*-polarized light at an incident angle of 86^{o} and a liquid-nitrogen cooled MCT detector. Clean gold substrates again served as background references. Each spectrum was collected using a minimum resolution of 2 cm^{-1} and represents an average of 1000 scans to obtain better signal-to-noise ratios in the range less than 1000 cm^{-1}. The former instrument shows less water interference while the latter instrument provides better detection in the range less than 1000 cm^{-1} because of our overall instrumental configurations.

CHAPTER 4

Thermodynamics of the Liquid Expanded to Condensed Phase Transition of Poly(L-Lactic Acid) in Langmuir Monolayers

The following chapter appeared as an article in Langmuir: **Ni, S. L.**; Lee, W. J.; Li, B. B.; Esker, A. R. "Thermodynamics of the liquid expanded to condensed phase transition of poly(L-lactic acid) in Langmuir monolayers," *Langmuir* **2006**, *22*, 3672-3677.

4.1 Abstract

Surface pressure–area (Π-*A*) isotherms show that poly(L-lactic acid), PLLA, Langmuir monolayers exhibit a liquid expanded to liquid condensed (LE/LC) phase transition at low surface pressure. Brewster angle microscopy images show circular domains where the LC phase is surrounded by the LE phase during phase coexistence. Morphology studies via atomic force microscopy measurements show that well-ordered patterns are only observed for Langmuir-Blodgett films prepared in the LC phase, while no ordered features are observed in the LE phase. The morphological differences confirm that during the LE/LC phase transition PLLA molecules form well-ordered structures at the air/water interface. Analysis by the two-dimensional Clausius-Clapeyron equation is used to predict the critical parameters (X_c). Both critical parameters, the critical temperature (T_c) and the critical pressure (Π_c), increase with increasing number average molar mass (M_n) as $X_c = X_{c,\infty} - KM_n^{-1}$, where $X_{c,\infty}$ is the value of the critical parameter at infinite molar mass and K is a constant. For PLLA, $T_{c,\infty}$ =

36.2 ± 0.3 ^{o}C and $\Pi_{c,\infty}$ = 4.53 ± 0.06 mN•m^{-1}. This study provides a model polymer system for examining critical behavior in two dimensions.

4.2 Introduction

Traditional amphiphilic molecules that form Langmuir monolayers at the air/water (A/W) interface contain hydrophilic heads that anchor onto a water subphase and hydrophobic tails that point towards air.[29] Langmuir monolayers have gained interest in fields of chemistry, physics, and life sciences,[36,81,210,211] and can serve as model systems for studying two-dimensional (2D) phase transitions and ordering,[60,74,212] as well as templates for 2D chemical and biological reactions.[38] The reduced dimensionality in Langmuir monolayers can also simplify model theoretical calculations.[39,40] The understanding of thermodynamic phase transitions in Langmuir monolayers is crucial when applying the Langmuir-Blodgett (LB) technique to fabricate thin molecular films on solid substrates.[28,31,32]

Long-chain fatty acids and lipids are widely studied as Langmuir monolayers at the A/W interface.[36] Π-*A* isotherm studies are used to elucidate the phase behavior of Langmuir monolayers. At low surface concentration, the molecules are widely separated with weak interactions, remaining in a 2D gaseous (G) state. An increase in surface concentration can lead to the formation of a liquid expanded (LE) phase. As the surface concentration progressively increases, condensed (LC) phases and even a solid (S) phase may appear. Brewster angle microscopy (BAM), grazing incidence x-ray

diffraction (GIXD), and fluorescence microscopy (FM) measurements show the existence of different tilted and untilted condensed phases for fatty acids and lipids.[36,79,80,213] The collapse of Langmuir monolayers often results in the appearance of solid-like multilayer domains.[214,215]

The LE/LC phase transition appears as a plateau in the isotherm.[60] The nonzero slope of the LE/LC phase transition, as observed in most Π-*A* isotherm studies, is strictly inconsistent with a first-order transition.[36,60] However, monolayer experiments using fluorescence imaging,[60] electron microscopy,[73] and BAM[65,74,75] are consistent with a first-order transition showing that large islands of the LC phase are dispersed in the LE phase. More often, the nonzero slopes in the LE/LC region are treated as artifacts produced by impurities, the formation of small molecular aggregates or surface micelles, or non-equilibrium effects such as finite compression rates.[36,71] The experimental evidence for a zero slope associated with the LE/LC phase transition has been obtained for lipid and fatty acid monolayers using a very careful experimental protocol: an ultra-clean system, pure materials, extremely slow compression rates, and a stable film.[216] Such an experimental protocol is difficult to follow for polymers due to their polydispersity and higher viscosity. The gas-liquid-expanded (G/LE) and LE/LC coexistence lines may also merge at low temperatures resulting in a triple point.[60]

Some theoretical models do predict nonzero slopes by considering the interactions between head groups, hydrophobic chains, and the effect of chain flexibility, that can qualitatively fit some features of the LE/LC phase transitions.[39,217,218] For instance,

Ruckenstein used a 2D lattice model to evaluate the surface equation of state.[219] In his model, headgroups behaved like a gas at the interface in the monolayer region due to the existence of free sites, and hydrocarbon chains behaved like liquids and solids in the LE and LC phases, respectively. A surface equation of state was thus established according to the definition of surface Helmholtz free energy, which has three major contributions: change of Helmholtz free energy of surfactant molecules at the interface, a 2D internal energy of mixing, and a 2D entropy of mixing. Π-*A* isotherms were generalized according to the surface equation of state, and depended on several factors such as dipole-dipole interactions, chain conformational free energy, dipole moment densities of different phases, etc. Ruckenstein successfully fit generalized Π-*A* isotherms with experimental results, suggesting the first-order nature of the LE/LC phase transitions.

Although LE/LC phase transitions have been widely reported for small molecules, LE/LC phase transitions in polymer monolayers have only received limited attention. Langmuir monolayers of robust amphiphilic polymers exhibit less complicated Π-*A* isotherms.[103,104] Π-*A* isotherms of polymers generally show a gas phase, a liquid phase and a solid-like phase. Crisp suggested that polymer Langmuir monolayers can be classified as either "condensed" or "expanded".[104] Expanded polymer monolayers exhibit a gradual rise in the surface pressure, while condensed polymer monolayers are identified by their high viscosity or rigidity, together with much steeper slopes on Π-*A* isotherms. It is necessary to mention that condensed or expanded polymer monolayers are different from condensed or expanded phases for fatty acids as polymer monolayers

often lack long hydrophobic tails like lipids that lead to the existence of complicated tilted or untilted phases at the A/W interface in lipid systems. Other than the poly(L-lactic acid) (PLLA) system reported here, only two other polymers have been reported to have a LE/LC phase transition. On of those, a comblike copolymer possessing long alkyl side chains is similar to lipids.[220] However, the other one, a dendritic linear block copolymer, lacks a lipid-like structure.[221]

Recently, there has been an increasing interest in studying Langmuir monolayers of biodegradable and biocompatible polymers, such as poly(ε-caprolactone) (PCL),[135] poly(lactic acid) (PLA),[155,156,222,223] and related copolymers.[224,225] PLA can be produced from renewable carbon sources and has been widely used for pharmaceutical applications.[226,227] Because of the chirality of the lactide monomer, PLA forms polyenantiomers such as PLLA and poly(D-lactic acid) (PDLA), both of which have a glass transition temperature around 50 ^{o}C and a melting point of ~ 180 ^{o}C.[142] Blends of PLLA and PDLA form 3_1-helices with a triclinic unit cell.[147] However, the individual polyenantiomers do not form a simple 3_1 helix. It has been reported that pure PLLA (or PDLA) crystallizes into left-handed (or right-handed) 10_3-helices, respectively, with a pseudo-orthorhombic unit cell (known as the α-form).[144,145]

Studies of PLA at the A/W interface reveal that pure PLLA or PDLA and their blends spontaneously form 10_3-helices at the A/W interface.[155] Further compression into the solid-like state does not alter the helical conformation of pure PLLA and PDLA. However, in solid-like domains, PLLA/PDLA stereocomplexes form 3_1-helices.[156]

In this study, PLLA Langmuir monolayers are examined at the A/W interface. A LE/LC phase transition is observed for this homopolymer system. The critical parameters, which are related to the difference in chain mobility or free volume (area), are dependent on molar mass. The morphology studies confirm that during the LE/LC phase transition, PLLA molecules are ordered at the A/W interface. This study provides a model system for studying critical phenomena in polymers confined to 2D. Furthermore, it also provides insight into the ordering and patterning of PLLA molecules on solid substrates *via* the LB-technique that may be suitable for cell adhesion studies.

4.3 Results and Discussion

Figure 4.1 shows the surface pressure–area per monomer (Π-A) isotherm of a M_n = 12.9 kg•mol^{-1} PLLA Langmuir film at 22.5 ^{o}C. Different regions are observed: (*i*) a highly compressible, low Π, liquid-like monolayer corresponding to an LE phase; (*ii*) a transition with a nonzero slope at $\Pi \cong 1.8$ mN•m^{-1}; (*iii*) a low compressibility region that may correspond to an LC phase; (*iv*) a plateau at $\Pi \cong 7.8$ mN•m^{-1}; and (*v*) a lower compressibility region corresponding to multilayer formation. The transition at low Π in region *ii* is believed to be an LE/LC phase transition, and will be discussed further in the following sections of this chapter. The area value at the inflection point of region *iii* (the LC phase) is around 0.18 nm^2•monomer^{-1}, which is consistent with the value reported by Klass *et al*.[223] The area value also indicates a special property of PLLA at the A/W interface, in that unlike conventional amphiphilic molecules at the A/W

interface with their hydrophilic parts anchored onto the subphase and hydrophobic parts pointing toward air, PLLA molecules lie mostly flat on the subphase due to their strongly hydrophilic character. The plateau (region *iv*) has previously been attributed to either bilayer formation or a random 2D chain-to-helix transition.[223] As compression continues, Π increases rapidly which corresponds to region *v*, where multilayers form.

BAM images reveal biphasic behavior during the LE/LC phase transition at low Π (region *ii*).[74,228,229] Prior to the LE/LC phase transition, no features are observed implying a homogeneous monolayer (region *i*, Figure 4.1a and 4.2a). During the LE/LC phase transition, LC domains are surrounded by the LE phase forming circular structures within the biphasic region (Figure 4.1b). The circular domains have been observed for small amphiphilic molecules such as ethylene glycol mono-n-hexadecyl ether, monomyristoyl-*rac*-glycerol, methyl dexadecanoate, and methyl hydrohexadecanoate;[74,228,229] however they have not been reported for Langmuir monolayers of polymers. During the LE/LC coexistence region, the circular domains become larger during compression, suggesting the growth of the LC domains during the LE/LC phase transition (Figure 4.2b-g). However, the growth rate is slow compared to the minimum compression rate. As a result, the circular domains simply disappear at non-equilibrium Π values well above the transition pressure, Π_{tr}, during compression at a constant rate to *A* values well into the LC phase (Figure 4.2i).

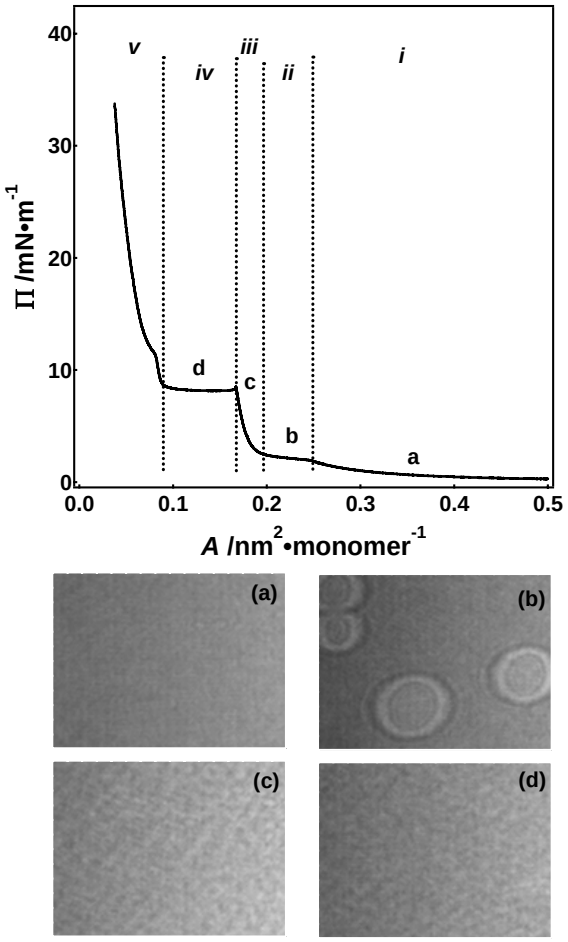

Figure 4.1: Π-*A* isotherm of a M_n = 12.9 kg•mol^{-1} PLLA Langmuir film obtained at T = 22.5 ^{o}C with a compression rate of 0.018 nm^2•monomer^{-1} •min^{-1}. Five regions are observed: (*i*) a LE phase; (*ii*) LE/LC coexistence; (*iii*) the formation of a LC monolayer; (*iv*) a plateau signifying film collapse; and (*v*) the formation of multilayers. The letters on the isotherm correspond to the BAM images at *A* values of: (a) 0.35, (b) 0.22, (c) 0.17, and (d) 0.14 nm^2•monomer^{-1}. Circular domains appear in the LE/LC coexistence region (*ii*), and disappear in the LC region (*iii*). All BAM images are 1.2 × 1.6 mm^2, cut from the original BAM images; and the film is symmetrically compressed from the top and bottom of each image. Each BAM image has an independent gray scale.

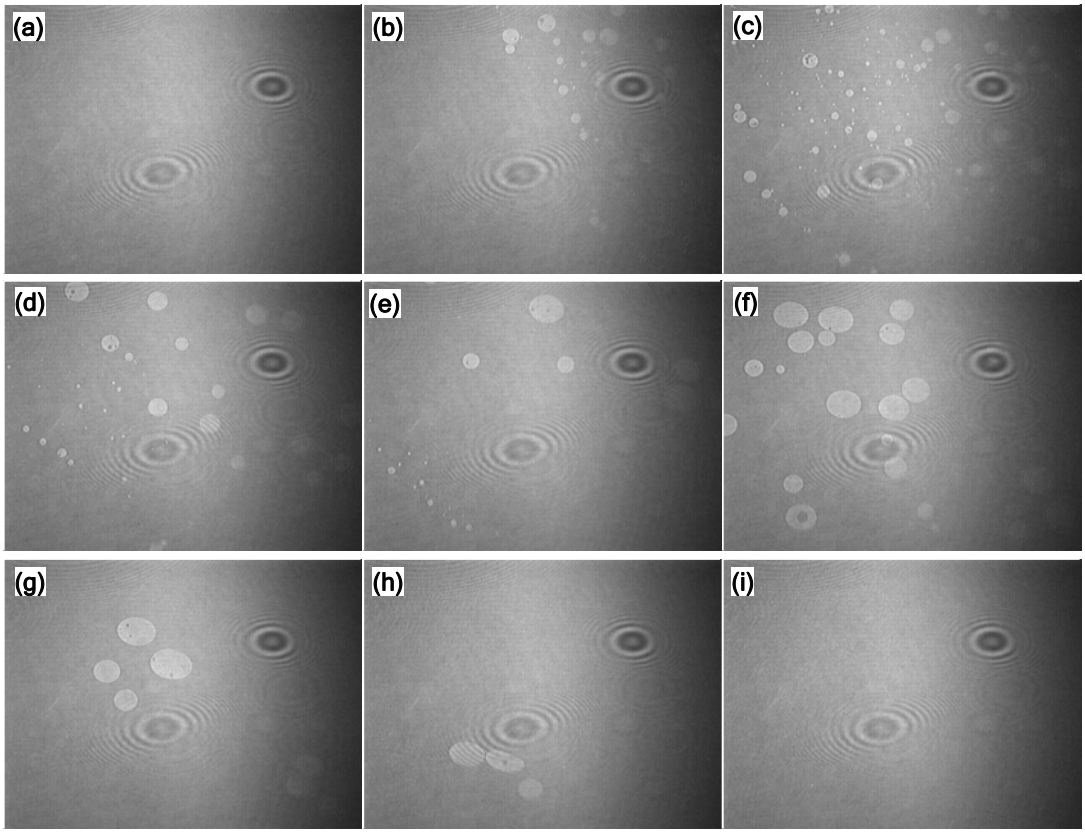

Figure 4.2: BAM images at T = 22.5 ^{o}C for a M_n = 12.9 kg•mol^{-1} PLLA Langmuir monolayer obtained at (A, Π) values of: (a) (0.26, 1.6), (b) (0.25, 1.9), (c) (0.24, 2.0), (d) (0.23, 2.1), (e) (0.22, 2.2), (f) (0.21, 2.3), (g) (0.20, 2.4), (h) (0.19, 2.7), and (i) (0.18, 3.8) (nm^2•monomer^{-1}, mN•m^{-1}). Circular domains appear in the LE/LC coexistence region (*ii*) above Π_{tr} = 1.8 mN•m^{-1}, and grow bigger during the phase transition as compression proceeds (b through g). The circular domains disappear after the film is compressed into the LC region at Π > 2.7 mN•m^{-1} (i). All BAM images are 4.8 × 6.4 mm^2, and the film is symmetrically compressed from the top and bottom of each image at a constant rate of 0.018 nm^2•monomer^{-1}•min^{-1}. Each BAM image has an independent gray scale.

4.3.1 The LE/LC Phase Transition: General

Isotherm studies of PLLA Langmuir films show a coexistence region between the LE and LC phase. A previous study with a related polymer, poly(D,L-lactic acid) (PDLLA50), carried out at the A/W interface and 25 ^{o}C claimed that a LE/LC phase transition occurred in a region of the isotherm corresponding to region *iv* in Figure 4.1.[222] BAM results clearly show biphasic behavior in region *ii* (Figure 4.1b, A = 0.22 nm^2•monomer^{-1});[74,228,229] moreover, the absence of similar morphological features in the BAM images taken at A = 0.14 nm^2•monomer^{-1} shows the plateau is not consistent with LE/LC coexistence in region i*v* of the isotherm (Figure 4.1d). The absence of large heterogeneous structures in the plateau region of the isotherm (Figure 4.1d) is most likely caused by small changes in thickness accompanying film collapse. As we will show shortly, this study provides clear evidence for a true LE/LC phase transition in region *ii* of the Π-*A* isotherm of a PLLA monolayer.

4.3.2 Zero-slope LE/LC Phase Transition with Successive Addition Experiments

The LE/LC phase transition does not show a zero slope coexistence region in the compression Π-A isotherms (Figure 4.1). This feature may be caused by nonequilibrium effects such as finite compression rates.[71] The effect of compression rate on the phase transition can be avoided with successive addition experiments. Figure 4.3 shows the Π-*A* isotherm of PLLA obtained from successive addition experiments. A flat transition is observed at Π = 1.9 mN•m^{-1} in the area range of 0.24 nm^2•monomer^{-1} to 0.19 nm^2•monomer^{-1}, confirming the first-order nature of the LE/LC

phase transition. No circular domains are observed with BAM during the LE/LC phase transition in addition experiments. This observation probably indicates that adding more spreading solution breaks up existing LC domains into sizes that are smaller than the lateral resolution of our BAM instrument.

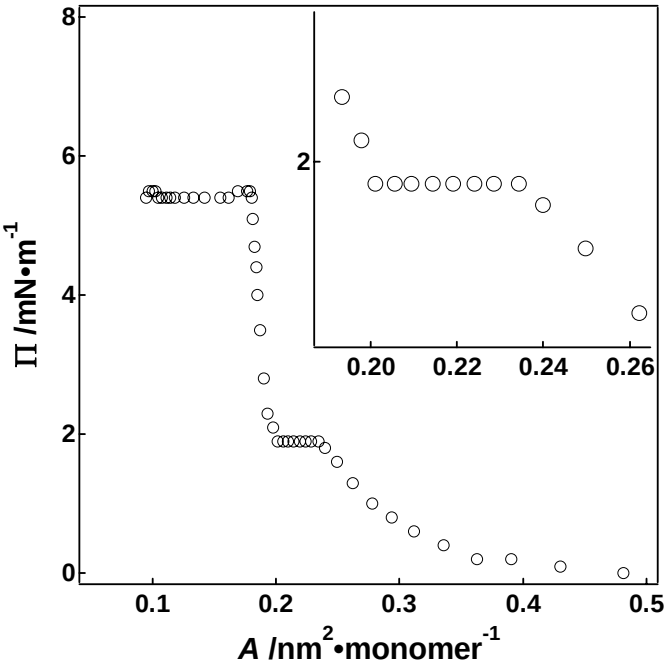

Figure 4.3: Π-*A* isotherm of M_n = 12.9 kg•mol^{-1} PLLA at T = 22.5 ^{o}C obtained from successive addition experiments. A zero slope LE/LC phase transition is observed at Π = 1.9 mN•m^{-1} in the area range of 0.24 nm^2•monomer^{-1} to 0.19 nm^2•monomer^{-1}.

4.3.3 Compressibility Differences between the LE and LC Phases

The compressibility (C) and the static elasticity (ε_s) are two important characteristics of Langmuir films. The static elasticity is defined as:

$$\varepsilon_s = C^{-1} = -A\left(\frac{\partial \Pi}{\partial A}\right)_T \qquad \text{(Eq. 4.1)}$$

and can be calculated from a Π-*A* isotherm. Figure 4.4 shows a plot of ε_s versus *A* for 12.9 kg•mol^{-1} PLLA at 22.5 ^{o}C for both compression and addition experiments. In the compression experiment (Figure 4.4a), two maxima are observed: $\varepsilon_{s,max\,1}$ = 5.8 mN•m^{-1} at *A* = 0.25 nm^2•monomer^{-1} and $\varepsilon_{s,max\,2}$ = 93.4 mN•m^{-1} at *A* = 0.17 nm^2•monomer^{-1}. The large difference in the maximum ε_s values is consistent with the existence of two distinct phases. For *A* values larger than 0.25 nm^2•monomer^{-1}, the Langmuir monolayer is in the compressible LE phase with relatively low static elasticity values. Between the two maxima, two phases coexist (the *A* range is between 0.24 and 0.20 nm^2•monomer^{-1}) where the ε_s values approach zero. Ideally, the ε_s values in the *A* range of 0.24 - 0.20 nm^2•monomer^{-1} should be 0 because of the first-order nature of the LE/LC phase transition. However, the nonzero slope in the Π-*A* isotherm leads to residual ε_s values around 2.5 mN•m^{-1}. ε_s values of zero are observed during the LE/LC phase transition for the successive addition isotherms (Figure 4.4b). The second maximum corresponds to the onset of the collapse of the Langmuir monolayer into solid multilayer. The LC phase exists in the *A* range of 0.20 - 0.17 nm^2•monomer^{-1} with ε_s values that are more than an order of magnitude greater than the LE phase. After the collapse begins, ε_s values fall to zero for *A* values corresponding to the plateau in the Π-*A* isotherm of a PLLA Langmuir film (Figure 4.1, region *iv*).

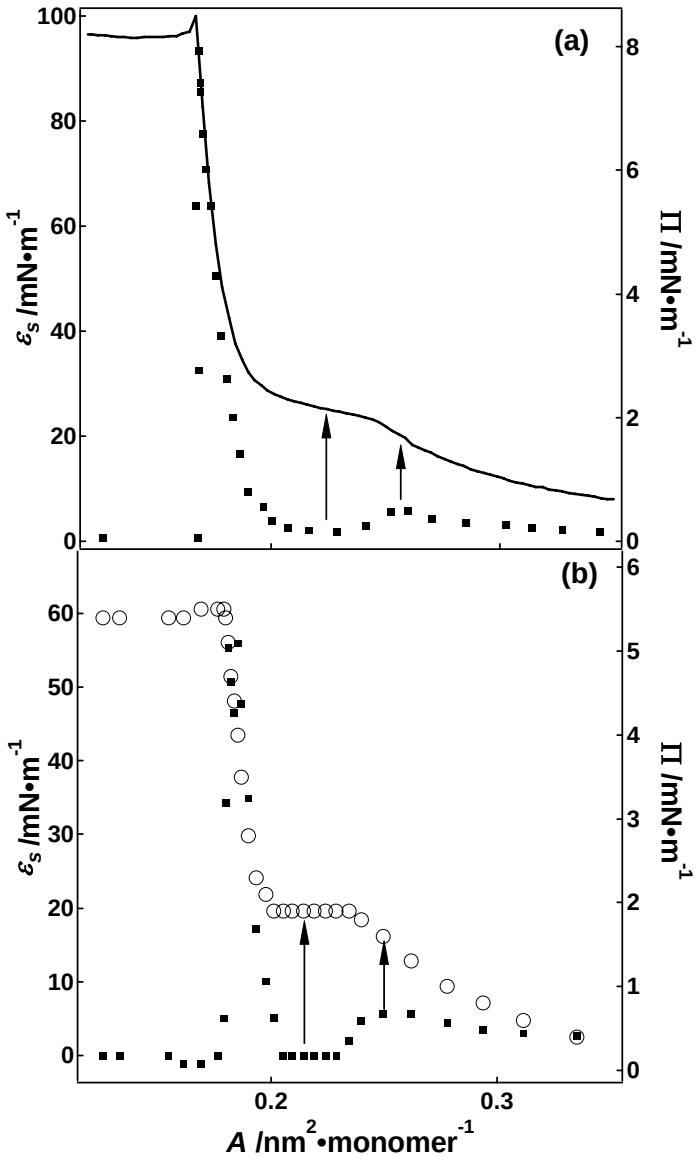

Figure 4.4: Plots of ε_s versus A (left-hand axis) for M_n = 12.9 kg•mol^{-1} PLLA at T = 22.5 ^oC (filled square) for: (a) compression, and (b) addition experiments. Two maxima are observed. Starting from large A, the first maximum (arrow to larger A) corresponds to the LE phase, the first minimum (arrow to smaller A) corresponds to LE/LC coexistence, and the second maximum corresponds to a LC monolayer followed by collapse into multilayer domains. The isotherms from Figures 4.1, solid line on (a), and 4.3, open circles on (b) are also plotted on the graph against the right-hand axis.

4.3.4 Temperature Dependence of the LE/LC Phase Transition

Figure 4.5 shows the temperature dependence of the LE/LC phase transition for 12.9 kg•mol^{-1} PLLA Langmuir films. With increasing temperature, the onset of the biphasic regime shifts to higher pressure values (Π_{tr}) and smaller areas per monomer (A_{tr}). The increase of Π_{tr} and the decrease of A_{tr} are necessary to overcome increasing thermal motion and chain flexibility at higher temperatures. As temperature increases, the length of the biphasic "plateau" decreases until the critical temperature is reached, T_c. At T_c, the biphasic regime is reduced to a single point (A_c, Π_c). Above T_c, no LC phase can form and the LE phase simply collapses for compression past the compression rate dependent collapse point ($A_{collapse}$, $\Pi_{collapse}$), *i.e.* $A < A_{collpase}$. In contrast to the LE/LC phase transition where Π_{tr} increases and A_{tr} decreases with increasing temperature, $\Pi_{collapse}$ decreases and $A_{collapse}$ increases with increasing temperature as shown in Figure 4.6. The decrease of $\Pi_{collapse}$ with increasing temperature is expected because PLLA molecules are in a less ordered arrangement at higher temperatures; meanwhile higher temperatures provide more thermal energy. Hence it is easier for Langmuir monolayers to overcome the energy barrier associated with the nucleation and growth of the 3D structures found in collapsed films at higher temperatures.

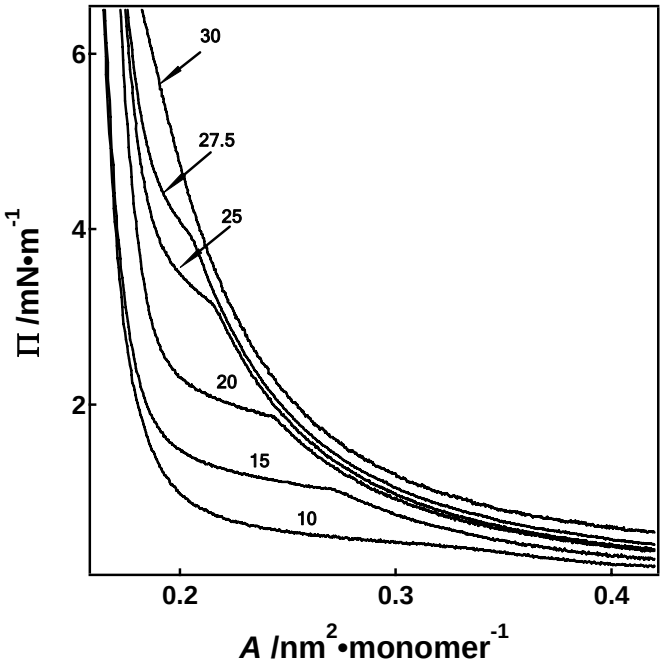

Figure 4.5: Temperature dependence of the LE/LC phase transition for M_n = 12.9 kg•mol^{-1} PLLA Langmuir films at the A/W interface. The experimental temperatures of the subphases are indicated by the numbers on the graph in units of ^oC. LE/LC phase coexistence is observed for isotherms below 27.5 ^oC, and is not observed at 30 ^oC, indicating the critical temperature (T_c) lies between 27.5 ^oC and 30 ^oC for 12.9 kg•mol^{-1} PLLA.

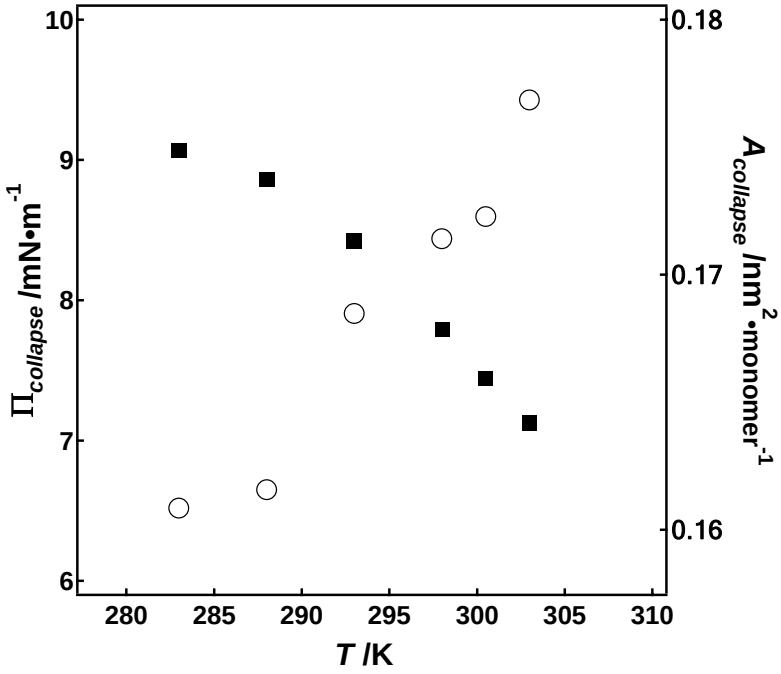

Figure 4.6: Temperature dependence of $\Pi_{collapse}$ (filled squares) and $A_{collapse}$ (open circles) for M_n = 12.9 kg•mol^{-1} PLLA Langmuir films at the A/W interface. $\Pi_{collapse}$ decreases and $A_{collapse}$ increases with increasing temperature.

Another feature of the LE/LC phase transition in Figure 4.5 is that as the critical temperature is approached from below, the nonzero slope becomes more pronounced. This feature has been explained qualitatively by Ruckenstein *et al.* using a lattice model involving long range dipole-dipole interactions, van der Waals interactions among the hydrocarbon chains, and the conformational free energy of the chain.[219] Similar factors may play a role here. The nonzero slope complicates the determination of T_c. As seen in Figure 4.5, T_c for 12.9 kg•mol^{-1} PLLA lies between 27.5 ^{o}C and 30 ^{o}C. However, the

experimental limitations with respect to temperature control and compression rates make it difficult to determine the exact T_c value.

In order to overcome the limitations discussed above, the 2D Clausius-Clapeyron equations are used to estimate T_c.[36,230] In Equations 4.2 and 4.3,

$$\Delta S_{tr} = \frac{d\Pi_{tr}}{dT}\left(A_{LC} - A_{LE}\right) \qquad \text{(Eq. 4.2)}$$

and

$$\Delta H_{tr} = T\frac{d\Pi_{tr}}{dT}\left(A_{LC} - A_{LE}\right) \qquad \text{(Eq. 4.3)}$$

where ΔS_{tr} and ΔH_{tr} are the temperature dependent entropy and enthalpy changes for the LE/LC phase transition, respectively, Π_{tr} is surface pressure at the onset of the LE/LC phase transition, and A_{LE} is the area per monomer in the liquid expanded phase at Π_{tr}, *i.e.* $A_{LE} = A_{tr}$. The A_{LC} value is obtained from an extrapolation of the Π-A isotherm in the LC region as described elsewhere.[230,231]

Figure 4.7 shows the temperature dependence of Π_{tr} for 12.9 kg•mol^{-1} PLLA. A linear relationship is observed with a slope of 0.20 ± 0.01 mN•m^{-1}•K^{-1}. The extrapolation to Π_{tr} = 0 yields the temperature T_0 = 8.9 ± 1.0 ^{o}C. The theoretical significance of T_0 is that above T_0, a plateau in the isotherm is observed and below T_0, no LE phase should exist.[231] The slope is used to calculate the entropy and enthalpy changes for the LE/LC phase transitions according to Equations 4.2 and 4.3. ΔH_{tr} and ΔS_{tr} are plotted as a function of subphase temperature in Figure 4.8. Negative ΔH_{tr} and ΔS_{tr} values are observed and expected as the LE/LC phase transition is a disorder to order

transition.[29] The slope of the ΔH_{tr} versus T plot in Figure 4.8a can be used to obtain the difference in heat capacity between the LE and LC phases:

$$\Delta C_p^{tr} = \left(\frac{\partial \Delta H_{tr}}{\partial T} \right)_p = 0.24 \pm 0.02 \quad \text{kJ•mol}^{-1}\text{•K}^{-1} \qquad \text{(Eq. 4.4)}$$

The extrapolation of ΔH_{tr} to zero yields T_c, which is determined to be 28.6 ± 1.8 °C for 12.9 kg•mol^{-1} PLLA. The result agrees with our experimental prediction that the T_c value of 12.9 kg•mol^{-1} PLLA lies between 27.5 °C and 30 °C in Figure 4.5.

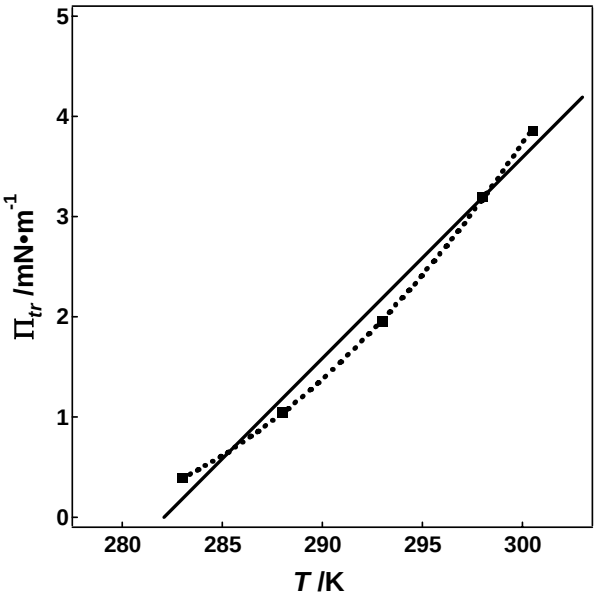

Figure 4.7: Temperature dependence of the LE/LC phase transition surface pressure, Π_{tr}, for M_n = 12.9 kg•mol^{-1} PLLA Langmuir films at the A/W interface. The solid line is the best linear fit yielding a slope of 0.20 ± 0.01 mN•m^{-1}•K^{-1} and a T_0 value of 8.9 ± 1.0 °C from the x-axis intercept. The dotted line is a quadratic fit, yielding temperature-dependent slope of -2.99 + 0.0109T with ultimate units of mN•m^{-1}•K^{-1}.

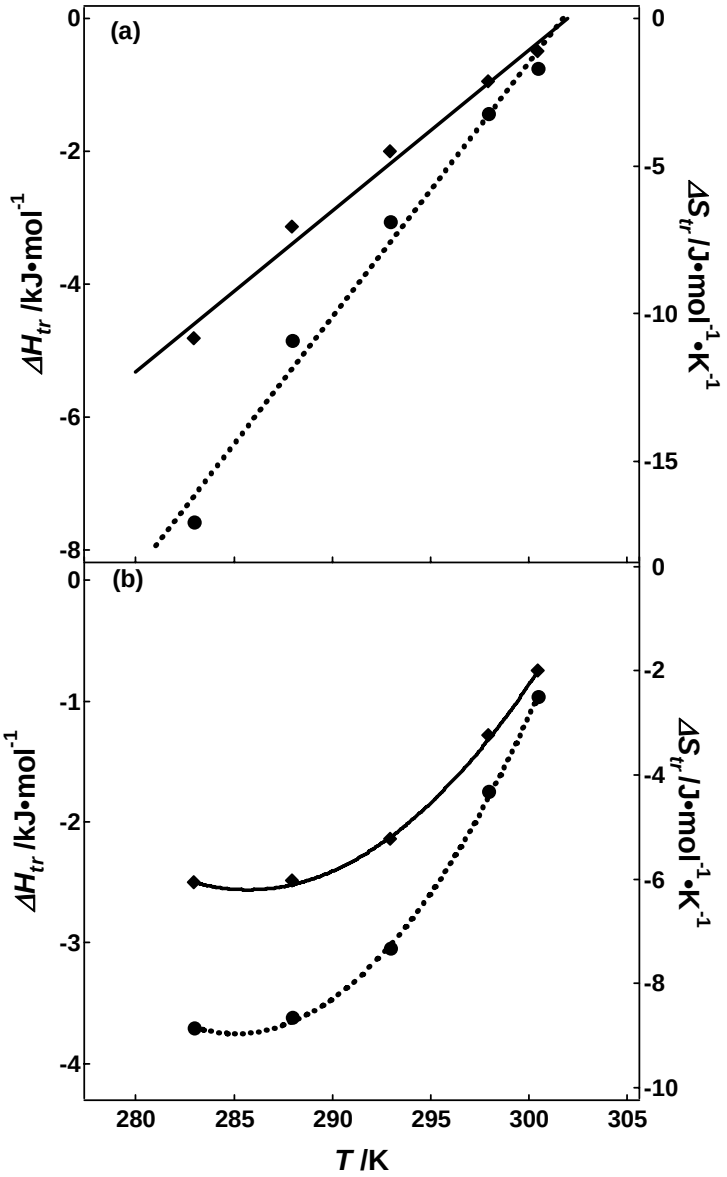

Figure 4.8: ΔS_{tr} (filled circles, right-hand axis) and ΔH_{tr} (filled squares, left-hand axis) as a function of temperature for the LE/LC phase transition of M_n = 12.9 kg•mol^{-1} PLLA. (a) Both ΔS_{tr} (dotted line) and ΔH_{tr} (solid line) are calculated using the linear fit from Figure 4.7. Using a linear extrapolation to $\Delta H_{tr} = 0$ yields $T_c = 28.6 \pm 1.8$ °C. (b) Both ΔS_{tr} (dotted line) and ΔH_{tr} (solid line) are calculated using the quadratic fit from Figure 4.7. Using a quadratic fit to extrapolate to $\Delta H_{tr} = 0$ yields $T_c = 29.2 \pm 1.2$ °C.

In addition, quadratic fitting is also applied to obtain the temperature dependence of Π_{tr} (Figure 4.7, dotted line). The temperature dependent slope is used to calculate ΔH_{tr} and ΔS_{tr} (as shown in Figure 4.8b). The extrapolation of ΔH_{tr} to zero with a quadratic fit yields T_c = 29.2 ± 1.2 ^{o}C for 12.9 kg•mol^{-1} PLLA. Within experimental error, both the linear and quadratic fits yield the same T_c value.

4.3.5 Molar Mass Dependence of the LE/LC Phase Transition

Figure 4.9 shows the LE/LC phase transition for different molar mass PLLA Langmuir films. To clearly show and compare the LE/LC phase transitions, only the region of the isotherms prior to collapse are shown. Complete isotherms are provided in Figure 4.10 for 12.9 kg•mol^{-1} PLLA and Figure 4.11 for the other molar masses, and will be discussed shortly. For each molar mass, similar qualitative trends for the LE/LC phase transition as discussed above for 12.9 kg•mol^{-1} PLLA are seen. Two major differences arise from a comparison of these isotherms: (1) The LE/LC phase transition shows different T_c values for PLLA Langmuir films with different molar masses. For example, T_c for 7.9 kg•mol^{-1} PLLA must be less than 25 ^{o}C because no LE/LC phase transition is observed at 25 ^{o}C, while T_c for 40.4 kg•mol^{-1} PLLA must be greater than 32.5 ^{o}C; and (2) At the same temperature, the LE/LC phase coexistence begins at different A_{tr} and Π_{tr} values. The isotherms for different molar mass PLLA samples were also analyzed by the 2D Clausius-Clapeyron equations and the results are summarized in Table 4.1 for both linear and quadratic fits. The Π_c and T_c values in Table 4.1 are consistent with Figure 4.9.

In Figure 4.10, at temperatures below T_c, *i.e.*, the experimental subphase temperatures $\leq$ 27.5 ^{o}C, five regions are observed for 12.9 kg•mol^{-1} PLLA monolayers as described in Figure 4.1: a LE phase, LE/LC phase coexistence, the formation of a condensed monolayer, a plateau signifying collapse of the monolayer, and the formation of multilayers. At temperatures above T_c, *i.e.*, the experimental subphase temperature = 30 ^{o}C, no LE/LC coexistence is observed, therefore only four regions are observed. Similar qualitative trends are observed in the complete isotherms for other molar masses (Figure 4.11). Furthermore, T_0 is predicted to be around 5 ^{o}C for 7.9 kg•mol^{-1} PLLA and around 10 ^{o}C for other molar masses if linear fitting is valid. However, quadratic fitting of Π_{tr} versus T data would yield much smaller estimates of T_0. The isotherms clearly show a LE phase at 6 ^{o}C for 7.9 kg•mol^{-1} PLLA and 10 ^{o}C for all molar masses. Due to the difficulty of accurately maintaining a subphase temperature lower than 8 ^{o}C, we are unable to prove the discrepancy in T_0 values between linear and quadratic fitting with our present experimental set-up.

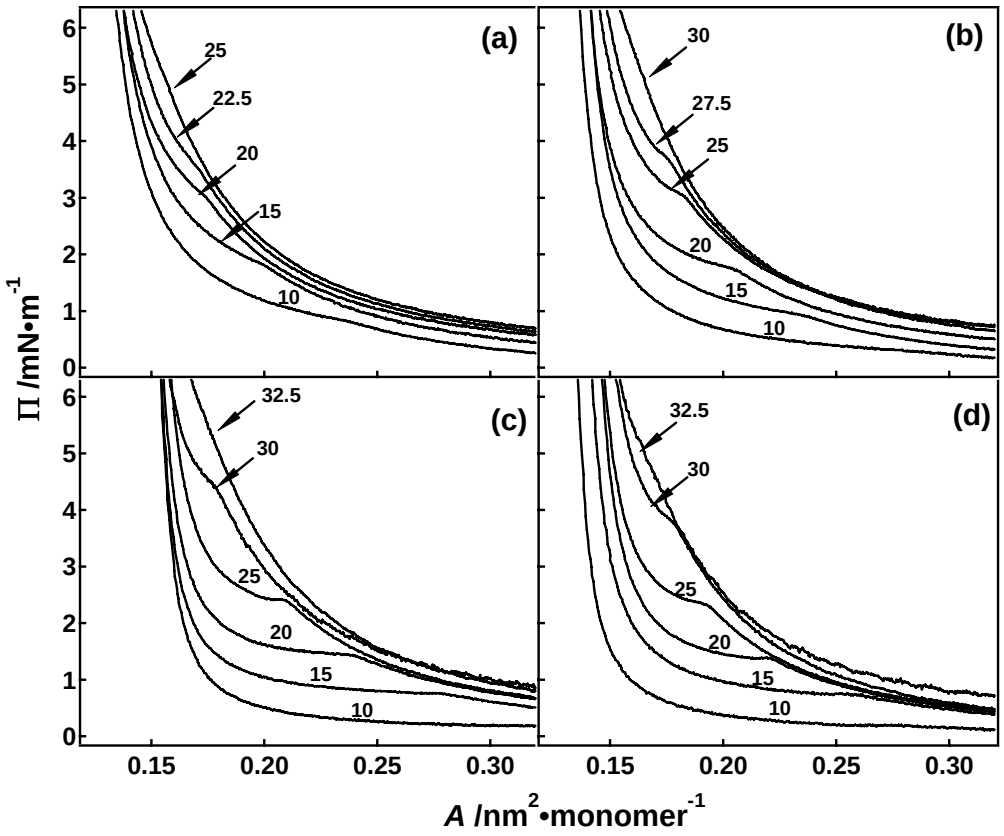

Figure 4.9: The temperature dependence of the LE/LC phase transition of PLLA Langmuir films with various molar masses (M_n): (a) 7.9, (b) 16.8, (c) 24.6, and (d) 40.4 kg•mol^{-1} at the A/W interface. The experimental temperatures of the subphase are indicated by the numbers on the graph in units of ^{o}C.

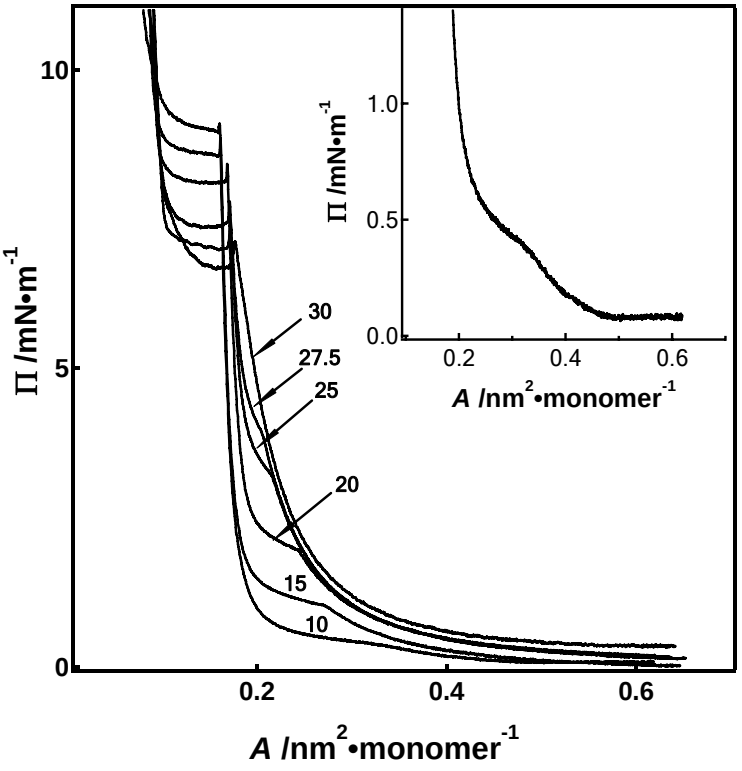

Figure 4.10: Π-*A* isotherms of M_n = 12.9 kg•mol^{-1} PLLA Langmuir films at different temperatures. The experimental temperatures of the subphase are indicated by the numbers on the graph (^{o}C). At temperatures below T_c, five regions are observed: a LE phase, LE/LC phase coexistence, the formation of a condensed monolayer, a plateau signifying collapse of the monolayer, and the formation of multilayers. At temperatures above T_c, no LE/LC coexistence phase is observed. T_0 is predicted to be around 9 ^{o}C for linear fitting of Π_{tr} versus T data, and the isotherm clearly shows a LE phase at 10 ^{o}C (the inset).

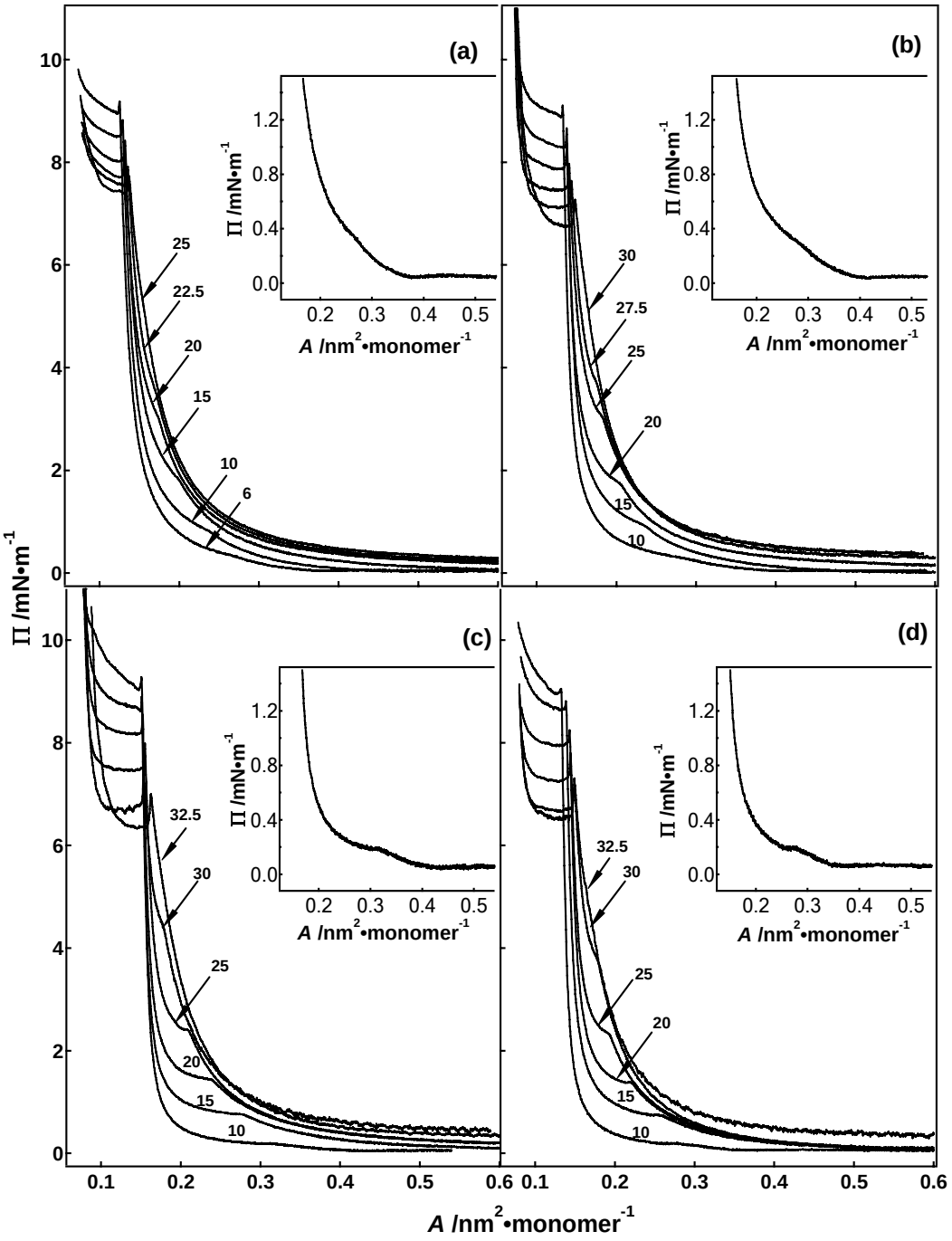

Figure 4.11: Π-*A* isotherms of M_n : (a) 7.9, (b) 16.8, (c) 24.3, and (d) 40.4 kg•mol^{-1} PLLA Langmuir films at different temperatures. The experimental temperatures of the subphase are indicated by the numbers on the graph (^oC). The insets show the existence of an LE phase at 6 ^oC for 7.9 kg•mol^{-1} PLLA and 10 ^oC for all molar masses.

Table 4.1: Thermodynamic quantities derived from isotherm measurements.

M_n (kg•mol^{-1})	$d\Pi_{tr}/dT$[a] (mN•m^{-1}•K^{-1})	T_0[a] (^{o}C)	$d\Delta H_{tr}/dT$[a] (kJ•mol^{-1}•K^{-1})	$d\Delta S_{tr}/dT$[a] (J•mol^{-1}•K^{-2})	T_c[a] (^{o}C)	Π_c[a] (mN•m^{-1})	T_c[b] (^{o}C)
7.9	**0.20** ± 0.01	**4.9**	**0.24** ± 0.01	**0.88** ± 0.05	**23.2**	**3.7** ± 0.3	**23.9**
12.9	**0.20** ± 0.01	**8.9**	**0.24** ± 0.02	**0.86** ± 0.06	**28.6**	**4.0** ± 0.4	**29.2**
16.8	**0.20** ± 0.02	**9.7**	**0.23** ± 0.02	**0.81** ± 0.06	**29.8**	**4.1** ± 0.3	**30.2**
24.6	**0.20** ± 0.03	**10.6**	**0.22** ± 0.01	**0.78** ± 0.02	**31.9**	**4.2** ± 0.2	**31.4**
40.4	**0.17** ± 0.02	**10.1**	**0.19** ± 0.01	**0.67** ± 0.04	**33.8**	**4.4** ± 0.3	**33.3**

[a] Errors represent ± one standard deviation, and the results are obtained through linear fitting

[b] T_c values obtained through quadratic fitting

Figure 4.12 shows that the surface pressure of the LE/LC phase transitions (Π_{tr}) decreases with increasing molar mass for a given temperature. This trend is consistent with free volume effects,[232,233] *i.e.*, PLLA molecules with smaller molar mass have a higher degree of molecular mobility; hence, higher Π_{tr} for the LE/LC phase transitions are observed. Furthermore, Π_c and T_c are also molar mass dependent as noted in Table 4.1 and shown in Figures 4.12 and 4.13. The relationship between T_c or Π_c and molar mass is described by:

$$X_c = X_{c,\infty} - \frac{K}{M_n} \qquad \text{(Eq. 4.5)}$$

where X_c is the critical parameter (Π_c or T_c), $X_{c,\infty}$ is the critical parameter at infinite molar mass, and K is a constant. For the LE/LC phase transition for PLLA molecules, $T_{c,\infty}$ = 36.2 ± 0.3 ^{o}C with K = 102 ± 3 K•kg•mol^{-1}, while $\Pi_{c,\infty}$ = 4.53 ± 0.06 mN•m^{-1} with K =

7.0 ± 0.8 mN•kg•m^{-1}•mol^{-1}. The functional form of Equation 4.4 is consistent with other free-volume dependent properties for polymers such as glass transition temperature (T_g), surface tension (γ), etc.

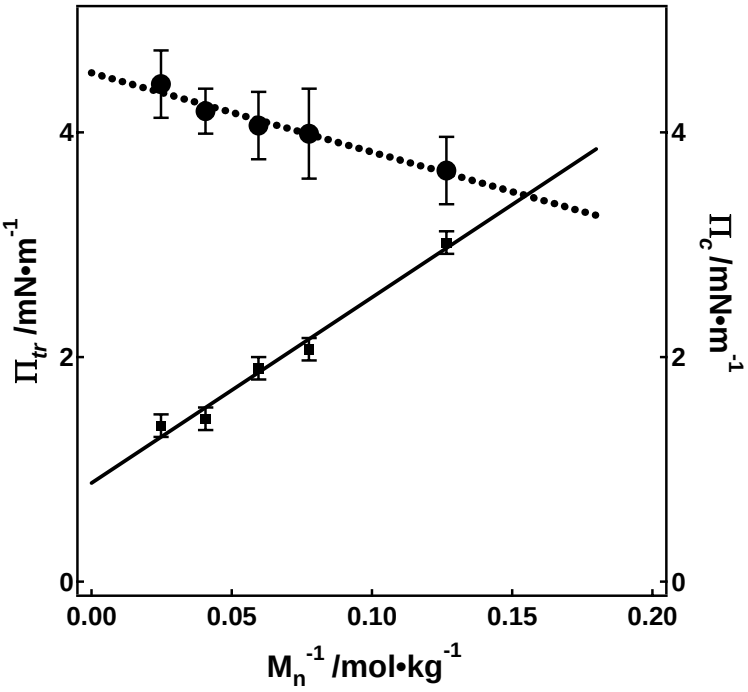

Figure 4.12: Molar mass dependence of: Π_{tr} (20 ^{o}C, square, solid line) and Π_c (circle, dotted line) for the LE/LC phase transition of PLLA Langmuir monolayers. Errors (± 0.1 mN•m^{-1}) for Π_{tr} are from the Wilhelmy plate measurements, and errors for Π_c are the same as in Table 4.1. Both Π_{tr} and Π_c are linearly dependent on M_n^{-1}. The intersection of both lines yields the minimum molar mass (M_n = 6.5 kg•mol^{-1}) that can exhibit an LE/LC phase transition at 20 ^{o}C. For the case of Π_c, Equation 4.4 yields values of $\Pi_{c,\infty}$ = 4.53 ± 0.06 mN•m^{-1} and K = 7.0 ± 0.8 mN•kg•m^{-1}•mol^{-1}.

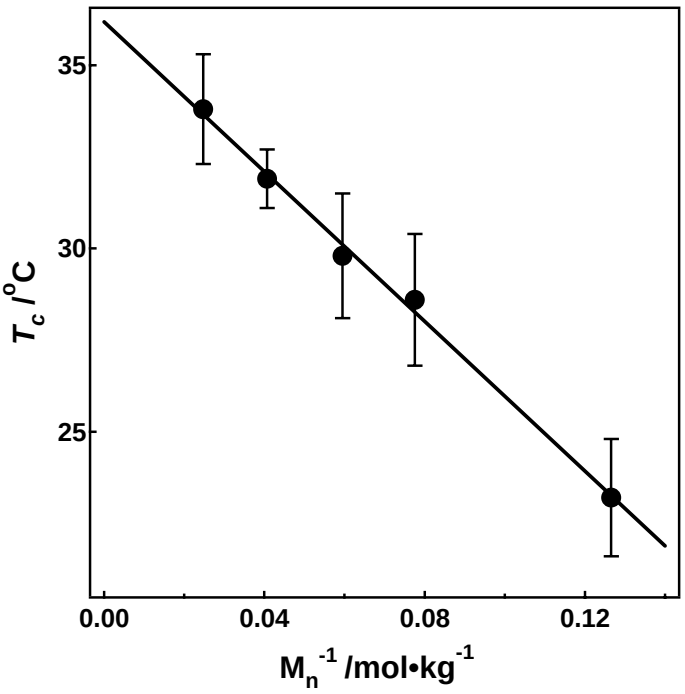

Figure 4.13: Molar mass dependence of the critical temperature, T_c, of the LE/LC phase transition of PLLA Langmuir monolayers. The error bars on the points correspond to the values in Table 4.1. The solid line corresponds to the best linear fit according to Equation 4.4, *i.e.* $T_c = T_{c,\infty} - KM_n^{-1}$, where $T_{c,\infty} = 36.2 \pm 0.3$ °C, and $K = 102 \pm 3$ K•kg•mol^{-1}.

It is also possible to predict whether PLLA molecules with a given molar mass will exhibit a LE/LC phase transition at a given temperature by comparing the transition surface pressure (Π_{tr}) and the critical pressure (Π_c) as done in Figure 4.12. It is observed that Π_{tr} is both temperature dependent and molar mass dependent (Figures 4.7 and 4.12); however, Π_c only depends on molar mass. Figure 4.12 shows that as molar

mass decreases, Π_{tr} at a given temperature increases, and Π_c decreases. If $\Pi_{tr} > \Pi_c$, it is not possible to form LC phase at that particular temperature. Hence the intersection of Π_{tr} vs. M_n^{-1} and Π_c vs. M_n^{-1} yields the molar mass below which no LE/LC phase transition can be observed at a given temperature. The data in Figure 4.12 suggest that at 20 ^oC, M_n = 6.5 kg•mol^{-1} is the smallest molar mass of PLLA that can exhibit a LE/LC phase transition. Equation 4.4 and Figure 4.13 yield a critical temperature around 20.3 ^oC for 6.5 kg•mol^{-1} PLLA. This prediction is also supported by the observation that 4.0 kg•mol^{-1} PLLA Langmuir films do not exhibit a LE/LC phase transition at 20 ^oC (Figure 4.14).

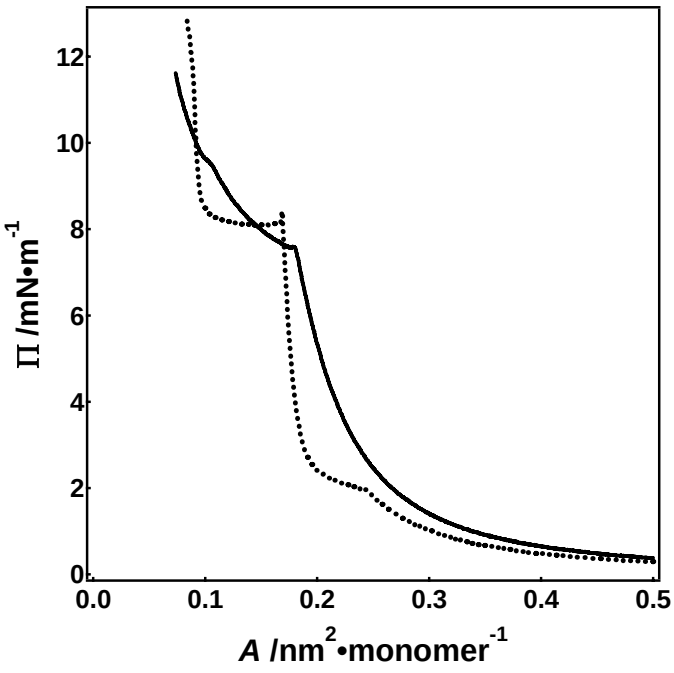

Figure 4.14: Π-*A* isotherms of M_n = 4.0 (solid line) and 12.9 (dotted line) kg•mol^{-1} PLLA Langmuir films at T = 20 ^{o}C. No LE/LC phase transition is observed for 4.0 kg•mol^{-1} PLLA at 20 ^{o}C, as expected.

4.3.6 Morphological Differences between the LE and the LC Phases

Atomic force microscopy (AFM) is used to examine PLLA LB-films for morphological differences between the LE and LC phase. PLLA LB-films are prepared at 22.5 ^{o}C both in the LE phase (Π ≅ 1.5 mN•m^{-1}) and the LC phase (Π ≅ 4.0 mN•m^{-1}). Figure 4.15 shows AFM images for PLLA LB-films. Well-ordered patterns are observed for LB-films prepared in the LC phase (Figure 4.15b), but not for the films prepared in the LE phase (Figure 4.15a) at 22.5 ^{o}C. PLLA LB-films prepared at Π ≅ 4.0 mN•m^{-1} at 35 ^{o}C (above T_c) also lack well-ordered patterns (Figure 4.15c). The

corresponding isotherm for 35 °C is provided in Figure 4.16 where no LE/LC phase is observed. The absence of well-ordered features at $T > T_c$ is consistent with PLLA molecules existing in an LE phase at 35 °C.

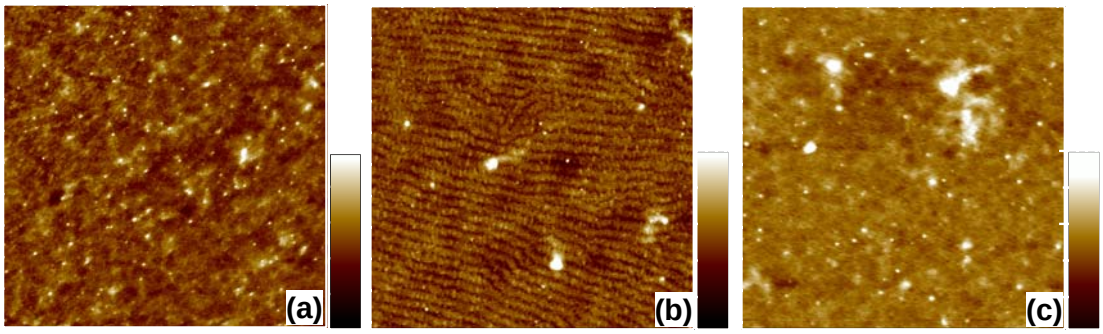

Figure 4.15: Tapping-mode AFM height images for M_n = 12.9 kg•mol^{-1} PLLA LB-films transferred at (a) $\Pi \cong 1.5$ and (b) $\Pi \cong 4.0$ mN•m^{-1} for T = 22.5 °C; and (c) $\Pi \cong$ 4.0 mN•m^{-1} for T = 35 °C on hydrophobic silicon wafers. Scan sizes are 2 × 2 μm^2 and z-ranges of the images are 5 nm. Well-ordered patterns are only observed in the LB-films prepared in the LC phase (b), and not in the LE phases (both a and c).

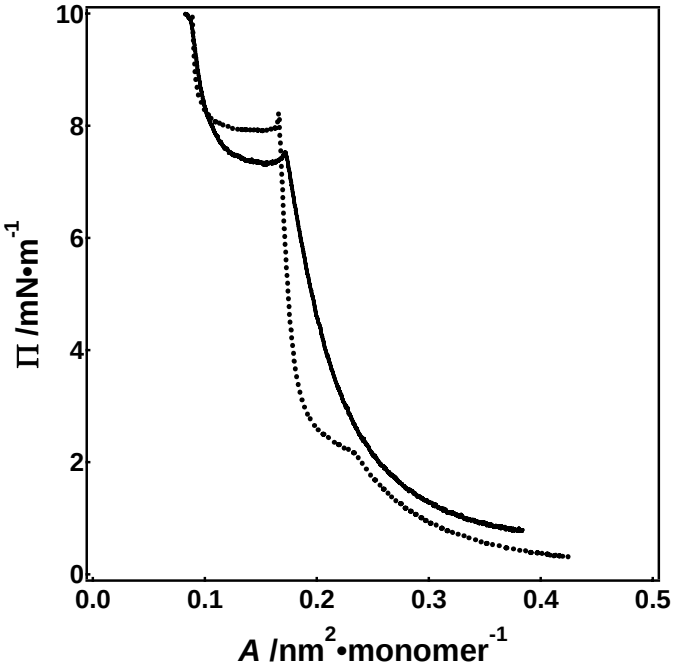

Figure 4.16: Isotherms of M_n = 12.9 kg•mol^{-1} PLLA Langmuir films at T = 22.5 ^{o}C (dotted line) and 35 ^{o}C (solid line). No LE/LC phase transition is observed at 35 ^{o}C.

4.4 Conclusions

In summary, PLLA Langmuir films exhibit a first order LE/LC phase transition in the monolayer regime. The strongly temperature dependent LE/LC phase transition is also molar mass dependent. The molar mass dependence of the LE/LC transition is consistent with expectations from free volume (area) theory. The morphological differences in the LB-films prepared in the LE phase and the LC phase reveal that PLLA molecules form ordered structures during the LE/LC phase transition. Well-ordered lamellar features formed in the LC phase (Figure 4.15b) are analyzed in Chapter 5.

CHAPTER 5

Nanoscale Surface Patterns from Poly(L-lactic acid) 10_3 Single Molecule Helices through the Langmuir-Blodgett Technique

Most of the following chapter appeared as a letter in Langmuir: **Ni, S. L.**; Yin, W.; Ferguson-McPherson, M. K.; Satija, S. K.; Morris, J. R.; Esker, A. R. "Nanoscale surface patterns from 10_3 single-chain helices of biodegradable poly(L-lactic acid)," *Langmuir* **2006**, *22*, 5969-5973.

5.1 Abstract

Atomic force microscopy, reflection absorption infrared spectroscopy, and x-ray reflectivity studies reveal that poly(L-lactic acid) molecules in Langmuir-Blodgett (LB) films exist as 10_3-helices over nearly the entire length of the polymer chain. This feature gives rise to highly ordered nanoscale smectic liquid crystalline-like surface patterns with low surface roughness and lamellar spacings that scale with molar mass. These studies provide a new approach for controlling surface morphology with a biodegradable polymer commonly used for drug delivery and tissue engineering.

5.2 Introduction

Nanometer-scale pattern formation *via* the organization of molecules is a key challenge in nanoscale science and technology.[234] Recently, there is an increasing interest in fabricating a surface with a polymer layer, which can dramatically alter the

properties of the surface for applications in adhesion, drug delivery, data storage, etc.[14,235,236] Various techniques have been used to fabricate nano-patterns with polymers onto solid surfaces, including soft lithography, nanoimprinting lithography, dip-pen nanolithography, polymer spin transfer printing, laser stereolithography, nanosphere lithography, and the Langmuir-Blodgett (LB) technique, etc.[17,19,21,237,238] Among these techniques, the LB-technique facilitates the fabrication of highly ordered films with monolayer by monolayer control of thickness and low surface roughness.[28,31,32,35] The LB-technique has been applied to prepare surface patterns using block copolymers[239] and phospholipids,[240] thereby providing control over surface structures and properties that is desirable for a number of applications such as cell adhesion.[241]

Controlling surface morphology with a biodegradable and biocompatible synthetic polymer, poly(lactic acid) (PLA), has attracted considerable interest because of its importance in tissue engineering and drug delivery.[226,227] In particular, crystallinity represents a fundamental material variable for controlling the surface morphology of poly(L-lactic acid) (PLLA) substrates.[1,2] PLLA substrates with different degrees of crystallinity can be obtained by annealing spin-coated films at different temperatures. Park and Griffith-Cima[2] suggested that cells proliferate less on crystalline regions than on amorphous regions. Washburn *et al.*[1] found that the rate of cell proliferation decreases with increasing surface roughness. Both results are consistent given the fact that a film's surface roughness generally increases as crystals form. However, it is still not clear whether the rate of cell proliferation is controlled by crystallinity, surface roughness,

or both factors. In this study, we use the LB-technique to prepare PLLA substrates with high crystallinity but relatively low surface roughness. These films may prove useful for exploring the effects of crystallinity and/or surface roughness on cell proliferation.

Bulk PLLA crystallization studies show that PLLA forms left-handed 10_3-helices with a pseudo-orthorhombic unit cell possessing dimensions of a = 1.07, b = 0.645, and c = 2.78 nm.[144,145] Previous studies of PLLA Langmuir films at the air/water (A/W) interface suggest that PLLA forms 10_3-helices in solution before spreading onto the water subphase.[155,156,223] Further compression into a solid-like state at the A/W interface does not alter the helical conformation. Our previous results in Chapter 4 show that PLLA Langmuir films exhibit a liquid expanded to condensed (LE/LC) phase transition in the monolayer region. PLLA molecules are ordered during the LE/LC phase transition, giving rise to highly-ordered lamellae in LB-films prepared from the LC region as observed on atomic force microscopy (AFM) images in Chapter 4. In this chapter, nanoscale surface patterns formed in the LC state of PLLA are explored.

5.3 Results and Discussion

5.3.1 Orientation of Lamellar Features on PLLA LB-films

Figure 5.1 shows that lamellar features are present in both height and phase images for M_n = 12.9 kg•mol^{-1} PLLA LB-films prepared in the LC phase at 22.5 ^{o}C. The lamellar features are parallel to the LB-film deposition direction, as shown in Figure 5.2, suggesting that the shape persistent features behave like rigid rod polymers.[242-246] The

periodicity is not significantly affected by the dipping rate (Figure 5.3). On the other hand, lamellar features are also observed in PLLA films prepared by the Langmuir-Schaeffer (LS) deposition (Figure 5.4). Lamellar features in the LS-films are not as sharp as in the LB-films, and are somewhat tilted relative to the compression barriers. To some extent, the angle reflects the difficulty of fixing the dipping angle for LS deposition.

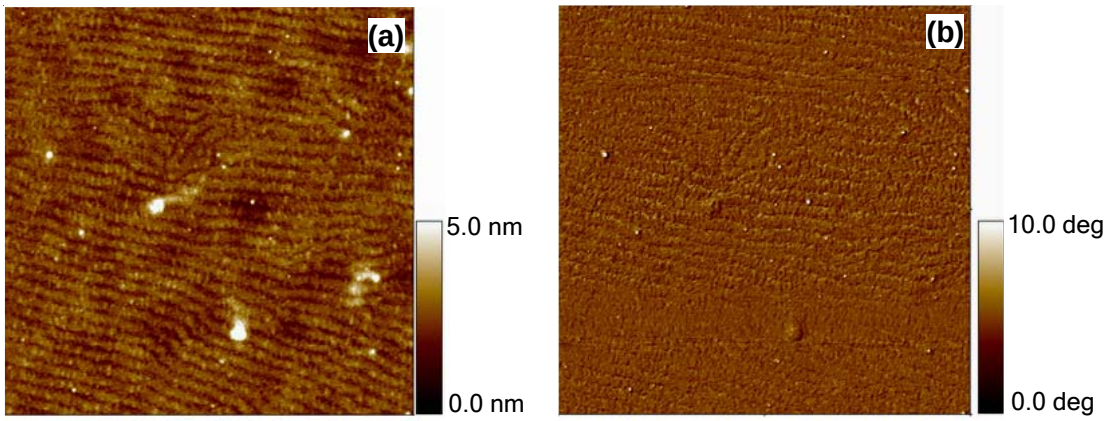

Figure 5.1: Tapping-mode AFM (a) height and (b) phase images for M_n = 12.9 kg•mol^{-1} PLLA LB-films transferred at Π = 4.0 mN•m^{-1} in the LC phase at T = 22.5 ^{o}C on a hydrophobic silicon wafer with a scan range of 2 × 2 μm^2.

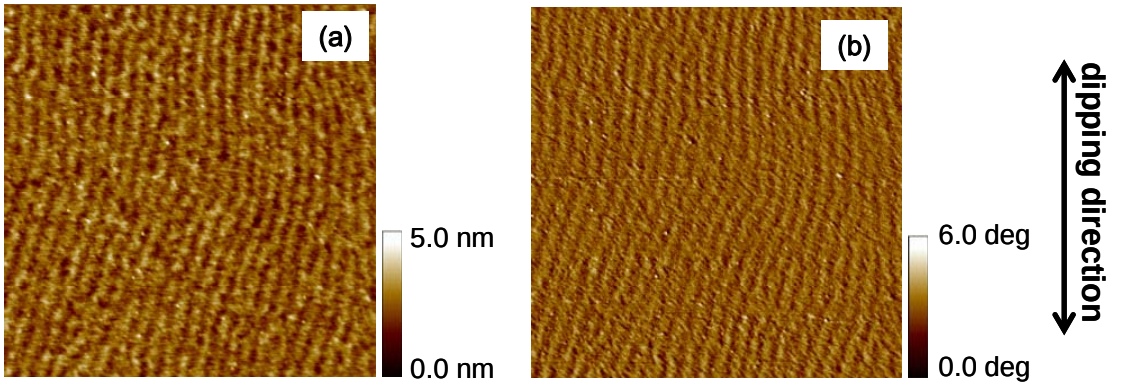

Figure 5.2: Tapping-mode AFM (a) height and (b) phase images of M_n = 12.9 kg•mol^{-1} PLLA LB-films prepared at Π = 4.0 mN•m^{-1} in the LC phase at T = 22.5 ^{o}C show that the lamellae are parallel to the dipping direction. The scan size is 2 × 2 μm^2.

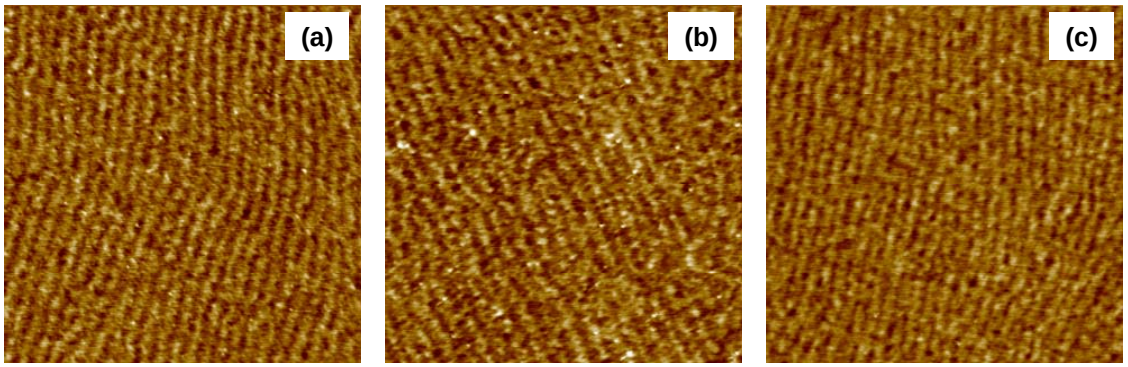

Figure 5.3: Tapping-mode AFM height images of M_n = 12.9 kg•mol^{-1} PLLA substrates prepared at Π = 4.0 mN•m^{-1} in the LC phase at T = 22.5 ^{o}C at dipping rates of (a) 10, (b) 20, and (c) 40 mm•min^{-1}. No obvious differences are observed over this range of dipping rates. The scan size is 2 × 2 μm^2.

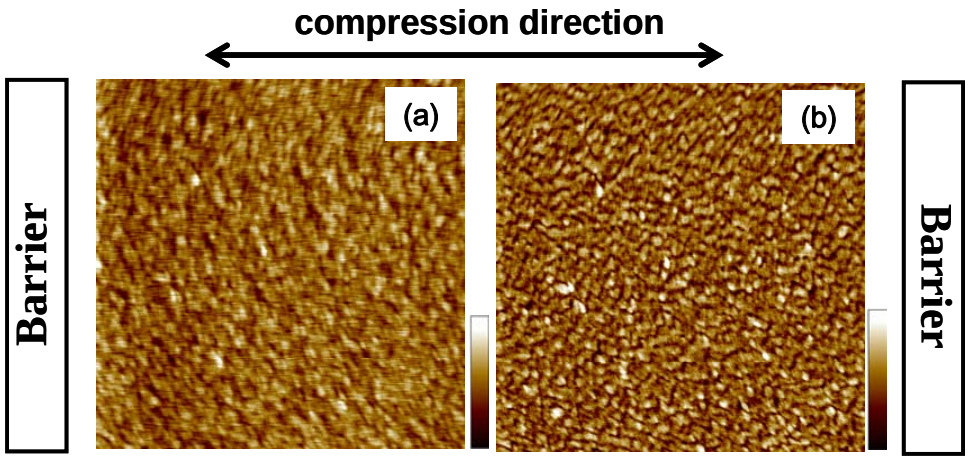

Figure 5.4: Tapping-mode AFM: (a) height and (b) phase images of M_n = 12.9 kg•mol^{-1} PLLA LS-films prepared at Π = 4.0 mN•m^{-1} in the LC phase at T = 22.5 ^{o}C show that the lamellae are not perfectly aligned parallel to the barriers (boxes). The scan size is 2 × 2 μm^2. The z range for the height image is 3 nm, and the z range for the phase image is 15^{o}.

On the basis of Figures 5.2-5.4, we can conclude that the anisotropic features are present at the A/W interface (Figure 5.4) but are not as well organized as in the LB-films. Anisotropic lamellar features, comprised of packed PLLA molecules, serve as shape persistent features and behave like rigid-rods. The anisotropic features are locally aligned at the A/W interface according to the model proposed by Wegner.[242] Hence for LS-films, anisotropic lamellae are observed but lack the longer range orientation observed in the LB-films. During LB-film deposition, the monolayer flow on the subphase as described by Schwiegk *et al.*[243] orients the shape persistent features parallel

to the dipping direction, giving rise to longer range orientation of lamellar features in the LB-films (Figure 5.2-5.3). The anisotropy of lamellar features has been observed for LB-films of rigid-rod polymers such as substituted phthalocyaninato-polysiloxanes[244] and their rare earth complexes.[245] The orientation in the rigid-rod polymers along the dipping direction was also confirmed by polarized infrared spectroscopy (IR) studies.[246]

5.3.2 Analysis of Lamellar Features on PLLA LB-films

The dimension of the lamellar features in the X-Y plane can be calculated from the 2 × 2 μm^2 image (Figure 5.1a). In this 2 × 2 μm^2 range, approximately 34 lamellae are observed, each of which has an in-plane dimension of around 62 nm. Actually the dimension of 62 nm includes the dimension of both the bright lamellae and dark regions. By comparing the size of the bright lamellae and dark regions, it is determined that the dimension of the crystalline lamellar features is around 55 nm. To measure the exact dimension of the lamellar feature, line scan analyses and two-dimensional (2D) fast Fourier transforms (FFT) are applied.

A 2D-Fourier transform of the 2 × 2 μm^2 AFM image in Figure 5.1a shows an anisotropic periodic structure with a length scale around 56 nm (Figure 5.5a). Two features are observed on the FFT spectra: an anisotropic diffuse ring, and a periodicity which is perpendicular to the lamellae. The periodicity is around 58 nm, as shown in Figure 5.5b.

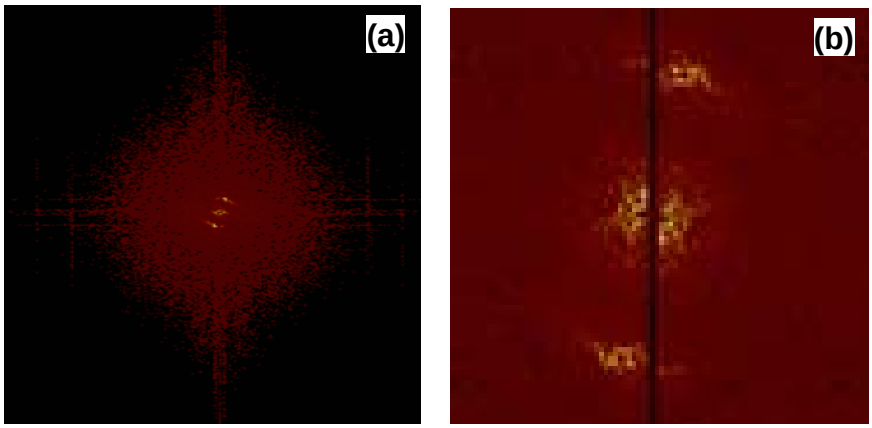

Figure 5.5: (a) FFT spectrum of the AFM image of M_n = 12.9 kg•mol^{-1} PLLA LB-films. The periodic pattern is enlarged as shown in (b), which reveals the periodicity of ~ 58 nm.

In order to clearly examine the lamellae, a 0.7 × 0.7 μm^2 portion (Figure 5.6a) is cut from the original 2 × 2 μm^2 AFM image (Figure 5.1a) and is subjected to a line scan analysis. The height profile can be fit with a simple sine wave with a periodicity of 63.6 ± 0.1 nm (Figure 5.6b).[247] This dimension includes both the bright and dark regions in the AFM image. An easier method is to directly measure the distance between maxima or minima for lamellar features (Figure 5.6a and 5.6b). The surface dimension of the bright lamellae is about 55.7 ± 0.5 nm. Reciprocal space analysis is also performed on the AFM image by a 2D FFT. A radial average of the squared amplitude is used to obtain the power spectrum, *P(k)*. The power spectrum, plotted in Figure 5.6c, can be adequately fit with a Lorentzian equation:

$$P(k) = A + B/[(k - k^*)^2 + C] \quad \text{(Eq. 5.1)}$$

where A, B, and C are free fitting parameters. It is observed that the power spectrum exhibits a maximum at $k^* = 17.0 \pm 0.5\ \mu m^{-1}$, indicating that the periodicity of the lamellae is around 58.1 ± 0.6 nm.[247]

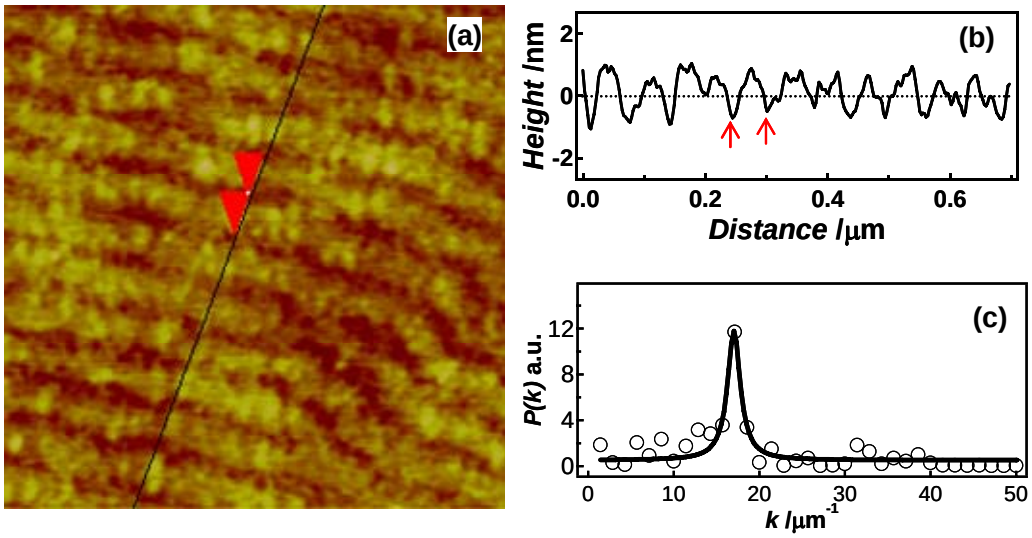

Figure 5.6: Line scan analysis of AFM height images of M_n = 12.9 kg•mol^{-1} PLLA LB-films: (a) AFM height image ($0.7 \times 0.7\ \mu m^2$) cut from the original image for PLLA LB-film shown in Figure 5.1a. (b) Height profile of the AFM image along the line drawn in (a). A line scan analysis reveals that the surface dimension of the lamellae is around 56 nm. (c) The power spectrum, *P(k)*, calculated from radial averages of the squared amplitudes is fit with a Lorentzian function exhibiting a periodicity of 58.1 ± 0.6 nm.

5.3.3 Hypothesis of PLLA Single Molecule 10_3-Helices

The estimates of the lamellar dimension are interesting because a M_n = 12.9 kg•mol^{-1} PLLA molecule contains approximately 180 repeating units, or a maximum of 18 10_3-helical repeating units. According to the pseudo-orthorhombic unit cell,[144,145] each 10_3-helix has a linear dimension of 2.78 nm (Figure 5.7). Hence a single chain of 12.9 kg•mol^{-1} PLLA will be 50 nm long if the entire chain is in a perfect 10_3-helical conformation. The similarity between the calculated chain length and the lamellar dimension from AFM images suggests that individual PLLA chains exist as 10_3-helices that persist over nearly the entire length of the chain with disordered chain ends. To confirm this hypothesis, molar mass scaling experiments are conducted.

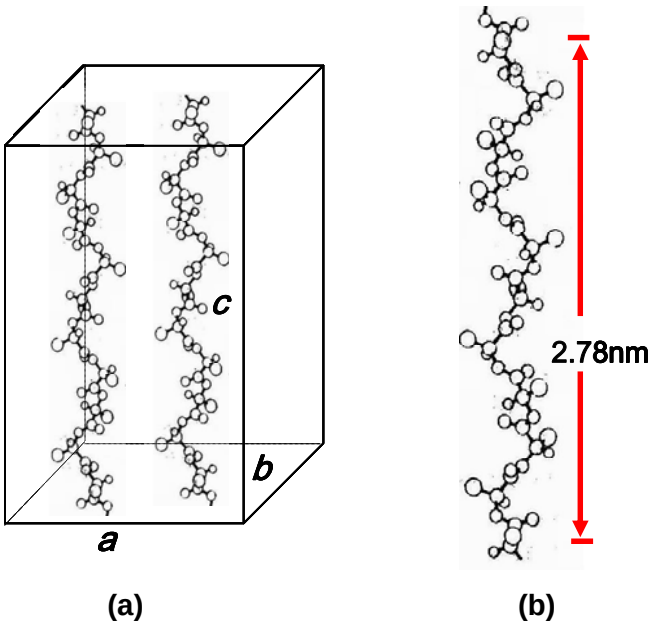

Figure 5.7: Schematic of PLLA 10_3-helices in a pseudo-orthorhombic unit cell: (a) two 10_3-helices are present in the unit cell, where a = 1.07 nm, b = 0.613 nm, and c = 2.78 nm. (b) A 10_3-helical repeating unit has a dimension of 2.78 nm.[143,144]

5.3.4 Molar Mass Dependence of Lamellar Dimensions on PLLA LB-films

PLLA LB-films of various molar masses are prepared in the LC phase and examined with AFM. Due to the existence of a molar mass dependent LE/LC phase transition as discussed in Chapter 4, the surface pressures at which the films are transferred vary with molar mass. At 22.5 ^{o}C, the surface pressure (Π) for the onset of the LE/LC phase transition is $\cong$ 3.5 mN•m^{-1} for 7.9 kg•mol^{-1}, and $\cong$ 2.0 mN•m^{-1} for other molar masses (Figure 4.9). Therefore, PLLA substrates are prepared at Π = 6.0 mN•m^{-1} for 7.9

kg•mol^{-1} PLLA, and at Π = 4.0 mN•m^{-1} for other molar masses to ensure that all PLLA LB-films are prepared in the LC monolayer region.

Lamellar patterns are observed for all AFM images as seen for representative AFM images in Figure 5.8. It is clear that as molar mass increases, the dimension of the lamellar features becomes larger. Lamellar spacings are determined following the same analysis scheme used for 12.9 kg•mol^{-1} PLLA. A linear relationship is observed in Figure 5.9 between lamellar spacing and the number average degree of polymerization (M_n/M_0, where M_0 is the molar mass of the repeating unit). The slope of the line in Figure 5.9 is 0.273 ± 0.007 nm•monomer^{-1}, which is in excellent agreement with the expected value of 0.278 nm•monomer^{-1} for PLLA 10_3-helices.[143,144] Based on this analysis, the contrast in the AFM images presumably arises from helical segments (bright regions) with amorphous chain ends (dark regions), yielding smooth PLLA LB-films with lamellar patterns. The root mean squared (*r.m.s.*) surface roughness value for Figure 5.6a is ~ 0.3 nm.

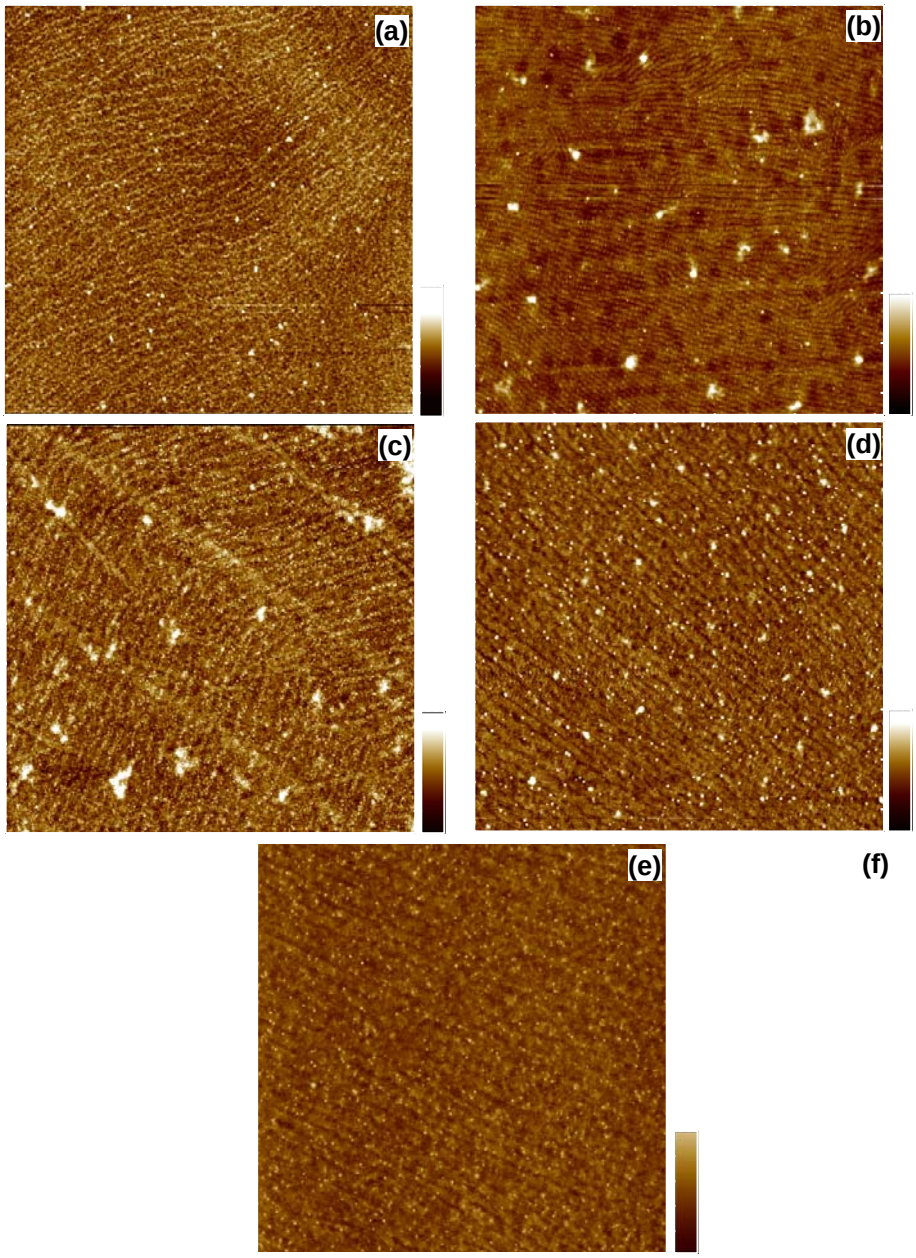

Figure 5.8: Tapping-mode AFM height images for PLLA LB-films with various molar masses prepared in the LC phase at $T = 22.5$ °C: (a) 7.9, (b) 12.9, (c) 16.8, (d) 24.6, and (e) 40.4 kg•mol^{-1}. The scan size is 5 × 5 μm^2 for all images with z ranges of 5 nm. Lamellar patterns are observed for all images, and the spacing increases with molar mass.

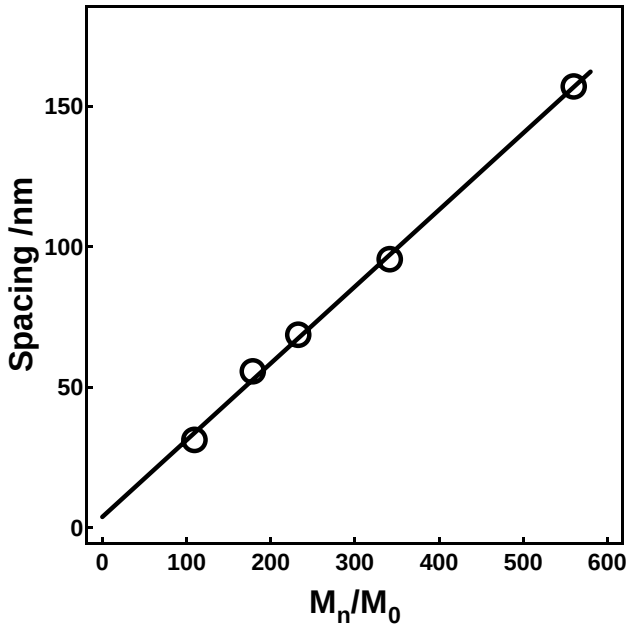

Figure 5.9: Lamellar spacing plotted against the number average of polymerization (M_n/M_0, where M_0 is the molar mass of the repeating unit). One standard deviation error bars for individual data points are smaller than the symbol size and are not displayed. The slope of the best linear fit (solid line) is 0.273 ± 0.007 nm•monomer^{-1}.

5.3.5 LB-Configurations to Measure the Thickness of a PLLA Monolayer

Based on the limiting area from the isotherm studies and lamellar dimensions from AFM results, PLLA molecules appear to lie flat on the subphase and in the plane of the LB-films. In order to further test this hypothesis, it becomes necessary to measure the thickness of a PLLA monolayer. Unfortunately, it is impossible to obtain the thickness of a PLLA monolayer from an AFM height profile because there is no defined reference line. Scratching the film could yield a baseline for measuring the thickness of the film

through an AFM height profile; however, the process may yield an errant result if the reference line is scratched too deeply into the Si substrate. X-ray reflectivity measurements appear to be a suitable method for measuring the thickness of a PLLA monolayer. However, direct measurements of the monolayer thickness will be ambiguous as the monolayer is very thin, < 1 nm. In order to obtain accurate results, it is necessary to prepare uniform PLLA LB-films, and the total thickness of the films should be larger than 1 nm. Uniform PLLA LB-films can be prepared in the monolayer region at $\Pi \cong 7.0$ mN•m^{-1}. However, efforts to deposit thicker PLLA films in the condensed region revealed that the deposition works well for several dipping cycles ($\cong 2$), but ultimately the transfer proceeded only on the upstroke with downstroke depositions yielding transfer ratios that drifted towards zero as the number of dipping cycles increased. For this reason, it was necessary for us to limit ourselves to making 2-layer (1 dipping cycle) LB-films. Nonetheless, x-ray reflectivity measurements on a 2-layer film are almost as ambiguous as measurements on a monolayer. Hence, a special film configuration as shown in Figure 5.10 was developed to prepare uniform LB-films which are thick enough for the x-ray reflectivity measurements.

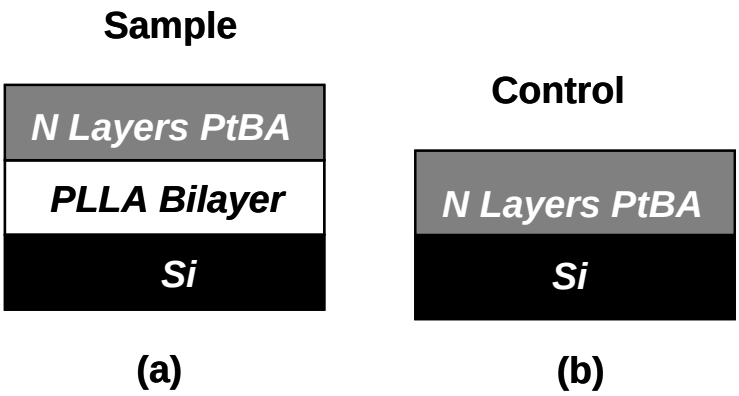

Figure 5.10: Schematic depiction of (a) sample and (b) control films for x-ray reflectivity measurements.

As depicted in Figure 5.10a, a LB-multilayer film of poly(tert-butyl acrylate) (PtBA) is transferred on top of a PLLA LB-bilayer on a HF etched Si wafer, to yield films with configurations of air//PtBA (variable thickness, *N* layers)//PLLA (bilayer)//Si, where "//" represents a distinct interface. PtBA is chosen for the top layer because it can quantitatively form LB-multilayer films with surface roughness values < 1 nm.[28] The PLLA bilayer is transferred at $\Pi \cong 7.0$ mN•m^{-1} (M_n = 12.9 kg•mol^{-1}), with a transfer ratio of $\cong 0.95 \pm 0.05$. PtBA is transferred at $\Pi \cong 19.0$ mN•m^{-1} on top of the PLLA bilayer. The number of PtBA layers (*N*) varies from 6 to 22, with an increment of 2 layers for each PtBA dipping cycle. Control substrates, Figure 5.10b, where PtBA was directly deposited onto a HF etched Si wafer were also prepared. The average transfer ratio is 1.05 ± 0.02 for PtBA on bare HF etched Si substrates, and 1.02 ± 0.02 for PtBA

transferred onto the PLLA bilayers. The transfer ratio values are consistent with uniform films for both PtBA and PLLA LB-layers.

5.3.6 X-ray Reflectivity Measurements

Figure 5.11 shows representative x-ray reflectivity profiles for a 22 layer PtBA control film and a sample film with 22 PtBA layers and 2 PLLA layers (M_n = 12.9 kg•mol^{-1}). The x-ray reflectivity profiles have been corrected for the fraction of the incident beam subtended by the sample by subtracting background scans. The periodic fluctuations seen in the reflectivity profiles represent Kiessig fringes, which arise from the distinct interface between the x-rays reflected from the Si//polymer and polymer//air interfaces. Two major differences are observed between the profiles shown in Figure 5.11: (1) the spacing between the minima or the maxima is smaller in PtBA//PLLA films compared to pure PtBA films, and (2) the amplitude of the Kiessig fringes for PtBA//PLLA films decay faster than pure PtBA films on Si substrates. The differences indicate that the films consisting of PtBA on top of the PLLA bilayers are thicker and have rougher surfaces than pure PtBA films with the same number of layers on bare Si. The roughness of both the film and the substrate are obtained by fitting the experimental profiles with theoretical curves in Microsoft Excel.[208] The roughness value for the pure PtBA film is ~ 0.5 nm, while the roughness value for PLLA//PtBA films is ~ 0.7 nm.

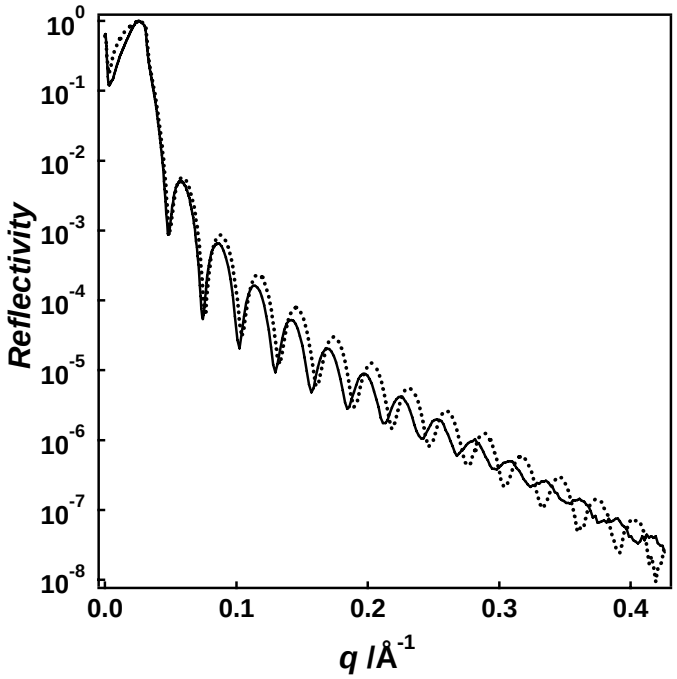

Figure 5.11: Representative x-ray reflectivity profiles for a 22 layer PtBA film (dotted curve) and a 22 layer PtBA film on top of a M_n = 12.9 kg•mol^{-1} PLLA bilayer (solid curve).

The scattering vector at each minimum, q_m, can be determined graphically from the experimental reflectivity curves. Film thickness, D, can be evaluated from the position of two adjacent minima:

$$D = \frac{2\pi}{\Delta q_m} \qquad \text{(Eq. 5.2)}$$

Equation 5.2 is no longer commonly used in x-ray reflectivity analyses. Instead film thickness is obtained from refraction-corrected minima described by Thompson *et al.*[182]

Refraction-corrected minima, Q_m, are defined as the difference between the scattering vectors at the minima and the scattering vector at the critical angle, q_{crit}:

$$Q_m = \sqrt{q_m^2 - q_{crit}^2} = 2\pi m / D \qquad \text{(Eq. 5.3)}$$

where m is an integer index for the minima. q_{crit} can be determined graphically or calculated from the expected composition and bulk density. For example, for a 22 layer PtBA films, the value of q_{crit} determined from Figure 5.11 is 0.02169, while the calculated value of q_{crit} is 0.02160, according to Equations 5.4 and 5.5:

$$q_{crit} = \frac{4\pi \sin(\theta_c)}{\lambda} \approx \frac{4\pi\theta_c}{\lambda} = \frac{4\pi}{\lambda}\sqrt{2\delta} = \sqrt{16\pi\rho_e r_e} \qquad \text{(Eq. 5.4)}$$

and

$$\rho_e = \frac{\rho N_A Z_e}{M_0} \qquad \text{(Eq. 5.5)}$$

where θ_c is the critical angle below which total reflection of x-rays occurs, λ is the wavelength of the x-rays, ρ_e is the electron density, $r_e = 2.828 \times 10^{-15}$ m is the classical electron radius, ρ is bulk mass density, M_0 is molar mass of monomer, N_A is Avogadro's constant, and Z_e is the total number of electrons in one monomer.

Q_m are calculated for both a 22 layer PtBA film and a 22 layer PtBA film on top of a 2 layer PLLA film (Figure 5.11). As shown in Figure 5.12, Q_m is linearly dependent on the minimum index. From Equation 5.3, it is clear that

$$\frac{dQ_m}{dm} = \frac{2\pi}{D} \qquad \text{(Eq. 5.6)}$$

and that the total thickness of the films can be obtained from the slope of the linear fits. The film thickness for a 22 layer PtBA film is 216.7 ± 0.4 Å, while the film thickness for a 22 layer PtBA film on top of a 2 layer PLLA film is 228.9 ± 0.9 Å. Hence the thickness of the 2 layer PLLA film is 12.2 ± 0.6 Å or 1.22 ± 0.06 nm.

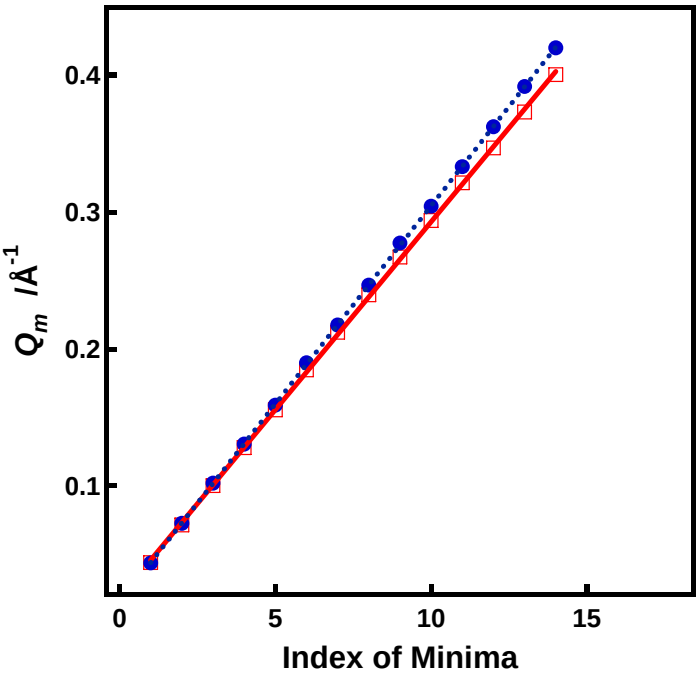

Figure 5.12: Refraction-corrected minima position, Q_m, versus minimum index for a 22 layer PtBA film (dotted line and filled circles) and a 22 layer PtBA film on top of a M_n = 12.9 kg•mol^{-1} PLLA bilayer (solid line and open squares).

As shown in Figure 5.10, a series of films are prepared with different numbers of PtBA layers (N) to obtain the thickness of a PLLA monolayer. Figure 5.13 shows x-ray reflectivity profiles for all the films, which are treated with the same method used to

determine D for the pair of N = 22 films. The film thicknesses are plotted against the PtBA layer number (N) for both pure PtBA films and PtBA//PLLA films (Figure 5.14). The linear relationships confirm that PtBA is quantitatively transferred onto both hydrophobic Si and the PLLA bilayer. The identical slopes (≅ 0.978 ± 0.003 nm layer^{-1}) provide the thickness of a PtBA monolayer.[28] The difference in the y-intercepts (≅ 1.24 ± 0.06 nm) provides the thickness of two PLLA layers on the basis of the film configuration. Hence the thickness of a PLLA monolayer is determined to be 0.62 ± 0.03 nm, and is consistent with the corresponding parameter of the pseudo-orthorhombic unit cell (b = 0.645 nm), as shown in Figure 5.7.[144,145] This result is consistent with the hypothesis that 10_3-helices lie flat in the plane of the film.

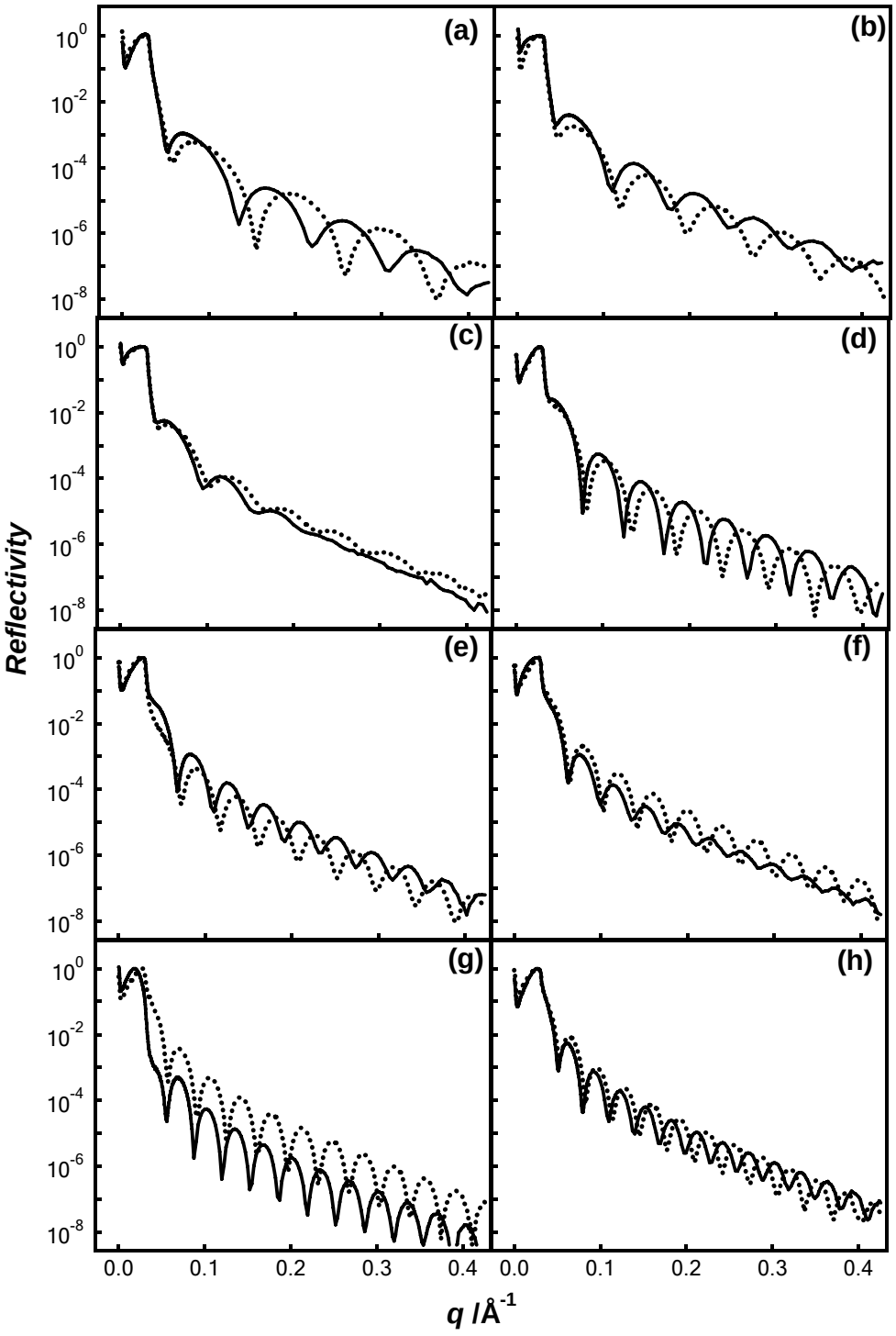

Figure 5.13: X-ray reflectivity profiles for pure PtBA films (dotted curves) and PtBA//PLLA bilayers (solid curves). The number of PtBA layers are (a) 6, (b) 8, (c) 10, (d) 12, (e) 14, (f) 16, (g) 18, and (h) 20.

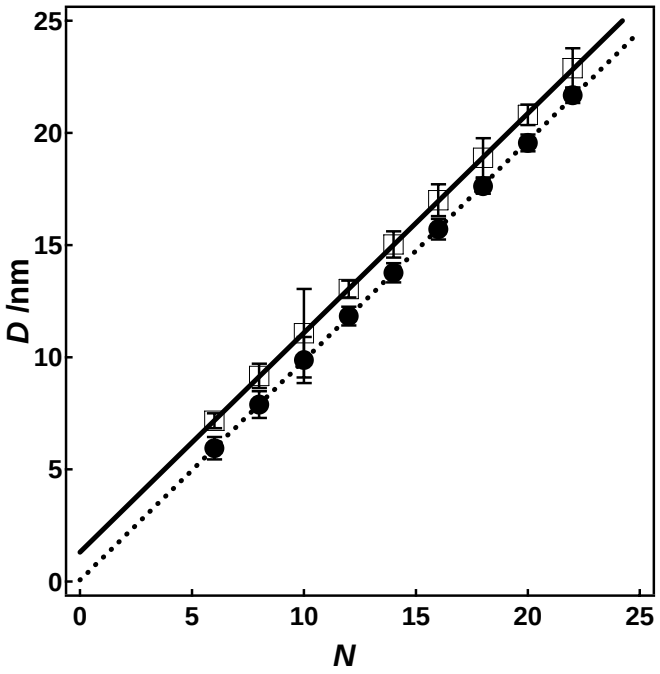

Figure 5.14: The dependence of the film thickness (*D*) on the number of PtBA layers (*N*) for pure PtBA films (dotted line and filled circles) and PtBA films on M_n = 12.9 kg•mol^{-1} PLLA bilayers (solid line and open squares).

5.3.7 Reflection Absorption Infrared Spectroscopy

In addition, the existence of helices is confirmed by reflection absorption infrared spectroscopy (RAIRS) studies on PLLA LB-films deposited on gold substrates. Figure 5.15 shows the RAIRS spectrum of a 10-layer 12.9 kg•mol^{-1} PLLA LB-film prepared at Π = 7.0 mN•m^{-1}. A peak is observed at 921 cm^{-1}, which is assigned to the coupling of C-C backbone stretching with the CH_3 rocking mode, and is sensitive to the 10_3 helical

chain conformation of PLLA α crystals.[248-254] Moreover, for amorphous samples, a band will appear at 955 cm^{-1}. To confirm this feature, PLLA spin-coated films are prepared and annealed at bulk crystallization temperature (T_x = 104 ^oC) for 10 hours. A band at 955 cm^{-1} is observed, suggesting amorphous features in the as-prepared spin-coated films (Figure 5.16a). After annealing 10 hours at 104 ^oC, the band at 955 cm^{-1} almost vanishes, whereas a band at 921 cm^{-1} appears indicating the growth of PLLA α crystals where segments of PLLA chains are in a 10_3 helical chain conformation (Figure 5.16b). In the RAIRS spectra of the as-prepared LB-films (Figure 5.15), the characteristic band of crystalline features at 921 cm^{-1} is observed while the characteristic band of amorphous features at 955 cm^{-1} is invisible. The presence of the characteristic band for PLLA α-crystals confirms the existence of 10_3-helices in the as-prepared PLLA LB-films. Furthermore, the absence of the characteristic band for amorphous PLLA suggests that the as-prepared PLLA LB-films are almost 100% helical. This suggestion agrees with the hypothesis that PLLA molecules exist as single-molecule 10_3-helices from AFM studies.

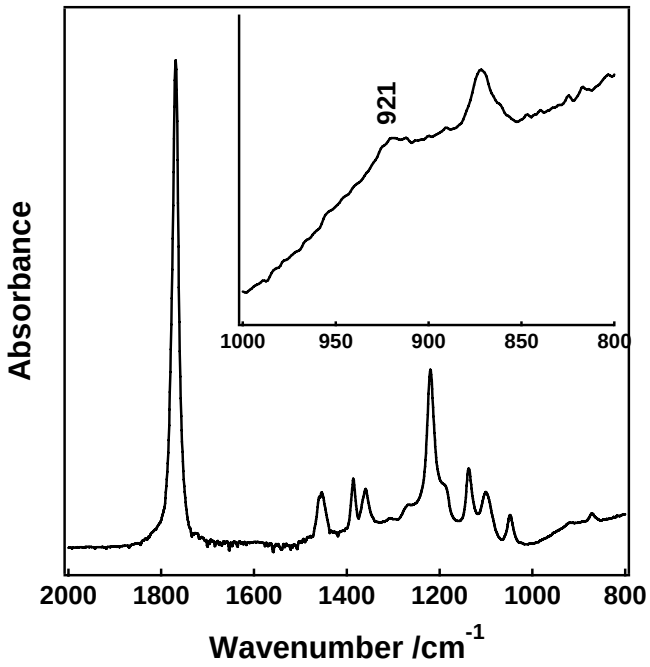

Figure 5.15: A RAIRS spectrum of a 10 layer M_n = 12.9 kg•mol^{-1} PLLA LB-film prepared in the LC monolayer region at Π = 7.0 mN•m^{-1} at T = 22.5 ^{o}C. An enlargement of the region between 1020 – 800 cm^{-1} is shown in the inset. The band characteristic of the 10_3 helical conformation of PLLA is observed at 921 cm^{-1}. This band confirms the existence of PLLA 10_3-helices in the as-prepared LB-films.[251,253] On the other hand, a band at 955 cm^{-1} which is characteristic of amorphous features, is absent, suggesting that the as-prepared PLLA LB-films are almost 100% crystalline.

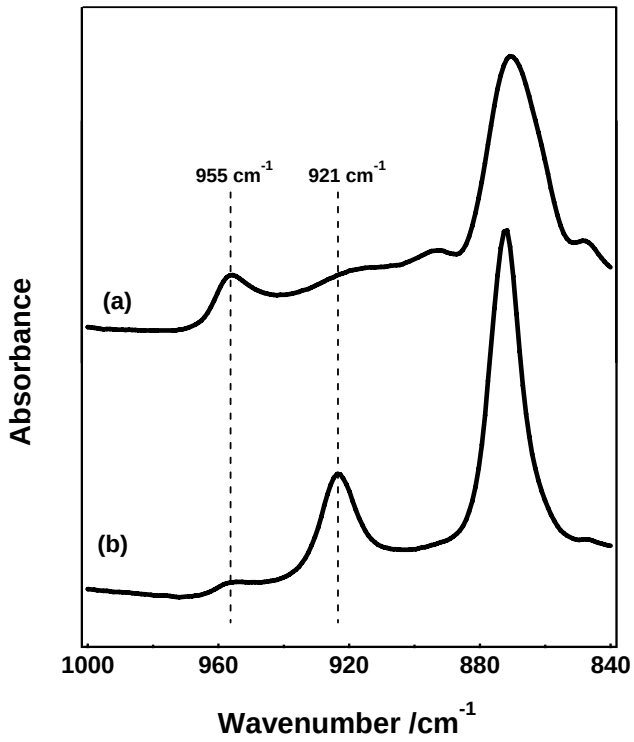

Figure 5.16: RAIRS spectra in the range for 1000 – 840 cm^{-1} of M_n = 12.9 kg•mol^{-1} PLLA spin-coated films: (a) as-prepared and (b) after annealing the as-prepared films at the bulk crystallization temperature (T_x = 104 ^oC) for 10 hours. The as-prepared spin-coated films show a band at 955 cm^{-1} that is characteristic of PLLA in an amorphous state. After annealing at T_x for 10 hours, PLLA α crystals grow as revealed by the appearance and growth of the band at 921 cm^{-1} that is characteristic of PLLA in 10_3 helical conformation.

5.3.8 LB-deposition Mechanism for PLLA Single Molecule Helices

The Y-type LB-deposition mechanism has been described and illustrated in Chapter 2. However, the description is based on molecules with lipid-like structures. Here, PLLA

clearly lacks a lipid-like structure but still forms a LB-bilayer by Y-type deposition. Hence some thought should be given to the deposition process.

As confirmed by AFM, x-ray, and RAIRS results, PLLA molecules lie flat on the subphase in a 10_3 helical conformation with amorphous chain ends. One consequence of this finding is that not all ester groups can bind to the water surface, nor can all of the methyl groups escape the water. After spreading, PLLA molecules adopt a 10_3 helical conformation and lie flat on the subphase (Figure 5.17a). In the LE phase, PLLA molecules are closer to each other but are still disordered (Figure 5.17b). In the LC phase, the molecules are well aligned in a manner where they are all parallel to each other, forming shape persistent lamellae (Figure 5.17c). The shape persistent lamellae preferentially align parallel to the barriers during compression, and as such the PLLA single molecule helices are perpendicular to the compression barriers. When a hydrophobic substrate is immersed into the subphase, the shape persistent lamellae are transferred onto the substrate with the lamellae parallel to the dipping direction while PLLA single molecules are perpendicular to the dipping direction (Figure 5.17d). The shape persistent lamellae (red stripes in Figure 5.17e) appear bright on AFM height images and are dark on AFM phase images for substrates prepared in the LC phase. The amorphous chain ends are then present at the edges of the lamellae, giving rise to the dark regions on AFM height images and bright regions of PLLA LB-films prepared in the LC state (Figure 5.17e). The difference in the brightness of the features on AFM height and phase images is consistent with expectations. Compared to the shape persistent lamellae,

the amorphous chain ends are not well packed leading to regions with smaller height and greater hardness variations because of the underlying silicon wafer.

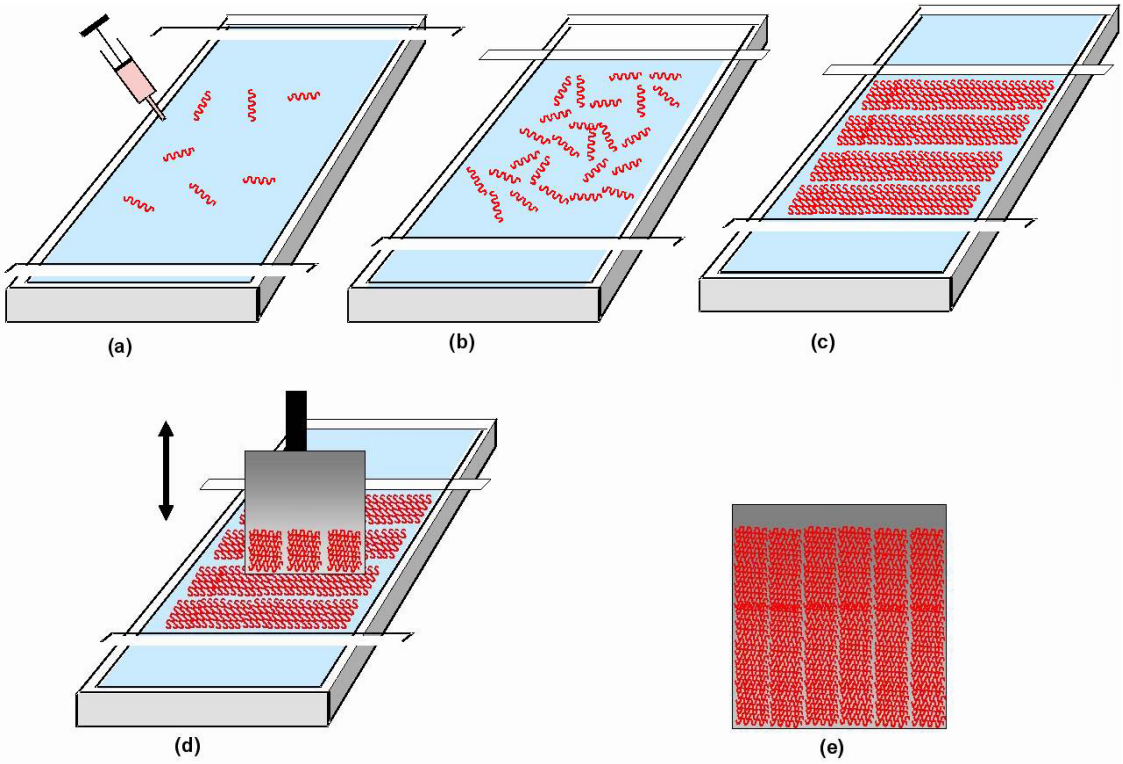

Figure 5.17: Schematic of the Y-type LB-deposition of PLLA molecules (red squiggly lines). (a) PLLA molecules adopt 10_3 helical conformations and are randomly lying flat on the subphase after spreading and in the gas-like state. (b) Disordered helices are present in the more dense LE phase. (c) Upon compression into the LC phase, PLLA single molecule helices are aligned forming shape persistent lamellae parallel to the barriers. (d) During Y-type LB-deposition, PLLA molecules are picked up with shape persistent lamellae parallel to the dipping direction, leading to (e) well-ordered lamellar structures on solid substrates. In (e), the regions observed between the red lamellar structures correspond to amorphous chain ends. The red stripes in (e) correspond to the bright features in the AFM height images and dark regions in the AFM phase images, while the amorphous chain ends appear dark in the AFM height images and bright in the AFM phase images (*e.g.* Figure 5.1).

5.4 Conclusions

In summary, the PLLA monolayer thickness from x-ray reflectivity measurements, the molar mass dependence of the lamellar dimensions from AFM images, and the existence of IR bands that are characteristic of PLLA molecules in 10_3 helical conformations, are consistent with PLLA molecules existing in a 10_3-helical conformation over nearly the entire length of a polymer chain in the LB-film and presumably at the A/W interface as well given previous studies by polarization modulation infrared reflection absorption spectroscopy.[155,156,223] It is also necessary to distinguish between the lamellar patterns in PLLA LB-films and conventional ones that arise from phase separation in block-copolymers[255,256] or crystallization in semi-crystalline polymers.[257,258] Unlike the lamellar patterns recently observed for isotactic poly(methyl methacrylate) where the lamellae represent folded-chain crystals,[154] the lamellae formed from single molecule helices of PLLA presumably have no chain-folding. In this respect, PLLA chains act like small liquid-crystalline molecules and rigid-rod polymers. For example, Wu *et al.* could see individual chains near liquid crystal defects in phthalocyanine systems.[259] More recently, single molecules of conjugated copolymers[260] and conductive polymers[261] have also been observed. Here, single molecule PLLA helices form smectic lamellar patterns in LB-films that also exhibit disinclinations.

CHAPTER 6

Collapse of Poly(L-lactic acid) Langmuir Monolayers at the Air/Water Interface: Buckling and Stacking versus Nucleation and Growth

6.1 Abstract

Two-dimensional (2D) to three-dimensional (3D) phase transitions in poly(L-lactic acid) (PLLA) Langmuir monolayers are studied by constant compression rate experiments and isobaric area relaxation experiments. During constant compression rate experiments, PLLA monolayers undergo a series of phase transitions from traditional Langmuir monolayers to solid-like multilayers. Hysteresis experiments and Brewster angle microscopy studies show that the solid multilayers can respread onto the subphase, primarily as monolayers, upon expansion. Nonetheless, atomic force microscopy studies on PLLA Langmuir-Blodgett (LB) films prepared in different Langmuir phases reveal that the lamellar features persist in all phases after the liquid expanded to liquid condensed phase transition that occurs during compression. The collapse of the Langmuir monolayer into multilayers is interpreted as the buckling and stacking of the lamellar monolayer as parts of the film slide over each other. Upon expansion, lamellae are observed over a wide range of surface concentrations. This observation is consistent with the hypothesis that PLLA single molecule 10_3-helices exist at all surface concentrations, which is confirmed by reflection absorption infrared spectroscopy studies on PLLA LB-films. On the other hand, during isobaric area relaxation experiments,

PLLA monolayers undergo "slow collapse" into 3D structures *via* a three step process: (1) the rearrangement of PLLA molecules into their most closely packed state, (2) molecular rearrangement to form stable nuclei, and (3) the growth of 3D structures. This proposed mechanism is an extension of the Vollhardt model.

6.2 Introduction

The stability of Langmuir monolayers at constant surface pressures during Langmuir-Blodgett (LB) deposition is crucial for the preparation of highly ordered structures with low defect densities.[262] Monolayer stability depends on the chemical nature of the amphiphiles, the monolayer – subphase interactions,[263,264] and the dynamics of compression.[265,266] Increasing the polarity of the headgroups or adding ions into the subphase can enhance the monolayer-subphase interactions thereby enhancing film stability.[267-269] The stability of Langmuir films is often related to collapse, which is defined as the process in which the two-dimensional (2D) Langmuir monolayers undergo a transition to a more stable three-dimensional (3D) phase.[270] The collapse surface pressure, $\Pi_{collapse}$, is referred to as the maximum surface pressure where a 2D monolayer can still exist. Monolayer collapse can be experimentally registered as a sharp decrease in surface pressure Π ("spikes") or plateaus at $\Pi_{collapse}$.[271] The collapse process can lead to the formation of either "organized" or "irregular" structures, depending on the nature of the amphiphiles. For instance, the "spike" at $\Pi_{collapse}$ followed by a plateau at lower Π

suggests the growth of "organized" structures, while a plateau at $\Pi_{collapse}$ corresponds to the growth of "irregular" features.[271]

Monolayer collapse can be thought of as a classical nucleation and growth process. At a certain surface pressure known as the equilibrium spreading pressure (Π_{esp}), the monolayer is in equilibrium with the bulk phase. If the monolayer is compressed into a region where Π is greater than Π_{esp}, the monolayer is metastable. As Π increases further, the barrier to nucleation decreases, and the formation of critical nuclei in the bulk phase becomes favorable. Three-dimensional structures can be formed once the critical nuclei are formed. A "slow collapse" mechanism is achieved by isobaric area relaxation experiments, in which Π is held at a constant value above Π_{esp} but below $\Pi_{collapse}$, and the decrease in the area of a monolayer with time is monitored.[272,273] Vollhardt applied a 2D "Avrami" equation to study the nucleation and growth mechanism in Langmuir monolayers.[274-276] The Vollhardt model considers two typical nucleation modes: instantaneous nucleation with monodisperse centers and progressive nucleation with polydisperse centers. The nucleation centers could be hemispheric or cylindrical, and the growth of the centers could be from the edge or the basal areas. A detailed discussion of the Vollhardt model will be described in the results and discussion section.

In most cases, monolayers collapse by the formation of bilayers, trilayers, or multilayers instead of a bulk phase, as discussed in Chapter 2 (Figure 2.10). Several different mechanisms have been proposed to explain the collapse of Langmuir monolayers. Ries proposed that collapse begins with buckles in the film that grow

larger in amplitude, fold over, and then break into disconnected multilayers.[277,278] However, Nikomorov showed that the Ries mechanism may fail in monolayers without defects.[279] Milner *et al.* demonstrated that a uniform monolayer should become unstable with respect to buckling only at zero surface tension, or only at $\Pi > 72.0$ $mN \bullet m^{-1}$.[280] This statement contradicts the fact that most Langmuir films collapse at $\Pi_{collapse}$ well below this limit. Diamant *et al.* proposed a modified model, suggesting that the buckling occurred at boundaries between monolayer phases as a result of instabilities that are related to height difference between phases of different spontaneous curvature.[281,282] This mode of buckling has been observed experimentally in some cases. For instance, buckling instabilities with very small amplitude (~ 1-2 nm) were confirmed for very rigid monolayers through light scattering[283,284] and diffraction studies.[285] The folding occurs in monolayers in which an isotropic liquid phase and islands of a condensed phase coexist. For example, in biphasic mixtures of dipalmitoylphosphatidylcholine (DPPC) and palmitoyloleoylphosphatidylglycerol (POPG), large-scale folding into the subphase was observed.[286] The folding is connected to the monolayer during compression and unfolding reversibly occurs when the film is expanded.

Recently, Ybert *et al.* proposed that the collapse of 2-hydroxytetracosanoic acid monolayers occurs with mixed mechanisms.[270] At low surface pressure, the film undergoes "slow collapse" to form multilayer islands. At high $\Pi_{collapse}$, folding is observed. At slow compression rates, "giant folds" into the subphase arise as defects, which are composed of bilayers that remain suspended under the film. At fast

compression rates, "multiple folds" with small-amplitudes are formed that extend across the subphase and are perpendicular to the compression direction.

In addition to isotherm studies, several imaging methods have been used to examine monolayer collapse. For example, lines of 30 - 50 μm width were observed during the collapse of behenic acid monolayers by Brewster angle microscopy (BAM).[262] BAM was used to examine collapse mechanisms of trisilanol polyhedral oligomeric silsesquioxane (POSS) molecules with different organic groups as coronae, as well as POSS molecules blended with poly(dimethyl siloxane) (PDMS).[214,287-292] BAM and scanning force microscopy were used to examine the stepwise collapse mechanisms for films of cyclolinear poly(organosiloxanes).[109] Dark-field imaging and atomic force microscopy (AFM) were also used to examine the collapse of 2-hydroxytetracosanoic acid monolayers with mixed mechanisms.[270]

In this chapter, the collapse behavior of poly(L-lactic acid) (PLLA) Langmuir monolayers is examined by constant compression rate experiments and isobaric area relaxation experiments. In constant compression rate experiments, PLLA Langmuir films are studied by isotherms, hysteresis loops, and BAM at the air/water (A/W) interface. The results reveal that the collapse of PLLA monolayers lead to the formation of multilayers which can respread onto the subphase upon expansion. The collapse is interpreted by atomic force microscopy studies as the cracking of the lamellar monolayers (which are composed of well-ordered PLLA 10_3-helices) causing parts of the film to slide over each other. This conclusion is supported by reflection absorption

infrared spectroscopy (RAIRS) studies which confirm the existence of 10_3-helices at all surface concentrations. In isobaric area relaxation experiments, the relaxation can be divided into three processes: (1) PLLA molecular rearrangement at the A/W interface to form most closely packed condensed PLLA monolayers, (2) molecular rearrangement to form stable nuclei, and (3) the growth of 3D structures.

6.3 Results and Discussion

6.3.1 Monolayer Collapse During Compression – Buckling and Stacking

6.3.1.1 Π-*A* Isotherm and BAM Experiments

Figure 6.1 shows a surface pressure–area per monomer (Π-*A*) isotherm of a 12.9 kg•mol^{-1} PLLA Langmuir film obtained during a hysteresis loop experiment. The compression isotherm exhibits five distinct regions: (1) a liquid expanded (LE) phase (A > 0.24 nm^2•monomer^{-1}); (2) a liquid expanded to condensed (LE/LC) phase transition at Π ≅ 2.0 mN•m^{-1} and 0.20 < A < 0.24 nm^2•monomer^{-1}; (3) a condensed (LC) phase (0.17 < A < 0.20 nm^2•monomer^{-1}); (4) a stable plateau at Π ≅ 8.0 mN•m^{-1} after a "spike" at Π ≅ 8.3 mN•m^{-1}; and (5) a lower compressibility region corresponding to multilayer formation for A < ~ 0.08 nm^2•monomer^{-1}. Regions (1) through (3) have been discussed in Chapters 4 and 5, and regions (4) and (5) will be discussed in this chapter. In region (4), the PLLA Langmuir monolayer collapses into 3D structures with a sharp "spike" around A ≅ 0.17 nm^2•monomer^{-1} or $\Pi_{collapse}$ ≅ 8.3 mN•m^{-1} (as shown in the inset of Figure 6.1), followed by a stable plateau. The "spike" in the isotherm is usually associated with

a kinetic effect, while the plateau is usually associated with the formation of a new phase. The plateau occurs at $\Pi_{plateau} \cong 8.0$ mN•m^{-1}, which is less than the collapse pressure, suggesting the formation of "organized" structures.[262,271] The plateau has previously been attributed to either bilayer formation or the random 2D chain-to-helix transition.[155,223] According to the surface area value where the plateau ends (~ 0.09 nm^2•monomer^{-1}), it is believed that the plateau corresponds to the coexistence of a monolayer and a bilayer. This idea is also supported by AFM results to be presented shortly. No obvious features are observed in BAM images during the plateau (Figure 6.2b), similar to the LC monolayer state (Figure 6.2a). The absence of features in BAM images is attributed to weak BAM contrast and low lateral resolution (at least 20 μm). The similarity in BAM images between the LC phase and the monolayer-bilayer coexistence region indicates that after collapse, PLLA molecules are still lying flat to the plane of the water interface. If the PLLA molecules stood up or folded upon compression, the change in the film thickness would have been large enough for BAM to detect the difference.[135] As compression continues, Π increases rapidly where multilayers start to form. BAM images (Figure 6.2c and 6.2d) are similar to those in the plateau region, which again is attributed to weak optical contrast between the different domains.

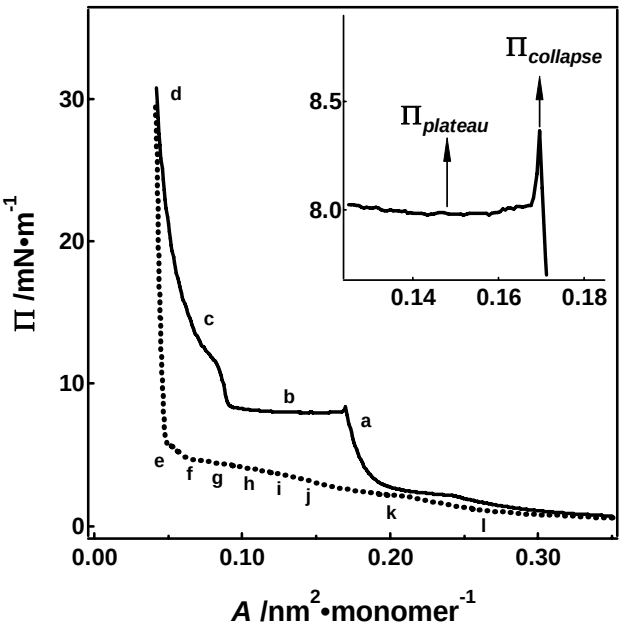

Figure 6.1: Π-*A* isotherm of M_n = 12.9 kg•mol^{-1} PLLA Langmuir films at T = 22.5 ^{o}C obtained from a single hysteresis loop with a compression rate of 0.016 nm^2•min^{-1}•monomer^{-1}. The inset shows the collapse of the monolayers at around $A \cong$ 0.17 nm^2•monomer^{-1} or $\Pi_{collapse} \cong$ 8.3 mN•m^{-1}. A plateau is also highlighted in the inset with $\Pi_{plateau} \cong$ 8.0 mN•m^{-1}. Upon compression to Π = 32.0 mN•m^{-1} (solid line), Π drops to Π ≅ 5.2 mN•m^{-1} upon expansion and decreases gradually as the expansion continues (dotted line). The letters on the isotherm correspond to the BAM images in Figure 6.2.

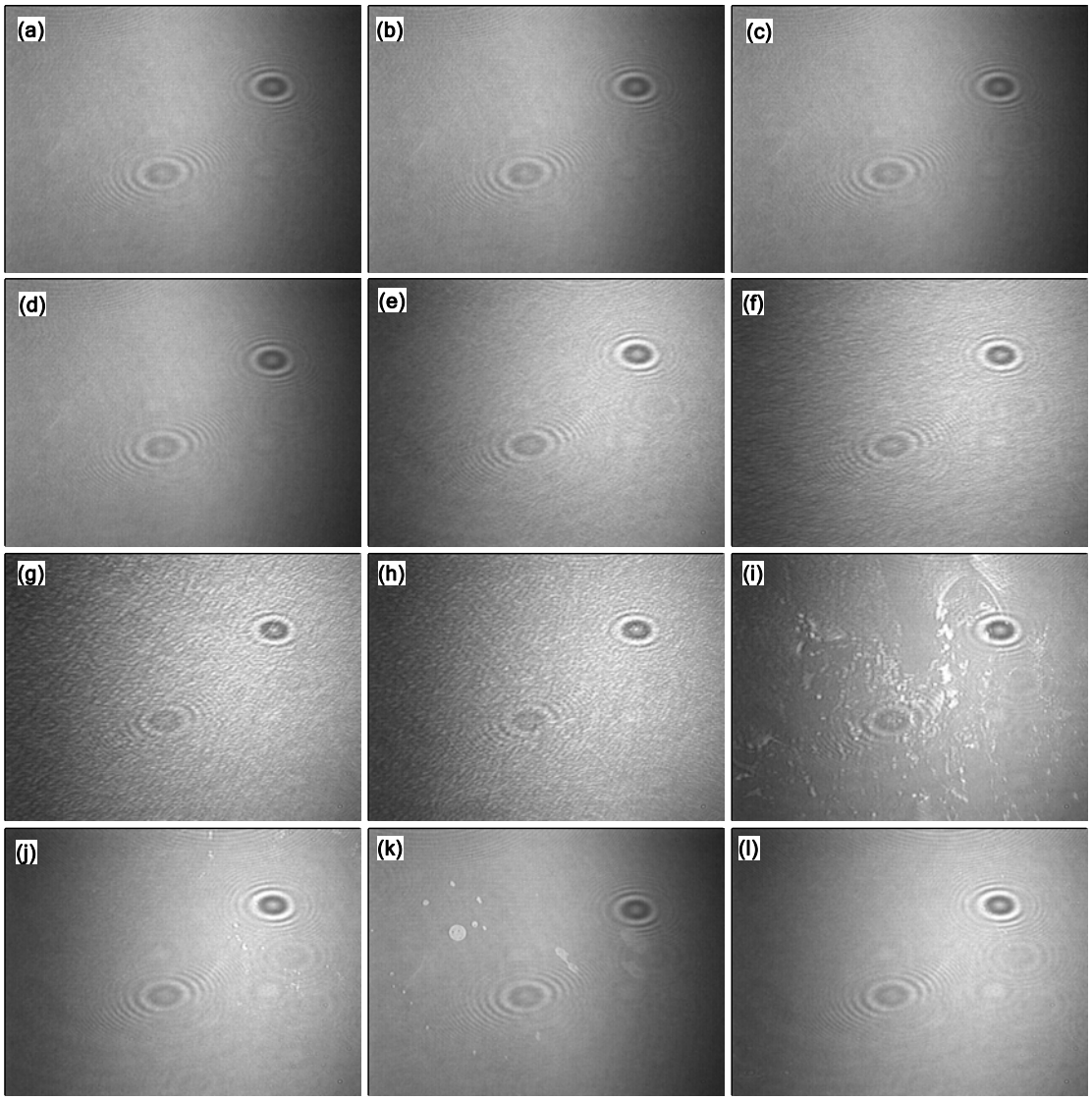

Figure 6.2: BAM images at *A* values of: a) 0.18, b) 0.13, c) 0.08, and d) 0.04 $nm^2 \bullet monomer^{-1}$ during compression, and e) 0.04, f) 0.06, g) 0.08, h) 0.10, i) 0.12, j) 0.15, k) 0.20, and l) 0.26 $nm^2 \bullet monomer^{-1}$ during expansion. No obvious features are observed in (b) through (d). During expansion, some heterogeneous features are observed (g through j). Circular domains are observed during the LC/LE phase transition (k), and disappear upon expansion back to the LE phase (l). All BAM images are 4.8×6.4 mm^2, and the film is symmetrically compressed from the top and bottom of each image. Each BAM image has an independent gray scale.

Surface pressure drops precipitously upon expansion but does not fall to zero, as was observed for hydrophobic aggregates in another system at the A/W interface.[288] Upon compression to Π = 32.0 mN•m^{-1}, Π drops to $\Pi \cong$ 5.2 mN•m^{-1} upon expansion and decreases gradually as the expansion continues (Figure 6.1). Such behavior indicates that some multilayer material respreads at the A/W interface upon expansion. During rapid expansion, the failure of PLLA to immediately respread may lead to some patches of bare surface or monolayer coverage. As a result, BAM images have sharper contrast (Figure 6.2e through 6.2h). Interestingly, the BAM images immediately after expansion, Figure 6.2f, 6.2g, and 6.2h, exhibit uniform domain sizes and macroscopic orientation. Upon expansion back into the condensed monolayer region (Π = 3.1 mN•m^{-1} and A = 0.15 nm^2•monomer^{-1}), heterogeneous features in the BAM images start to disappear (Figure 6.2j). The expansion isotherm retraces the compression isotherm in the liquid LE phase, suggesting that PLLA molecules can respread onto the subphase almost completely after the hysteresis cycle. BAM images show circular domains in LC/LE coexistence region (Figure 6.2k), just like the ones seen during compression. The circular domains disappear after expansion into the LE phase (Figure 6.2l).

Compression-expansion hysteresis experiments and BAM images suggest that PLLA Langmuir monolayers collapse into multilayers during compression. Upon expansion, the multilayer structures can respread onto the subphase. However, BAM, with micrometer scale resolution, does not reveal any direct proof of the collapse mechanism. On the other hand, AFM can provide nanometer scale morphological information, hence

AFM may be used to yield insight into the collapse mechanism. In order to apply AFM to study the morphological changes, PLLA Langmuir-Blodgett (LB) films are prepared in different phases.

6.3.1.2 Transfer Information for LB-Film Deposition

LB-films prepared at various Π values from different phases of the Π-*A* isotherm have different transfer ratio data, as summarized in Table 6.1. As expected, the transfer ratio values vary strongly with Π because of the phase behavior noted in the discussion of the Π-*A* isotherms. The transfer ratio values for PLLA deposited at Π = 1.5 $mN \bullet m^{-1}$ vary wildly between zero (minimum) and 3.9 (maximum), reflecting the LE state of the PLLA monolayer. In the LE state, low surface density PLLA films have weaker lateral interactions at the A/W interface than they do in the more condensed phases. During the compression process, the transfer ratio values for the first layer increase with increasing Π. The transfer ratio values in the condensed region, the most closely packed monolayer state, approach unity for Y-type deposition for a few cycles. In spite of the fact that the transfer ratio values for the first layer increase with Π, the average transfer ratio values decrease with Π after the condensed monolayer region, indicating that the solid-like multilayers could not be deposited as well as the LC monolayers onto the solid substrates. LB-films were also deposited during the expansion process. The transfer ratio value at Π = 10.0 $mN \bullet m^{-1}$ (where the sudden Π drop occurs) is extremely low, probably because of the fact that PLLA films are still solid-like with some open-water regions. PLLA films at Π = 4.1 $mN \bullet m^{-1}$ or $A \cong 0.13$ $nm^2 \bullet monomer^{-1}$ (the plateau during

the expansion process) are liquid-like and more uniform leading to a higher transfer ratio. However, the transfer ratio value is still lower than for films transferred at Π = 8.0 $mN \bullet m^{-1}$ or $A \cong 0.13\ nm^2 \bullet monomer^{-1}$ (the plateau during the compression process). Similarly the transfer ratio value at Π = 2.5 $mN \bullet m^{-1}$ ($A \cong 0.18\ nm^2 \bullet monomer^{-1}$) during expansion is lower than that at Π = 4.0 $mN \bullet m^{-1}$ ($A \cong 0.18\ nm^2 \bullet monomer^{-1}$) during compression. This feature probably arises from the fact that PLLA respreading from multilayer aggregates partially compensates for material removed from the interface during the transfer process.

Table 6.1: Average transfer ratios for PLLA LB-films.[a]

	Compression						***Expansion***[b]		
Π ($mN \bullet m^{-1}$)	**1.5**	**4.0**	**7.0**	**8.0**	**13.0**	**30.0**	***10.0***	***4.1***	***2.5***
Down	**0.24** ±0.30	**0.80** ±0.11	**0.95** ±0.05	**1.18** ±0.01	**1.75** ±0.0	**1.87** ±0.13	***-0.07*** *±0.02*	***-0.80*** *±0.04*	***-0.75*** *±0.03*
Up	**0.47** ±0.15	**0.78** ±0.08	**0.82** ±0.03	**0.92** ±0.01	**0.36** ±0.1	**0.35** ±0.13	***0.01*** *±0.02*	***0.73*** *±0.05*	***0.60*** *±0.06*

[a] Errors represent the maximum fluctuation around the mean value during the transfer process

[b] Transfer ratio values during expansion process are itallized

6.3.1.3 Surface Morphology of PLLA LB-films

AFM measurements are applied to examine surface morphology of PLLA LB-films prepared in different phases. Figure 6.3 shows the AFM height images for PLLA LB-films prepared at different Π values during compression. There are no obvious ordered features in the LB-films prepared in the LE phase ($\Pi \cong 1.5\ mN \bullet m^{-1}$, Figure 6.3a),

while well-ordered lamellar features exist in the LC phase ($\Pi \cong 4.0$ mN•m^{-1}, Figure 6.3b), which have been discussed in Chapters 4 and 5. As the compression proceeds, the Langmuir monolayer collapses into multilayers. AFM results ($\Pi \cong 8.0$ mN•m^{-1}, Figure 6.3c) reveal that the plateau is the coexistence between a monolayer and a bilayer, where the well-ordered lamellar features are observed as a background, and a second lamellar layer is on top. The appearance of aggregates on top of the existing lamellar features is more obvious when the Langmuir film is compressed to higher Π values corresponding to thicker multilayers. AFM images obtained for PLLA LB-films prepared in the multilayer region (Figure 6.3d-f) clearly reveal a stacking of lamellar structures with irregular domain shapes. The existence of lamellar features after the LE/LC phase transition suggest that PLLA single molecule helices exist at the A/W interface over the entire surface concentration range during the compression process. RAIRS studies will be presented shortly to support this supposition. The collapse of the Langmuir film appears to occur when cracking of the lamellar monolayer causes parts of the film to slide over each other much like the shifting of plates along a fault line during an earthquake. This mechanism is described as "buckling and stacking".

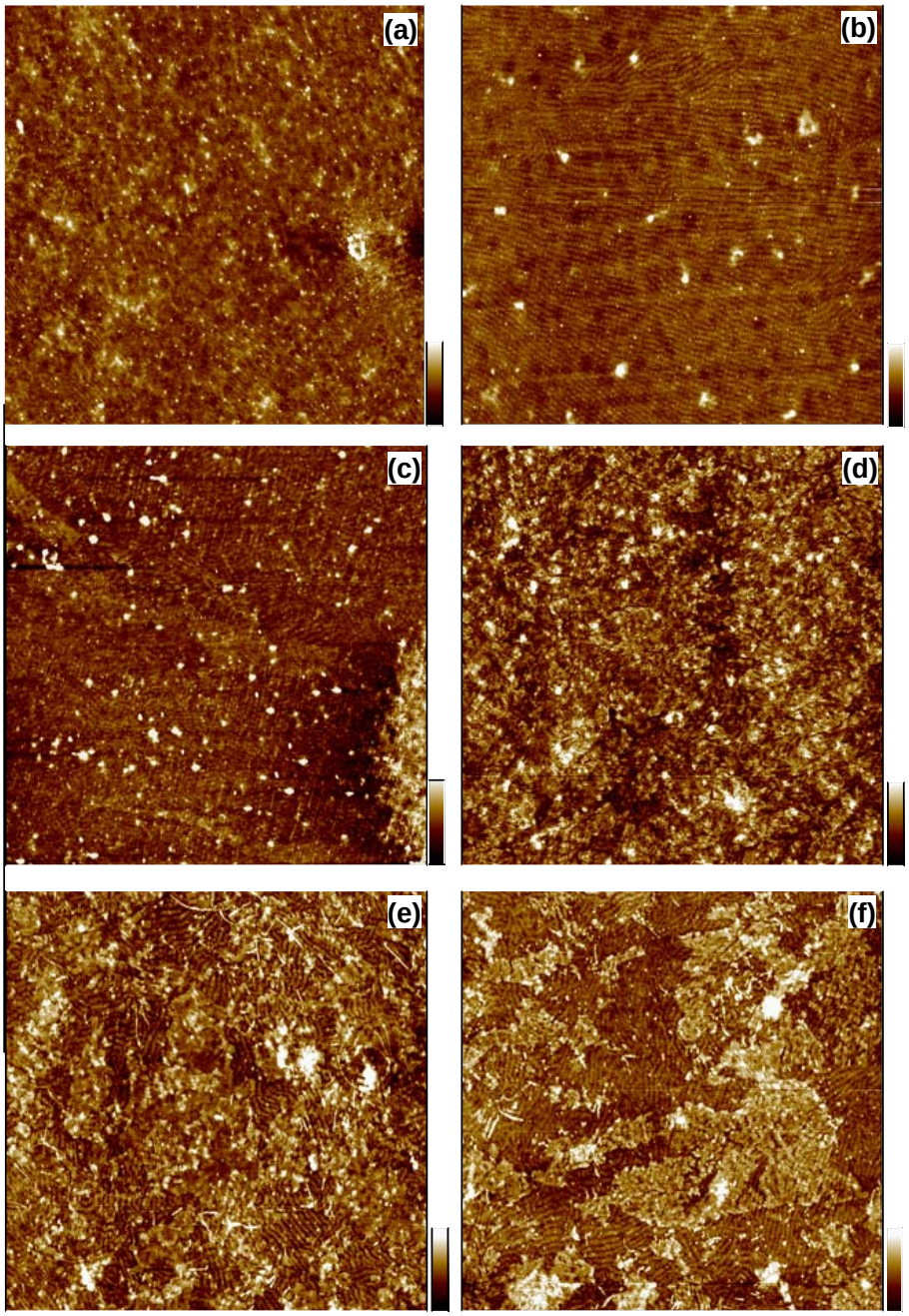

Figure 6.3: AFM height images for M_n = 12.9 kg•mol^{-1} PLLA LB-films transferred at various Π values and T = 22.5 ^{o}C during the compression process onto a hydrophobic silicon wafer with a scan range of 5 × 5 μm^2 and z range of 5 nm. Π values are: a) 1.5, b) 4.0, c) 8.0 (plateau); d) 13.5, e) 30.0, and f) 40.0 mN•m^{-1}. Multilayer formation is observed. Lamellar features are present in all the images and the lateral dimension remains constant. The collapse of lamellae on existing lamellar features is also observed with the formation of multilayers.

The idea that monolayer collapse occurs through buckling and stacking of lamellae onto existing lamellae can be supported with roughness analysis. Table 6.2 summarizes the root mean square (r.m.s.) surface roughness (R_{rms}) values obtained from the 5 × 5 μm^2 AFM height images (Figure 6.3). PLLA substrates prepared in different Langmuir film phases *via* the LB-technique have relatively small R_{rms} values. The R_{rms} values increase slightly (≈ 2X) as the PLLA Langmuir film goes from the LC monolayer to multilayer phases during compression. The R_{rms} values of PLLA LB-films prepared after collapse are slightly larger because 3D structures are present.

Table 6.2: Root mean squared surface roughness values (R_{rms}) and lamellar spacings (d) for M_n = 12.9 kg•mol^{-1} PLLA LB-films prepared in different Langmuir phases at 22.5 ^oC.

	Compression						***Expansion*[a]**		
Π (mN•m^{-1})	**1.5**	**4.0**	**8.0**	**13.5**	**30.0**	**40.0**	***30.0***	***10.0***	***2.5***
R_{rms} (nm)	**0.45**	**0.46**	**0.69**	**0.75**	**0.76**	**0.82**	***1.09***	***0.44***	***0.46***
d (nm)[b]	**NA**	**55.7**	**55.2**	**54.8**	**54.5**	**55.0**	***55.2***	***55.5***	***55.3***
Figure Ref.	**6.3a**	**6.3b**	**6.3c**	**6.3d**	**6.3e**	**6.3f**	***6.5a***	***6.5b***	***6.5c***

[a] Expansion values are itallized

[b] Determined by line scan analysis with error bars ± 0.5 nm.

Roughness calculations on different sections in AFM images of PLLA LB-films obtained in the multilayer region (Figure 6.4) provide interesting results: the R_{rms} values in the lamellar background are ~ 0.46 nm, the same as the R_{rms} values for the substrates with well-ordered lamellar features prepared in the monolayer region (Figure 6.3b); while

the R_{rms} values for the aggregate patches are ~ 0.56 nm. The similarity in the R_{rms} values between the lamellar background and aggregates along with the fact that the lamellar spacing remains constant supports the proposal that multilayer formation occurs through a bulking and stacking of the existing lamellae.

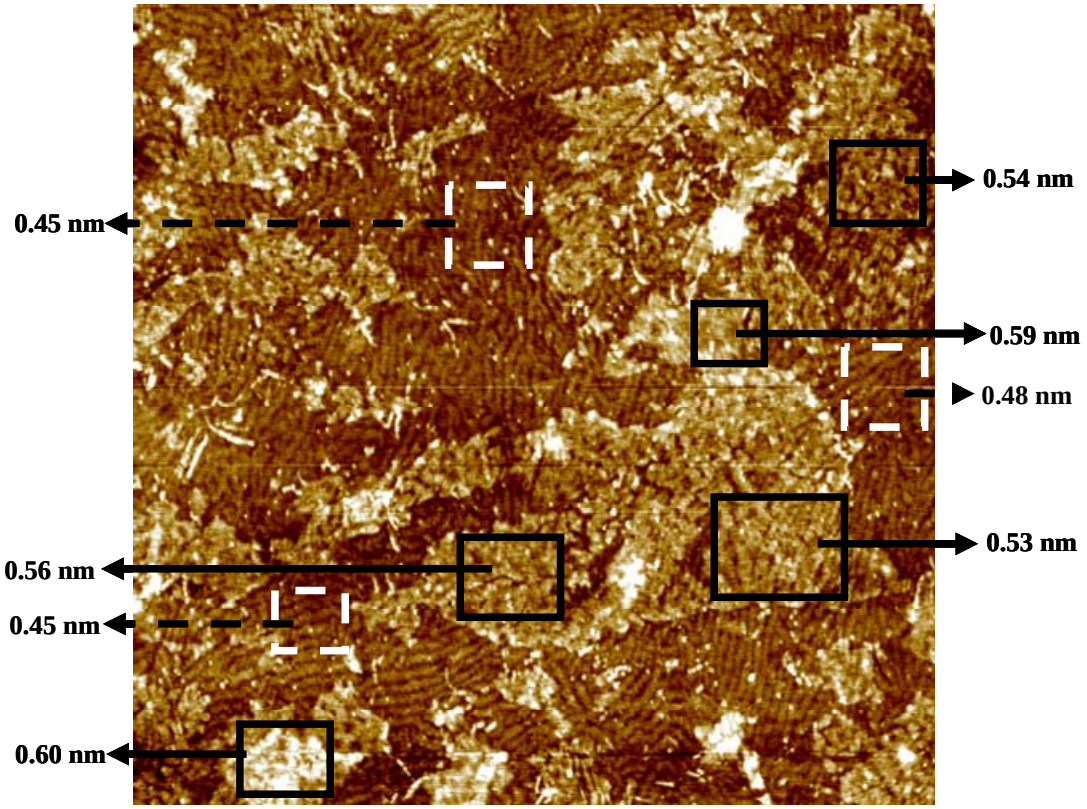

Figure 6.4: Roughness analysis of a M_n = 12.9 kg•mol^{-1} PLLA LB-film prepared at Π = 40.0 mN•m^{-1} and T = 22.5 ^{o}C in the multilayer region. The R_{rms} values of the background lamellar features (white dotted box) are the same as those of the well-ordered LB-films prepared in the monolayer region. The R_{rms} values of the aggregate patches (solid box) are slightly larger, supporting the proposal that the multilayer formation occurs through a bulking and stacking of existing lamellae.

Interestingly, during film expansion, lamellar structures are seen over a wide *A* and Π range. Upon expansion, the surface morphology of the LB-films (Figure 6.5a) is similar to LB-films prepared at similar Π values in the multilayer region during compression (Figure 6.3f). Lamellar features are present with aggregates formed on top of the lamellae. As the expansion proceeds, the multilayer material respreads onto the subphase as inferred from AFM images. Well-ordered lamellar features are also observed for the LB-films prepared during the expansion plateau (ca. Π = 2.5 $mN \bullet m^{-1}$ and $A \cong 0.18$ $nm^2 \bullet monomer^{-1}$ in Figure 6.5c). The AFM results during expansion (Figure 6.5) suggest that the lamellar structure is stable at all Π values above the LE/LC threshold. The dimensions of the lamellar features during the compression and expansion processes are identical (Table 6.2), suggesting that the lamellar structure is fixed during the LE/LC phase transition and subsequent LB-deposition process. During the compression and expansion processes, PLLA molecules are neither degraded nor folded. Moreover, it is also observed that PLLA LB-films prepared at $A \cong 0.18$ $nm^2 \bullet monomer^{-1}$ during compression (at $\Pi \cong 4.0$ $mN \bullet m^{-1}$) and expansion (at $\Pi \cong 2.5$ $mN \bullet m^{-1}$) have similar lamellar features (Figure 6.3b and 6.5c) and similar R_{rms} values, confirming that the respreading of PLLA molecules onto the subphase results in the reformation of monolayers at the A/W interface during expansion.

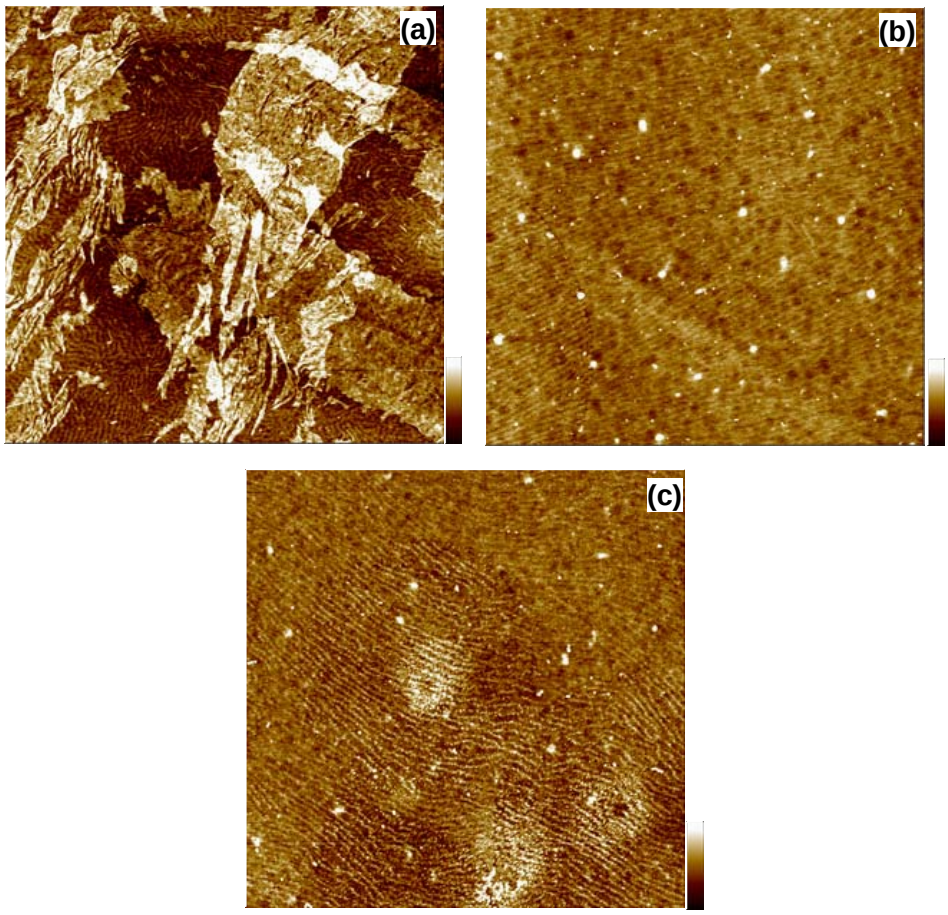

Figure 6.5: Representative AFM height images for M_n = 12.9 kg•mol^{-1} PLLA LB-films transferred onto a hydrophobic silicon wafer at various Π values and at T = 22.5 ^{o}C during the expansion process. The AFM scan ranges are 5 × 5 μm^2 and z ranges are 5 nm. Π values are: a) 30.0, b) 10.0, and c) 2.5 mN•m^{-1} (plateau at A ≅ 0.18 nm^2•monomer^{-1}). Multilayer structures disappear during expansion, indicating that the respreading of multilayer material onto the subphase must occur. Lamellar features with the same dimension as observed in the LC monolayer during compression are observed over a wider range of A values for the expanding films.

6.3.1.4 Reflection Absorption Infrared Spectroscopy of PLLA LB-films

The existence of lamellar features in AFM images of PLLA LB-films prepared in all Langmuir film phases after the LE/LC phase transition suggests that PLLA molecules retain 10_3 helical conformations at all surface concentrations during compression and expansion processes. This is confirmed by RAIRS studies. Figure 6.6 shows the RAIRS spectra of PLLA LB-films prepared in different phases during the compression and expansion processes. All spectra are obtained using a nitrogen purge Nicolet NEXUS 670 FT-IR spectrometer using *p*-polarized light at an incident angle of 86 ^{o} and a liquid nitrogen cooled MCT (mercury-cadmium-telluride) detector. Each spectrum represents an average of 1000 scans and only the range less than 1000 cm^{-1} is shown. The characteristic crystalline band at 921 cm^{-1}, which is assigned to the coupling of C-C backbone stretching with the CH_3 rocking mode, is present for all PLLA LB-films. On the other hand, the mode characteristic of the amorphous phase at 955 cm^{-1} is not observed. Furthermore, the presence of the 921 cm^{-1} band in LB-films prepared in the LE phase indicates that PLLA molecules take on a 10_3 helical conformation at low surface pressure. This feature is different from previous IR studies of PLLA Langmuir films by Klass *et al.*, who claimed that helical formation is compression-induced and occurs during the plateau after collapse.[223] A follow-up paper by Pelletier *et al.* compared IR spectra for PLLA Langmuir films before and after plateau, and suggested that PLLA forms 10_3-helices after being spread at the A/W interface.[155] No conformational change occurs during the collapse, and 10_3 helical conformation remains

the same during the compression process. Pelletier's suggestions are different from Klass's observation, and in their paper, Pelletier *et al.* did not present IR spectra showing the existence of 10_3-helices at low surface pressures to support their suggestions. Our results clearly present the existence of 10_3-helices at low surface pressures upon spreading, which can be used to support Pelletier's conclusions. However, there still remains a question: when do the helices form, in the dilution solution, during spreading, or at the A/W interface after spreading? No evidence has been reported to answer this question yet.

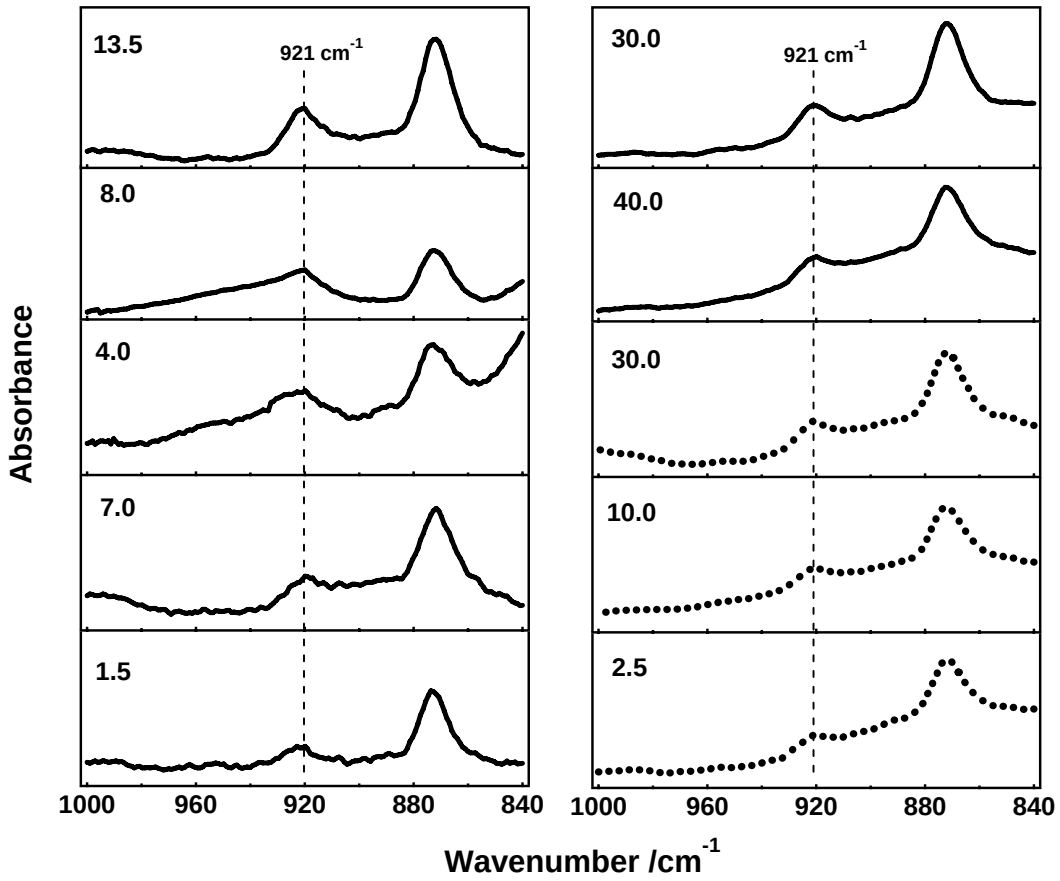

Figure 6.6: RAIRS spectra in the range 1000 – 840 cm^{-1} for M_n = 12.9 kg•mol^{-1} PLLA LB-films prepared at various Π values in different phases at T = 22.5 °C on gold with five dipping cycles. The Π values are indicated by the numbers on the graph. LB-films prepared at Π = 1.5, 4.0, 7.0, 8.0, 13.5, 30.0, and 40.0 mN•m^{-1} (solid lines) were obtained during the compression process, while LB-films prepared at Π = 2.5, 10.0, and 30.0 mN•m^{-1} (dotted lines) were deposited during the expansion process. The characteristic band for crystalline PLLA at 921 cm^{-1} is observed for all LB-films, consistent with the existence of PLLA 10_3-helices at all surface concentrations.

6.3.1.5 Buckling and Stacking

Figure 6.7 provides a schematic to better illustrate the buckling and stacking mechanism. In the LC phase, PLLA molecules are aligned forming lamellar features that are shape persistent and parallel to the barriers (Figure 6.7a as discussed in Chapter 5). Upon further compression, a fault line is formed between the shape persistent lamellae, leading to a "convergent boundary" (Figure 6.7b). During collapse, two lamellar features approach to each other, and one lamellar monolayer may move on top of the other monolayer, forming 3D structures (Figure 6.7c). The buckling and stacking mechanism leads to formation of irregular aggregates which are composed of lamellar features.

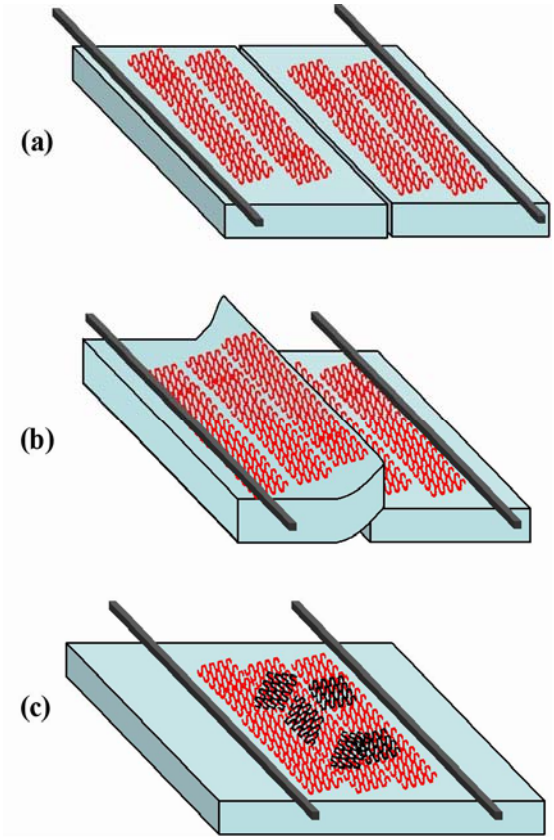

Figure 6.7: Schematic of the buckling and stacking mechanism: (a) A PLLA monolayer in the LC phase with lamellar features parallel to the barriers; (b) Upon compression, buckling occurs with the appearance of a "convergent boundary"; and (c) Stacking of lamellae on top of existing lamellar monolayers leading to 3D structures.

6.3.1.6 Hysteresis Studies

Hysteresis loop experiments are also used to examine the stability and respreading of Langmuir films. Completely reversible compression-expansion cycles are expected to be observed for monolayers being compressed in a 2D system before entering the metastable region. In the metastable region, completely reversible hysteresis loops may

be possible if critical 3D nuclei have not grown through a "slow collapse" mechanism. Completely reversible hysteresis loops are not observed after the monolayer collapses.

The behavior of PLLA Langmuir films during hysteresis experiments is explored at different target Π values in different Langmuir phases at 22.5 ^{o}C (Figure 6.8). Each curve in Figure 6.8 represents a fresh monolayer. It is observed that the monolayer exhibits completely reversible compression-expansion cycles until it is compressed past the "spike" in the isotherm, where the phase transition between a monolayer and bilayer begins. Previous studies showed that no area relaxation is observed for $\Pi < 5.0$ mN•m^{-1}, and S-shaped isobars are observed at Π values close to the collapse pressure during a constant compression rate process, $\Pi_{collapse} = 8.3$ mN•m^{-1} (Figure 6.1).[223] Therefore, the complete reversibility for a target $\Pi = 1.5$, 2.2, and 4.0 mN•m^{-1} are expected (Figure 6.8a-c). However, the complete reversibility seen for compression to $\Pi = 7.0$ mN•m^{-1} is not expected (Figure 6.8d). PLLA monolayers at $\Pi = 7.0$ mN•m^{-1} are in the metastable region, where bulk solid phases may nucleate and grow.[274-276] However, if expansion immediately follows compression, a bulk solid phase does not have time to nucleate and grow; therefore in the metastable region the complete reversibility may be observed. Actually, an isobaric experiment at $\Pi = 6.9$ mN•m^{-1} shows that the solid phase starts to nucleate and grow almost 5 hours after compression to the target pressure at room temperature.[223] Hence, longer induction times for the formation of stable nuclei favor reversibility during the hysteresis experiment.

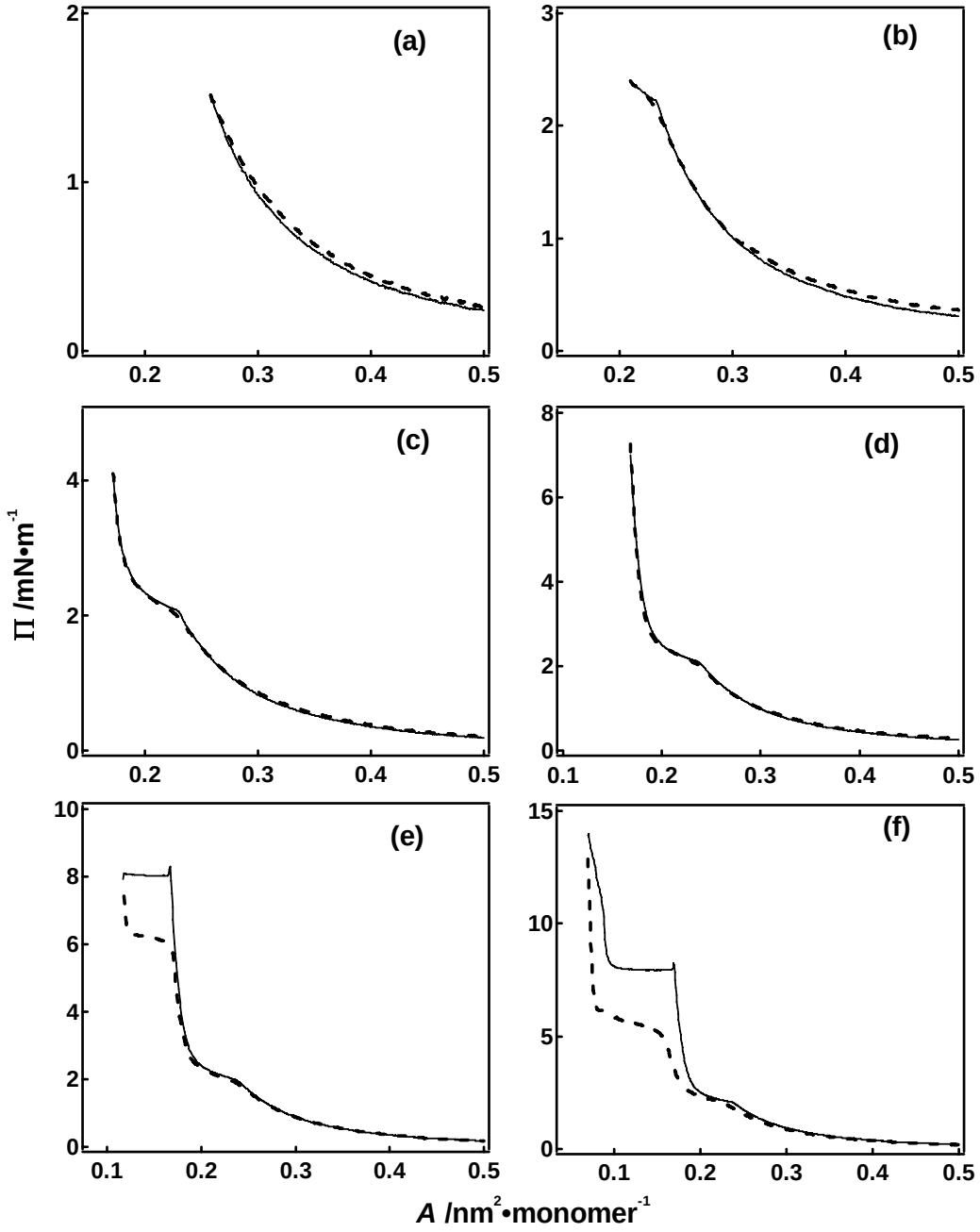

Figure 6.8: Hysteresis experiments for M_n = 12.9 kg•mol^{-1} PLLA Langmuir films at the A/W interface. The monolayer is compressed to a target Π followed by immediate expansion with the same experimental parameters (T = 22.5 ^{o}C, and barrier speed = 20 cm^2•min^{-1}). The target Π values are: (a) 1.5, (b) 2.2, (c) 4.0, (d) 7.0, (e) 8.0 (plateau), and (f) 14.0 mN•m^{-1}. The solid lines represent the compression isotherms, while the dashed lines represent the expansion isotherms. The monolayer is stable until it is compressed past the "spike" at Π = 8.3 mN•m^{-1}.

Complete reversibility is not observed for PLLA Langmuir films compressed past the collapse transition (Figure 6.1, and Figure 6.8e and f). Upon expansion, Π precipitously drops to a value that depends on the maximum Π value during compression. The higher the Π value obtained during compression, the lower the Π value that is observed upon sudden expansion (as summarized in Table 6.3). This behavior may be correlated with film thickness as compression to higher Π values leads to thicker films, which could inhibit respreading upon sudden expansion leading to larger drops in Π. Upon expansion of the film it is quite obvious that multilayer structures exist on the surface, and that the multilayer structure is somewhat solid-like.

After compression into the plateau region, the coexisting monolayer and bilayers can not respread instantaneously with decreasing surface pressure; therefore the expansion isotherm does not retrace the compression isotherm upon expansion (Figure 6.8e). After a sharp drop, a plateau is observed suggesting the coexistence of bilayer and monolayer. Interestingly, the expansion isotherm rejoins the compression isotherm at $\Pi \cong 5.4$ mN•m^{-1} and $A \cong 0.18$ nm^2•monomer^{-1}, and then retraces the compression isotherm, suggesting that a stable PLLA monolayer reforms after respreading, as observed in AFM images (Figure 6.5c). Upon compression to a point where A is small enough for complete bilayer formation ($\Pi = 14.0$ mN•m^{-1}), Π drops to ~ 6.0 mN•m^{-1} followed by a plateau (bilayer – monolayer coexistence), after which another decrease in Π is observed at $\Pi \cong 5.4$ mN•m^{-1} and $A \cong 0.18$ nm^2•monomer^{-1}, again indicating the formation of a monolayer

(Figure 6.8f). However, such a trend is not observed for hysteresis experiments at Π = 32.0 (Figure 6.1) where Π drops below 5.4 $mN \bullet m^{-1}$ upon expansion. Nonetheless, no matter how large the maximum Π value is, all expansion processes retrace the compression isotherms in the LE phase. This result is consistent with the conclusion from BAM images that almost all of the solid-like multilayer aggregates respread at Π values below the LE/LC transition.

Table 6.3: Summary of compression-expansion hysteresis experiments.

Target Π ($mN \bullet m^{-1}$)	**4.0**	**7.0**	**8.0**	**10.5**	**14.0**	**32.0**	**36.0**
A shift × 10^3 ($nm^2 \bullet monomer^{-1}$)	**3.8**[a]	**4.8**[a]	**5.0**[b]	**8.6**[b]	**9.8**[b]	**10.2**[b]	**10.8**[b]
Area loss (× 100 %)	**2.1**	**2.7**	**2.8**	**4.8**	**5.4**	**5.7**	**6.0**
$\Pi_{plateau,e}$ 1st expansion ($mN \bullet m^{-1}$)[c]	-	-	**6.3**	**6.2**	**6.0**	**5.1**	**4.7**
$\Pi_{plateau,e}$ 2nd expansion ($mN \bullet m^{-1}$)[c]	-	-	**6.2**	**6.2**	**5.9**	**5.2**	**5.2**

[a] Area shifts stand for the differences between the monomer areas at the target Π
[b] Area shifts stand for the differences between monomer area at collapse points
[c] $\Pi_{plateau,e}$ value at which the plateau starts to appear during expansion

In order to confirm that most of the multilayer aggregates respread onto the subphase following expansion, a second hysteresis cycle is obtained immediately after completing the first cycle. It has been observed that the shapes of the Π-*A* isotherms for the second hysteresis cycle are the same as those of the first cycle (Figure 6.9, 6.10, and 6.11). The second hysteresis loops at low target Π (Π below the formation of the LC phase) completely retrace the first hysteresis isotherm (Figure 6.9).

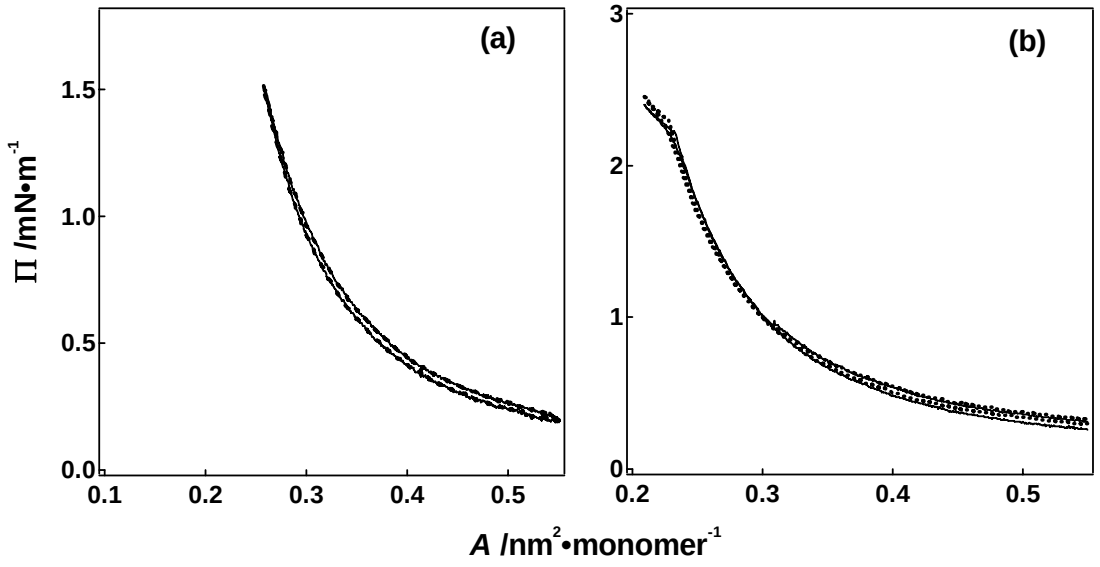

Figure 6.9: Two cycle hysteresis experiments for M_n = 12.9 kg•mol^{-1} PLLA Langmuir films before the formation of condensed phases at T = 22.5 ^{o}C. Target Π values of: (a) 1.5 and (b) 2.2 mN•m^{-1} (LE/LC plateau). The solid lines represent hysteresis loops for the first cycle, and the dotted lines represent hysteresis loops for the second cycle. No area loss is observed between the first and second loops.

For target Π greater than the transition Π for the LE/LC phase transition, the second compression isotherms do not retrace the first compression cycle. Instead, they shift to smaller A values relative to the initial compression isotherm (Figure 6.10). Possible reasons for the area shifts may be that some molecules are "lost" during the first hysteresis cycle.[293-295] Incomplete respreading of aggregates may also lead to area loss.[296-298] The moving barriers of the trough may induce the orientation of PLLA molecules causing pressure gradients, hence some monolayer areas may not fully recover

upon expansion.[299,300] It is observed that the area loss increases with target Π values (Table 6.3). The area losses at Π = 4.0, 7.0, and 8.0 (plateau) mN•m^{-1} are quite similar, suggesting that the monolayer/bilayer transition may be somewhat reversible so long as one does not compress too deeply into the collapsed region.

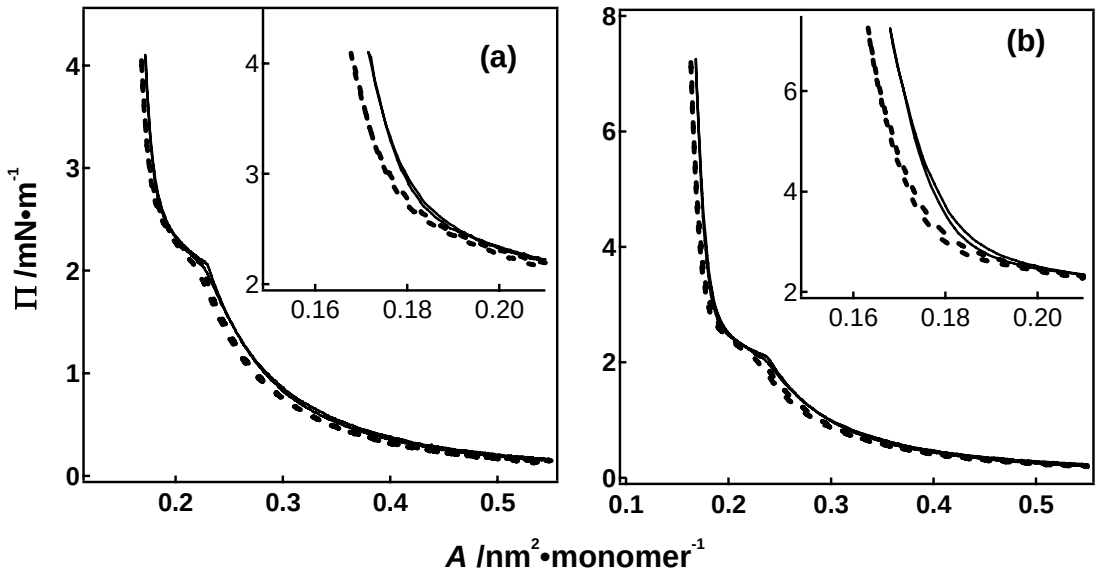

Figure 6.10: Two cycle hysteresis experiments for M_n = 12.9 kg•mol^{-1} PLLA Langmuir films in the condensed phase at T = 22.5 ^{o}C. Target Π values of: (a) 4.0 and (b) 7.0 mN•m^{-1}. The solid lines represent hysteresis loops for the first cycle, and the dashed lines represent hysteresis loops for the second cycle. Small area losses are observed between the first and second cycles, and are highlighted in the insets.

After the formation of thicker multilayers (upturn in Π following compression through the plateau at Π = 8.0 mN•m^{-1}), area losses almost double, suggesting that

thicker multilayers may be more inhibited to completely respread onto the subphase (Figure 6.11). Nonetheless, the area loss is not remarkable.[153,223,301] The largest area loss is less than 6 % when the second hysteresis cycle immediately follows the first as shown in Table 6.3. During the second expansion, the respreading of the multilayer aggregates, the coexistence of bilayer and monolayer, and the formation of a nearly homogeneous monolayer are also observed. Pausing between the two hysteresis loops shows that the second hysteresis loop with and without a 60 minute pause is almost identical (Figure 6.12), suggesting that the respreading of PLLA molecules onto the subphase is essentially complete after the expansion process and is unaffected by waiting between the two cycles.

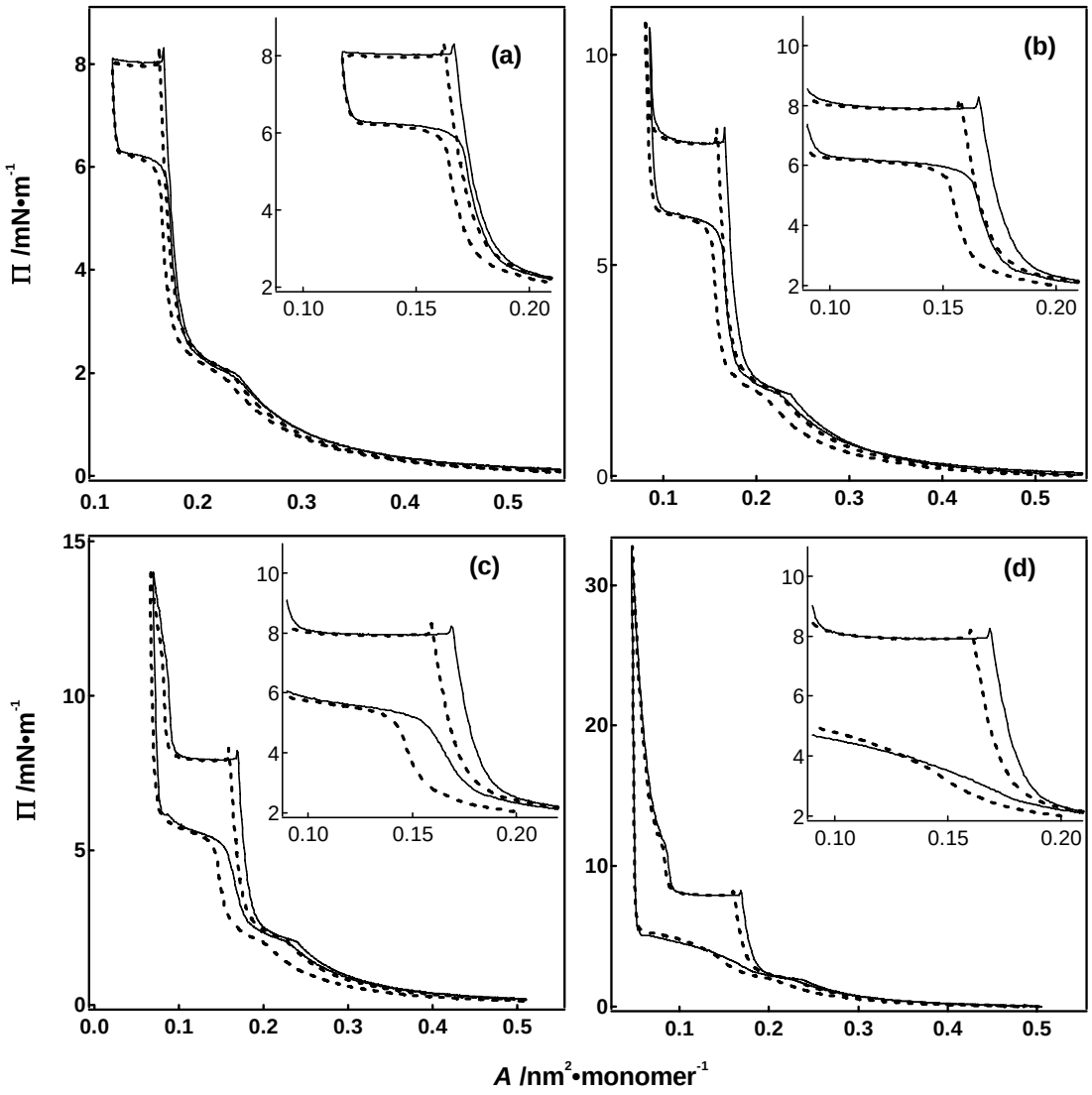

Figure 6.11: Two cycle hysteresis experiments for M_n = 12.9 kg•mol^{-1} PLLA Langmuir films after collapse at T = 22.5 ^{o}C. Target Π values of: (a) 8.0 (monolayer-bilayer coexistence plateau), (b) 10.5, (c) 14.0, and (d) 32.0 mN•m^{-1}. The solid lines represent hysteresis loops for the first cycle, and the dashed lines represent hysteresis loops for the second cycle. Area losses are highlighted in the insets and listed in Table 6.3.

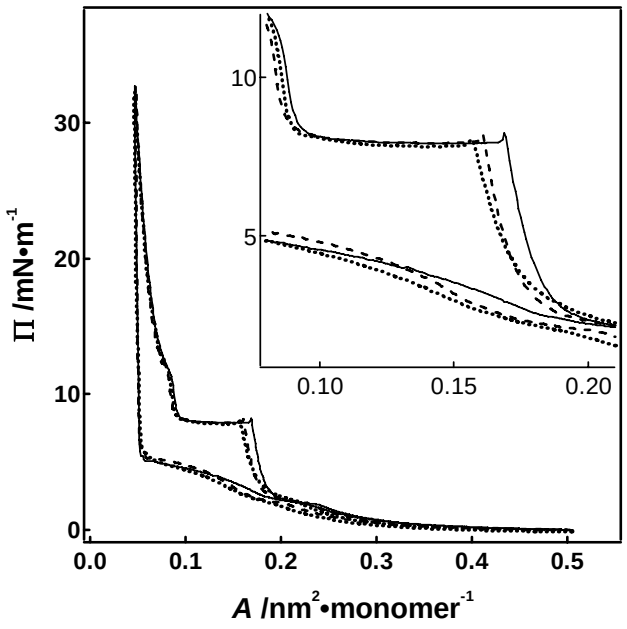

Figure 6.12: Two cycle hysteresis experiments for M_n = 12.9 kg•mol^{-1} PLLA Langmuir films at Π = 32.0 mN•m^{-1} and T = 22.5 ^{o}C with and without a 60 minute pause between the two cycles. The solid line is hysteresis loop obtained during the first cycle. The dashed line corresponds to second hysteresis loop which was obtained immediately following the first cycle. The dotted line represents second hysteresis loop which was obtained one hour after the first cycle. No significant differences are observed between the second hysteresis isotherms, suggesting that respreading of the PLLA molecules onto the subphase is essentially complete at the end of the first expansion step.

In addition, different time intervals are also applied between the compression and expansion processes. The choice of time intervals are on the basis of the relaxation experiments as shown in Figure 6.13. For a relaxation experiment at Π = 36.0 mN•m^{-1},

the sharp decrease in Π (to Π ≈ 25 $mN \bullet m^{-1}$) occurs in the first 5 minutes, and then Π decays more gradually to Π ≈ 20 $mN \bullet m^{-1}$ over the next 30 minutes. At longer times, Π achieves a nearly constant value of Π ≈ 12.5 $mN \bullet m^{-1}$. Figure 6.14 shows hysteresis experiments with waiting time intervals of 0, 1, 15, 45, 120, and 420 minutes between the compression and expansion steps of the first hysteresis cycle. The results are summarized in Table 6.4. As the pause between the first compression and expansion process increases, the area loss between the first and second hysteresis cycles increases, suggesting that during the Π relaxation process, multilayers are reorganizing to form structures that are more difficult to be respread onto the subphase during the expansion process.

In summary, normal hysteresis experiments support the conclusion that almost all PLLA molecules can respread onto the subphase after the expansion of the film irregardless of the number of hysteresis cycles performed. However, allowing time between compression and expansion does lead to aggregates that inhibit respreading at the A/W interface.

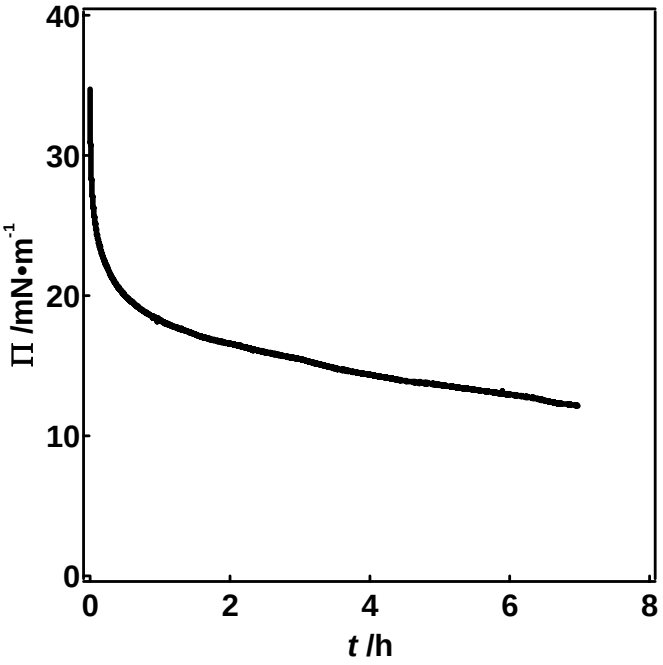

Figure 6.13: Π relaxation experiment (Π vs *t* curve) for M_n = 12.9 kg•mol^{-1} PLLA Langmuir films at 36.0 mN•m^{-1} at 22.5 ^{o}C.

Table 6.4: Results for hysteresis experiments of M_n = 12.9 kg•mol^{-1} PLLA Langmuir films with different time intervals between the first compression and expansion processes during the first hysteresis cycle at Π = 36.0 mN•m^{-1} and T = 22.5 ^{o}C.

time interval (min)	**0**	**1**	**15**	**45**	**120**	**420**
A shift × 10^3 (nm^2•monomer^{-1})[a]	**10.8**	**18.2**	**19.6**	**21.6**	**28.7**	**28.8**
Area loss (× 100 %)	**6.0**	**10.1**	**10.9**	**12.0**	**15.9**	**16.0**
$\Pi_{plateau,e}$ 1st expansion (mN•m^{-1})[b]	**4.7**	**4.7**	**4.2**	**2.8**	**2.5**	**3.2**
$\Pi_{plateau,e}$ 2nd expansion (mN•m^{-1})[b]	**5.2**	**5.1**	**5.3**	**5.1**	**5.7**	**5.2**

[a] Area shifts stand for the differences between the monomer areas at the target Π

[b] $\Pi_{plateau,e}$ value at which the plateau starts to appear during expansion

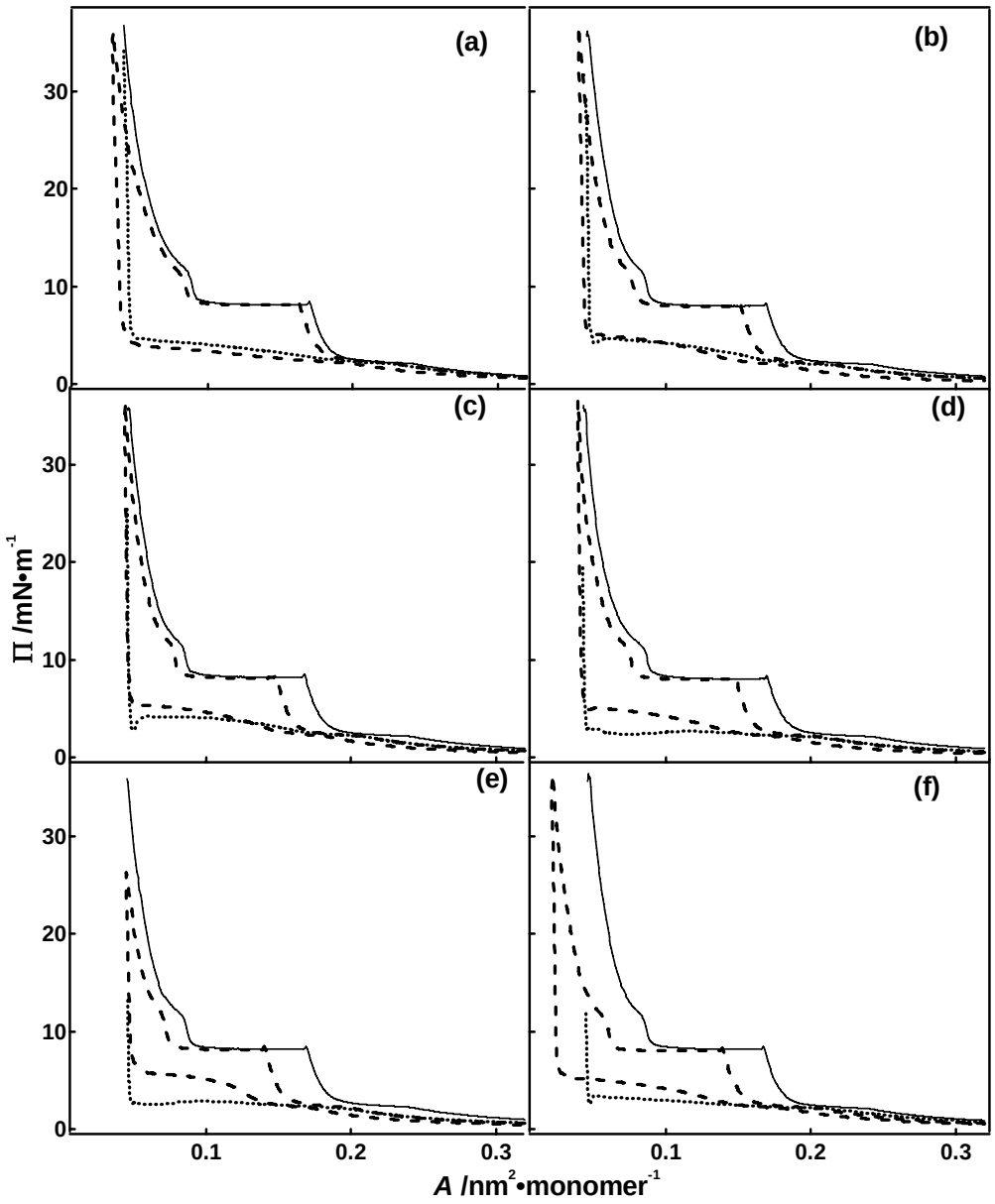

Figure 6.14: Two cycle hysteresis loops for M_n = 12.9 kg•mol^{-1} PLLA Langmuir films with different time intervals between the compression and expansion processes of the first hysteresis cycle at T = 22.5 ^{o}C. Target Π = 36.0 mN•m^{-1}, with time intervals of: (a) 0, (b) 1, (c) 15, (d) 45, (e) 120, and (f) 420 minutes. The solid line represents the compression isotherm during the first hysteresis cycle, the dotted line represents the expansion isotherm during the first hysteresis cycle, and the dashed line represents the isotherm during the second hysteresis cycle. During the first hysteresis experiments with a pause between the compression and expansion stage, the isotherms are discontinuous because of Π relaxation.

6.3.2 "Slow-Collapse" – Nucleation and Growth

As discussed in the first part of this chapter, buckling and stacking of PLLA lamellae on top of the lamellar monolayer is the mechanism of collapse during constant compression rate experiments. No obvious proof is observed in AFM images showing the nucleation and growth of 3D structures or a "slow collapse" process. The absence of the nucleation and growth mechanism is possible in constant compression rate experiments. If the compression rate is much faster than the nucleation rate of stable 3D critical nuclei or the subsequent growth process, monolayer collapse will be achieved by buckling and stacking. If the compression rate is slower than the nucleation rate for the formation of stable 3D critical nuclei and the subsequent growth rate for 3D structures, the nucleation and growth mechanism may lead to 3D structures different from those obtained through the buckling and stacking mechanism. In this portion of the chapter, "slow collapse" of PLLA Langmuir films is examined through isobaric area relaxation experiments.

6.3.2.1 The Vollhardt Model

As a 2D analogy to the Avrami model used in polymer crystallization studies,[302-304] Vollhardt applies a nucleation and growth mechanism to describe 2D to 3D collapse processes in metastable Langmuir monolayers under the assumption of ideal homogeneous nucleation.[274-276] The collapse rate is described by the convolution of the nucleation and growth rates. The effect of overlapping growth centers also contribute to the collapse rate during the growth process. Two typical homogeneous nucleation

modes are considered in the Vollhardt model, instantaneous nucleation leading to monodisperse centers (Figure 6.15a) and progressive nucleation leading to polydisperse centers (Figure 6.15b). The geometry of the nucleation centers could be hemispheres (Figure 6.16a) or cylinders (Figure 6.16b), and the growth of the centers could be from the edges(Figure 6.17a) or basal areas (Figure 6.17b).

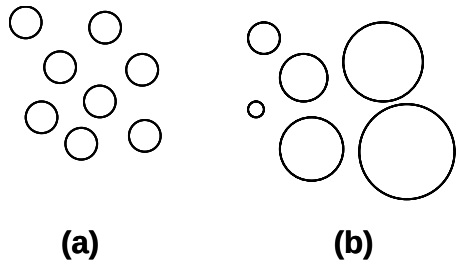

Figure 6.15: Schematic of nucleation modes considered in the Vollhardt model: (a) instantaneous nucleation leading to monodisperse centers and (b) progressive nucleation leading to polydisperse centers.[274-276]

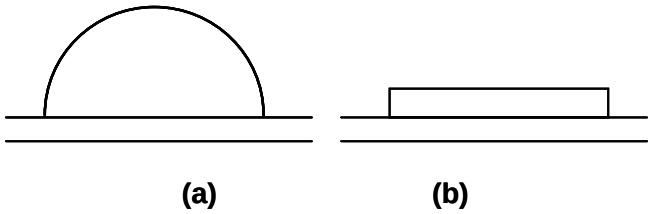

Figure 6.16: Geometry of the nucleation centers in the Vollhardt model: (a) hemisphere and (b) cylinder.[274-276]

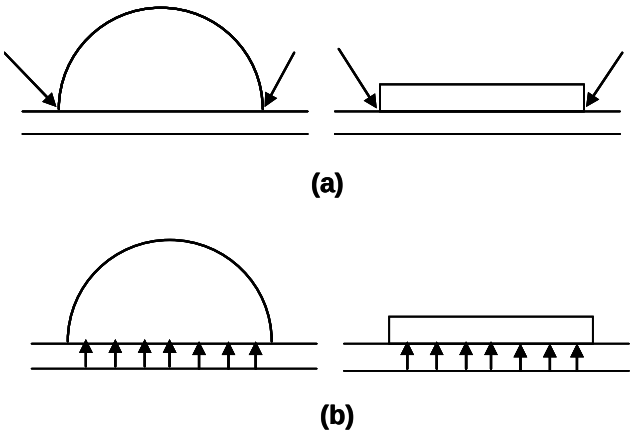

Figure 6.17: Growth mechanism of the nucleation centers: (a) from the edges and (b) from the basal areas in the Vollhardt model.[274-276]

The Vollhardt model leads to an expression describing the overall nucleation and growth rate allowing for overlapping centers (Equation 6.1)

$$z = \frac{A_i - A(t)}{A_i - A_\infty} = 1 - \exp\left[-K_x\left(t - t_i\right)^x\right] \qquad \text{(Eq. 6.1)}$$

where z is the real normalized area of the monolayer, A_i is the area per monomer at the start of the isobaric experiments, $A(t)$ is the area per monomer at time t on the basis of the surface concentration, A_∞ is the area per monomer for t goes to infinity, K_x is a model specific constant for different nucleation and growth models, x is a characteristic quantity obtained from isobaric area relaxation experiments for a specific nucleation model, and t_i is the amount of time for the induction of the nucleation.[274-276]

6.3.2.2 Isobaric Area Relaxation Experiments

Figure 6.18 shows isobaric area relaxation curves at different Π prior to $\Pi_{collapse}$ for M_n = 12.9 kg•mol^{-1} PLLA Langmuir films at 22.5 ^{o}C. The isobaric area relaxation

curves obtained at different Π have similar shapes and exhibit a plateau prior to a dramatic decrease in *A(t)*. However, the length of the plateau decreases with increasing Π. Another plateau is observed at the end of relaxation experiments corresponding to A_∞. Interestingly, all isobaric area relaxation curves approach similar A_∞ values independent of A_i, suggesting that similar structures are formed. This feature will be discussed shortly. Furthermore, the isobaric area relaxation experiments at different Π have different time scales. For example, at Π = 5.7 $mN \bullet m^{-1}$, a long plateau is observed prior to the dramatic decrease in area and the isobaric area relaxation process takes about 50 hours. At Π = 7.5 $mN \bullet m^{-1}$, almost no plateau is observed prior to the dramatic decrease in area and the isobaric area relaxation process takes ~ 1 hour.

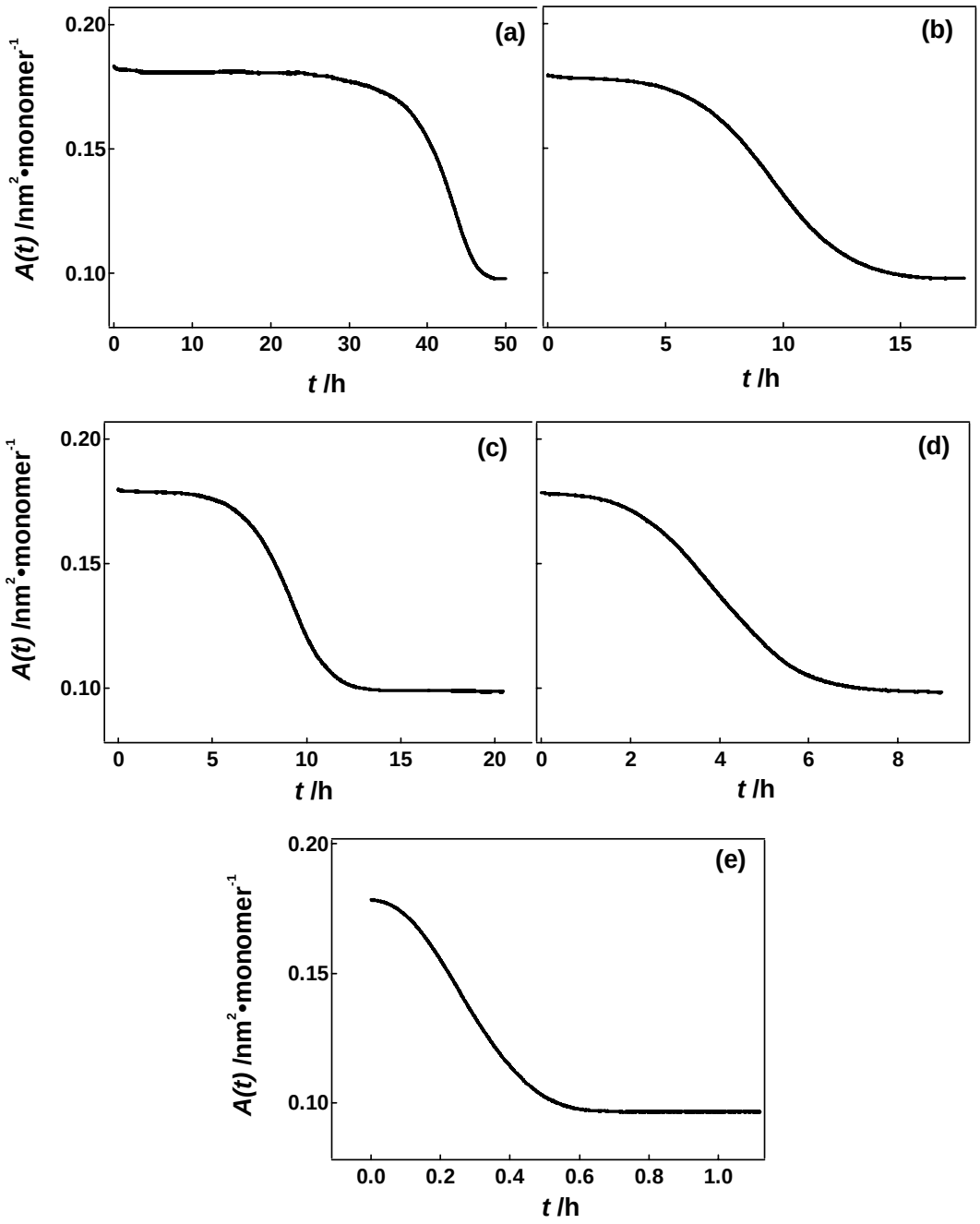

Figure 6.18: $A(t)$ versus t curves for M_n = 12.9 kg•mol^{-1} PLLA Langmuir films at T = 22.5 ^{o}C during isobaric area relaxation experiments at various Π values: (a) 5.7, (b) 6.6, (c) 6.9, (d) 7.2, and (e) 7.5 mN•m^{-1}. As Π increases, the length of the plateau prior to the dramatic decrease in *A(t)* becomes shorter and the area relaxation process takes less time.

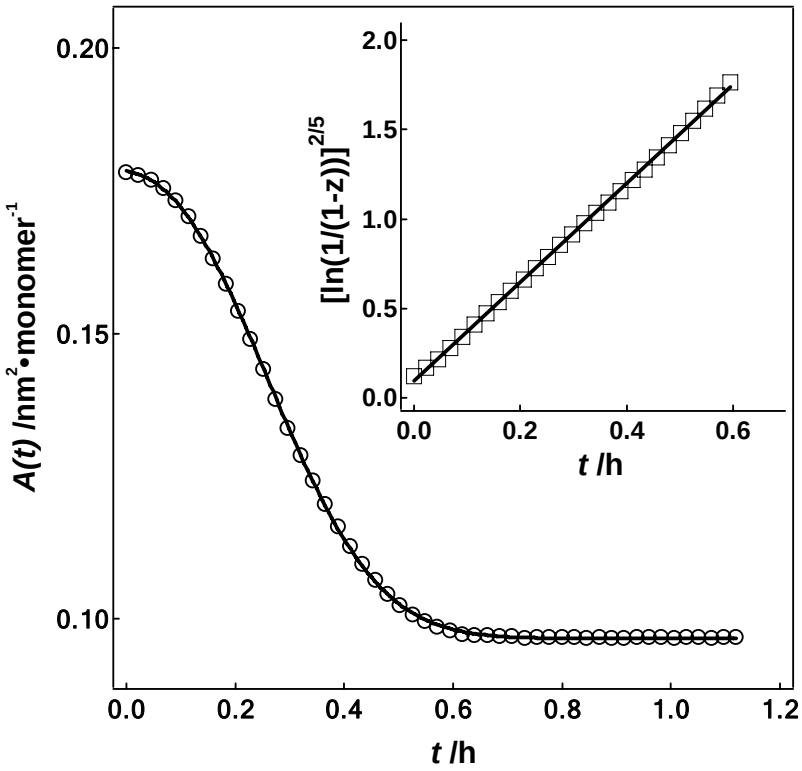

Figure 6.19: $A(t)$ versus t for M_n = 12.9 kg•mol^{-1} PLLA Langmuir films at T = 22.5 ^{o}C during isobaric area relaxation experiments at Π = 7.5 mN•m^{-1} (circles) along with the fitting result for progressive nucleation with hemispherical edge growth (x = 2.5 according to Equation 6.1, solid line). The solid line in the inset represents the evaluation of the best linear fit according to Equation 6.2.

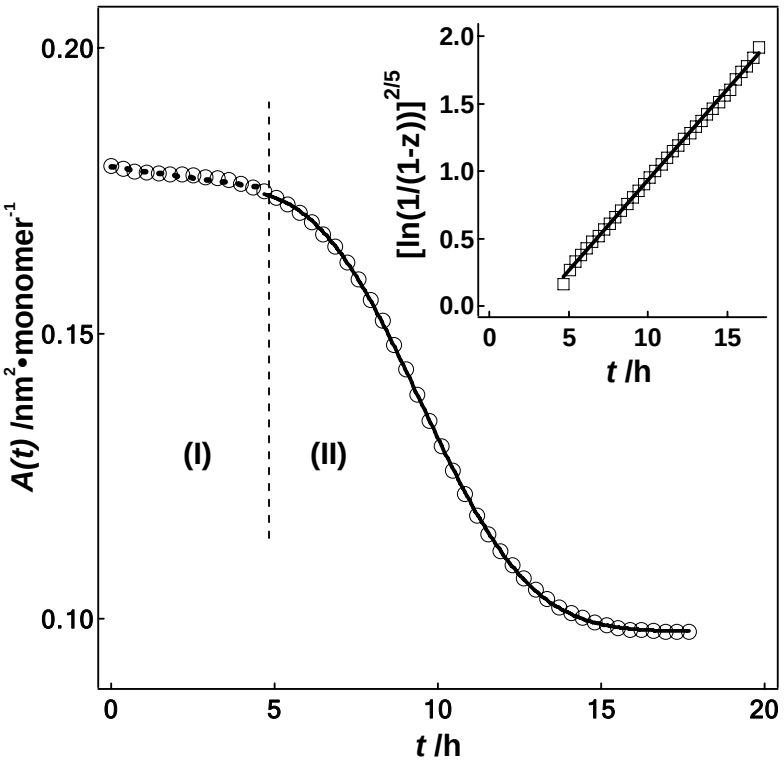

Figure 6.20: $A(t)$ versus t for M_n = 12.9 kg•mol^{-1} PLLA Langmuir films at T = 22.5 ^{o}C during isobaric area relaxation experiments at Π = 6.6 mN•m^{-1} (circles). Linear fit (dashed line) in region (I) yields the rate of area decrease because of the rearrangement of PLLA molecules in the LC phase (0.00064 ± 0.00004 nm^2•monomer^{-1}•h^{-1}). The area relaxation curve in region (II) is fit with the Vollhardt model (solid line), suggesting instantaneous nucleation with hemispherical growth from basal areas (x = 3 according to Equation 6.1). The solid line in the inset represents the evaluation of the best linear fit according to Equation 6.2.

Fitting the experimental results directly with the Vollhardt model may yield misleading results. For instance, fitting the isobaric area relaxation curve obtained at Π = 7.5 $mN \bullet m^{-1}$ with the Vollhardt model yields complete agreement (Figure 6.19); however, the isobaric area relaxation curve obtained at Π = 6.6 $mN \bullet m^{-1}$ can only be partly fit with the Vollhardt model (Figure 6.20). The plateau prior to the dramatic decrease in *A(t)* can not be fit with the Vollhardt model. One may suggest that the plateau is the induction period of the nucleation; however, the suggestion can be unreliable in two respects: (1) the induction time of the nucleation has been considered in the Vollhardt model (Equation 6.1), hence it should be possible to fit the plateau if the Vollhardt model is correct; (2) although the length of the plateau varies with Π values, all plateaus end at similar *A(t)* values (~ 0.178 $nm^2 \bullet monomer^{-1}$), as seen in Figure 6.18. We suggest that the "slow collapse" of PLLA Langmuir monolayers during the isobaric area relaxation experiments consist of two processes: (1) the rearrangement of PLLA molecules into the most closely packed condensed (LC) phase with well-ordered alignment; and (2) the nucleation of highly ordered features that grow into 3D structures. The first process can be thought of as an ordering process for a certain range of Π values, and the second process can be fit with the Vollhardt nucleation and growth model.

During the first process, the rearrangement of PLLA molecules into the most closely packed condensed phase causes the area per monomer to decrease. However, after the LE/LC phase transition, PLLA molecules have been ordered at the A/W interface. Therefore the area decrease due to the rearrangement of PLLA molecules in the LC phase

into the most closely packed condensed phase is very small (generally from 0.185 to 0.178 $nm^2 \bullet monomer^{-1}$), resulting in a plateau in the *A(t)* versus *t* curve. It is reasonable to suggest that the more the monolayer has been compressed into the LC phase, the less time it will take for PLLA molecules to rearrange at the A/W interface into the most closely packed condensed phase. If the monolayer has been compressed into the most closely packed condensed phase, there will be no decrease in area because of molecular rearrangement and therefore no plateau. This feature is observed for isobaric area relaxation curves obtained at Π = 7.5 $mN \bullet m^{-1}$, where the monolayer immediately nucleates and grows to 3D structures upon compression to the target pressure.

The rearrangement of molecules into the most closely packed condensed phase at various Π values are observed in Figure 6.18. The rate of rearrangement can be evaluated from the length of the plateau (t_{arr}). It is also possible to compare the rate of area decrease, r_A. r_A values at certain Π can be obtained from the linear fit of the plateau. For instance, the rearrangement of PLLA molecules in the condensed phase into the most closely packed condensed phase at Π = 6.6 $mN \bullet m^{-1}$ takes about 4 hours, corresponding to $r_A = 0.00064 \pm 0.00004$ $nm^2 \bullet monomer^{-1} \bullet h^{-1}$ (Figure 6.20). It is observed that r_A values increase with Π , as summarized in Table 6.5.

PLLA Langmuir monolayers undergo nucleation and growth process after the molecules are in the most closely packed condensed phase. This process can be fit with the Vollhardt model. Figure 6.20 shows the fitting of the experiment data at Π = 6.6 $mN \bullet m^{-1}$ in region (II) with the Vollhardt model described in Equation 6.1. The value of

the characteristic exponent, x, is determined to be 2.94 ± 0.08, suggesting an instantaneous nucleation with hemispherical growth from basal area. Another approach is also applied to fit the results. Different nucleation mechanisms with different x exponents have been evaluated by converting Equation 6.1 into a linear relationship and fitting the experimental data:

$$\left[\ln\frac{1}{1-z}\right]^{1/x} = K_x^{1/x}(t-t_i) \qquad \text{(Eq. 6.2)}$$

The best fitting model (in the inset of Figure 6.20) corresponds to instantaneous nucleation with hemispherical edge growth (x = 3), while the other models, i.e. x = 1.5, instantaneous nucleation with hemispherical edge growth, x = 2.5, progressive nucleation with hemispherical edge growth, and x = 4, progressive nucleation with hemispherical growth from basal areas, deviate substantially from the experimental data.

The isobaric area relaxation curves obtained at Π = 5.7, 6.9, and 7.2 mN•m^{-1} are analyzed with two processes as described in the proceeding paragraph for Π = 6.6 mN•m^{-1}. The fitting results with one standard deviation error bars for the best fit are summarized in Table 6.5. The isobaric area relaxation curves obtained at Π = 7.5 mN•m^{-1} are fit directly with the Vollhardt model, as shown in Figure 6.19 and the fitting results are also included in Table 6.5.

Table 6.5: Coefficients obtained from fitting the isobaric area relaxation experiments for PLLA Langmuir monolayer at various Π values and T = 22.5 ^{o}C with Vollhardt's model.

Π^{a}	r_A ($\times 10^{-4}$)^{b}	A_i ^{c}	A_∞ ^{c}	K_x ^{d}	t_i (h)	x
5.7	**0.073**	**0.172**	**0.096**	**3.3× 10^{-5}**	**31.0**	**4.1**
	± 0.001	± 0.001	± 0.001	± 0.1× 10^{-5}	± 0.8	± 0.2
6.6	**0.64**	**0.175**	**0.098**	**0.0028**	**6.1**	**2.94**
	± 0.04	± 0.001	± 0.001	± 0.0009	± 0.3	± 0.08
6.9	**0.90**	**0.172**	**0.099**	**0.009**	**4.9**	**2.98**
	± 0.07	± 0.001	± 0.001	± 0.0004	± 0.3	± 0.08
7.2	**1.7**	**0.177**	**0.099**	**0.014**	**0.24**	**2.96**
	± 0.2	± 0.002	± 0.001	± 0.002	± 0.06	± 0.07
7.5	**NA**	**0.179**	**0.097**	**12.3**	**-0.31**	**2.46**
		± 0.001	± 0.001	± 0.1	± 0.01	± 0.04

Units: ^{a} mN•m^{-1}; ^{b} nm^{2}•monomer^{-1}•h^{-1}; ^{c} nm^{2}•monomer^{-1}; ^{d} h$^{-1/x}$.
Error bars represent ± one standard deviation.

As seen in Table 6.5, the nucleation and growth process starts at similar initial areas (A_i = 0.175 nm^{2}•monomer^{-1}) and ends at similar limiting areas (A_∞ = 0.098 nm^{2}•monomer^{-1}) for isobaric area relaxation experiments at all Π values in the metastable monolayer region. The limiting area value (A_∞) is one-half of the A value corresponding to monolayer formation, suggesting that "slow collapse" results in the formation of a bilayer, supporting our conclusion in the first part of this chapter that the plateau after the collapse in the Π-A isotherms during the constant compression rate experiments is the coexistence of monolayer and bilayer.

x values obtained from the fitting isobaric area relaxation data with Vollhardt's model can be used to predict the nucleation and growth mechanism, as listed in Table 6.6. The data are consistent with PLLA monolayers undergoing different nucleation and growth mechanisms at different Π values in the metastable region. For instance, at Π = 5.7 $mN \bullet m^{-1}$, the fitting results suggest progressive nucleation of hemispheres with 3D structures growing from the basal areas; at Π = 6.6, 6.9, and 7.2 $mN \bullet m^{-1}$, instantaneous nucleation of hemispheres and growth from the basal areas are predicted; and at Π = 7.5 $mN \bullet m^{-1}$, Vollhardt's model is consistent with progressive nucleation of hemispheres and edge growth. The observation that as Π increases, the growth of 3D structures changes from the basal areas to the edges is reasonable. At lower Π values, PLLA molecules may have more time to diffuse within the plane to grow from the basal area. At Π close to $\Pi_{collapse,}$ the isobaric area relaxation process is more like a constant compression rate experiment, where PLLA does not have sufficient time to diffuse into the basal areas before encountering the edges of the growing 3D structures. On the basis of this explanation, it is also reasonable to suggest that the nucleation mode at lower Π would have longer induction time forming monodisperse centers, while at higher Π progressive nucleation of polydisperse centers are expected. This is confirmed in Table 6.6 for isobaric area relaxation experiments at Π = 6.6, 6.9, 7.2, and 7.5 $mN \bullet m^{-1}$. It should be noted that the fitting results at Π = 5.7 $mN \bullet m^{-1}$ do not support our conclusion. One possible reason for this conflict is that the isobaric area relaxation experiment at Π = 5.7

$mN \bullet m^{-1}$ takes about 50 hours. Evaporation of the subphase over such a long experimental period could influence the observed experimental results.

Table 6.6: Predicted nucleation and growth mechanisms for isobaric experiments of PLLA Langmuir monolayers at different Π and T = 22.5 °C.

Π ($mN \bullet m^{-1}$)	x	Geometry of Centers	Nucleation	Growth
5.7	4	Hemisphere	Progressive	Basal area
6.6	3	Hemisphere	Instantaneous	Basal area
6.9	3	Hemisphere	Instantaneous	Basal area
7.2	3	Hemisphere	Instantaneous	Basal area
7.5	2.5	Hemisphere	Progressive	Edge

The difference in K_x values indicates that for the same nucleation and growth mechanism, the closer the monolayer is to the collapse, the faster the growth occurs. This is reasonable, because K_x represents the convolution of the nucleation and the growth rates, both of which increase with Π for isobaric area relaxation experiments. This conclusion is also in agreement with the time scale of the completion of the isobaric experiments at different surface pressures.

It is interesting to compare the calculated induction times (t_i) obtained from fitting the data with the Vollhardt model for PLLA Langmuir monolayers undergoing isobaric area relaxation at different Π. It is observed that as Π increases, t_i values decrease. When Π is close to $\Pi_{collapse}$ (in the case of Π = 7.5 $mN \bullet m^{-1}$), t_i values are negative, indicating that nucleation starts during the compression prior to reaching the target Π for Π close to

$\Pi_{collapse}$. Another feature that should be addressed is the comparison of the induction time with the time for the rearrangement of PLLA molecules into the most closely packed phase (t_{arr}) that we suggested was the first step of the isobaric area relaxation experiments. It is found that t_i is always a little smaller than t_{arr}, suggesting that there is no distinct boundary between the rearrangement process and the nucleation and growth process. The isobaric area relaxation processes may include a molecular rearrangement process, a combination of molecular rearrangement along with the induction of nucleation, and the nucleation and growth process. We do not believe that the rearrangement process is the same as the induction process envisioned by Vollhardt as the model does not fit the plateau. Indeed, in isobaric area relaxation experiments of octadecanoic acid Langmuir monolayers, Vollhardt fit his experimental results with the model, and the fit does not include the plateau.[275] He did not provide a reason for why the model did not fit the plateau.

In order to verify the suggestion that the isobaric area relaxation processes are a combination of several processes, imaging techniques should be used. Unfortunately, in-situ BAM experiments failed to provide any morphological features during the experiments. This feature is attributed to contrast and lateral resolution limitations of our BAM instrument, as discussed in the constant compression rate experiments. It may be possible to explore the morphological differences in isobaric area relaxation experiments at different Π through LB-films and AFM. These experiments are suggested as future work in Chapter 8.

6. 4 Conclusions

In summary, Π-*A* isotherms and BAM measurements show that, with continuously increasing surface pressure *via* compression, PLLA Langmuir films undergo monolayer, bilayer, and multilayer transitions at the A/W interface at room temperature. Different surface morphologies are observed along with the phase transitions. The collapse process during constant compression rate experiments involves the buckling and stacking of lamellae consisting of PLLA single molecule helices. Upon expansion, the aggregates respread onto the subphase, leading to well-ordered lamellar features that are similar to those observed in the LC monolayer. On the other hand, isobaric area relaxation experiments reveal "slow collapse" through a nucleation and growth mechanism. In contradiction to the model proposed by Vollhardt, we propose PLLA Langmuir monolayers undergo a rearrangement into a most closely condensed phase prior to the nucleation and growth of 3D structures. While the rearrangement of PLLA molecules qualitatively could be considered as an induction process, the Vollhardt model can not quantitatively fit this portion of the isobaric area relaxation experiments.

PLLA Langmuir monolayers can be a good model for studying the nucleation and growth mechanisms for several reasons: (1) a rearrangement process could correspond to the alignment of rigid rod-like PLLA helices in the LC phase prior to the nucleation and growth of 3D aggregates from the metastable monolayer; (2) isobaric area relaxation experiments may result in different surface morphologies if the substrates are prepared at different *A(t)*. More importantly, a perfect bilayer structure may be obtained at the end

of the area relaxation process; (3) unaligned PLLA helices in the LE phase at a temperature above the critical temperature of the LE/LC phase transition (described in Chapter 4) may undergo a different nucleation and growth mechanism.

CHAPTER 7

Characterization of Highly Order Poly(L-lactic acid) Langmuir-Blodgett Films by Infrared Spectroscopy

7.1 Abstract

Reflection absorption infrared spectroscopy (RAIRS) results confirmed the existence of poly(L-lactic acid) (PLLA) 10_3-helices at all surface concentrations after spreading during the phase transitions in Langmuir films at the air/water interface as described in Chapter 6. In this chapter, RAIRS is used to explore the crystalline character of PLLA Langmuir-Blodgett (LB) films prepared from various film states. Although PLLA LB-films prepared in different Langmuir film states have different surface roughnesses, RAIRS results suggest that they have similar helical contents. Moreover, the helical content of the as-prepared LB-films is relatively high compared to the PLLA bulk samples and thermally recrystallized spin-coated films. RAIRS is also used to study thermally annealed PLLA LB-films. The highly crystalline features in LB-films can be destroyed by heating the films above the bulk melting temperature of PLLA. Annealing studies by RAIRS are completely consistent with the proposed structure of highly oriented 10_3-helices. Our results provide strategies for fabricating PLLA substrates with controlled surface morphology and crystallinity that may be suitable for cell adhesion studies. Furthermore, PLLA LB-films can also serve as model systems for examining the crystallization behavior of a biodegradable polymer in ultra-thin confined structures.

7.2 Introduction

The crystallization behavior of poly(L-lactic acid) (PLLA) has attracted considerable interest because of its effects on the biodegradable and biocompatible properties of PLLA. Until now, three different PLLA crystal forms (α, β, and γ) have been reported. The α-form is believed to grow during cold- or melt-crystallization processes and has a 10_3 helical chain conformation.[142,145] The β-form was first found in solution-spun fibers,[142,305,306] and can also be obtained at a high draw ratio and high drawing temperature. PLLA molecules in β crystals exist in a left-handed 3_1 helical conformation. A new γ-form was obtained through epitaxial crystallization by Cartier *et al.*[307]

Conventional crystallization research on PLLA was conducted for bulk systems and/or in thin films on the order of several hundred nanometers to several hundred micrometers at a temperature near the crystallization temperature (T_x) for crystals formed from dilute solutions or melts.[149] Lamellar single crystals of PLLA have been observed by several research groups. For example, lamellar crystals with a lamellar thickness of around 10 nm were grown from dilute solutions in toluene and p-xylene by Kalb *et al.*,[150] lozenge-shaped crystals were produced from acetonitrile solution by Miyata *et al.*,[151] and more recently both lozenge- and hexagonal-shaped single crystals were obtained from dilute solutions in p-xylene by Iwata *et al.*[152] Such crystallization research on PLLA can be extended to monolayer studies in two dimensions (2D) at the air/water (A/W) interface. The crystallization environment at the A/W interface (crystallization temperature, solvent,

etc.) and the film state are different from conventional crystallization studies. One of the principle advantages of conducting PLLA crystallization studies at the A/W interface is that the experimental temperature is well below temperatures where thermal degradations are common. Several semicrystalline polymers have been examined at the A/W interface and the formation of crystals has been reported. For example, isotactic poly(methyl methacrylate) (i-PMMA) forms a 10_1 double helix at the A/W interface.[153,154] Poly(ε-caprolactone) (PCL) forms dendritic crystals at the A/W interface at room temperature.[135] PLLA exists as 10_3-helices at the A/W interface at all surface concentrations as described in Chapters 5 and 6. PLLA and poly(D-lactic acid) (PDLA) blends spontaneously form 10_3-helices at the A/W interface in the liquid-like phase; however, in the solid-like state the PLLA/PDLA stereocomplex forms 3_1-helices.[155,156,223]

Various techniques have been applied to examine the crystallization behavior of PLLA, such as spectral techniques (vibrational spectroscopy),[308] optical microscopy, atomic force microscopy (AFM), electron microscopy, scattering techniques, calorimetric methods, etc.[308] Among the spectral techniques, Raman and infrared spectroscopy (IR) can explore variations in: (a) conformation, (b) degree of crystallinity, (c) nature of crystalline and non-crystalline order, and (d) intra- and intermolecular interactions.[309-311] It is also possible to predict molecular symmetry because IR and Raman are collected following selection rules. Raman and Fourier transform infrared (FTIR) spectroscopy have been applied to examine the crystallization process of some semicrystalline

polymers, such as polyethylene (PE),[312] isotactic polypropylene (i-PP),[313] isotactic polystyrene (i-PS),[314] etc.

Several important papers have been published concerning the IR and Raman spectra of poly(lactic acid) (PLA). For example, Kister *et al.* investigated the effects of morphology and conformation of PLA on IR and Raman spectra. Kang *et al.* utilized Raman spectroscopy to characterize disordered structures of PLA.[315] Recently, Zhang *et al.* published a series of papers discussing the IR spectral differences of PLLA during cold-crystallization and melt-crystallization processes.[248-252] Their results suggested that different forms of chain packing occur during these two processes. The authors also examined the effect of the crystallization temperature on the IR spectra, proposing that different crystal structure of PLLA samples were formed after annealing at different temperatures. For instance, cold-crystallization at 78 ^{o}C resulted in PLLA α crystals with a 10_3 helical conformation. Melt-crystallization at temperature below 120 ^{o}C may leads to PLLA α crystals with "distorted" 10_3-helices having a different packing of the helical chains compared to standard α crystals, while melt-crystallization above 120 ^{o}C leads to the formation of PLLA α crystals.

IR studies have also been conducted on PLLA Langmuir films. For instance, PLLA and PLLA/PDLA mixtures have been examined as Langmuir monolayers at the A/W interface by polarization-modulation infrared reflection-absorption spectroscopy (PM-RAIRS).[155,156,223] In this chapter, PLLA Langmuir-Blodgett (LB) films prepared in different film states are examined by RAIRS. The effect of thermal annealing

treatments are also probed by RAIRS. Our results provide some insight into the crystallization behavior of PLLA in ultra-thin films.

7.3 Results and Discussion

7.3.1 Comparison of RAIRS Spectra Obtained with Different Spectrometers

As stated in Chapter 3, RAIRS spectra are obtained with two different spectrometers: a Bruker IFS 66v/D spectrometer operated under vacuum, and a nitrogen purge Nicolet NEXUS 670 FT-TR spectrometer. RAIRS spectra of a 5 cycle M_n = 12.9 kg•mol^{-1} PLLA LB-films prepared at 7.0 mN•m^{-1} and 22.5 ^{o}C obtained with these two spectrometers are shown in Figure 7.1. RAIRS spectra obtained from both spectrometers have identical band positions and similar band intensities in the range of 2000 – 1000 cm^{-1}. The spectra obtained with the Bruker IFS 66v/S spectrometer under vacuum have almost no water vapor interference; however, the MCT (mercury-cadmium-telluride) detector leads to poor signal detection at low wavenumbers (< 1000 cm^{-1}) with this instrument, as shown in Figure 7.1a. For RAIRS spectra obtained with the nitrogen purge Nicolet NEXUS 670 FT-IR spectrometer, water vapor may be present and leads to both positive and negative bands in the range from 2000 - 1400 cm^{-1} depending on how long the system is purged; however better signal detection at low wavenumbers (< 1000 cm^{-1}) is afforded by the Nicolet MCT detector (Figure 7.1b). Nonetheless, RAIRS spectra obtained with both spectrometers are essentially the same, and there is no obvious reason to suggest that one of the two units is better. In this

chapter, RAIRS spectra obtained with the Bruker IFS 66v/S spectrometer under vacuum are used for comparison in the range of 2000 cm^{-1} – 1000 cm^{-1}, while RAIRS spectra obtained with the nitrogen purge Nicolet NEXUS 670 FT-IR spectrometer are used to show the existence of characteristic bands in the wavenumber range less than 1000 cm^{-1}.

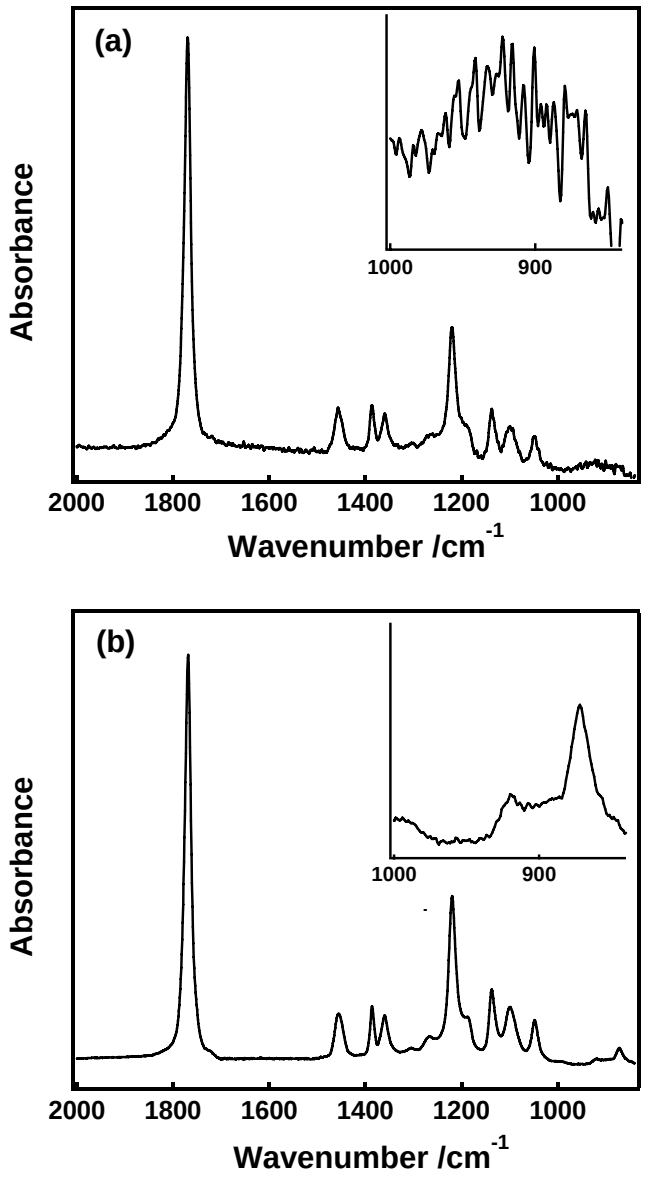

Figure 7.1: RAIRS spectra for M_n = 12.9 kg•mol^{-1} PLLA LB-films obtained with: (a) a Bruker IFS 66v/S spectrometer under vacuum, and (b) a nitrogen purge Nicolet NEXUS 670 FT-IR spectrometer. RAIRS spectra obtained from both instruments have identical band positions and similar band intensities in the range of 2000 – 1000 cm^{-1}. The Bruker IFS 66v/S spectrometer under vacuum shows less water interference while the nitrogen purge Nicolet NEXUS 670 FT-IR spectrometer provides better detection in the range less than 1000 cm^{-1} (as shown in the insets).

7.3.2 IR Spectra of PLLA Samples

Figure 7.2 shows IR spectra for a bulk sample of M_n = 12.9 kg•mol^{-1} PLLA obtained by attenuated total reflectance Fourier transform infrared spectroscopy (ATR-FTIR), and spin-coated and LB-films of the same PLLA sample by RAIRS. Table 7.1 provides band positions and mode assignments for the IR spectra. In accordance with PLLA bulk crystallization studies, a band previously assigned to the CH_3 asymmetric deformation mode is observed at around 1456 cm^{-1}. Zhang *et al.* observed that this mode shows a very small wavenumber shift to higher values and its intensity only increases slightly during the crystallization processes.[248-252] As a result, most crystallization studies treat this band as an internal standard with the assumption that its position and intensity are independent of the degree of crystallinity (and helical content).[253,254] Therefore, IR spectra are normalized to have the same band intensity at 1456 cm^{-1}, and difference in other bands can be used to discuss differences in the degree of crystallinity (and helical content). In the as-prepared PLLA LB-films, this band is observed at 1457 cm^{-1}. All IR spectra in Figure 7.2 have been normalized to have the same band height at 1457 cm^{-1} in PLLA LB-films. A band at 921 cm^{-1}, which is assigned to the coupling of C-C backbone stretching with the CH_3 rocking mode, is observed for bulk and LB-films, indicating the existence of 10_3-helical chain conformations in PLLA α crystals. A band, characteristic of amorphous PLLA, at 955 cm^{-1} is observed for bulk samples and spin-coated films, but not for LB-films. These features suggest that the as-received

PLLA bulk sample is semicrystalline, spin-coated films are amorphous, and as-prepared LB-films are highly crystalline. The differences in band shape, positions, and intensities are mainly observed in the range between 2000 – 1000 cm^{-1} in the IR spectra, and will be discussed in greater detail in the following sections.

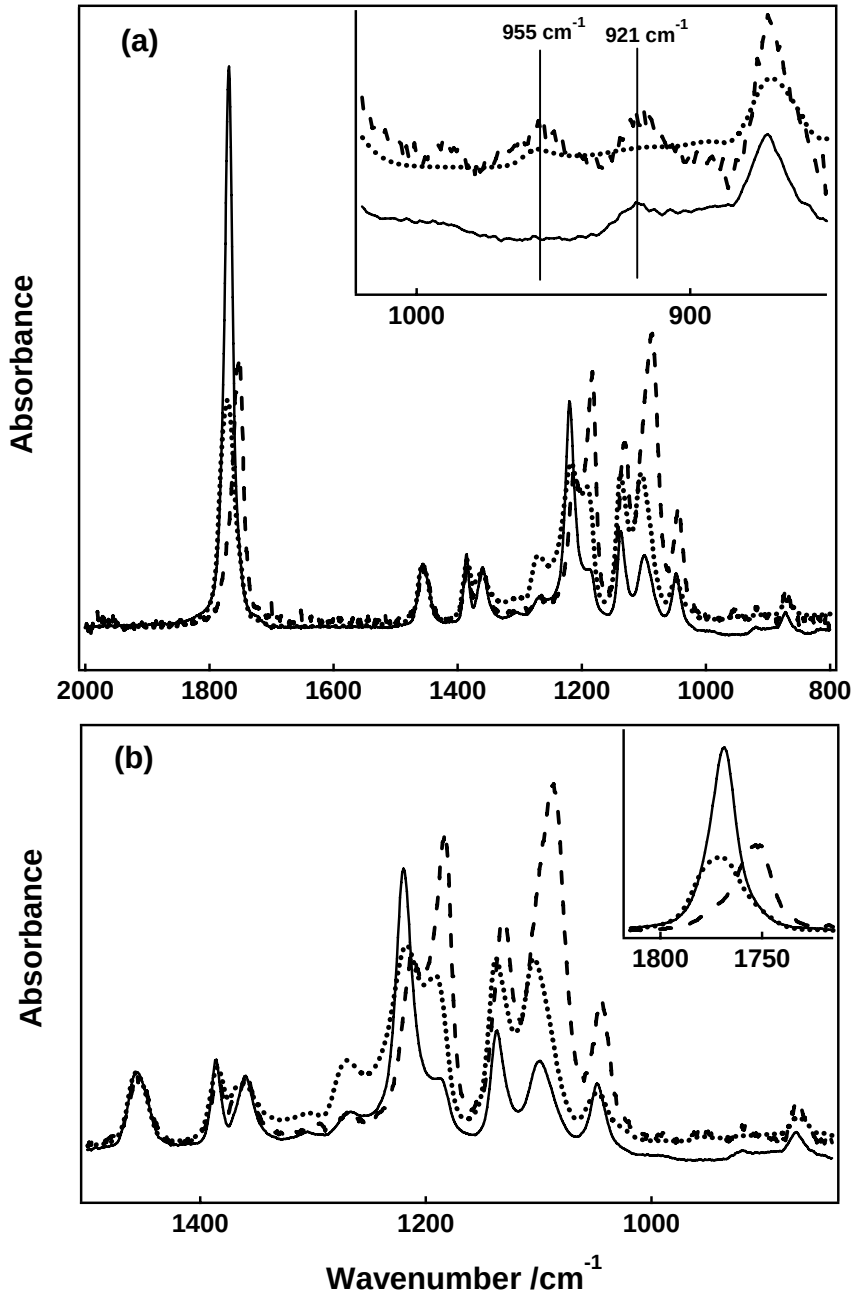

Figure 7.2: IR spectra of M_n = 12.9 kg•mol^{-1} PLLA: (a) ATR-FTIR spectrum of a bulk sample (dashed line); and RAIRS spectra of a spin-coated film (dotted line) and a 10-layer LB-film (prepared at Π = 7.0 mN•m^{-1} at T = 22.5 ^{o}C, solid line). The same spectra as (a) highlighting the region between 1500 – 840 cm^{-1} are shown in (b). The insets of (a) and (b) expand the regions between 1000 – 840 cm^{-1} and 1815 – 1715 cm^{-1}, respectively. All spectra were normalized to have the intensity of the band at 1457 cm^{-1} match the as-prepared LB-film.

Table 7.1. IR band assignments for M_n = 12.9 kg•mol^{-1} PLLA samples: as-received bulk samples, and as-prepared spin-coated and LB-films.[248-254,315-319]

IR Frequencies (cm^{-1})			Assignments[a]
Bulk	Spin-coated films	LB-films	
2997	2997	2997	$\nu_{as}(CH_3)$
2950	2950	2950	$\nu_{s}(CH_3)$
1753	1768	1769	ν(C=O)
1456	1456	1457	$\delta_{as}(CH_3)$
1385	1385	1387	$\delta_{s}(CH_3)$
1359	1360	1360	δ(CH)
1268	1266	1264	ν(CH) + ν(COC)
1211	1217	1220	ν_{as}(COC) + $r_{as}(CH_3)$
1183	1190	1190	ν_{as}(COC) + $r_{as}(CH_3)$
1130	1138	1137	$r_{s}(CH_3)$
1087	1100	1100	ν_{s}(COC)
1044	1048	1048	ν(C-CH_3)
956	955	-	$r(CH_3)$ + ν(CC)
920	-	921	$r(CH_3)$ + ν(CC)
872	871	871	ν(C-COO)

[a] s = symmetric; as = asymmetric.

7.3.3 ATR-FTIR of PLLA Bulk

The bulk PLLA spectrum in Figure 7.2 is obtained directly from the as-received powder sample. IR results suggest that the as-received PLLA bulk sample is semicrystalline, a conclusion supported by differential scanning calorimetry (DSC) measurements (Figure 7.3). During the first heating cycle (Figure 7.3(a)), a clear glass transition temperature (T_g) at 70 ^{o}C is observed along with a small crystallization peak at T_x = 110 ^{o}C and a melting peak at T_m = 175 ^{o}C. During the first cooling cycle (Figure

7.3(b)), there is a larger crystallization peak at T_x = 104 °C. During the second heating cycle (Figure 7.3(c)), there is no discernable T_g or T_x and only a boarder melting peak at T_m = 174 °C. During the second cooling cycle (Figure 7.3(d)), the magnitude and position of T_x is comparable to the first cooling cycle. Based on this information, it is clear that the as-received PLLA bulk contains both amorphous and crystalline PLLA.

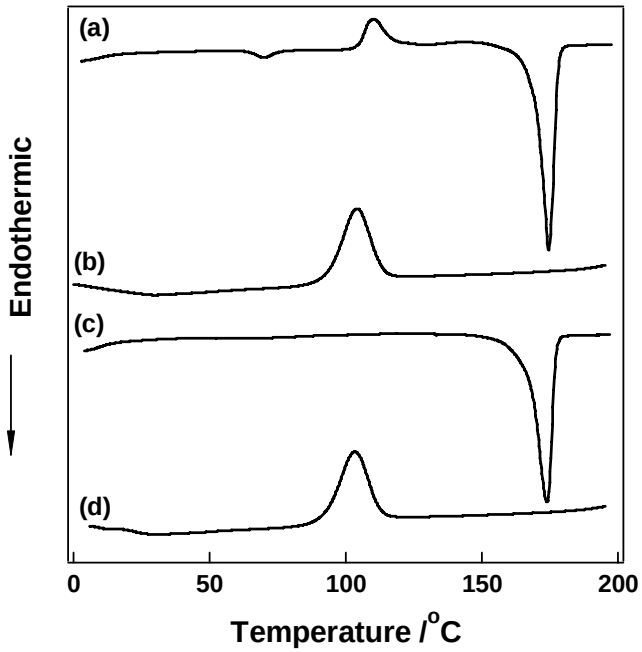

Figure 7.3: DSC curves of a M_n = 12.9 kg•mol^{-1} PLLA bulk samples. Curves (a) and (b) are heating and cooling traces, during the first cycle, respectively; while curves (c) and (d) are heating and cooling traces, during the second cycle, respectively. According to the second cycle, the melting temperature is 174 °C; and the crystallization temperature is 104 °C for bulk PLLA. The heating rate during testing was 10 °C•minute^{-1}, with an intermediate hold time of 1 minute at 200 °C.

To compare the differences in the IR bands for the amorphous and crystalline state, three other bulk spectra were obtained. The first spectrum corresponds to the as-received PLLA sample annealed at 104 ^{o}C under vacuum for 10 hours, to produce a material with a higher degree of crystallinity. The second sample was annealed at 200 ^{o}C for an hour, and was rapidly cooled by setting the sample (in a DSC pan) on a pre-iced (0 ^{o}C) aluminum block to rapidly quench the sample below T_g and produce a "less crystalline" sample. The third sample was obtained by annealing the less crystalline sample at 104 ^{o}C under vacuum for 10 hours. The spectra are shown in Figure 7.4, and the results are summarized in Table 7.2, after normalizing the mode at 1457 cm^{-1} to a 10-layer LB-film prepared at Π = 7.0 mN•m^{-1}. The observed spectral changes are similar to those observed during cold crystallization of PLLA in the literature:[252] (1) The bands at 1753, 1268, 1211, 1183, 1130, 1087, and 1044 cm^{-1} are strongly dependent on whether PLLA is in the amorphous or crystalline state; (2) The band at 1753 cm^{-1}, corresponding to the ν(C=O), shifts to higher wavenumbers with a higher intensity as crystallinity increases; (3) The intensity of the band at 1268 cm^{-1} decreases dramatically with increasing crystallinity, etc. These observations will facilitate the discussion how crystallinity affects IR spectra in the following sections.

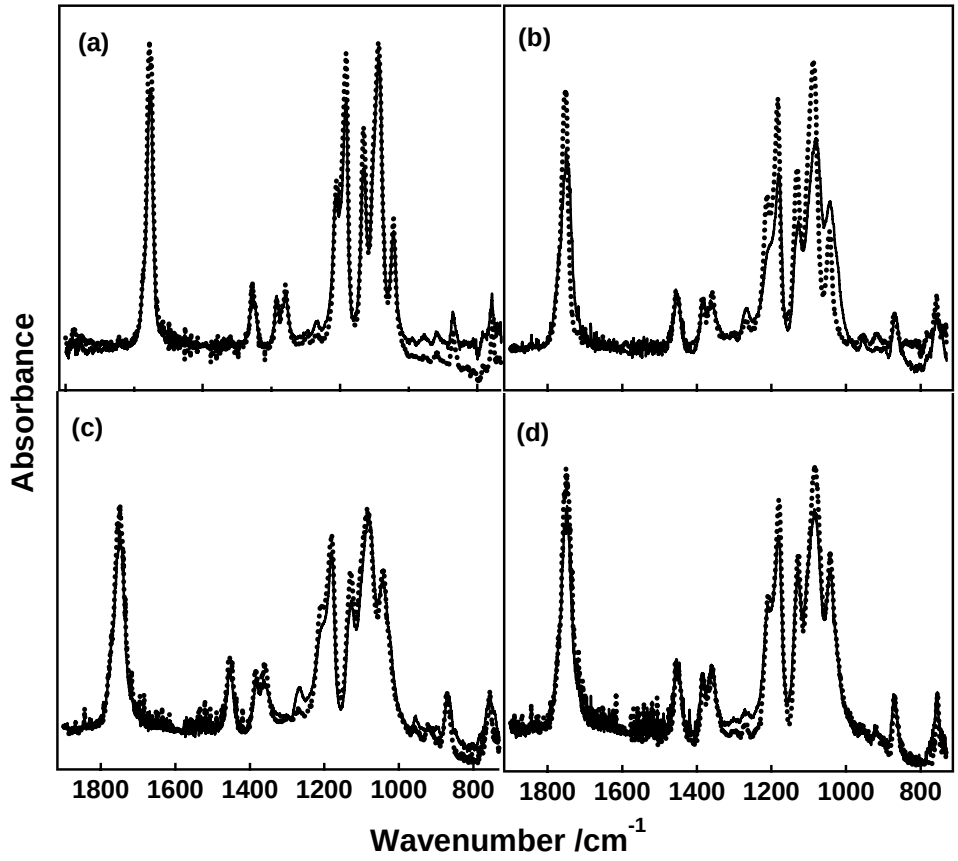

Figure 7.4: ATR-FTIR spectra of M_n = 12.9 kg•mol^{-1} PLLA bulk samples subjected to different thermal treatments: (a) An as-received sample annealed at 104 ^{o}C for 10 hours (dotted line) vs. the as-received PLLA sample (solid line); (b) An as-received PLLA sample annealed at 200 ^{o}C for one hour followed by fast cooling to room temperature ("less crystalline" sample, solid line) vs. the as-received PLLA sample (dotted line); (c) An "less crystalline" sample annealed at 104 ^{o}C for 10 hours (dotted line) vs. the less crystalline sample (solid line); and (d) An as-received PLLA sample annealed at 200 ^{o}C for one hour followed by slow-cooling to 104 ^{o}C (at the speed of 1 ^{o}C•minute^{-1}) where the sample was held for 10 hours (dotted line) vs. the "amorphous" sample annealed at 104 ^{o}C for 10 hours (solid line). The spectra of thermally treated samples were normalized to match the band intensity at 1457 cm^{-1} for a 10-layer LB-film prepared at Π = 7.0 mN•m^{-1}. Noise in the spectrum from 1700 – 1500 cm^{-1} is from water vapor.

Table 7.2: M_n = 12.9 kg•mol^{-1} PLLA peak frequencies and relative intensities for bulk samples and LB-films.[a]

Bulk PLLA											
I	**1753**		**1456**	**1385**	**1359**	**1268**	**1211**	**1183**	**1130**	**1087**	**1044**
	(4.34)		(1.0)	(0.92)	(0.98)	(0.48)	(2.60)	(4.19)	(3.02)	(4.82)	(1.99)
II	**1756**	**1750**	**1456**	**1386**	**1360**	**1268**	**1211**	**1183**	**1131**	**1088**	**1044**
	(5.42)	(4.92)	(1.0)	(0.94)	(1.16)	(0.34)	(2.98)	(5.20)	(3.92)	(5.30)	(2.32)
III		**1751**	**1457**	**1383**	**1360**	**1268**	**1206**	**1180**	**1128**	**1082**	**1042**
		(2.78)	(1.0)	(0.72)	(0.62)	(0.60)	(1.46)	(2.46)	(1.80)	(2.95)	(2.08)
IV	**1756**	**1751**	**1456**	**1386**	**1360**	**1268**	**1211**	**1180**	**1130**	**1085**	**1042**
	(2.98)	(3.18)	(1.0)	(0.84)	(0.92)	(0.28)	(1.82)	(2.81)	(2.28)	(3.20)	(2.33)
V	**1756**	**1749**	**1456**	**1386**	**1360**	**1268**	**1209**	**1180**	**1130**	**1082**	**1040**
	(3.41)	(3.43)	(1.0)	(0.72)	(0.83)	(0.14)	(1.97)	(3.33)	(2.54)	(3.82)	(2.56)
PLLA LB-film											
I	**1769**		**1457**	**1387**	**1360**	**1266**	**1220**	**1190**	**1137**	**1100**	**1048**
	(10.1)		(1.0)	(0.99)	(0.77)	(0.31)	(3.09)	(0.60)	(1.08)	(0.69)	(0.52)
II	**1769**		**1457**	**1387**	**1360**	**1266**	**1220**	**1190**	**1137**	**1100**	**1048**
	(12.0)		(1.0)	(0.95)	(1.10)	(0.06)	(3.89)	(0.33)	(1.11)	(0.69)	(0.86)
III	**1765**	**1752**	**1456**	**1386**	**1360**	**1266**	**1214**	**1192**	**1137**	**1100**	**1051**
	(5.73)	(2.22)	(1.0)	(0.70)	(0.55)	(0.88)	(1.83)	(1.67)	(1.54)	(1.66)	(0.41)
IV	**1768**	**1752**	**1457**	**1386**	**1360**	**1266**	**1217**	**1189**	**1137**	**1100**	**1048**
	(8.98)	(2.08)	(1.0)	(0.76)	(0.86)	(0.31)	(2.98)	(1.20)	(1.55)	(1.47)	(0.44)
V	**1768**	**1752**	**1457**	**1386**	**1360**	**1266**	**1216**	**1190**	**1136**	**1100**	**1048**
	(6.20)	(2.19)	(1.0)	(0.75)	(0.68)	(0.57)	(2.34)	(1.88)	(1.86)	(1.85)	(0.41)

[a] Band intensities relative to the band at 1457 cm^{-1} are shown in parentheses below the band frequencies;
I: As-received (bulk) or as-prepared (LB-film); **II**: "Crystallized from **I**" sample obtained by annealing the as-received or as-prepared sample (**I**) at 104 ^{o}C under vacuum for 10 hours; **III**: "Less crystalline" (or "lower helical content") sample obtained by annealing the as-received or as-prepared sample (**I**) at 200 ^{o}C under vacuum for an hour and rapidly quenching back to room temperature; **IV**: "Recrystallized from **III**" samples obtained by annealing the "less crystalline" (or "lower helical content") sample (**III**) at 104 ^{o}C under vacuum for 10 hours; **V**: "Semi-crystalline" sample obtained by annealing the as-received or as-prepared sample (**I**) at 200 ^{o}C under vacuum for an hour and slowly cooling back to 104 ^{o}C (at ≅ 1 ^{o}C•minute^{-1}) where it remained for 10 hours.

7.3.4 RAIRS Studies of PLLA Spin-coated Films

IR results suggest that PLLA spin-coated films are amorphous. Annealing studies of PLLA spin-coated films may address IR spectral changes with the degree of crystallinity. Several significant differences are observed after annealing the spin-coated film at 104 ^{o}C for 10 hours under vacuum (Figure 7.5): (1) A band at 921 cm^{-1} appears while a band at 955 cm^{-1} almost disappears, confirming the growth of PLLA α crystals during annealing; (2) The intensities of the bands at 1768 cm^{-1} and 1217 cm^{-1} increase after annealing; (3) The intensity of the band at 1266 cm^{-1} decreases after annealing; (4) The "reversed" intensities of the ν_{as}(COC) + r_{as}(CH_3) modes at 1217 cm^{-1} and 1190 cm^{-1} sharpen after annealing; (5) The band intensities at 1138 cm^{-1} and 1100 cm^{-1} decrease while the band intensity at 1048 cm^{-1} increases after annealing. These approaches are different from the annealing results of PLLA bulk samples; however, they agree with the results reported for PLLA spin-coated films during melt crystallization,[251] suggesting that PLLA spin-coated films melt at a temperature lower than 104 ^{o}C. The melt crystallization process yields a material with a higher degree of crystallinity than the as-prepared spin-coated film.

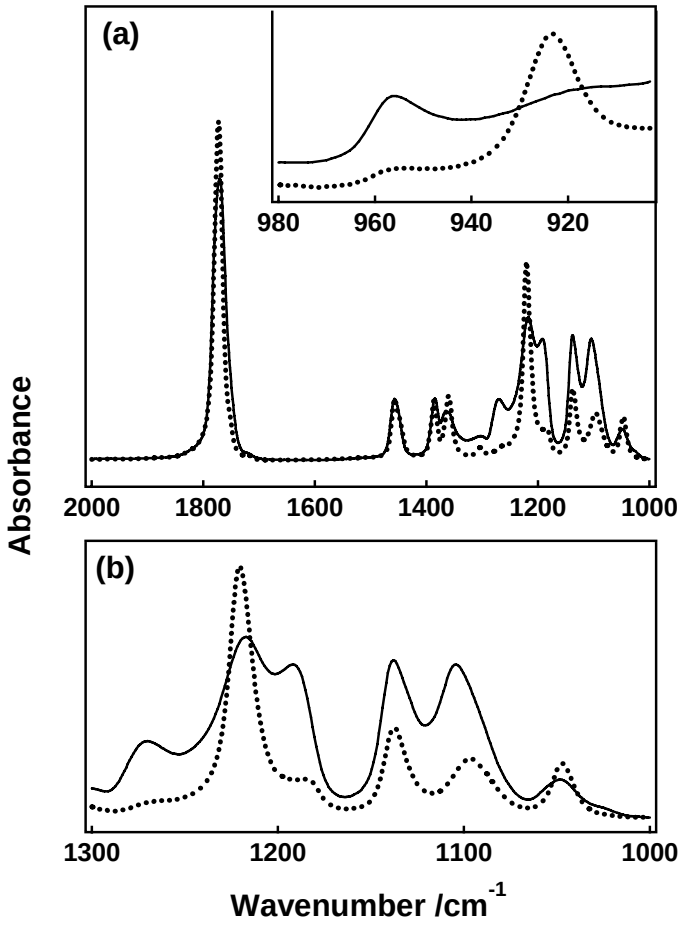

Figure 7.5: RAIRS spectra of M_n = 12.9 kg•mol^{-1} PLLA spin-coated films: (a) 2000 – 1000 cm^{-1} and (b) 1300 – 1000 cm^{-1}. The inset in (a) highlights the spectral region from 980 – 900 cm^{-1}. The solid line corresponds to an as-prepared film, and the dotted line corresponds to an as-prepared film annealed at 104 ^{o}C for 10 hours. Both spectra were normalized to match the as-prepared 5 cycle LB-films (prepared at Π = 7.0 mN•m^{-1}) spectrum band height at 1457 cm^{-1}.

7.3.5 RAIRS Studies of PLLA LB-films

7.3.5.1 RAIRS Spectra of the As-prepared PLLA LB-films

A RAIRS spectrum of a PLLA LB-film prepared in the condensed monolayer region (prepared at Π = 7.0 mN•m^{-1}) is shown in Figure 7.2, and the band intensities relative to the band intensity at 1457 cm^{-1} are summarized in Table 7.2 (**I** on the bottom half of Table 7.2). In contrast to the spectrum of the bulk sample (Figure 7.2 and 7.4), the band positions and band intensities in the RAIRS spectra of PLLA LB-films show some dramatic differences. Prior to this discussion, however, it is necessary to address the key features of RAIRS spectra for PLLA LB-films. A band at 921 cm^{-1}, which is assigned to the coupling of C-C backbone stretching with the CH_3 rocking mode for the 10_3 helical chain conformation of PLLA α crystals,[248-252] is present in all RAIRS spectra of PLLA LB-films, independent of the phase state of the Langmuir film. This observation was unexpected in light of the morphological differences described in Chapter 6. Figure 7.6a shows RAIRS spectra between 2000 and 1000 cm^{-1} for PLLA LB-films prepared in different Langmuir film states (indicated by Π values on the spectra): 1.5 (the liquid expanded phase), 4.0 (the condensed monolayer), 7.8 (the plateau which is the coexistence of monolayer and bilayer), 13.5 (multilayer), and 30.0 (thicker multilayer) mN•m^{-1} during compression; and 10.0 and 2.5 mN•m^{-1} during expansion. No major differences are observed in band positions and shapes for the spectral features of the RAIRS spectra for PLLA LB-films prepared at different Π values. This observation indicates that the overall conformation of PLLA at the A/W interface remains constant

during the entire compression and expansion cycle.[155] However, the absolute intensities of all bands for 5 dipping cycles LB-films differ. The intensity increases with increasing target Π for LB-films prepared during compression, and decreases with decreasing target Π for LB-films prepared during expansion. Differences in IR intensities may be related to differences in the degree of crystallinity, the helical content, the type of PLLA crystal that forms, or the amount of material on the substrate according to Beer's law because transfer ratios are not Π independent as discussed in Chapter 6.[248-252]

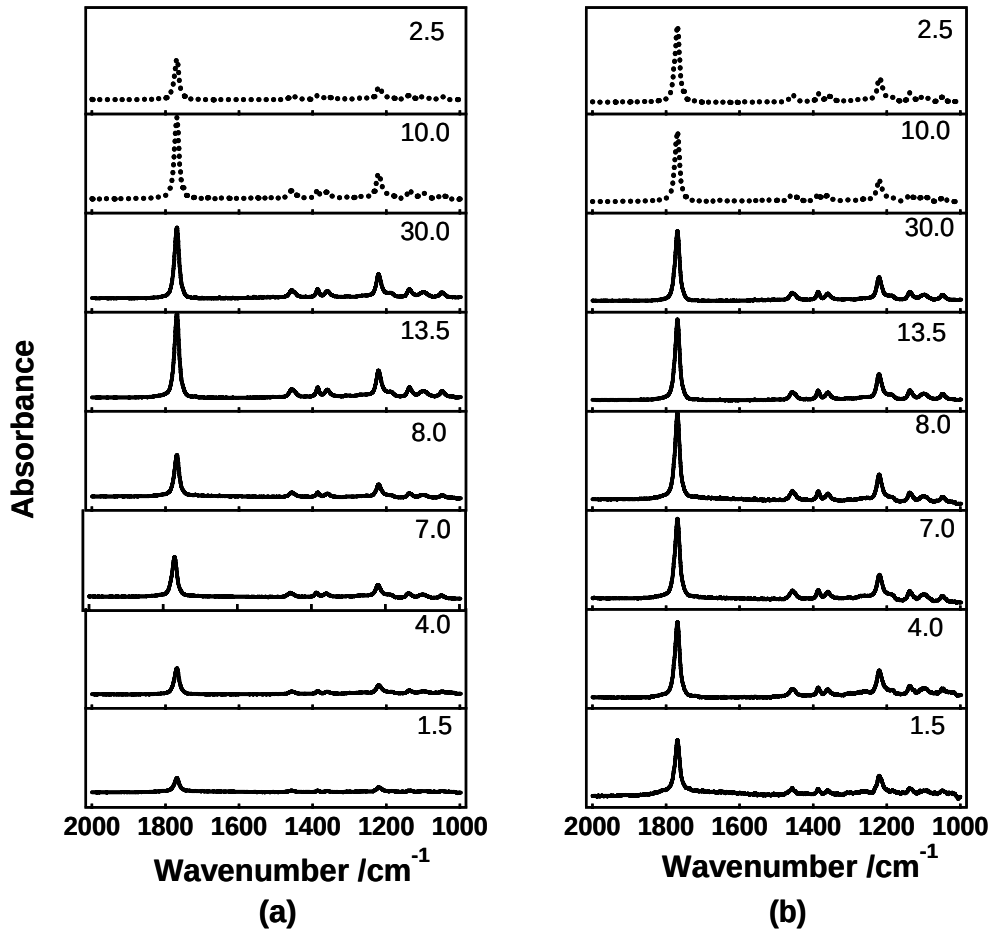

Figure 7.6: (a) RAIRS spectra in the range of 2000 – 1000 cm^{-1} for five dipping cycle LB-films of M_n = 12.9 $kg \bullet mol^{-1}$ PLLA at various Π values on gold substrates coated with a self-assembled monolayer (SAM). The Π values are given on the graph in units of $mN \bullet m^{-1}$. LB-films prepared at Π = 1.5, 4.0, 7.0, 8.0, 13.5, and 30.0 $mN \bullet m^{-1}$ (solid lines) were obtained during the compression, while LB-films prepared at Π = 2.5 and 10.0 $mN \bullet m^{-1}$ (dotted lines) were deposited during the expansion process. All spectra have the same scale. (b) RAIRS spectra normalized to match the band intensity at 1457 cm^{-1} for the LB-film prepared at Π = 7.0 $mN \bullet m^{-1}$ (Figure 7.7). After normalization, it is clear that intensity differences observed in (a) arise from differences in transfer ratios for films formed at different Π.

Figure 7.7 shows that PLLA LB-films prepared with five dipping cycles at Π = 7.0 $mN \bullet m^{-1}$ have the same band positions as LB-films prepared with one dipping cycle (2 layers) at the same Π value, but have proportionally higher band intensity values. The normalization of the RAIRS spectra of 5 cycle and bilayer PLLA LB-films with the same band height at 1457 cm^{-1} yields almost identical RAIRS spectra (the inset of Figure 7.7), suggesting that the difference in band heights in RAIRS spectra are due to the difference in thickness (or the amount of material deposited onto the substrates), instead of the difference in the degree of crystallinity. Due to the difficulty in preparing uniform multilayer PLLA LB-films, the band intensities of LB-films with five dipping cycles are not exactly five times larger than the corresponding band intensities in the RAIRS spectra of LB-films with one dipping cycle. The same trend is also observed for LB-films prepared at other surface pressures. On the basis of the RAIRS spectra, it is clear that PLLA LB-multilayer films have the same configuration as PLLA LB-bilayer films prepared at Π = 7.0 $mN \bullet m^{-1}$ where the transfer ratios are ~ 1.0 (*i.e.*, quantitative transfer). While the subsequent discussion could proceed with bilayer films, we chose to use multilayers to provide signal amplification.

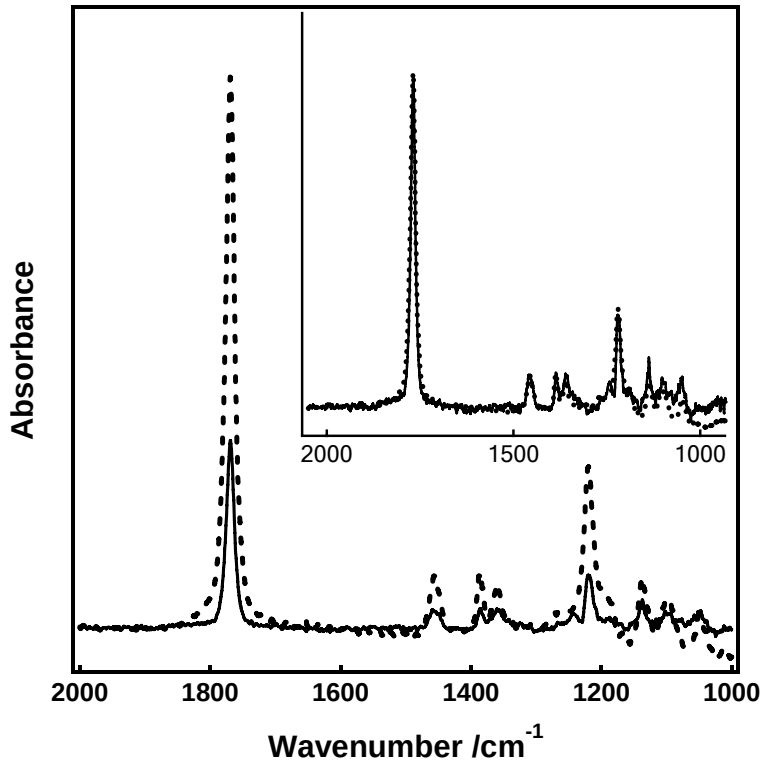

Figure 7.7: RAIRS spectra for M_n = 12.9 kg•mol^{-1} PLLA LB-films transferred at Π = 7.0 mN•m^{-1} on gold substrates coated with a SAM with different numbers of dipping cycles. The dotted line corresponds to the spectrum of a LB-film with five dipping cycles, while the solid line corresponds to the spectrum of a LB-film with one dipping cycle (2 layers). The LB-films with 5 dipping cycles have the same band positions as the LB-films with one dipping cycle, but higher band intensities. The inset shows that normalizing the spectra to have the same band intensity at 1457 cm^{-1} yields nearly identical results.

All the LB-films in Figure 7.6 were prepared with five dipping cycles. At higher Π values, PLLA Langmuir films become thicker during the compression process, indicating that more material can be deposited onto the solid substrate for the same number of dipping cycles (assuming comparable transfer ratios), thereby leading to a higher intensity in the RAIRS spectra relative to the film at Π = 7.0 mN•m^{-1}. During the initial stage of the expansion process, Π drops precipitously with a small change in *A*, hence the RAIRS spectrum of the LB-films transferred at Π = 10 mN•m^{-1} during expansion shows similar intensity to the film transferred at Π = 30 mN•m^{-1} during compression. The normalization of all spectra prepared in different states to have the same band height at 1457 cm^{-1} (shown in Figure 7.6b) indicates that the spectral intensity differences can be explained by the amount of the material on the substrates as expected according to Beer's law. Hence, it is possible to draw the conclusion that PLLA LB-films prepared in different Langmuir film states have similar degrees of crystallinity.

7.3.5.2 Comparison of RAIRS Spectra of PLLA LB-films and Bulk

From Table 7.2, the bands at 1753 cm^{-1}, 1211 cm^{-1}, 1183 cm^{-1}, 1130 cm^{-1}, and 1087 cm^{-1} in the as-received bulk PLLA spectrum are shifted to 1769 cm^{-1}, 1220 cm^{-1}, 1190 cm^{-1}, 1137 cm^{-1}, and 1100 cm^{-1}, respectively for the as-prepared LB-films. Such high-wavenumber shifts have been reported by Zhang *et al.* for PLLA during cold-crystallization.[248-252] From Table 7.2, it is also clear that there are dramatic changes in the band intensities. The ν(C=O) and ν_{as}(COC) + r_{as}(CH_3) modes for the LB-films (1769 cm^{-1} and 1220 cm^{-1}, respectively) are substantially more intense than the

corresponding modes in the as-received bulk spectrum (1753 cm^{-1} and 1211 cm^{-1}, respectively). Additionally, the bands corresponding to the $\nu(CH) + \nu(COC)$, $\nu_{as}(COC) + r_{as}(CH_3)$, $r_s(CH_3)$, $\nu_s(COC)$, and $\nu(C\text{-}CH_3)$ modes in the LB-films (1266 cm^{-1}, 1190 cm^{-1}, 1137 cm^{-1}, 1100 cm^{-1}, and 1048 cm^{-1}, respectively) are significantly less intense than the corresponding bands in the as-received bulk spectrum (1268 cm^{-1}, 1183 cm^{-1}, 1130 cm^{-1}, 1087 cm^{-1}, and 1044 cm^{-1}, respectively). Several scenarios exist for these differences. First, the semicrystalline nature of PLLA requires the consideration of how the IR spectra of amorphous and semi-crystalline PLLA differ. Second, the potential for orientation effects within the LB-films arising from in-plane vs. out of plane vibrations need to be considered. Finally, both effects could be present requiring some attempt to deconvolute these factors. Based on these considerations, the most significant differences between the as-received bulk spectrum and the as-prepared LB-film spectrum are: (1) The change in the carbonyl stretch between the LB-film (1769 cm^{-1}) vs. the as-received bulk spectrum (1753 cm^{-1}); (2) The low intensity of the band at 1266 cm^{-1} in the LB-film; (3) The relative intensities of the $\nu_{as}(COC) + r_{as}(CH_3)$ modes at 1220 cm^{-1} and 1190 cm^{-1} in the LB-film are "reversed" relative to the as-received bulk spectrum; and (4) The relative intensities of the $r_s(CH_3)$ and $\nu_s(COC)$ modes at 1130 and 1087 cm^{-1}, respectively, in the LB-film are also "reversed" relative to the as-received bulk spectrum. In order to address these issues, annealing studies were used to determine the effects of crystallinity on the LB-films, just as was done for the bulk sample earlier in this chapter (Section 7.3.3).

7.3.5.3 RAIRS Studies of Annealed PLLA LB-films

The spectrum of the as-prepared LB-film annealed at 104 ^{o}C (**II** on the bottom half of Table 7.2) for 10 hours shows that the intensity of the band at 1769 cm^{-1} increases and the band at 1266 cm^{-1} is nearly eliminated (Figure 7.8). The "reversed" intensities of the ν_{as}(COC) + r_{as}(CH_3) modes at 1220 cm^{-1} and 1190 cm^{-1} for the as-prepared LB-film relative to the as-received bulk sample also sharpen upon annealing at 104 ^{o}C. The band characteristic of crystalline PLLA at 921 cm^{-1} is present in both spectra. These observations are consistent with results for PLLA spin-coated films suggesting that the PLLA LB-films melt at a temperature below 104 ^{o}C. This hypothesis is consistent with AFM images which show that melting-recrystallization of PLLA molecules in LB-films results in the formation of 3D structures with much greater thickness (~ 25 nm) than the as-prepared LB-films (~ 2 nm) (Figure 7.9).

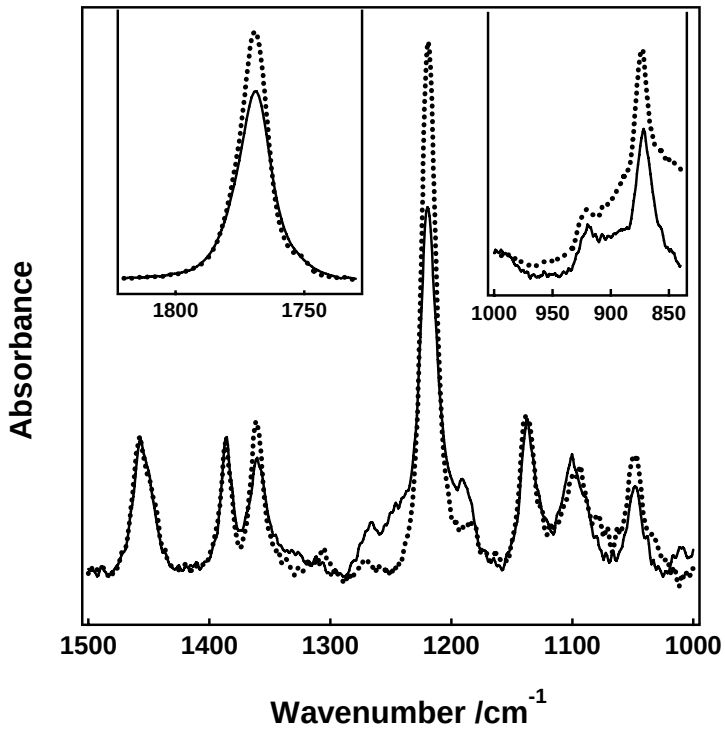

Figure 7.8: RAIRS spectra for 5 cycle M_n = 12.9 kg•mol^{-1} PLLA LB-films which were transferred at Π = 7.0 mN•m^{-1} at T = 22.5 ^{o}C before (solid line) and after thermal annealing at 104 ^{o}C for 10 hours (dotted line). The insets expand the spectral regions from 1820 to 1730 cm^{-1} and 1000 to 840 cm^{-1}. The spectra of thermally treated samples were normalized so that the band at 1457 cm^{-1} matches the as-prepared LB-film.

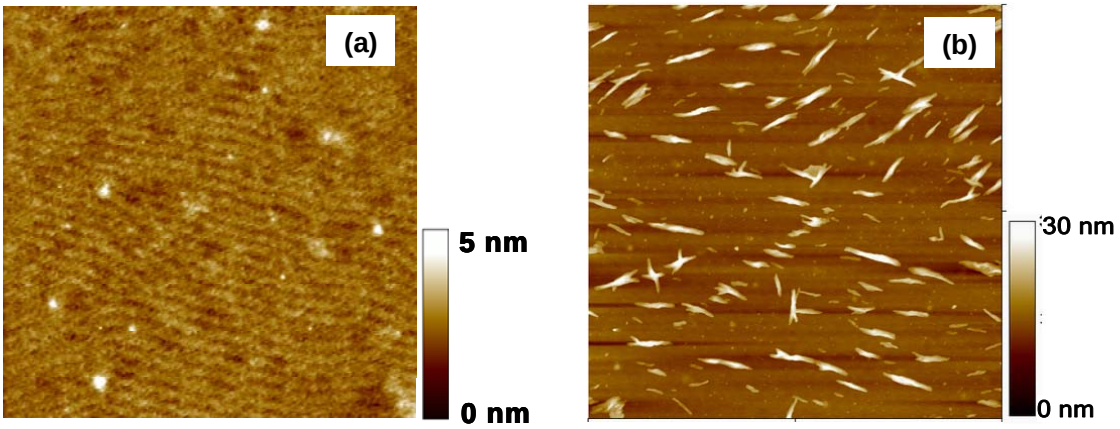

Figure 7.9: AFM height images of 2 layer M_n = 12.9 kg•mol^{-1} PLLA LB-films which were transferred at Π = 7.0 mN•m^{-1} and T = 22.5 ^{o}C: (a) before and (b) after thermal annealing at 104 ^{o}C for 10 hours. After annealing, lamellae features are destroyed and larger 3D structures with irregular shapes are observed.

Upon annealing and rapid quenching back to room temperature (**III** on the bottom half of Table 7.2), the "lower helical content" spectrum (Figure 7.10) shows that: (1) The carbonyl stretch at 1769 cm^{-1} shifts to 1765 cm^{-1} and broadens, with a decrease in the band intensity. Another band appears at 1752 cm^{-1}, close to that of the as-received PLLA bulk spectrum; (2) The intensity of the band at 1266 cm^{-1} increases to a magnitude comparable to the as-received and "less crystalline" bulk samples; (3) For the ν_{as}(COC) + r_{as}(CH_3) modes, the band at 1220 cm^{-1} shifts to 1214 cm^{-1} which is comparable to the bulk "less crystalline" spectrum (1211 cm^{-1}), while the band at 1192 cm^{-1} grows dramatically, although it does not grow enough to "reverse" the intensities of the two

modes as seen in bulk spectrum; and (4) Upon annealing the LB-films and rapidly cooling them to room temperature, the relative intensities of the $r_s(CH_3)$ and $\nu_s(COC)$ modes increase dramatically compared to the as-prepared film, but also fail to show a "reversal" in intensity seen in the as-received bulk spectrum; instead, the intensities of these modes become very similar. The melting of the lamellar features is confirmed by AFM images (Figure 7.11). Annealing the "lower helical content" LB-film at 104 ^oC for 10 hours (**IV** on the bottom half of Table 7.2) increases the helical content (Figure 7.12), as discussed above for the thermal treatment of PLLA bulk samples. However, the annealed "lower helical content" LB-film has less helical content than the as-prepared LB-film as seen in Table 7.2.

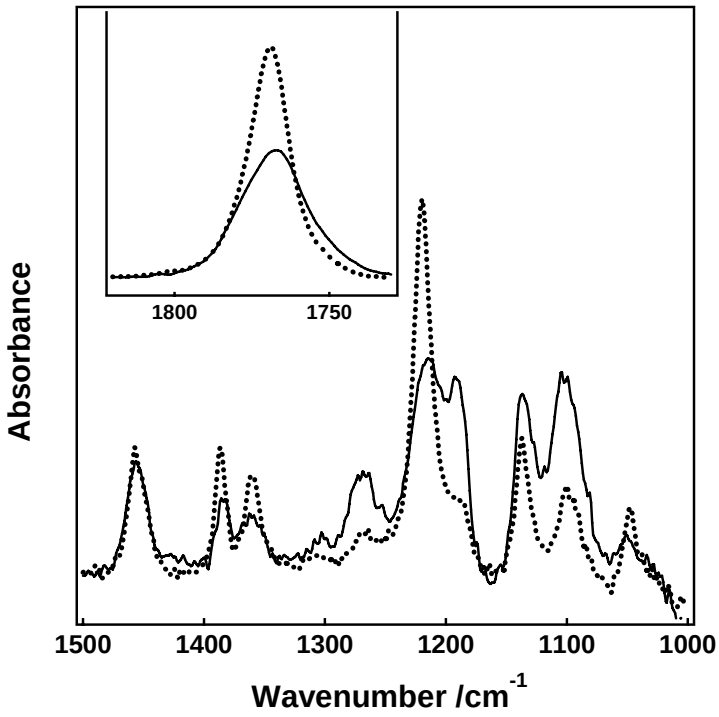

Figure 7.10: RAIRS spectra for 5 cycle M_n = 12.9 kg•mol-1 PLLA LB-films which were transferred at Π = 7.0 mN•m^{-1} and T = 22.5 ^{o}C before (dotted line) and after thermal annealing at 200 ^{o}C for one hour followed with subsequent rapid cooling to room temperature ("lower helical content" LB-film, solid line). The inset expands the spectral region from 1820 to 1730 cm^{-1}. The spectrum of the thermally treated sample was normalized to match the band intensity at 1457 cm^{-1} to the spectrum of the as-prepared LB-film.

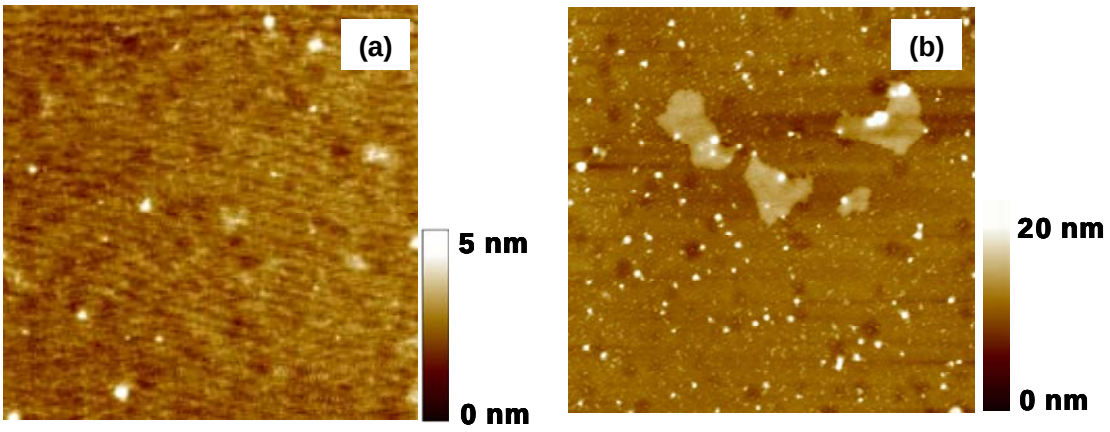

Figure 7.11: AFM height images for 2 layer M_n = 12.9 kg•mol^{-1} PLLA LB-films which were transferred at Π = 7.0 mN•m^{-1}: (a) before and (b) after thermal annealing at 200 ^{o}C for 1 hour with subsequent rapid cooling to room temperature. After annealing, lamellar features are gone and only 3D structures remain.

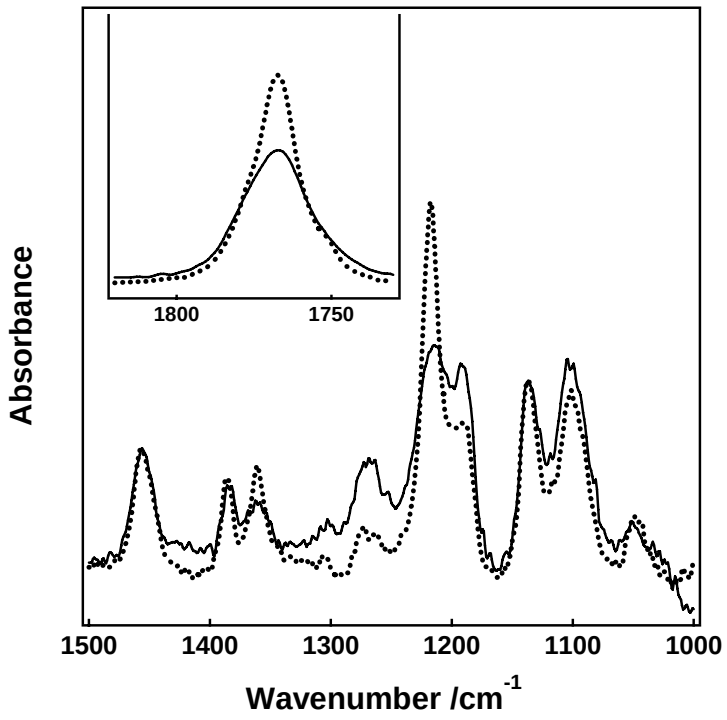

Figure 7.12: RAIRS spectra of an as-prepared 5 cycle LB-film (Π = 7.0 kg•mol^{-1}) of M_n = 12.9 kg•mol^{-1} PLLA annealed at 200 ^{o}C for 1 hour, subsequently rapid-cooled to room temperature (solid line) and a final step of annealing at 104 ^{o}C for 10 hours (dotted line). The inset enlarges the spectral region from 1820 to 1730 cm^{-1}. The spectrum of the thermally treated sample was normalized to have the same band intensity at 1457 cm^{-1} as the as-prepared LB-film.

It is important to note that the differences in IR spectra for thermally treated samples presented thus far are not caused by the thermal degradation of PLLA at temperatures above its bulk T_m. Figure 7.13 shows RAIRS spectra of PLLA LB-films annealed at 200 ^{o}C for different periods of time. An extra broad band appears at ~ 1573 cm^{-1} for PLLA LB-films annealed at 200 ^{o}C longer than 1 hour. The intensity of this band increases with increasing annealing time at 200 ^{o}C. The mode at 1573 cm^{-1} along with the band at 1413 cm^{-1} has been suggested as the absorption band of carboxylate anions by Blazewicz *et al.*[320] These two modes are not observed in the IR spectra of PLLA LB-films annealed less than 1 hour, suggesting that thermal degradation is not an issue for PLLA LB-films annealed less than 1 hour at 200 ^{o}C.

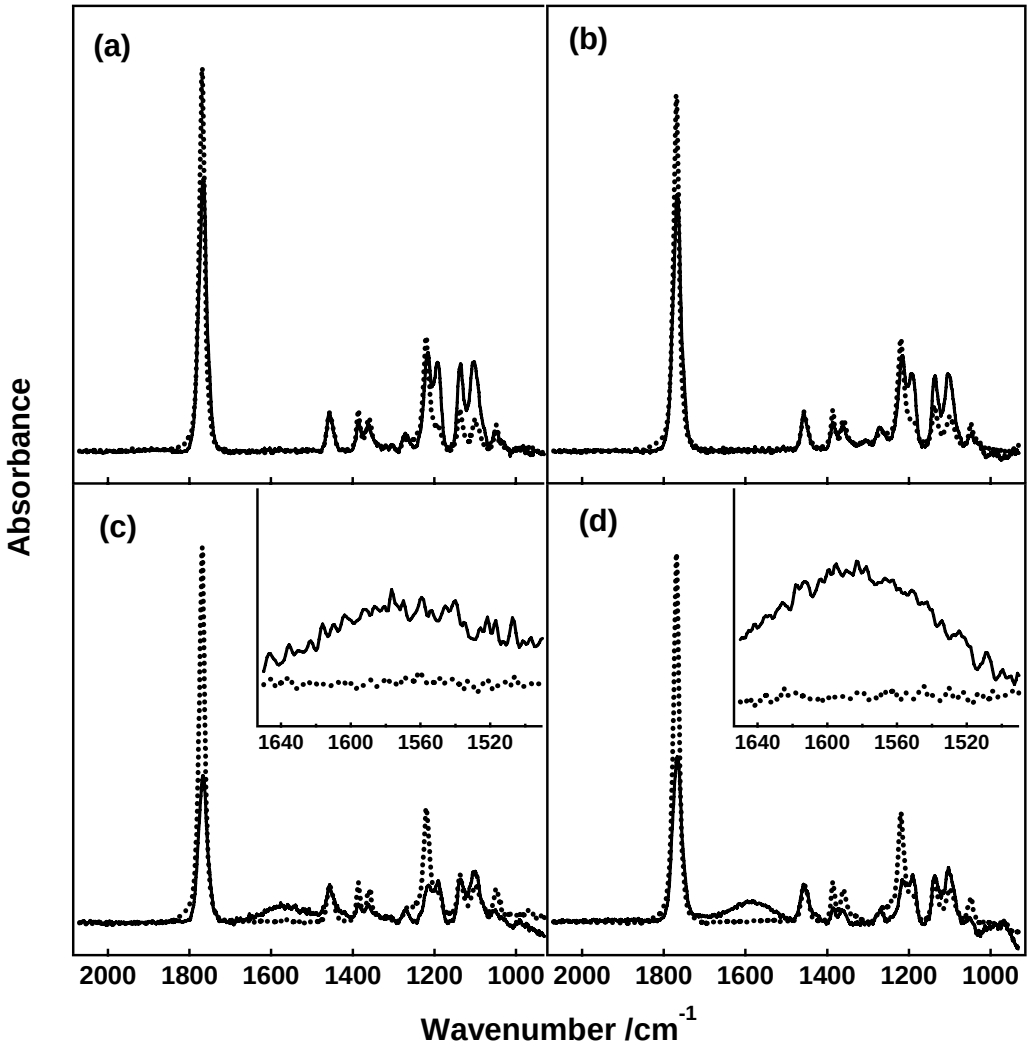

Figure 7.13: RAIRS spectra of thermally treated M_n = 12.9 kg•mol^{-1} PLLA LB-films. Each graph represents a 5 cycle LB-film prepared at Π = 7.0 mN•m^{-1} and T = 22.5 ^{o}C. The dotted lines correspond to IR spectra of the as-prepared LB-films, and the solid lines correspond to the as-prepared LB-films thermally annealed at 200 ^{o}C for different periods of time: (a) 0.5, (b) 1, (c) 2, and (d) 3 hours, followed by slow cooling to 104 ^{o}C (at the speed of 1 ^{o}C•minute^{-1}) where the sample was held for 10 hours. The spectra of thermally treated samples were normalized to match their band intensity at 1457 cm^{-1} to the as-prepared LB-film.

For the last set of annealing studies, a LB-film sample was annealed at 200 ^{o}C for an hour and was then slowly cooled (1 ^{o}C•minute^{-1}) to 104 ^{o}C and was held at 104 ^{o}C for 10 hours to produce a "semi-crystalline" film (**V** on the bottom half of Table 7.2, Figure 7.14). The key effects shown from the "semi-crystalline" spectrum are: (1) The carbonyl stretch at 1769 cm^{-1} shifts to 1768 cm^{-1}, with a decrease in the band intensity. Another band appears at 1752 cm^{-1}, as seen in the "lower helical content" LB-film (**III** on the bottom half of Table 7.2); (2) The intensity of the band at 1266 cm^{-1} increases to a magnitude comparable to the as-received, "less crystalline" bulk sample and the "lower helical content" LB-film; (3) The ν_{as}(COC) + r_{as}(CH_3) modes, the band at 1220 cm^{-1}, shifts to 1216 cm^{-1} a value that is comparable to the "lower helical content" LB-film spectrum (1215 cm^{-1}), while the band at 1190 cm^{-1} grows dramatically, almost enough to "reverse" the intensities of the two modes as seen in bulk spectra; and (4) Upon annealing the LB-film at 200 ^{o}C and slow cooling to 104 ^{o}C, the relative intensities of the r_s(CH_3) and ν_s(COC) modes at 1136 cm^{-1} and 1100 cm^{-1} increase dramatically compared to the as-prepared film. Both bands have nearly identical intensities; however, the "reversal" in intensity seen in bulk sample (Figure 7.2) is not yet observed.

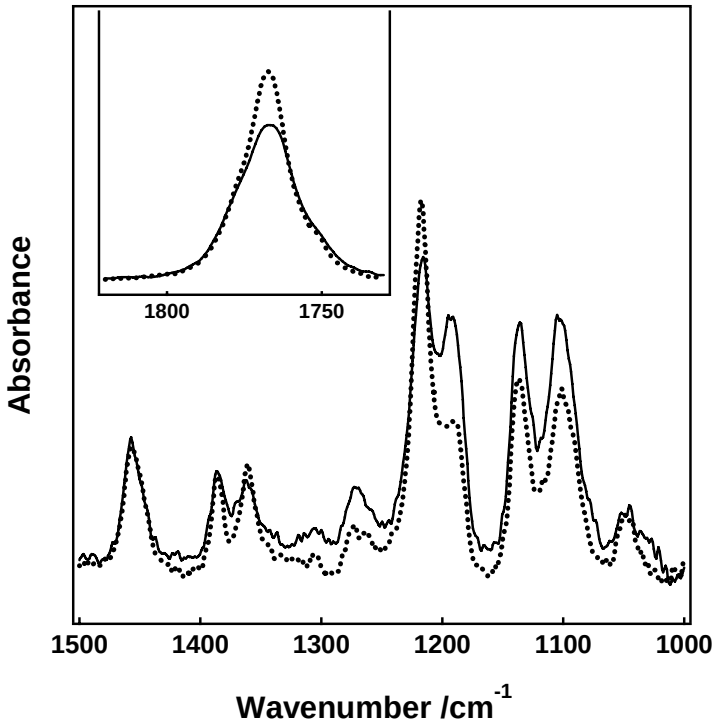

Figure 7.14: RAIRS spectra of M_n = 12.9 kg•mol^{-1} PLLA "semicrystalline" LB-films with different cooling methods. The solid line corresponds to annealing the as-prepared LB-film at 200 ^{o}C for 1 hour followed by slow cooling to 104 ^{o}C (at the rate of 1 ^{o}C•minute^{-1}) where the film was held at a constant temperature for 10 hours. The dotted line represents annealing the "lower helical content" LB-film at 104 ^{o}C for 10 hours. The inset highlights the spectral region from 1820 to 1730 cm^{-1}. Both spectra were normalized in terms of their band intensity at 1457 cm^{-1} to match the as-prepared LB-film.

In order to interpret these observations, the following point needs to be noted. Upon annealing under vacuum at 200 ^{o}C, the self-assembled monolayer (SAM) placed on the

gold surface to facilitate LB-deposition is destroyed and removed disordering the film. Hence any orientation effects present in the as-prepared LB-films will be substantially reduced in the annealed samples. With this consideration, the following conclusions are drawn: (1) The ν(C=O) stretch at 1769 cm^{-1} corresponds to a carbonyl that is essentially exhibiting E_1 mode behavior.[155,156,253,254] Upon annealing the as-prepared LB-film at 104 ^{o}C, the E_1 mode becomes even stronger. Based on previous bulk studies, and the fact that increasing crystallinity causes the E_1 mode to grow and the A mode (1753 cm^{-1}) to shrink, the as-prepared LB-films appear to be in an extraordinarily ordered crystalline state; (2) The growth in intensity of the mode at 1266 cm^{-1} upon annealing to an "lower helical content" state is also consistent with melting a crystalline LB-film; (C) For the $\nu_{as}(COC)$ + $r_{as}(CH_3)$ modes, helical content can not be the only answer. All the bulk spectra show that the intensity of the lower frequency mode (1183 cm^{-1}) is larger than the higher frequency mode (1211 cm^{-1}). Even after annealing the LB-film above the bulk T_m, this does not occur. Hence, it appears that the COC bond lies in the plane of the film, leading to substantial attenuation in the RAIRS spectra which are known to be sensitive to the orientation of the film.[197,321] The results also suggest that some degree of orientation is retained after annealing; and (4) Growth in the intensity of both the 1137 and 1100 cm^{-1} modes upon annealing and quenching is not consistent with the effects of helical content as the bulk spectra show that both modes should grow with increasing helical content. Hence, their low intensity in the as-prepared LB-films is also consistent with in-plane vibrations that are attenuated in the RAIRS spectra.

Finally, the observed changes in the RAIRS spectra of the LB-films upon annealing are completely consistent with the proposed structure of 10_3-helices in the bulk crystalline state and highly oriented 10_3-helices on a surface.[155,156,223] Moreover, the ability to disorder the film through removal of the SAM suggests these 10_3-helices lie flat on the LB-film substrate in a highly ordered structure.

7.4 Conclusions

RAIRS results show that the as-prepared PLLA LB-films have relatively high helical content compared to the as-prepared and recrystallized spin-coated films. Annealing the already highly ordered LB-films at the bulk crystallization temperature suggests a melting-recrystallization process resulting in surfaces with similar helical contents but different surface morphologies. Thermal annealing above the bulk melting temperature can destroy the ordering and dramatically decrease helical content. Annealing studies by RAIRS are completely consistent with the proposed structure of highly oriented 10_3-helices. RAIRS results also proved that PLLA single molecule helices exist in PLLA LB-films prepared from all phases of the Langmuir monolayer. Our results provide a method for preparing highly crystalline and smooth surfaces which may be useful for cell adhesion studies. These surfaces may also be useful as a model system for studying crystallization of PLLA thin films.

CHAPTER 8

Conclusions and Suggestions for Future Work

8.1 Overall Conclusions

A first-order liquid expanded to condensed (LE/LC) phase transition is observed for poly(L-lactic acid) (PLLA) Langmuir monolayers at the air/water (A/W) interface. LE/LC phase transitions have been widely reported for small molecules with lipid-like structures;[39,60,73-75,210,217,218,228,322] however, LE/LC phase transitions in polymer Langmuir monolayers are uncommon. Only two polymers have been reported to have a LE/LC phase transition other than the PLLA system studied in this project. One is a comblike copolymer possessing long alkyl side chains which is similar to lipids,[220] and the other is a dendritic linear block copolymer lacking a lipid-like structure.[221] Our observation of the LE/LC phase transition is the first such observation for a homopolymer Langmuir monolayer. Morphological proof for the LE/LC phase transition in PLLA monolayers is obtained from Brewster angle microscopy (BAM). The BAM images show the presence of circular domains at the start of the phase transition, similar to those observed for small molecules. The LE/LC phase transition is both temperature and molar mass dependent. Temperature dependent experiments show the critical behavior of the LE/LC phase transition is much like gas – liquid phase transitions in three-dimensions (3D). Analysis through the two-dimensional (2D) Clausius-Clapeyron equation yields critical parameters

that are linearly dependent on molar mass, suggesting that the LE/LC phase transitions are free-volume dependent.

The LE/LC phase transition represents a disorder to order transition, which is consistent with a negative entropy change and atomic force microscopy (AFM) studies. Well-ordered lamellar features are observed for PLLA Langmuir-Blodgett (LB) films prepared in the LC phase. The dimension of the lamellar patterns is comparable to the length of a PLLA single chain if PLLA exists in a 10_3 helical conformation over the entire length of the chain. A hypothesis is proposed that PLLA molecules lie flat on the subphase in a 10_3 helical conformation, and behave like rigid-rods. This hypothesis is confirmed with molar mass scaling experiments, x-ray reflectivity experiments, and reflection absorption infrared spectroscopy (RAIRS) studies. During the LE/LC phase transition, PLLA single molecule 10_3-helices are ordered at the A/W interface. PLLA helices are further ordered by shear during LB-deposition, yielding LB-films with highly ordered structures and very smooth surfaces.

Two different collapse mechanisms are suggested for PLLA monolayers at the A/W interface. First, during constant compression rate experiments, rigid PLLA monolayers at temperatures below the critical temperature (T_c) for the LE/LC phase transition are believed to collapse through buckling and stacking of ordered lamellae into 3D multilayers. The multilayers can respread onto the subphase upon expansion, as confirmed by isotherm studies, BAM, and AFM measurements. During the buckling and stacking process, PLLA single molecule helices do not degrade or dissolve into the

subphase, and the ordered structures formed after the LE/LC phase transitions are quite robust. Second, "slow collapse" of PLLA Langmuir monolayers during isobaric area relaxation experiments is believed to proceed through a nucleation and growth mechanism as proposed by Vollhardt.[274-276] However, relaxation behavior can not be completely fit with the Vollhardt model. A mechanism is proposed for the "slow collapse" of PLLA Langmuir monolayers at temperatures below T_c: (i) rearrangement of PLLA molecules in the metastable LC region into a most closely packed LC phase; (ii) a combination of molecular rearrangement along with the induction of nucleation; and (iii) the growth of 3D structures. These two collapse mechanisms may provide a method of controlling surface morphology of PLLA LB-films.

One of the objectives of this research is to prepare PLLA substrates with controllable surface morphology and degree of crystallinity. Surface morphology can be controlled by knowing the phase behavior of the surface behavior of PLLA Langmuir monolayers at the A/W interface, as summarized above. The degree of crystallinity can be studied by RAIRS for PLLA LB-films. It is found that the as-prepared PLLA LB-films have a relatively high degree of crystallinity, consistent with the hypothesis of Pelletier *et al.* that PLLA molecules exist in a 10_3 helical conformation at the A/W interface.[155] Annealing studies are also performed on LB-films, which may provide insight into investigating crystallization behavior of PLLA in thin films.

Considering the above points, PLLA Langmuir monolayers are an excellent model system for studying critical behavior in 2D, 2D to 3D transitions during "slow collapse"

processes, and for obtaining substrates with controllable surface morphologies and degrees of crystallinity.

8.2 Suggestions for Future Work

The most important observation in this dissertation is the LE/LC phase transition for PLLA Langmuir monolayers at the A/W interface, which can provide insight for studying critical behavior in 2D. If theoretical models could be developed to reproduce the molar mass dependent critical behavior observed in this system, insight into the importance of water, shape persistence, and packing could be obtained. Such information would allow focused experimental studies of other polymers that may show LE/LC phase transitions at experimentally accessible temperatures. However, this suggestion does not match the expertise of the current research group. In this section, I will point out some experimental challenges that can be addressed in our laboratory.

8.2.1. Determination of the Binodal Boundary for the LE/LC Phase Transition

The LE/LC phase transition is dependent on temperature as described in Chapter 4. The isotherms obtained during constant compression rate experiments at different temperatures (Figure 4.5 and Figure 8.1a) can be used to generate a phase diagram for the LE/LC phase transition, as shown in Figure 8.1b. In Figure 8.1b, the dashed line represents the LE/LC binodal boundary, the shaded area shows the LE/LC phase coexistence region, and the solid straight lines inside the shaded area represent tie lines between the LE and LC phases at specific temperatures. Figure 8.1b may not be a completely true phase diagram for the LE/LC phase transition during finite compression

rate experiments, because PLLA molecules are in non-equilibrium states. As a result, the LE/LC phase coexistence regions are not flat during constant compression rate experiments. Hence extrapolation is used to determine the end of the phase coexistence region in Figure 8.1b, which was described in Section 4.3.4.[230,231] The extrapolation may introduce errors in determining the binodal boundary. The errors may be reduced if slower compression rates are used. This suggestion may be fulfilled with a modification of the present trough by using a different motor or a different gear system. Furthermore, the errors can be avoided if zero slope LE/LC phase coexistence regions are obtained, as in successive addition experiments.

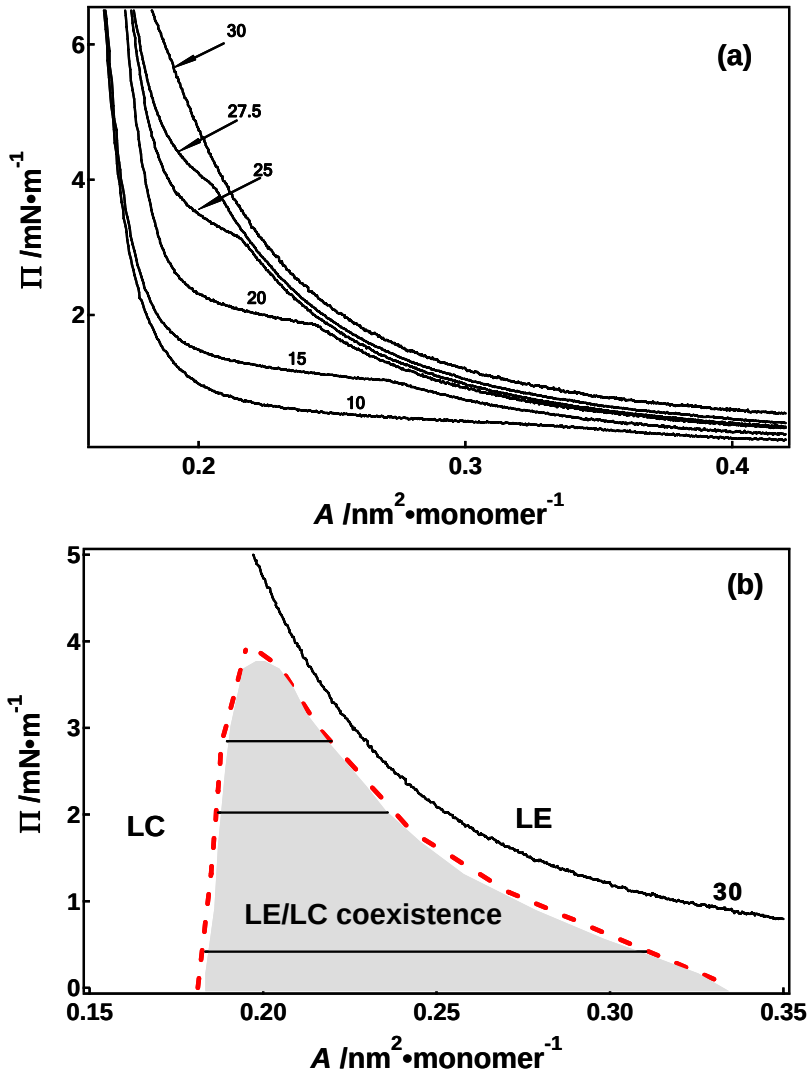

Figure 8.1: (a) Π-*A* isotherms of the LE/LC phase transitions obtained during constant compression rate experiments for M_n = 12.9 kg•mol^{-1} PLLA Langmuir monolayers at different temperatures. The temperature values are given on the graph in units of ^oC. (b) shows a phase diagram for the LE/LC phase transition generated from the constant compression rate isotherms for the 12.9 kg•mol^{-1} PLLA Langmuir monolayers in (a). The dashed line represents the binodal phase boundary, the shaded area represents the LE/LC coexistence region, and the solid straight lines represent tie lines at a constant temperature value.

Flat isotherms in the coexistence region for the LE/LC phase transitions are observed during successive addition experiments as described in Chapter 4. The flat coexistence region can be used to define both ends of the phase transition, which can be used to determine the binodal phase boundary of the phase diagram. Successive addition experiments are useful at or below room temperature; however, phase diagrams generated from successive addition experiments may be invalid at high temperatures because of the evaporation of the subphase as addition experiments take longer to perform. Another limitation when generating phase diagrams from successive addition experiments is that no imaging technique can be used to visualize the phase transition. During successive addition experiments, the LC phase can not grow as it is continuously disrupted during spreading. As a result, the circular domains that are observed during constant compression rate experiments are usually not present in BAM images during the successive addition experiments. This feature has been discussed in Chapter 4. Even though the isotherm is flat, some may question the validity of calling this a LE/LC phase transition without morphological proof. In order to overcome this problem, a cooling experiment is suggested to map out the binodal phase boundary.

The cooling experiment is a 2D analog of cloud point experiment. The Langmuir monolayer can be compressed at a temperature above T_c to an area (A) value in the monolayer state. Then the temperature of the subphase can be continuously decreased. The appearance of circular domains in BAM images would signify the boundary for the coexistence region. The temperature (T) and surface pressure (Π) values at which the

phase coexistence starts can be recorded and used as data points along with the A values to obtain the binodal phase boundary. By repeating these experiments at different A values, it is possible to generate a phase diagram.

In order to generate a phase diagram from cooling experiments, modification of our current experimental setup or additional experiments need to be performed: (1) A thermocouple should be placed into the subphase to determine the actual subphase temperature. Although a relationship has been established between the temperatures of the subphase and the circulating system in Chapter 3 (Figure 3.2), the temperature probe on the subphase can provide more accurate temperatures because of the lag between the circulating system and the subphase. (2) The relationship between surface tension for water (γ_0) and temperature (T) needs to be verified in order to obtain actual Π values. As we discussed in Chapter 2, Π is the difference between γ_0 and the surface tension of the film covered surface (γ) at a specific temperature. Before the start of a cooling experiment, Π is set zero for the pure water surface at T_1 above T_c. After spreading and compression of PLLA Langmuir monolayers to a specific A value, Π increases indicating that γ decreases. During cooling, T decreases leading to changes in γ_0, γ, and Π. The Wilhelmy plate technique used in our experimental setup reports Π instead of γ values. As a result, the Π value (Π_{app}) recorded at a lower temperature ($T_2 < T_1$) is the difference between γ_0 at T_1 and γ at T_2. Π_{app} can not be directly used to determine the phase boundary. Instead, actual Π values (Π_{real}) can be calculated from Equation 8.1:

$$\Pi_{real} = \Pi_{app} + \Delta\gamma_0 = \Pi_{app} + \gamma_0(T_2) - \gamma_0(T_1) \qquad \text{(Eq. 8.1)}$$

where $\gamma_0(T_2)$ and $\gamma_0(T_1)$ are surface tension values at T_2 and T_1, respectively, and $\Delta\gamma_0$ is the difference in surface tension values at T_2 and T_1. As seen in Equation 8.1, both T_1 and T_2 must be known to correct Π_{app}.

Attention needs to be paid to the cooling rate when performing cooling experiments. The cooling rate must be slow enough to observe domains when they can form rather than at a kinetically limited lower T value. Preliminary results have been conducted to prove that the cooling experiments can be used to obtain the LE/LC phase transition. In this experiment, a M_n = 12.9 kg•mol^{-1} PLLA Langmuir monolayer is compressed to A = 0.208 nm^2•monomer^{-1} at 30 ^{o}C, a temperature above its T_c (= 28.6 ^{o}C). Next, the position of the barriers is held constant while the temperature of the circulating system is decreased rapidly to 10 ^{o}C with ice in a period of less than 1 minute. Time is zeroed. During the cooling process, Π_{app} decreases and circular domains are observed in BAM images after about 15 minutes (Figure 8.2), suggesting that the LE/LC phase transition has occurred. These preliminary results confirm that BAM is a good technique to reveal the start of the LE/LC phase coexistence during the cooling experiments, from which an accurate phase diagram can be generated. Furthermore, these preliminary results also reveal that a certain period of time is needed to observe biphasic behavior during fast cooling experiments. The length of the period may depend on the final temperature to which the subphase temperature is rapidly decreased. Both the length of the period and the dimension of circular domains can be used to estimate phase separation kinetics.

Knowing the kinetics for the formation of the LC phase is important for determining a slow enough cooling rate for carrying our the cloud point experiments.

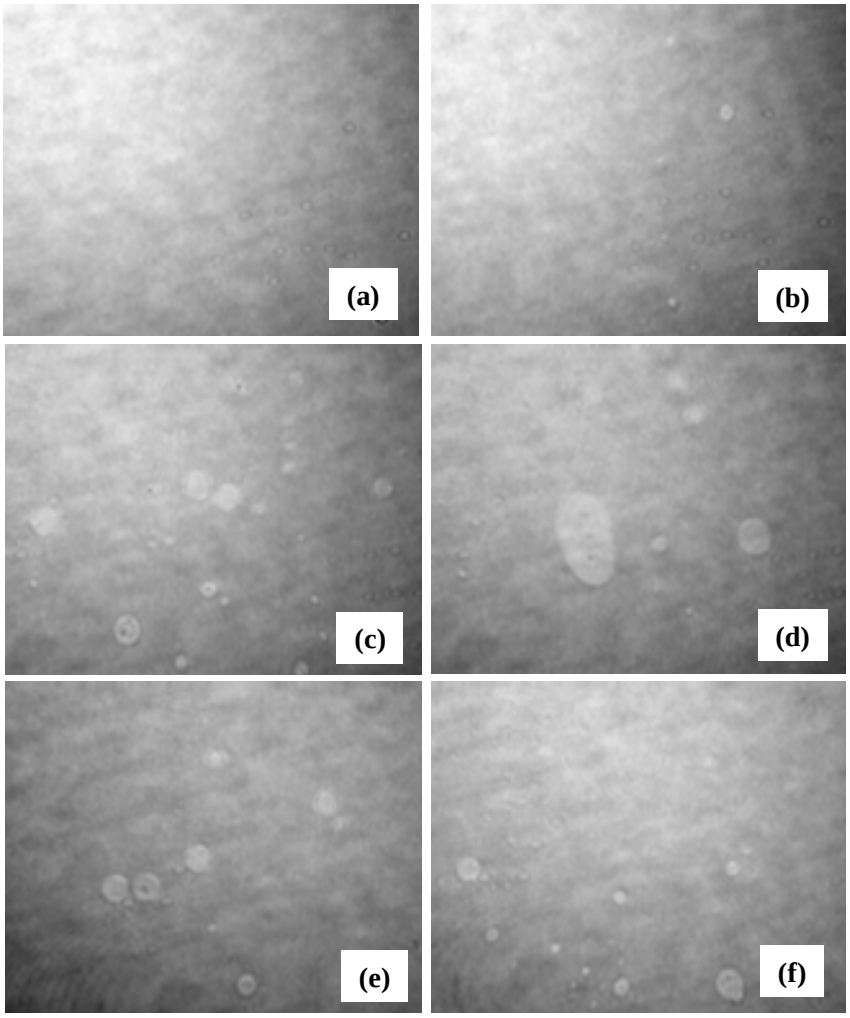

Figure 8.2: BAM images obtained during cooling experiments. A M_n = 12.9 kg•mol^{-1} PLLA Langmuir monolayer is compressed to Π = 4.0 mN•m^{-1} at 30 ^{o}C. No features are observed (a). The temperature of the circulating system is then decreased rapidly to 10 ^{o}C, and time is zeroed. Circular domains start to appear after about 15 minutes as shown in (b) – (g): (b) 15 min and Π_{app} = 0.5 mN•m^{-1}, (c) 17 min and Π_{app} = 0.2 mN•m^{-1}, (d) 19 min and Π_{app} = 0.0 mN•m^{-1}, (e) 22 min and Π_{app} = -0.3 mN•m^{-1}, and (f) 25 min and Π_{app} = - 0.4 mN•m^{-1}.

8.2.2 Collapse Mechanism above T_c

PLLA Langmuir monolayers collapse through a buckling and stacking mechanism during constant compression rate experiments at temperatures below T_c as described in Chapter 6. This mechanism may not be valid for compression experiments conducted at temperatures above T_c because PLLA molecules are no longer in a well-ordered LC phase. Instead, nucleation and growth mechanisms may be more reasonable as PLLA molecules are collapsing from a disordered LE phase. Figure 8.3 shows preliminary AFM images on LB-films obtained in the monolayer, the plateau, and the multilayer regions for a PLLA Langmuir film at 35 ^{o}C. No ordered features are observed in the LB-film prepared in the LE monolayer region (Figure 8.3a), confirming that the LE/LC phase transition is the process that leads to the ordering of PLLA molecules. The AFM image in the plateau region is consistent with the nucleation and growth process of 3D structures (Figure 8.3b). Interestingly, well-ordered square patterns are observed in the multilayer region (Figure 8.3c). The square patterns observed here have the same linear dimension as the lamellar patterns observed for PLLA LB-films prepared from the LC phase at 22.5 ^{o}C (Chapters 4 and 5). However, the square patterns are consistent with 3D features grown through a nucleation and growth mechanism.

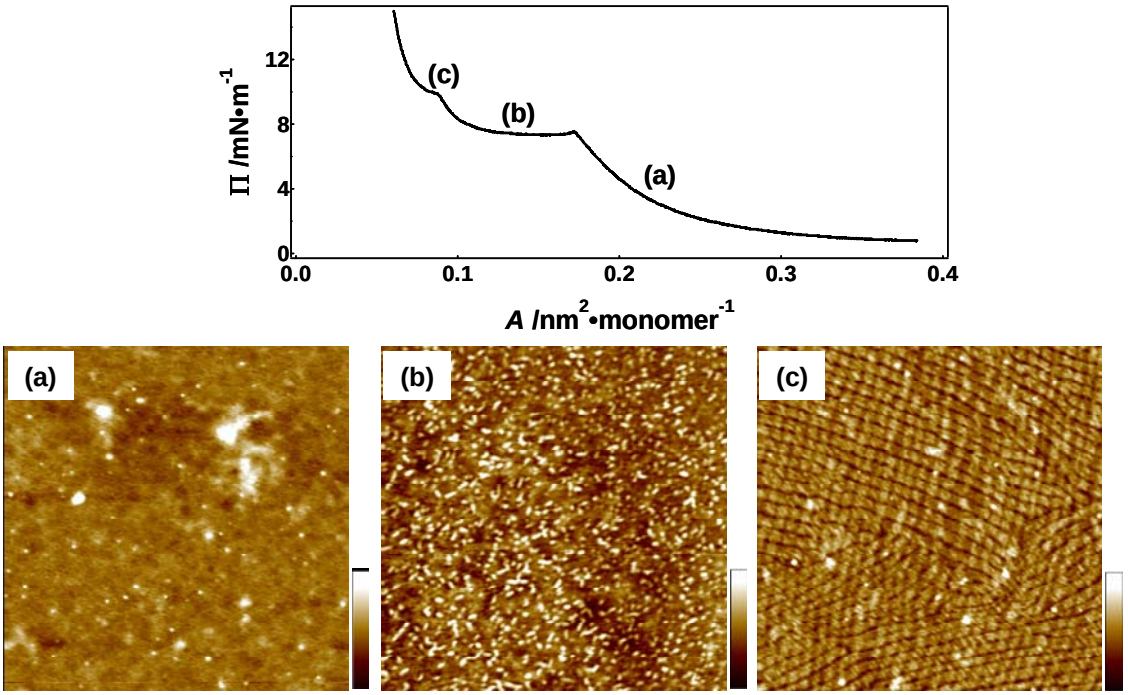

Figure 8.3: Representative tapping mode AFM height images for M_n = 12.9 kg•mol^{-1} PLLA bilayer LB-films prepared at 35 ^{o}C: (a) LE monolayer (Π = 4.0 mN•m^{-1}), (b) plateau (A ~ 0.14 nm^2•monomer^{-1}), and (c) multilayer (Π = 10.0 mN•m^{-1}) regions. The 5 nm z-scale images are 2 × 2 μm^2. The Π - A isotherm obtained at 35 ^{o}C is provided to show where the LB-films for the AFM images were prepared.

Different collapse mechanisms at temperatures above or below T_c can also be examined through hysteresis loop experiments. Figure 8.4 shows representative hysteresis loop isotherms for PLLA Langmuir films at 35 ^{o}C. The key differences between the hysteresis loops obtained at 35 ^{o}C and at 22.5 ^{o}C (Chapter 6) are: (1) After collapse, significantly larger area loss between the first and second cycle are observed for

experiments at 35 ^{o}C (~ 20 % area loss) relative to 22.5 ^{o}C (~ 6 % area loss); (2) A "spike" near the collapse pressure ($\Pi_{collapse}$) is present in the first cycle; however, it is absent during the second cycle at 35 ^{o}C; and (3) A phase transition at Π = 10.5 mN•m^{-1} also disappears at 35 ^{o}C during the second compression process. These observations confirm that PLLA monolayers at temperatures above and below T_c have different collapse mechanisms. For example, M_n = 12.9 kg•mol^{-1} PLLA collapse at 22.5 ^{o}C follows the buckling and stacking mechanism leading to multilayers that can respread onto the subphase. On the other hand, PLLA monolayers may collapse through a nucleation and growth mechanism at 35 ^{o}C. On the basis of the preliminary hysteresis loop experiments, one might speculate that 3D structures formed at 35 ^{o}C may not completely respread onto the subphase following film expansion and serve as nuclei during the second compression step.

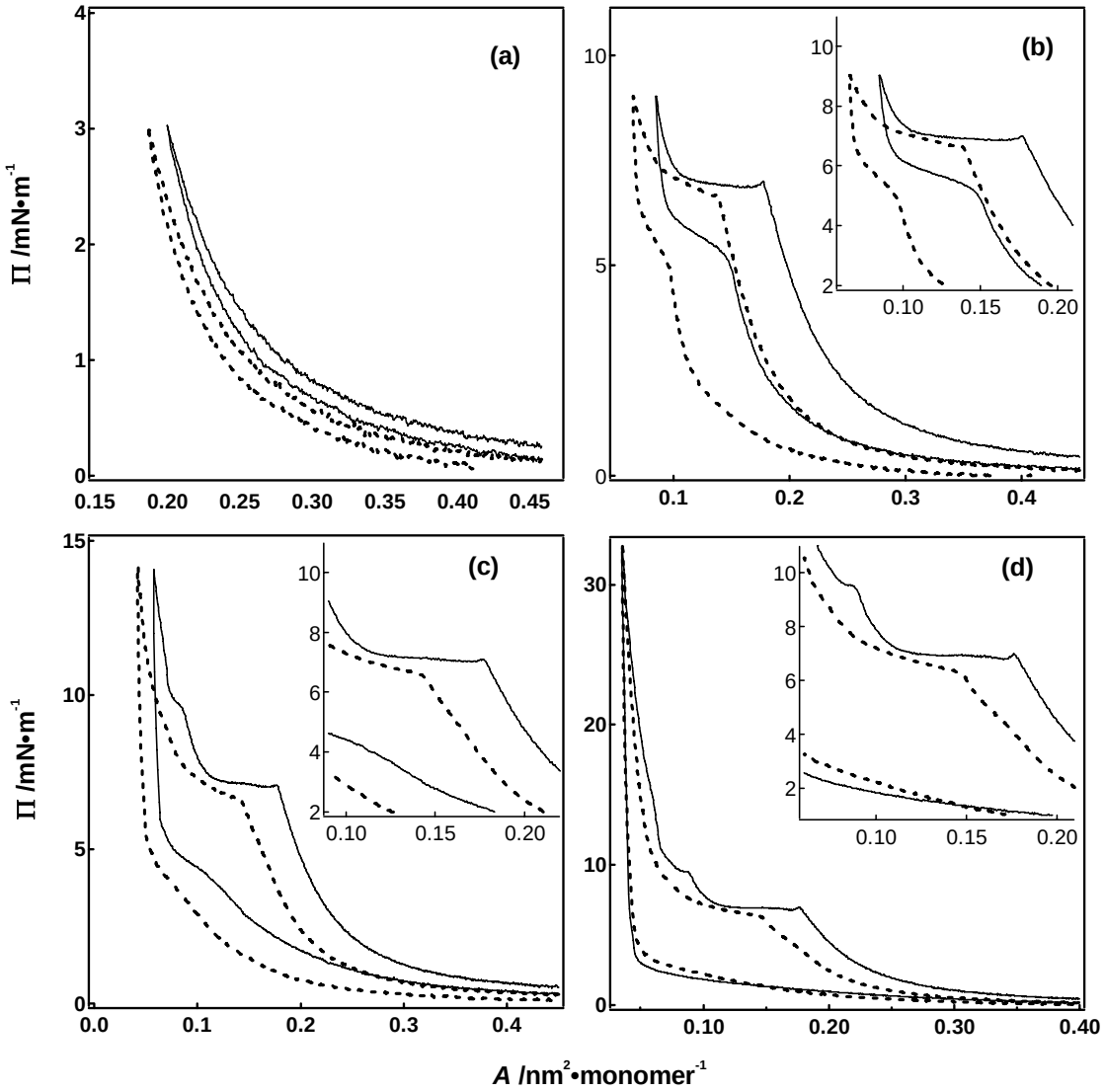

Figure 8.4: Two cycle hysteresis experiments for M_n = 12.9 kg•mol^{-1} PLLA Langmuir films at 35 ^{o}C at different target Π values: (a) 3.0 (LE monolayer), (b) 9.0, (c) 14.0, and (d) 32.0 mN•m^{-1}. The solid lines represent the isotherms during the first cycle, and the dashed lines represent the isotherms during the second cycle. Area losses between cycles and the disappearance of the "spike" for the collapse transition of the first compression step during the second cycle are highlighted in the insets.

In order to further confirm the nucleation and growth mechanism of PLLA monolayer collapse at 35 ^{o}C, several experiments need to be performed: (1) PLLA LB-films shown in Figure 8.3c may provide electron diffraction patterns that confirm the formation of 3D crystals. (2) Molar mass scaling and reflection absorption spectroscopy (RAIRS) experiments should be conducted to verify that the square patterns obtained in the multilayer region (Figure 8.3c) after collapse are comprised of single-molecule PLLA helices. The molar mass scaling experiment is quite similar to the scaling experiments discussed in Chapter 5. Control Π-*A* isotherm experiments will be needed to determine if the collapse behavior depends on molar mass. If the collapse behavior depends on molar mass, specific Π values where square patterns are present in LB-films may vary with molar mass. (3) Examination of LB-films prepared during expansion processes can provide information about whether or not respreading is complete. LB-films obtained during the second compression step may have different surface morphologies compared to the ones obtained during the first compression step, because of the presence of residual 3D structures that act like nuclei during subsequent hysteresis loops. (4) It may also be interesting to spread chloroform onto the subphase after the first hysteresis cycle to try to dissolve residual 3D structures. If chloroform can dissolve residual 3D structures, the isotherm obtained during the second compression process should be more similar to the one obtained during the first compression process. (5) The nucleation and growth process is dependent on compression rate. LB-films prepared in the plateau at different compression rates may contain nuclei of different sizes.

In addition, isobaric area relaxation experiments should also be conducted to study the nucleation and growth mechanism. Preliminary results are provided in Figure 8.5. It is observed that isobaric area relaxation processes at lower surface pressure also contain a plateau which can not be fit with the Vollhardt model. This feature may indicate a molecular rearrangement process, similar to isobaric area relaxation experiments at 22.5 ^{o}C. Isobaric area relaxation experiments at pressures close to $\Pi_{collapse}$ can be completely fit with the Vollhardt model. Similar trends are observed at 35 ^{o}C and 22.5 ^{o}C: as Π approaches $\Pi_{collapse}$, the nucleation mode changes from instantaneous to progressive, while the growth mode changes from basal area to edge, as summarized in Table 8.1. Table 8.1 also reveals that the fitting results at Π = 6.0 mN$\bullet$m^{-1} and 35 ^{o}C do not support our suggestion because this isobaric area relaxation experiment takes about 5 hours. A similar discrepancy has been observed for isobaric area relaxation experiment at Π = 5.7 mN$\bullet$m^{-1} and 22.5 ^{o}C, where evaporation of the subphase over a long experimental period was suggested to be the cause of the discrepancy as discussed in Chapter 6. In order to obtain more accurate isobaric area relaxation curves at temperatures above room temperature, evaporation of the subphase needs to be minimized. Modification of our experimental set-up should be performed for this purpose. For instance, the Langmuir trough may require a smaller and better sealed box, and the box and all the accessories inside the box need to be maintained at the same temperature as the subphase to help minimize subphase evaporation. An autoleveling device may also need to be purchased or constructed.

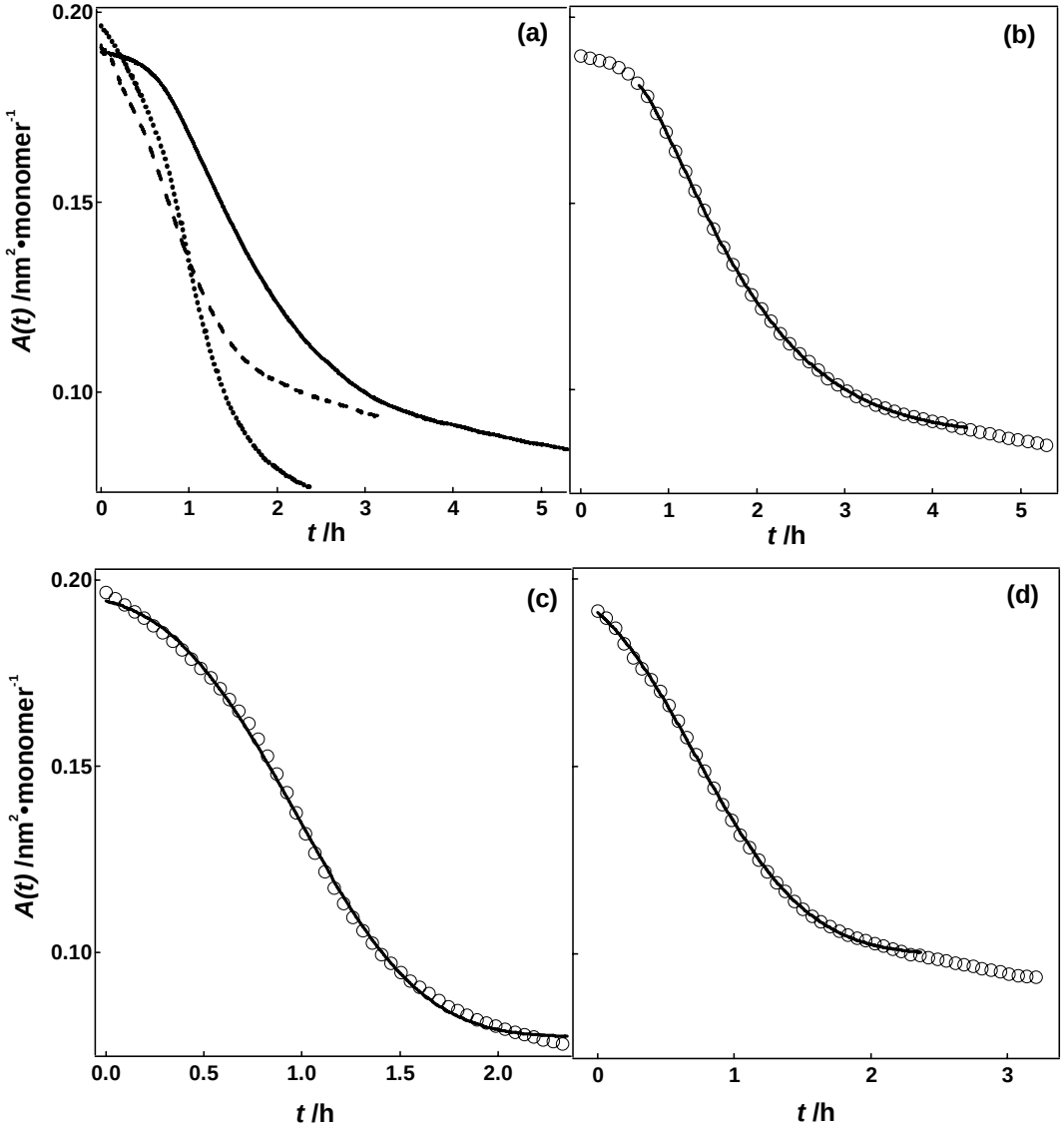

Figure 8.5: (a) $A(t)$ versus t curves for M_n = 12.9 kg•mol^{-1} PLLA Langmuir films at 35 ^{o}C during isobaric area relaxation experiments at various Π values: 6.0 (solid line), 6.3 (dotted line), and 6.6 (dashed line) mN•m^{-1}. The curves in (a) are fit with the Vollhardt model as shown in: (b) 6.0, (c) 6.3, and (d) 6.6 mN•m^{-1}. In (b) through (d), circles represent experimental data, and the solid lines represents fitting results in accordance with the Vollhardt model.

Table 8.1: Coefficients obtained from fitting the isobaric experiments in Figure 8.5 with the Vollhardt model for M_n = 12.9 kg•mol^{-1} PLLA Langmuir monolayers at various Π and T = 35 ^{o}C.

Π[a]	A_i [c]	A_∞ [c]	K_x [d]	t_i (h)	x		
6.0	**0.182**	**0.088**	**0.64**	**0.63**	**1.5**	**Instantaneous**	**Edge**
	± 0.001	± 0.001	± 0.01	± 0.01	± 0.1		
6.3	**0.196**	**0.077**	**0.21**	**-0.42**	**3.2**	**Instantaneous**	**Basal Area**
	± 0.001	± 0.001	± 0.01	± 0.02	± 0.3		
6.6	**0.197**	**0.099**	**0.46**	**-0.52**	**2.4**	**Progressive**	**Edge**
	± 0.001	± 0.001	± 0.05	± 0.02	± 0.2		

8.2.3 Controlling Surface Morphology

Our studies have shown that we have the ability to control surface morphology along with the degree of crystallinity. Substrates with various surface morphologies have been reported in this dissertation. For instance, PLLA LB-films prepared in different Langmuir film states for $T < T_c$ show uniform lamellar structures as well as stacked features. The lamellar features are destroyed upon annealing the PLLA LB-films at temperatures above PLLA's bulk crystallization temperature. PLLA substrates prepared at temperatures above T_c exhibit morphologies that are consistent with the nucleation and growth of 3D structures.

There are other methods by which new surface patterns can be obtained. For example, PLLA substrates prepared at different times during an isobaric area relaxation experiment may show different surface morphologies varying from scattered 3D domains

to perfect bilayer structures. LB-films could be one way to tap this diversity of structures. However, Y-type LB-deposition with a hydrophobic substrate may mean that only one LB-film can be prepared for each fresh monolayer spread at the A/W interface. This will be particularly true if the deposition process perturbs the isobaric area relaxation process too severely. Alternatively, if a hydrophilic substrate is used for LB-deposition, a morphological gradient can be obtained by slowly lifting the substrate through the interface from the subphase over the entire time scale of the isobaric area relaxation experiment.

Another method for controlling surface morphology is to use PLLA-related materials as a template for functional surfaces. For example, highly-ordered PLLA LB-films prepared in the LC phase are almost 100 % crystalline. In Chapter 5, the contrast in AFM images for the lamellar structures was attributed to single molecule 10_3-helices with amorphous chain ends. In principle, isocyannate chemistry can be used with an appropriate nonsolvent to functionalize the terminal hydroxyl groups. This strategy could yield films with spatially ordered functionality on the nanoscale. Similarly, PLLA could be modified prior to LB-film formation. PLLA block copolymers could be purchased or prepared to control the size of the amorphous regions in LB-films as well as the functionality. Moreover, fillers and nanoparticles can be added into the system. These additives should preferentially assemble in the amorphous regions. The properties of these additives may lead to potentially interesting electronic and optical properties.

8.2.4 Thermal Properties of PLLA LB-films

RAIRS studies along with AFM images in Chapter 6 reveal that annealing PLLA LB-films at bulk crystallization temperatures (T_x = 104 ^{o}C) is a melt crystallization process. This feature suggests that the melting temperature (T_m) of PLLA LB-films composed of single molecule 10_3-helices is below the bulk T_x. Correctly determining T_m of PLLA LB-films becomes important in addressing the difference in crystallization behavior between PLLA single molecule 10_3-helices in 2D and PLLA 10_3-helices in α crystals in bulk. T_m of PLLA LB-films can be determined using *in-situ* AFM by visualizing the changes of surface morphology or differential scanning calorimetry (DSC) from endothermic peaks.

Preliminary *in-situ* AFM results obtained during heating an as-prepared PLLA LB-film (prepared at Π = 4.0 mN•m^{-1} and T = 22.5 ^{o}C) with a heating rate of 0.5 ^{o}C•minute^{-1} are shown in Figure 8.6. Well-ordered lamellar features are present for the as-prepared LB-films prior to heating (Figure 8.6a). When the temperature is raised to ~ 66 ^{o}C, isolated droplets are observed (Figure 8.6b), suggesting that the lamellae are melting and the melting temperature is less than 66 ^{o}C. Upon further heating, the dimension of the droplets increases (Figure 8.6c-e). After being kept at T_x for 12 hours, large 3D structures are observed, a surface morphology that is similar to the one obtained by annealing the as-prepared LB-films at T_x for 10 hours under vacuum. *In-situ* AFM studies suggest that 2D lamellae first melt into droplets, which grow into larger 3D structures through Ostwald ripening.[323,324] On the basis of preliminary *in-situ* annealing

studies, it should be possible to estimate melting temperatures of 2D lamellae by *in-situ* AFM annealing. When performing these experiments, it will be important to make sure the heating rate is slow relative to the scan rate. Alternatively, step scans with respect to temperature can be used to narrow estimates of T_m.

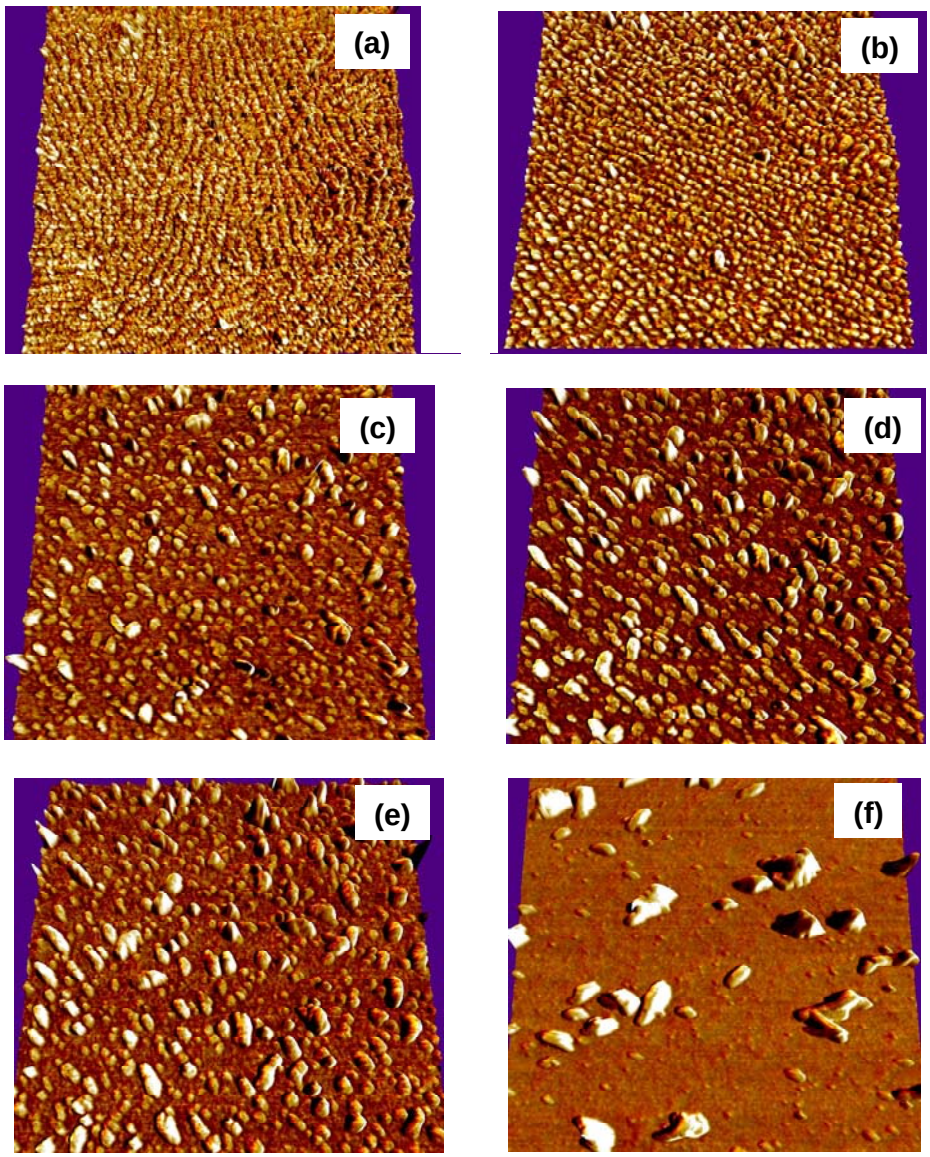

Figure 8.6: AFM images obtained during *in-situ* annealing of an as-prepared PLLA LB-film. AFM images (z-range in parenthesis) correspond to different temperatures: (a) 25 ^{o}C (3 nm), (b) 66 ^{o}C (3.4 nm), (c) 82 ^{o}C (7.6 nm), (d) 96 ^{o}C (10.5 nm), and (e) 104 ^{o}C (11 nm). (f) is obtained after keeping the LB-film at 104 ^{o}C for 10 hours. Scan sizes are 2 × 2 μm^2, and the heating rate is 0.5 ^{o}C•minute^{-1}.

DSC may also be a suitable technique for evaluating the melting temperatures of 2D lamellae. Figure 8.7a shows preliminary DSC results obtained for a 300 cycle PLLA LB-film prepared from the multilayer region at 22.5 ^{o}C. During the first heating step, two endothermic regions at ~ 40 – 80 ^{o}C and 175 ^{o}C are present. The region ~ 40 – 80 ^{o}C corresponds to the melting of PLLA LB-films; and the region around ~ 175 ^{o}C corresponds to the melting of PLLA crystals that form after the melt recrystallization process. DSC results suggest that PLLA LB-films start melting at a temperature around 40 ^{o}C. Hence, DSC may be useful for focusing *in-situ* AFM measurements to the appropriate temperature ranges.

In addition to evaluating the melting temperatures of 2D lamellae, DSC can also be used to examine thermal properties of annealed PLLA LB-films. Figure 8.7b presents preliminary DSC results for a 300 cycle PLLA LB-film that has been annealed at 104 ^{o}C for 10 hours. No endothermic peaks are observed in the temperature range of 40 – 80 ^{o}C (Figure 8.7b), in stark contrast to the as-prepared LB-film (Figure 8.7a). Instead, an exothermic peak is observed at ~ 60 ^{o}C, suggesting that the crystallization process is not complete after PLLA LB-films are annealed at 104 ^{o}C for 10 hours. In order to confirm this idea, PLLA LB-films can be annealed at 104 ^{o}C for different periods of time. The difference in the exothermic peak position and intensity can be used to evaluate the crystallization kinetics during the melt crystallization process. The crystallization kinetics can also be examined with *in-situ* RAIRS studies, which will be discussed in next section.

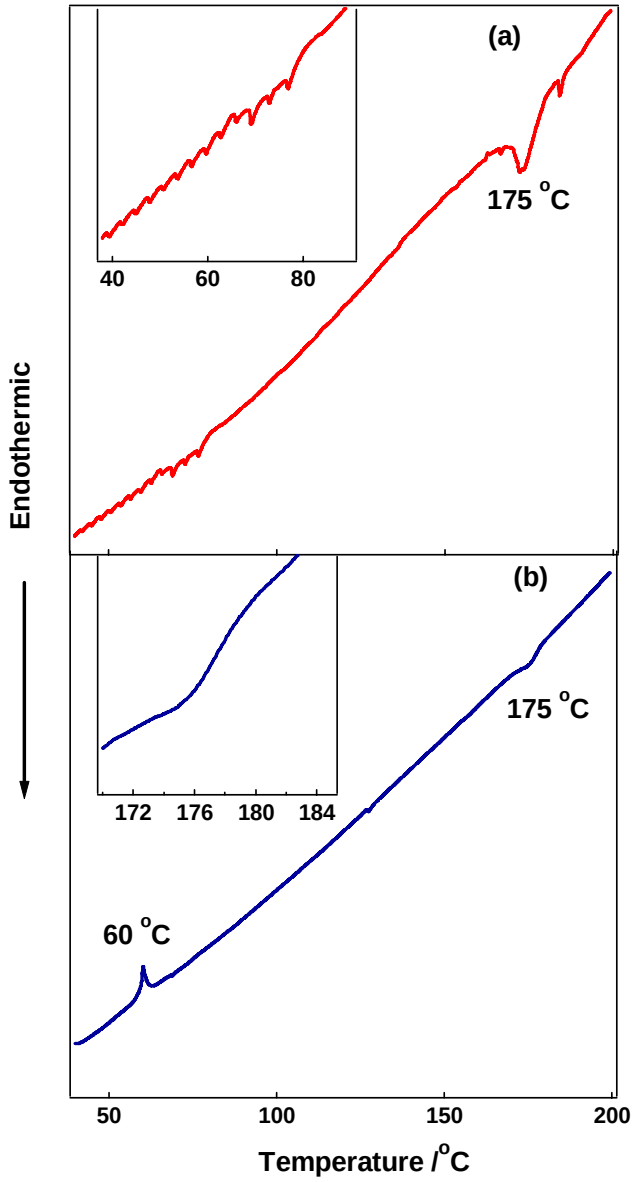

Figure 8.7: DSC thermograms during the first heating step: (a) an as-prepared 300 cycle M_n = 12.9 kg•mol^{-1} PLLA LB-film, and (b) an as-prepared 300 cycle PLLA LB-film annealed at 104 °C for 10 hours. The heating rate is 5 °C•minute^{-1}. Insets enlarge key features of the temperature ranges from 40 to 90 °C and from 170 to 185 °C in (a) and (b), respectively.

Anyone considering DSC measurements needs to consider the following experimental "trick". PLLA LB-films are deposited on thin silicon wafers for DSC measurements. In order to fit the substrates into the DSC pan, the substrates need to be broken into small pieces. During DSC measurements, the silicon wafer which has a high heat capacity absorbs heat. As a result, there is a large heat drift making it difficult to observe heat changes for PLLA thin films. In order to avoid this problem, a DSC pan with the same amount of clean silicon wafer should be used as a background instead of an empty DSC pan, the norm for bulk studies.

8.2.5 Crystallization Kinetics in PLLA LB-films with *in-situ* RAIRS

RAIRS results in Chapter 6 and preliminary DSC results for thermally annealed PLLA LB-films along with preliminary *in-situ* AFM results for as-prepared PLLA LB-films in the previous section suggest that crystallization of PLLA molecules confined in thin films may be interesting for kinetic studies. *In-situ* RAIRS becomes an appropriate technique to examine crystallization kinetics of PLLA in LB-films. Two different types of experiments are possible for PLLA LB-films: (1) observe RAIRS spectral changes as a function of temperature, and (2) observe the RAIRS spectral changes as a function of time at a specific crystallization temperature. The first approach can yield T_m and other thermal transitions, while the second is a classical isothermal crystallization or melting experiment. A heating stage has been built; however, correctly measuring the temperature of the surface remains a challenge.

Proper adhesives that can withstand up to 200 ^{o}C and do not outgas need to be used. The outgassing of adhesives can damage optics and must be avoided.

8.2.6 Cell Adhesion Studies

One of the major objectives of this research is to prepare substrates to study cell-material interactions. Cell adhesion studies have been conducted by several groups, and their techniques can be adopted to the substrates prepared in this study. For instance, Washburn *et al.* investigated the proliferation of osteoblastic MC3T3-E1 cells on surfaces with different nanometer scale structures.[1] Cells were stained with 4,6-diamidino-2-phenylindole hydrochloride (DAPI) for cell-counting measurements with automated fluorescence microscopy. In order to obtain dependence of cell proliferation on nanometer-scale roughness and a sensitive estimate of the critical roughness for which a decrease in proliferation is observed, the authors developed a gradient library by heating the substrates with a custom-built temperature gradient stage (Figure 8.8). Gradients can be prepared in this study with similar approach, or may be prepared during the LB-deposition process. For instance, a gradient PLLA LB-film can be obtained by depositing LB-films in different Langmuir film states on the same substrates for $T < T_c$. This LB-film thus prepared would have different surface roughnesses, but similar degrees of crystallinity. A gradient PLLA LB-film can also be obtained during an isobaric area relaxation experiment as described in 8.2.3. Such substrates will allow one to separate crystallinity and surface roughness effects on cell proliferation.

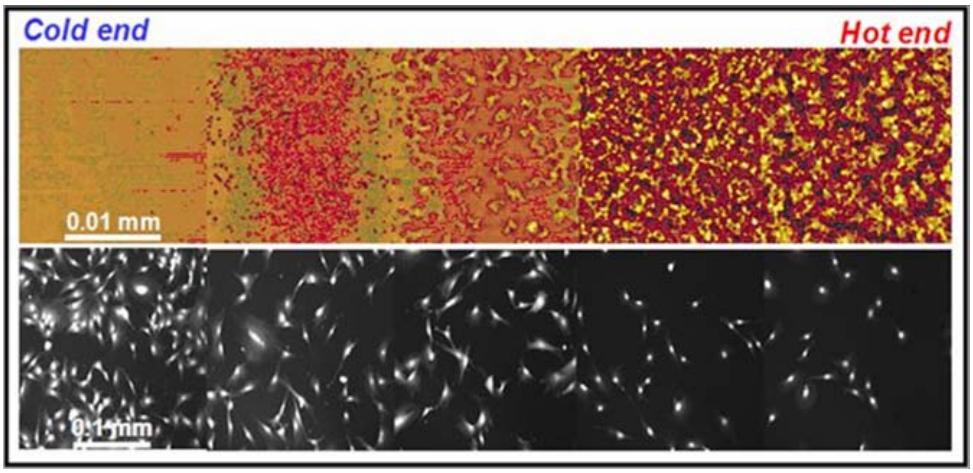

Figure 8.8: Montage of representative images of PLLA morphology from AFM measurements (top panel, field of view in each image is 20 μm), and corresponding cell count from fluorescent microscopy (bottom panel, field of view in each image is 150 μm). The PLLA substrate was prepared by spin-coating a 3 % (by mass) chloroform solution and annealing the substrate on a custom-built temperature gradient stage with limits of the stage held at 44 ^{o}C and 100 ^{o}C. It is observed that MC3T3-E1 osteoblasts cells grew better on the smooth areas (Reprinted from *Biomaterials*, *25*, Washburn, N. R. *et al.*, High-throughput investigation of osteoblast response to polymer crystallinity: influence of nanometer-scale roughness on proliferation, 1215-1224, Copyright (**2004**), with permission from Elsevier).[1]

Bibliography

(1) Washburn, N. R.; Yamada, K. M.; Simon, C. G.; Kennedy, S. B.; Amis, E. J. *Biomaterials* **2004**, *25*, 1215-1224.

(2) Park, A.; Griffith-Cima, L. G. *J. Biomed. Mater. Res.* **1996**, *31*, 117-130.

(3) Armitstead, K.; Goldbeck-Wood, G. *Adv. Polym. Sci.* **1992**, *100*, 219-312.

(4) Locklin, J.; Bao, Z. N. *Anal. Bioanal. Chem.* **2006**, *384*, 336-342.

(5) Muccini, M. *Nature Mater.* **2006**, *5*, 605-613.

(6) Sariciftci, N. S.; Smilowitz, L.; Heeger, A. J.; Wudl, F. *Science* **1992**, *258*, 1474-1476.

(7) Yu, G.; Gao, J.; Hummelen, J. C.; Wudl, F.; Heeger, A. J. *Science* **1995**, *270*, 1789-1791.

(8) Burroughes, J. H.; Bradley, D. D. C.; Brown, A. R.; Marks, R. N.; MacKay, K.; Friend, R. H.; Burns, P. L.; Holmes, A. B. *Nature* **1990**, *347*, 539-541.

(9) Brown, A. R.; Pomp, A.; Hart, C. M.; de Leeuw, D. M. *Science* **1995**, *270*, 972-974.

(10) Sirringhaus, H.; Tessler, N.; Friend, R. H. *Science* **1998**, *280*, 1741-1744.

(11) Balazs, A. C.; Singh, C.; Zhulina, E.; Chern, S.-S.; Lyatskaya, Y.; Pickett, G. *Prog. Surf. Sci.* **1997**, *55*, 181-269.

(12) Holy, C. E.; Fialkov, J. A.; Davies, J. E.; Shoichet, M. S. *J. Biomed. Mater. Res.* **2003**, *65A*, 447-453.

(13) Ma, P. X.; Zhang, R. Y. *J. Biomed. Mater. Res.* **2001**, *56*, 469-477.

(14) Sigal, G. B.; Mammen, M.; Dahmann, G.; Whitesides, G. M. *J. Am. Chem. Soc.* **1996**, *118*, 3789-3800.

(15) Halperin, A.; Tirrell, M.; Lodge, T. P. *Adv. Polym. Sci.* **1992**, *100*, 31-71.

(16) Miller, C.; Shanks, H.; Witt, A.; Rutkowski, G.; Mallapragada, S. *Biomaterials* **2001**, *22*, 1263-1269.

(17) Xia, Y. N.; Whitesides, G. M. *Annu. Rev. Mater. Sci.* **1998**, *28*, 153-184.

(18) Vozzi, G.; Flaim, C.; Ahluwalia, A.; Bhatia, S. *Biomaterials* **2003**, *24*, 2533-2540.

(19) Matsuda, T.; Mizutani, M.; Arnold, S. C. *Macromolecules* **2000**, *33*, 795-800.

(20) Lu, Y.; Chen, S. C. *Adv. Drug Deliv. Rev.* **2004**, *56*, 1621-1633.

(21) Lu, Y.; Chen, S. C. *Nanotechnology* **2003**, *14*, 505-508.

(22) Jennings, G. K.; Brantley, E. L. *Adv. Mater.* **2004**, *16*, 1983-1994.

(23) White, M. *Thin Solid Films* **1973**, *18*, 157-172.

(24) Brewer, G. E. F. In *Coatings Technology Handbook*; Tracton, A. A., Ed.; CRC Press: Boca Raton, 2006; Vol. 26, p 1-6.

(25) Petty, M. C. In *Surfaces and Interfaces for Biomaterials*; Vadgama, P., Ed.; Woodhead Publishing Ltd.: Cambridge, UK, 2005, p 60-82.

(26) Cox, J. K.; Eisenberg, A.; Lennox, R. B. *Curr. Opin. Colloid Interface Sci.* **1999**, *4*, 52-59.

(27) Petty, M. C. In *Encyclopedia of Nanoscience and Nanotechnology*; Nalwa, H. S., Ed.; American Scientific Publishers: Stevenson Ranch, 2004; Vol. 8, p 295-304.

(28) Esker, A. R.; Mengel, C.; Wegner, G. *Science* **1998**, *280*, 892-895.

(29) Gaines, G. L. *Insoluble Monolayers at Liquid-Gas Interfaces*; Interscience: New York, 1966.

(30) Peterson, I. R. In *Molecular Electronics*; Ashwell, G. J., Ed.; Research Studies Press, John Wiley and Sons: New York, 1992, p 117-206.

(31) Petty, M. C. *Langmuir-Blodgett Film: An Introduction*; Cambridge University Press: Cambridge, 1996.

(32) Sackmann, E. *Science* **1996**, *271*, 43-48.

(33) Swalen, J. D.; Allara, D. L.; Andrade, J. D.; Chandross, E. A.; Garoff, S.; Israelachvili, J.; McCarthy, T. J.; Murray, R.; Pease, R. F.; Rabolt, J. F.; Wynne, K. J.; Yu, H. *Langmuir* **1987**, *3*, 932-950.

(34) Ulman, A. *An Introduction to Ultrathin Organic Films: From Langmuir-Blodgett to Self-Assembly*; Academic Press: Boston, 1991.

(35) Zasadzinski, J. A.; Viswana, T. R.; Madsen, L.; Garnaes, J.; Schwartz, D. K. *Science* **1994**, *263*, 1726-1733.

(36) Kaganer, V. M.; Mohwald, H.; Dutta, P. *Rev. Mod. Phys.* **1999**, *71*, 779-819.

(37) Braslau, A.; Deutsch, M.; Pershan, P. S.; Weiss, A. H.; Alsnielsen, J.; Bohr, J. *Phys. Rev. Lett.* **1985**, *54*, 114-117.

(38) Debreczeny, M. P.; Svec, W. A.; Wasielewski, M. R. *Science* **1996**, *274*, 584-587.

(39) Cantor, R. S.; Dill, K. A. *Langmuir* **1986**, *2*, 331-337.

(40) Shin, S.; Wang, Z. G.; Rice, S. A. *J. Chem. Phys.* **1990**, *92*, 1427-1434.

(41) Tabor, D. *J. Colloid Interface Sci.* **1980**, *75*, 240-245.

(42) Scott, J. C. *Oil on Troubled Waters. A Bibliography on the Effects of Surface-active Films on Surface-wave Motions*; Multi-Science Publishing Co. Ltd: London, 1979.

(43) Dynarowicz-Latka, P.; Dhanabalan, A.; Oliveira, O. N. *Adv. Colloid Interface Sci.* **2001**, *91*, 221-293.

(44) Franklin, B. *Phil. Trans. Res. Soc. (London)* **1774**, *64*, 445-460.

(45) Giles, C. H. *Chem. Ind.* **1969**, 1616-1624.

(46) Giles, C. H.; Forrester, S. D. *Chem. Ind.* **1970**, 80-87.

(47) Tanford, C. *Ben Franklin Stilled the Waves*; Duke University Press: Durham and London, 1989.

(48) Pockels, A. *Nature* **1891**, *43*, 437-439.

(49) Pockels, A. *Nature* **1893**, *48*, 152-154.

(50) Pockels, A. *Nature* **1894**, *50*, 223-224.

(51) Rayleigh, L. *Phil. Mag.* **1899**, *48*, 321-337.

(52) Hardy, W. B. *Proc. Roy. Soc. London* **1912**, *A86*, 610-635.

(53) Langmuir, I. *J. Am. Chem. Soc.* **1917**, *39*, 1848-1906.

(54) Langmuir, I. *Trans. Faraday Soc.* **1920**, *15*, 62-74.

(55) Blodgett, K. B. *J. Am. Chem. Soc.* **1935**, *57*, 1007-1022.

(56) Blodgett, K. B.; Langmuir, I. *Phys. Rev.* **1937**, *51*, 964-982.

(57) Gaines, G. L.; Roberts, R. W. *Nature* **1963**, *197*, 787.

(58) Naselli, C.; Rabe, J. P.; Rabolt, J. F.; Swalen, J. D. *Thin Solid Films* **1985**, *134*, 173-178.

(59) Stenhagen, E. *Trans. Faraday Soc.* **1938**, *34*, 1328-1337.

(60) Knobler, C. M. *Science* **1990**, *249*, 870-874.

(61) Williams, A. A.; Day, B. S.; Kite, B. L.; McPherson, M. K.; Slebodnick, C.; Morris, J. R.; Gandour, R. D. *Chem. Comm.* **2005**, *40*, 5053-5055.

(62) Collins, S. J.; Mahesh, G. N.; Radhakrishnan, G.; Dhanabalan, A. *Colloids Surf. A: Physicochem. Eng. Aspects* **1995**, *95*, 293-297.

(63) Ringard-Lefebvre, C.; Baszkin, A. *Langmuir* **1994**, *10*, 2376-2381.

(64) Walton, A. J. *Phys. Educ.* **1972**, *7*, 491-498.

(65) Petty, M. C.; Barlow, W. A. In *Langmuir-Blodgett Films*; Roberts, G., Ed.; Plenum Press: New York, 1990, p 93-132.

(66) Wilhelmy, L. *Ann. Physik* **1863**, *195*, 177-217.

(67) Fox, H. W.; Zisman, W. A. *Rev. Sci. Instrum.* **1948**, *19*, 274.

(68) Ellison, A. H. *J. Phys. Chem.* **1962**, *66*, 1867-1872.

(69) Richard, J.; Barraud, A.; Vandevyver, M.; Ruaudelteixier, A. *Thin Solid Films* **1988**, *159*, 207-214.

(70) Atkins, P.; de Paula, J. *Physical Chemistry*; 8 ed.; W. H. Freeman: New York, 2006.

(71) Pallas, N. R.; Pethica, B. A. *Langmuir* **1985**, *1*, 509-513.

(72) Riviere, S.; Henon, S.; Meunier, J.; Schwartz, D. K.; Tsao, M. W.; Knobler, C. M. *J. Chem. Phys.* **1994**, *101*, 10045-10051.

(73) Gaonkar, A. G.; Neuman, R. D. *J. Colloid Interface Sci.* **1984**, *98*, 112-119.

(74) Islam, M. N.; Kato, T. *Langmuir* **2005**, *21*, 10920-10922.

(75) Overbeck, G. A.; Honig, D.; Mobius, D. *Langmuir* **1993**, *9*, 555-560.

(76) Mowald, H. *Rep. Prog. Phys.* **1993**, *56*, 653-685.

(77) Ries, H. E.; Kimball, W. A. *Proc. Intern. Congr. Surface Activity, 2nd* **1957**, *1*, 75-84.

(78) Mann, E. K.; Langevin, D. *Langmuir* **1991**, *7*, 1112-1117.

(79) Henon, S.; Meunier, J. *Rev. Sci. Instrum.* **1991**, *62*, 936-939.

(80) Honig, D.; Mobius, D. *J. Phys. Chem.* **1991**, *95*, 4590-4592.

(81) McConnell, H. M. *Annu. Rev. Phys. Chem.* **1991**, *42*, 171-195.

(82) Dutta, P.; Peng, J. B.; Lin, B.; Ketterson, J. B.; Prakash, M.; Georgopoulos, P.; Ehrlich, S. *Phys. Rev. Lett.* **1987**, *58*, 2228-2231.

(83) Earnshaw, J. C.; McGivern, R. C.; Winch, P. J. *J. Phys. (Paris)* **1988**, *49*, 1271-1293.

(84) Langevin, D. *J. Colloid Interface Sci.* **1981**, *80*, 412-425.

(85) Brooks, C. F.; Fuller, G. G.; Frank, C. W.; Robertson, C. R. *Langmuir* **1999**, *15*, 2450-2459.

(86) Deng, J. J. Ph. D Dissertation, Virginia Tech, Blacksburg, VA 2005.

(87) Bhattacharyya, K.; Castro, A.; Sitzmann, E. V.; Eisenthal, K. B. *J. Chem. Phys.* **1988**, *89*, 3376-3377.

(88) Rasing, T.; Shen, Y. R.; Kim, M. W.; Valint, P.; Bock, J. *Phys. Rev. A* **1985**, *31*, 537-539.

(89) Drude, P. *Ann. Physik* **1891**, *279*, 126-157.

(90) Meunier, J. *Colloids Surf. A: Physicochem. Eng. Aspects* **2000**, *171*, 33-40.

(91) Riviere, S.; Henon, S.; Meunier, J. *Phys. Rev. E* **1994**, *49*, 1375-1382.

(92) Tabe, Y.; Yokoyama, H. *Langmuir* **1995**, *11*, 699-704.

(93) Deschenaux, R.; Megert, S.; Zumbrunn, C.; Ketterer, J.; Steiger, R. *Langmuir* **1997**, *13*, 2363-2372.

(94) Gehlert, U.; Vollhardt, D.; Brezesinski, G.; Mohwald, H. *Langmuir* **1996**, *12*, 4892-4896.

(95) Vollhardt, D.; Melzer, V. *J. Phys. Chem. B* **1997**, *101*, 3370-3375.

(96) Werkman, P. J.; Schouten, A. J.; Noordegraaf, M. A.; Kimkes, P.; Sudholter, E. J. R. *Langmuir* **1998**, *14*, 157-164.

(97) Brezesinski, G.; Scalas, E.; Struth, B.; Mohwald, H.; Bringezu, F.; Gehlert, U.; Weidemann, G. *J. Phys. Chem.* **1995**, *99*, 8758-8762.

(98) Friedenberg, M. C.; Fuller, G. G.; Frank, C. W.; Robertson, C. R. *Langmuir* **1996**, *12*, 1594-1599.

(99) Lauger, J.; Robertson, C. R.; Frank, C. W.; Fuller, G. G. *Langmuir* **1996**, *12*, 5630-5635.

(100) Overbeck, G. A.; Honig, D.; Wolthaus, L.; Gnade, M.; Mobius, D. *Thin Solid Films* **1994**, *242*, 26-32.

(101) Weidemann, G.; Gehlert, U.; Vollhardt, D. *Langmuir* **1995**, *11*, 864-871.

(102) Honig, D.; Mobius, D. *Chem. Phys. Lett.* **1992**, *195*, 50-52.

(103) Schaub, M.; Mathauer, K.; Schwiegk, S.; Albouy, P. A.; Wenz, G.; Wegner, G. *Thin Solid Films* **1992**, *210*, 397-400.

(104) Crisp, D. J. *J. Colloid Sci.* **1946**, *1*, 49-70.

(105) Fox, H. W.; Taylor, W.; Zisman, W. A. *J. Ind. Eng. Chem.* **1947**, *39*, 1401-1409.

(106) Noll, W.; Steinbach, H.; Sucker, C. *J. Polym. Sci., Polym. Symp.* **1971**, *34*, 123-139.

(107) Granick, S.; Clarson, S. J.; Formoy, T. R.; Semlyen, J. A. *Polymer* **1985**, *26*, 925-929.

(108) Fang, J. Y.; Dennin, M.; Knobler, C. M.; Godovsky, Y. K.; Makarova, N. N.; Yokoyama, H. *J. Phys. Chem. B* **1997**, *101*, 3147-3154.

(109) Buzin, A. I.; Godovsky, Y. K.; Makarova, N. N.; Fang, J. Y.; Wang, X.; Knobler, C. M. *J. Phys. Chem. B* **1999**, *103*, 11372-11381.

(110) Mann, E. K.; Henon, S.; Langevin, D.; Meunier, J. *J. Phys. II* **1992**, *2*, 1683-1704.

(111) Watanabe, M.; Kosaka, Y.; Sanui, K.; Ogata, N.; Oguchi, K.; Yoden, T. *Macromolecules* **1987**, *20*, 452-454.

(112) Watanabe, M.; Kosaka, Y.; Oguchi, K.; Sanui, K.; Ogata, N. *Macromolecules* **1988**, *21*, 2997-3003.

(113) Shuler, R. L.; Zisman, W. A. *J. Phys. Chem.* **1970**, *74*, 1523-1534.

(114) Sauer, B. B.; Yu, H. *Macromolecules* **1989**, *22*, 786-791.

(115) Henderson, J. A.; Richards, R. W.; Penfold, J.; Thomas, R. K.; Lu, J. R. *Macromolecules* **1993**, *26*, 4591-4600.

(116) Kuzmenka, D. J.; Granick, S. *Macromolecules* **1988**, *21*, 779-782.

(117) Rennie, A. R.; Crawford, R. J.; Lee, E. M.; Thomas, R. K.; Crowley, T. L.; Roberts, S.; Qureshi, M. S.; Richards, R. W. *Macromolecules* **1989**, *22*, 3466-3475.

(118) Sauer, B. B.; Yu, H.; Kim, M. W. *Langmuir* **1989**, *5*, 278-280.

(119) Faure, M. C.; Bassereau, P.; Lee, L. T.; Menelle, A.; Lheveder, C. *Macromolecules* **1999**, *32*, 8538-8550.

(120) Ahmed, F.; Hategan, A.; Discher, D. E.; Discher, B. M. *Langmuir* **2003**, *19*, 6505-6511.

(121) Kim, C.; Yu, H. *Langmuir* **2003**, *19*, 4460-4464.

(122) Cardenas-Valera, A. E.; Bailey, A. I. *Colloids Surf. A: Physicochem. Eng. Aspects* **1993**, *79*, 115-127.

(123) Harris, J. M. In *Poly(ethylene glycol) Chemistry*; Harris, J. M., Ed.; Plenum Press: New York, 1992, p 1-14.

(124) Lasic, D. D.; Needham, D. *Chem. Rev.* **1995**, *95*, 2601-2628.

(125) Naumann, C. A.; Brooks, C. F.; Fuller, G. G.; Knoll, W.; Frank, C. W. *Langmuir* **1999**, *15*, 7752-7761.

(126) Naumann, C. A.; Brooks, C. F.; Wiyatno, W.; Knoll, W.; Fuller, G. G.; Frank, C. W. *Macromolecules* **2001**, *34*, 3024-3032.

(127) Foreman, M. B.; Coffman, J. P.; Murcia, M. J.; Cesana, S.; Jordan, R.; Smith, G. S.; Naumann, C. A. *Langmuir* **2003**, *19*, 326-332.

(128) Gabrielli, G.; Guarini, G. G. T. *J. Colloid Interface Sci.* **1978**, *64*, 185-187.

(129) Sutherland, J. E.; Miller, M. L. *J. Polym. Sci., Polym. Lett.* **1969**, *7*, 871-876.

(130) Penner, T. L.; Mostchmann, H. R.; Armstrong, N. J.; Ezenyilimba, M. C.; Williams, D. J. *Nature* **1994**, *367*, 49-51.

(131) Mengel, C.; Esker, A. R.; Meyer, W. H.; Wegner, G. *Langmuir* **2002**, *18*, 6365-6372.

(132) Naito, K. *J. Colloid Interface Sci.* **1989**, *131*, 218-225.

(133) Lee, W. K.; Nowak, R. W.; Gardella, J. A. *Langmuir* **2002**, *18*, 2309-2312.

(134) Lee, W. K.; Gardella, J. A. *Langmuir* **2000**, *16*, 3401-3406.

(135) Li, B. B.; Wu, Y. T.; Liu, M. H.; Esker, A. R. *Langmuir* **2006**, *22*, 4902-4905.

(136) Garlotta, D. *J. Polym. Environ.* **2002**, *9*, 63-84.

(137) Drumright, R. E.; Gruber, P. R.; Henton, D. E. *Adv. Mater.* **2000**, *12*, 1841-1846.

(138) Shih, C. *J. Control. Release* **1995**, *34*, 9-15.

(139) Ivanova, T.; Panaiotov, I.; Boury, F.; Proust, J. E.; Benoit, J. P.; Verger, R. *Colloids Surf. B: Biointerfaces* **1997**, *8*, 217-225.

(140) Ivanova, T.; Panaiotov, I.; Boury, F.; Saulnier, P.; Proust, J. E.; Verger, R. *Colloids Surf. B: Biointerfaces* **2000**, *17*, 241-254.

(141) Migliaresi, C.; Cohn, D.; DeLollis, A.; Fambri, L. *J. Appl. Polym. Sci.* **1991**, *43*, 83-95.

(142) Hoogsteen, W.; Postema, A. R.; Pennings, A. J.; Tenbrinke, G.; Zugenmaier, P. *Macromolecules* **1990**, *23*, 634-642.

(143) Kricheldorf, H. R.; Kreiser-Saunders, I.; Boettcher, C. *Polymer* **1995**, *36*, 1253-1259.

(144) Okihara, T.; Tsuji, M.; Kawaguchi, A.; Katayama, K.; Tsuji, H.; Hyon, S. H.; Ikada, Y. *J. Macromol. Sci., Phys.* **1991**, *B30*, 119-140.

(145) De Santis, P.; Kovacs, A. J. *Biopolymers* **1968**, *6*, 299-306.

(146) Marega, C.; Marigo, A.; Dinoto, V.; Zannetti, R.; Martorana, A.; Paganetto, G. *Makromolekulare Chemie* **1992**, *193*, 1599-1606.

(147) Ikada, Y.; Jamshidi, K.; Tsuji, H.; Hyon, S. H. *Macromolecules* **1987**, *20*, 904-906.

(148) Pyda, M.; Bopp, R. C.; Wunderlich, B. *J. Chem. Thermodynamics* **2004**, *36*, 731-742.

(149) Abe, H.; Kikkawa, Y.; Inoue, Y.; Doi, Y. *Biomacromolecules* **2001**, *2*, 1007-1014.

(150) Kalb, B.; Pennings, A. J. *Polymer* **1980**, *21*, 607-612.

(151) Miyata, T.; Masuko, T. *Polymer* **1997**, *38*, 4003-4009.

(152) Iwata, T.; Doi, Y. *Macromolecules* **1998**, *31*, 2461-2467.

(153) Brinkhuis, R. H. G.; Schouten, A. J. *Macromolecules* **1991**, *24*, 1487-1495.

(154) Kumaki, J.; Kawauchi, T.; Yashima, E. *J. Am. Chem. Soc.* **2005**, *127*, 5788-5789.

(155) Pelletier, I.; Pezolet, M. *Macromolecules* **2004**, *37*, 4967-4973.

(156) Bourque, H.; Laurin, I.; Pezolet, M.; Klass, J. M.; Lennox, R. B.; Brown, G. R. *Langmuir* **2001**, *17*, 5842-5849.

(157) Honig, E. P. *J. Colloid Interface Sci.* **1973**, *43*, 66-72.

(158) Holley, C.; Bernstein, S. *Phys. Rev.* **1937**, *52*, 525.

(159) Cemel, A.; Fort, T.; Lando, J. B. *J. Polym. Sci., Polym. Chem. Ed.* **1972**, *10*, 2061-2083.

(160) Langmuir, I.; Schaefer, V. J.; Sobotka, H. *J. Am. Chem. Soc.* **1937**, *59*, 1751-1759.

(161) Honig, E. P.; Hengst, J. H.; den Engelsen, D. *J. Colloid Interface Sci.* **1973**, *45*, 92-102.

(162) Langmuir, I.; Schaefer, V. J. *J. Am. Chem. Soc.* **1938**, *60*, 1351-1360.

(163) Bubert, H.; Jenett, H. *Surface and Thin Film Analysis*; Wiley-VCH: Weinheim, 2002.

(164) Binnig, G.; Quate, C. F.; Gerber, C. *Phys. Rev. Lett.* **1986**, *56*, 930-933.

(165) Sarid, D. *Scanning Force Microscopy*; Oxford University Press: New York, 1991.

(166) Friedbacher, G. In *Surface and Thin Film Analysis*; Bubert, H., Jenett, H., Eds.; Wiley-VCH: Weinheim, 2002.

(167) Meyer, G.; Amer, N. M. *Appl. Phys. Lett.* **1988**, *53*, 1045-1047.

(168) Hansma, P. K.; Cleveland, J. P.; Radmacher, M.; Walters, D. A.; Hillner, P. E.; Bezanilla, M.; Fritz, M.; Vie, D.; Hansma, H. G.; Prater, C. B.; Massie, J.; Fukunaga, L.; Gurley, J.; Elings, V. *Appl. Phys. Lett.* **1994**, *64*, 1738-1740.

(169) Patil, R.; Reneker, D. H. *Polymer* **1994**, *35*, 1909-1914.

(170) Reneker, D. H.; Mazur, J. *Polymer* **1988**, *29*, 3-13.

(171) Zasadzinski, J. A.; Viswanathan, R.; Schwartz, D. K.; Garnaes, J.; Madsen, L.; Chiruvolu, S.; Woodward, J. T.; Longo, M. L. *Colloids Surf. A: Physicochem. Eng. Aspects* **1994**, *93*, 305-333.

(172) DeRose, J. A.; Leblanc, R. M. *Surf. Sci. Rep.* **1995**, *22*, 73-126.

(173) Viswanathan, R.; Schwartz, D. K.; Madsen, L.; Zasadzinski, J. A. *Mater. Res. Soc. Sym. Proc.* **1994**, *332*, 429-434.

(174) Reading, M.; Hourston, D. J.; Song, M.; Pollock, H. M.; Hammiche, A. *Am. Lab.* **1998**, *30*, 13-17.

(175) Russell, T. P. *Mater. Sci. Rep.* **1990**, *5*, 171-271.

(176) Zabel, H. *Appl. Phys. A* **1994**, *58*, 159-168.

(177) Gibson, P. N. In *Surface and Thin Film Analysis*; Bubert, H., Jenett, H., Eds.; Wiley-VCH: Weinheim, 2002, p 208-221.

(178) Daillant, J.; Gibaud, A. *X-ray and Neutron Reflectivity: Principles and Applications*; Springer: New York, 1999.

(179) Kiessig, H. *Ann. Physik* **1931**, *10*, 715-768.

(180) Kiessig, H. *Ann. Physik* **1931**, *10*, 769-788.

(181) Parratt, L. G. *Phys. Rev.* **1954**, *95*, 359-369.

(182) Thompson, C.; Saraf, R. F.; Jordan-Sweet, J. L. *Langmuir* **1997**, *13*, 7135-7140.

(183) Kundu, S.; Datta, A.; Hazra, S. *Phys. Rev. E* **2006**, *73*, 051608/1-051608/7.

(184) Malkova, S.; Long, F.; Stahelin, R. V.; Pingali, S. V.; Murray, D.; Cho, W. H.; Schlossman, M. L. *Biophys. J.* **2005**, *89*, 1861-1873.

(185) Gidalevitz, D.; Huang, Z. Q.; Rice, S. A. *Proc. Natl. Acad. Sci. U. S. A.* **1999**, *96*, 2608-2611.

(186) Arias-Marin, E.; Arnault, J. C.; Guillon, D.; Maillou, T.; Le Moigne, J.; Geffroy, B.; Nunzi, J. M. *Langmuir* **2000**, *16*, 4309-4318.

(187) Kapp, D. S.; Wainfan, N. *Phys. Rev.* **1965**, *138*, 1490-1495.

(188) Lesslauer, W. *Acta Cryst. B* **1974**, *B30*, 1932-1937.

(189) Matsuda, A.; Sugi, M.; Fukui, T.; Lizima, S.; Miyahara, M.; Otsubo, Y. *J. Appl. Phys.* **1977**, *48*, 771-774.

(190) Panambur, G.; Robert, C.; Zhang, Y. B.; Bazuin, C. G.; Ritcey, A. M. *Langmuir* **2003**, *19*, 8859-8866.

(191) Schalchli, A.; Benattar, J. J.; Tchoreloff, P.; Zhang, P.; Coleman, A. W. *Langmuir* **1993**, *9*, 1968-1970.

(192) Vidya, V.; Ambily, S.; Narang, S. N.; Major, S.; Talwar, S. S. *Colloids Surf. A: Physicochem. Eng. Aspects* **2002**, *198*, 383-388.

(193) Bisset, D. C.; Iball, J. *Proc. Phys. Soc., London* **1954**, *67A*, 315-322.

(194) Pomerantz, M.; Segmuller, A. *Thin Solid Films* **1980**, *68*, 33-45.

(195) Pomerantz, M.; Segmuller, A.; Netzer, L.; Sagiv, J. *Thin Solid Films* **1985**, *132*, 153-162.

(196) Hinrichs, K. In *Surface and Thin Film Analysis*; Bubert, H., Jenett, H., Eds.; Wiley-VCH: Weinheim, 2002.

(197) Trenary, M. *Annu. Rev. Phys. Chem.* **2000**, *51*, 381-403.

(198) Greenler, R. G. *J. Chem. Phys.* **1969**, *50*, 1963-1968.

(199) Greenler, R. G. *J. Chem. Phys.* **1966**, *44*, 310-315.

(200) Ferguson-McPherson, M. K. Ph. D Dissertation, Virginia Tech, Blacksburg, VA 2005.

(201) Hayden, B. E. In *Vibrational Spectroscopy of Molecules on Surfaces*; Yates, J. T., Madey, T. E., Eds.; Plenum Press: New York, 1987, p 267-344.

(202) Allara, D. L.; Swalen, J. D. *J. Phys. Chem.* **1982**, *86*, 2700-2704.

(203) Porter, M. D.; Bright, T. B.; Allara, D. L.; Chidsey, C. E. D. *J. Am. Chem. Soc.* **1987**, *109*, 3559-3568.

(204) Snyder, R. G.; Maroncelli, M.; Strauss, H. L.; Hallmark, V. M. *J. Phys. Chem.* **1986**, *90*, 5623-5630.

(205) Naselli, C.; Rabolt, J. F.; Swalen, J. D. *J. Chem. Phys.* **1985**, *82*, 2136-2140.

(206) Dote, J. L.; Mowery, R. L. *J. Phys. Chem.* **1988**, *92*, 1571-1575.

(207) Hayes, N. W.; Beamson, G.; Clark, D. T.; Law, D. S.-L.; Raval, R. *Surf. Interface Anal.* **1996**, *24*, 723-728.

(208) Esker, A. R.; Grull, H.; Satija, S. K.; Han, C. C. *J. Polym. Sci., Part B: Polym. Phys.* **2004**, *42*, 3248-3257.

(209) Welp, K. A.; Co, C.; Wool, R. P. *J. Neutron. Res.* **1999**, *8*, 37-46.

(210) Knobler, C. M.; Desai, R. C. *Annu. Rev. Phys. Chem.* **1992**, *43*, 207-236.

(211) Mohwald, H. *Annu. Rev. Phys. Chem.* **1990**, *41*, 441-476.

(212) Dutta, P. *Studies in Interface Science* **2002**, *16*, 1-12.

(213) Kaganer, V. M.; Loginov, E. B. *Phys. Rev. E* **1995**, *51*, 2237-2249.

(214) Deng, J. J.; Viers, B. D.; Esker, A. R.; Anseth, J. W.; Fuller, G. G. *Langmuir* **2005**, *21*, 2375-2385.

(215) Ybert, C.; Lu, W. X.; Moller, G.; Knobler, C. M. *J. Phys.: Condens. Matter* **2002**, *14*, 4753-4762.

(216) Hifeda, Y. F.; Rayfield, G. W. *Langmuir* **1992**, *8*, 197-200.

(217) Firpo, J. L.; Dupin, J. J.; Albinet, G.; Bois, A.; Casalta, L.; Baret, J. F. *J. Chem. Phys.* **1978**, *68*, 1369-1374.

(218) Shin, K.; Rafailovich, M. H.; Sokolov, J.; Chang, D. M.; Cox, J. K.; Lennox, R. B.; Eisenberg, A.; Gibaud, A.; Huang, J.; Hsu, S. L.; Satija, S. K. *Langmuir* **2001**, *17*, 4955-4961.

(219) Ruckenstein, E.; Li, B. Q. *J. Phys. Chem. B* **1998**, *102*, 981-989.

(220) Baskar, G.; Gaspar, L. J. M.; Mandal, A. B. *Langmuir* **2003**, *19*, 9051-9057.

(221) Lee, I. C.; Frank, C. W.; Wursch, A.; Hedrick, J. L. *Polym. Prepr. (Am. Chem. Soc., Div. Polym. Chem.)* **2005**, *46*, 494-495.

(222) Boury, F.; Gulik, A.; Dedieu, J. C.; Proust, J. E. *Langmuir* **1994**, *10*, 1654-1656.

(223) Klass, J. M.; Lennox, R. B.; Brown, G. R.; Bourque, H.; Pezolet, M. *Langmuir* **2003**, *19*, 333-340.

(224) Romeu, N. V.; Minones, J.; Iribarnegaray, E.; Conde, Q.; Casas, M. *Colloid Polym. Sci.* **1997**, *275*, 580-586.

(225) Boury, F.; Olivier, E.; Proust, J. E.; Benoit, J. P. *J. Colloid Interface Sci.* **1993**, *160*, 1-9.

(226) Langer, R.; Tirrell, D. A. *Nature* **2004**, *428*, 487-492.

(227) Allen, D.; Westerblad, H. *Science* **2004**, *305*, 1112-1113.

(228) Islam, M. N.; Kato, T. *Langmuir* **2005**, *21*, 2419-2424.

(229) Yue, X. L.; Steffen, P.; Dobner, B.; Brezesinski, G.; Mohwald, H. *Colloids Surf. A: Physicochem. Eng. Aspects* **2004**, *250*, 57-65.

(230) Grigoriev, D.; Miller, R.; Wustneck, R.; Wustneck, N.; Pison, U.; Mohwald, H. *J. Phys. Chem. B* **2003**, *107*, 14283-14288.

(231) Yue, B. Y.; Jackson, C. M.; Taylor, J. A. G.; Mingins, J.; Pethica, B. A. *J. Chem. Soc., Faraday Trans.* **1976**, *72*, 2685-2693.

(232) Fox, T. G.; Flory, P. J. *J. Appl. Phys.* **1950**, *21*, 581-591.

(233) Galla, H. J.; Hartmann, W.; Theilen, U.; Sackmann, E. *J. Membr. Biol* **1979**, *48*, 215-236.

(234) Geissler, M.; Xia, Y. N. *Adv. Mater.* **2004**, *16*, 1249-1269.

(235) Prime, K. L.; Whitesides, G. M. *Science* **1991**, *252*, 1164-1167.

(236) Santini, J. T.; Richards, A. C.; Scheidt, R.; Cima, M. J.; Langer, R. *Angew. Chem., Int. Ed.* **2000**, *39*, 2397-2407.

(237) McAlpine, M. C.; Friedman, R. S.; Lieber, D. M. *Nano Lett.* **2003**, *3*, 443-445.

(238) Park, J.; Kim, Y. S.; Hammond, P. T. *Nano Lett.* **2005**, *5*, 1347-1350.

(239) Li, S.; Clarke, C. J.; Lennox, R. B.; Eisenberg, A. *Colloids Surf. A: Physicochem. Eng. Aspects* **1998**, *133*, 191-203.

(240) Moraille, P.; Badia, A. *Angew. Chem., Int. Ed.* **2002**, *41*, 4303-4306.

(241) Sivasankar, S.; Brieher, W.; Lavrik, N.; Gumbiner, B.; Leckband, D. *Proc. Natl. Acad. Sci. U. S. A.* **1999**, *96*, 11820-11824.

(242) Wegner, G. *Thin Solid Films* **1992**, *216*, 105-116.

(243) Schwiegk, S.; Vahlenkamp, T.; Xu, Y. Z.; Wegner, G. *Macromolecules* **1992**, *25*, 2513-2525.

(244) Yase, K.; Schwiegk, S.; Lieser, G.; Wegner, G. *Thin Solid Films* **1992**, *210*, 22-25.

(245) Wang, X. Y.; Chen, Y. L.; Liu, H. G.; Jiang, J. Z. *Thin Solid Films* **2006**, *496*, 619-625.

(246) Sauer, T.; Arndt, T.; Batchelder, D. N.; Kalachev, A. A.; Wegner, G. *Thin Solid Films* **1990**, *187*, 357-374.

(247) Nisato, G.; Ermi, B. D.; Douglas, J. F.; Karim, A. *Macromolecules* **1999**, *32*, 2356-2364.

(248) Zhang, J. M.; Duan, Y. X.; Sato, H.; Tsuji, H.; Noda, I.; Yan, S. K.; Ozaki, Y. *Macromolecules* **2005**, *38*, 8012-8021.

(249) Zhang, J. M.; Sato, H.; Tsuji, H.; Noda, I.; Ozaki, Y. *Macromolecules* **2005**, *38*, 1822-1828.

(250) Zhang, J. M.; Sato, H.; Tsuji, H.; Ozaki, Y. *J. Molecular Struc.* **2005**, *735-736*, 249-257.

(251) Zhang, J. M.; Tsuji, H.; Noda, I.; Ozaki, Y. *J. Phys. Chem. B* **2004**, *108*, 11514-11520.

(252) Zhang, J. M.; Tsuji, H.; Noda, I.; Ozaki, Y. *Macromolecules* **2004**, *37*, 6433-6439.

(253) Kister, G.; Canssanas, G.; Vert, M. *Polymer* **1998**, *39*, 267-273.

(254) Kister, G.; Cassanas, G.; Vert, M. *J. Raman Spectroscopy* **1995**, *26*, 307-311.

(255) Bates, F. S. *Science* **1991**, *251*, 898-905.

(256) Folkes, M. J.; Keller, A. *J. Polym. Sci., Part B: Polym. Phys.* **1976**, *14*, 833-846.

(257) Fischer, E. W. *Z. Naturforsch* **1957**, *12a*, 753-754.

(258) Keller, A. *Philos. Mag.* **1957**, *2*, 1171-1175.

(259) Wu, J. H.; Lieser, G.; Wegner, G. *Adv. Mater.* **1996**, *8*, 151-154.

(260) Sakaguchi, H.; Matsumura, H.; Gong, H.; Abouelwafa, A. M. *Science* **2005**, *310*, 1002-1006.

(261) Bocharova, V.; Kiriy, A.; Vinzelberg, H.; Monch, I.; Stamm, M. *Angew. Chem., Int. Ed.* **2005**, *44*, 6391-6394.

(262) Angelova, A.; Vollhardt, D.; Ionov, R. *J. Phys. Chem.* **1996**, *100*, 10710-10720.

(263) Angelova, A.; Reiche, J.; Ionov, R.; Janietz, D.; Brehmer, L. *Thin Solid Films* **1994**, *242*, 289-294.

(264) Pezron, E.; Claesson, P. M.; Berg, J. M.; Vollhardt, D. *J. Colloid Interface Sci.* **1990**, *138*, 245-254.

(265) Kato, T. *Langmuir* **1990**, *6*, 870-872.

(266) Kato, T.; Hirobe, Y.; Kato, M. *Langmuir* **1991**, *7*, 2208-2212.

(267) Binks, B. P. *Adv. Colloid Interface Sci.* **1991**, *34*, 343-432.

(268) Ariga, K.; Shin, J. S.; Kunitake, T. *J. Colloid Interface Sci.* **1995**, *170*, 440-448.

(269) Vollhardt, D. *Adv. Colloid Interface Sci.* **1993**, *47*, 1-23.

(270) Ybert, C.; Lu, W. X.; Moller, G.; Knobler, C. M. *J. Phys. Chem. B* **2002**, *106*, 2004-2008.

(271) McFate, C.; Ward, D.; Olmsted, J. *Langmuir* **1993**, *9*, 1036-1039.

(272) Smith, R. D.; Berg, J. C. *J. Colloid Interface Sci.* **1980**, *74*, 273-286.

(273) Barraud, A.; Leloup, J.; Maire, P.; Ruaudelteixier, A. *Thin Solid Films* **1985**, *133*, 133-139.

(274) Vollhardt, D.; Retter, U. *J. Phys. Chem.* **1991**, *95*, 3723-3727.

(275) Vollhardt, D.; Retter, U.; Siegel, S. *Thin Solid Films* **1991**, *199*, 189-199.

(276) Vollhardt, D.; Retter, U. *Langmuir* **1992**, *8*, 309-312.

(277) Ries, H. E.; Kimball, W. A. *J. Phys. Chem.* **1955**, *59*, 94-95.

(278) Ries, H. E. *Nature* **1979**, *281*, 287-289.

(279) Nikomarov, E. S. *Langmuir* **1990**, *6*, 410-414.

(280) Milner, S. T.; Joanny, J. F.; Pincus, P. *Europhys. Lett.* **1989**, *9*, 495-500.

(281) Diamant, H.; Witten, T. A.; Ege, C.; Gopal, A.; Lee, K. Y. C. *Phys. Rev. E* **2001**, *63*, 061602/1-061602/12.

(282) Diamant, H.; Witten, T. A.; Gopal, A.; Lee, K. Y. C. *Europhys. Lett.* **2000**, *52*, 171-177.

(283) Saint-Jalmes, A.; Gallet, F. *Euro. Phys. J. B* **1998**, *2*, 489-494.

(284) Saint-Jalmes, A.; Graner, F.; Gallet, F.; Houchmandzadeh, B. *Europhys. Lett.* **1994**, *28*, 565-571.

(285) Bourdieu, L.; Daillant, J.; Chatenay, D.; Braslau, A.; Colson, D. *Phys. Rev. Lett.* **1994**, *72*, 1502-1505.

(286) Gopal, A.; Lee, K. Y. C. *J. Phys. Chem. B* **2001**, *105*, 10348-10354.

(287) Deng, J. J.; Farmer-Creely, C. E.; Viers, B. D.; Esker, A. R. *Langmuir* **2004**, *20*, 2527-2530.

(288) Deng, J. J.; Hottle, J. R.; Polidan, J. T.; Kim, H. J.; Farmer-Creely, C. E.; Viers, B. D.; Esker, A. R. *Langmuir* **2004**, *20*, 109-115.

(289) Deng, J. J.; Polidan, J. T.; Hottle, J. R.; Farmer-Creely, C. E.; Viers, B. D.; Esker, A. R. *J. Am. Chem. Soc.* **2002**, *124*, 15194-15195.

(290) Hottle, J. R.; Deng, J. J.; Kim, H. J.; Farmer-Creely, C. E.; Viers, B. D.; Esker, A. R. *Langmuir* **2005**, *21*, 2250-2259.

(291) Hottle, J. R.; Kim, H. J.; Deng, J. J.; Farmer-Creely, C. E.; Viers, B. D.; Esker, A. R. *Macromolecules* **2004**, *37*, 4900-4908.

(292) Kim, H. J.; Deng, J. J.; Lalli, J. H.; Riffle, J. S.; Viers, B. D.; Esker, A. R. *Langmuir* **2005**, *21*, 1908-1916.

(293) Bienkowski, R.; Skolnick, M. *J. Colloid Interface Sci.* **1972**, *39*, 323-330.

(294) Macritchie, F. *J. Colloid Interface Sci.* **1981**, *79*, 461-464.

(295) Kuo, R.-R.; Chang, C.-H.; Yang, Y.-M.; Maa, J.-R. *J. Colloid Interface Sci.* **2003**, *257*, 108-115.

(296) Notter, R. H.; Taubold, R.; Mavis, R. D. *Exp. Lung Res.* **1982**, *3*, 109-127.

(297) Cho, D.; Cornec, M. *Korean J. Chem. Eng.* **1999**, *16*, 371-376.

(298) Snik, A. F. M.; Kruger, A. J.; Joos, P. *J. Colloid Interface Sci.* **1978**, *66*, 435-439.

(299) Malcolm, B. R. *J. Colloid Interface Sci.* **1985**, *104*, 520-529.

(300) Peng, J. B.; Barnes, G. T. *Langmuir* **1990**, *6*, 578-582.

(301) Brinkhuis, R. H. G.; Schouten, A. J. *Macromolecules* **1992**, *25*, 2732-2738.

(302) Avrami, M. *J. Chem. Phys.* **1939**, *7*, 1103-1112.

(303) Avrami, M. *J. Chem. Phys.* **1940**, *8*, 212-224.

(304) Avrami, M. *J. Chem. Phys.* **1941**, *9*, 177-184.

(305) Eling, B.; Gogolewski, S.; Pennings, A. J. *Polymer* **1982**, *23*, 1587-1593.

(306) Puiggali, J.; Ikada, Y.; Tsuji, H.; Cartier, L.; Okihara, T.; Lotz, B. *Polymer* **2000**, *41*, 8921-8930.

(307) Cartier, L.; Okihara, T.; Ikada, Y.; Tsuji, H.; Puiggali, J.; Lotz, B. *Polymer* **2000**, *41*, 8909-8919.

(308) Koenig, J. L. *Spectroscopy of Polymers*; American Chemical Society: Washington DC, 1992.

(309) Chalmers, J. M.; Hannah, R. W.; Mayo, D. W. In *Handbook of Vibrational Spectroscopy*; Chalmers, J. M., Griffiths, P. R., Eds.; John Wiley & Sons: Chichester, 2002, p 1893-1918.

(310) Bower, D. I.; Maddams, W. F. *The Vibrational Spectroscopy of Polymers*; Cambridge University Press: Cambridge, 1989.

(311) Mallapragada, S. K.; Narasimhan, B. In *Encyclopedia of Analytical Chemistry*; Meyers, R., Ed.; John Wiley & Sons: Chichester, 2002, p 7644-7658.

(312) Bulkin, B. J.; Lewin, M.; DeBlase, F. J. *Macromolecules* **1985**, *18*, 2587-2594.

(313) Zhu, X. Y.; Yan, D. Y.; Fang, Y. P. *J. Phys. Chem. B* **2001**, *105*, 12461-12463.

(314) Duan, Y. X.; Zhang, J. M.; Shen, D. Y.; Yan, S. K. *Macromolecules* **2003**, *36*, 4874-4879.

(315) Kang, S. H.; Hsu, S. L.; Stidham, H. D.; Smith, P. B.; Leuger, M. A.; Yang, X., Z. *Macromolecules* **2001**, *34*, 4542-4548.

(316) Cohn, D.; Younes, H. *J. Biomed. Mater. Res.* **1982**, *22*, 993-1009.

(317) Lee, J. K.; Lee, K. H.; Jin, B. S. *Eur. Polym. J.* **2001**, *37*, 907-914.

(318) Sawai, D.; Takahashi, K.; Sasashige, A.; Kanamoto, T.; Hyon, S. H. *Macromolecules* **2003**, *36*, 3601-3605.

(319) Qin, D.; Kean, R. T. *Appl. Spectrosc.* **1998**, *52*, 488-495.

(320) Blazewicz, M.; Gajewska, M. C.; Paluszkiewicz, C. *J. Molec. Struc.* **1999**, *483*, 519-524.

(321) Ulman, A. *ACS Symp. Series* **1991**, *447*, 144-159.

(322) Knobler, C. M. *Adv. Chem. Phys.* **1990**, *77*, 397-449.

(323) Ostwald, W. *Lehrbuch der allgemeinen Chemie. Second edition.*; W. Engelmann: Leipzig, 1896.

(324) Ostwald, W. *Z. Phys. Chem.* **1897**, *22*, 289.

Vita

Suolong Ni was born on February 10, 1976, in Jintan, Jiangsu, China, to Shuchun Ni and Shuangbao Xu. After growing up in Jintan with his sister, Jie Ni, and graduating at the top of his class from Hua Luogen Middle School in 1994, Suolong attended Nanjing University as a direct admission student. He studied in the Department for Intensive Instructions and did his undergraduate research with Prof. Changzheng Yang in the Department of Chemistry starting in 1996. After obtaining his Bachelor of Science degree in 1998, Suolong worked as a research assistant for Prof. Yang. Suolong started his graduate studies in the Department of Polymer Science and Engineering at Nanjing University in 1999, and obtained his Master of Science degree in July 2002. In the Fall of 2002, Suolong started his Ph. D study in physical chemistry under the supervision of Prof. Alan R. Esker in the Department of Chemistry at Virginia Tech. Suolong worked as a graduate teaching assistant, graduate research assistant, and course instructor in the Department of Chemistry at Virginia Tech during his graduate studies. Upon completion of his graduate studies in Blacksburg in December 2006, Suolong will move back to China to take a position with DuPont China Holding Co., Ltd.